Parton phenomena in doped quantum magnets and quantum simulators

from Hubbard models to lattice gauge theories

Lukas Homeier

München 2024

Parton phenomena in doped quantum magnets and quantum simulators

from Hubbard models to lattice gauge theories

Lukas Homeier

Dissertation
der Fakultät für Physik
der Ludwig-Maximilians-Universität
München

vorgelegt von
Lukas Josef Anton Homeier
aus Regensburg

München, den 22. Mai 2024

To my family

Zusammenfassung

Stark korrelierte Elektronen zeigen einige der exotischsten Verhaltensweisen, unter anderem die Fraktionalisierung der fundamentalen Bausteine – die Elektronen – in kleinere sogenannte Partons. Diese Partons können entweder in einem deconfined Zustand vorliegen, wie in Quantenspinflüssigkeiten, oder confined als gebundene Zustände existieren, wie in dotierten antiferromagnetischen Mott Isolatoren.

In dieser Dissertation betrachten wir die mikroskopische, innere Struktur von gebundenen Partonzuständen in dotierten Quantenmagneten, was uns zu dem Phänomen einer emergenten Feshbach Resonanz führt – ein bekanntes Konzept in Teilchen- und Atomphysik. Für Fermi-Hubbard-artige Modelle finden wir starke attraktive Paarwechselwirkungen zwischen Ladungsträgern mit robuster $d_{x^2-y^2}$-Wellen Symmetrie konsistent mit der Phänomenologie von Supraleitung in Cupraten. Der vorgeschlagene Feshbach Paarungsmechanismus ist möglicherweise eine neue Erklärung für den lang ersehnten Paarungskleber in Hochtemperatursupraleitern aus Kupferverbindungen.

Darüberhinaus etablieren wir effektive Partonmodelle für gemischt-dimensionale doppelschichtige Hubbardmodelle, für welche wir bemerkenswert hohe Bindungsenergien vorhersagen und exzellente Übereinstimmung mit numerischen Simulationen finden. Zusätzlich diskutieren wir mögliche Signaturen von Feshbach Resonanzen in gemischt-dimensionalen 1D Leitern sowie deren Relevanz für kürzlich entdecke Hochtemperatursupraleiter aus Nickelverbindungen.

Um die emergenten Partonphänomene zu testen, schlagen wir neue Schemata für die analoge Quantensimulation von dotieren Quantenmagneten vor. Insbesondere entwickeln wir ein Schema um antiferromagnetische *t-J-V-W* Modelle in drei internen Zuständen von kalten Molekülen oder Rydberg Atomen in Gittern aus optischen Fallen zu realisieren. Der dipolare Ursprung der magnetischen Wechselwirkung erlaubt uns zuvor experimentell unerreichbare Parameterbereiche zu studieren. Wir präsentieren vorläufige experimentelle Resultate, welche in Rydberg tweezer arrays erzielt wurden.

Ein weiterer typischer Rahmen um Partonphänomene zu beschreiben sind Gittereichtheorien. Deren Quantensimulation würde uns nicht nur erlauben die effektiven Niedrigenergie Theorien von stark korrelierten Elektronen zu untersuchen, sondern auch Themen von Teilchenphysik bis hin zu Quanteninformation. Allerdings erweist sich die großskalige Quantensimulation von Gittereichtheorien mit dynamischer Materie und jenseits von $(1+1)$D als anspruchsvoll. In dieser Dissertation fokussieren wir uns auf top-down Methoden um Gittereichtheorien zu simulieren, wobei die Eichstruktur aus starken energetischen Blockaden hervorgeht.

Insbesondere entwickeln wir theoretische Methoden um abelsche $\mathbb{Z}_2$ Gittereichtheorien mit hard-core bosonischer Materie in $(2+1)$D mit experimentell realisierbaren Zweiteilchen Ising Wechselwirkungen zu stabilisieren. Dies erlaubt uns ein realistisches, großskaliges Schema für die analoge Quantensimulation von $\mathbb{Z}_2$ Gittereichtheorien in Rydberg tweezer arrays zu entwicklen. Außerdem finden wir, dass antiferromagnetische $\mathrm{SU}(N)$ Heisenberg Wechselwirkungen ausreichen um nicht-abelsche Eichstrukturen energetisch zu stabilisieren. Darüberhinaus schlagen wir ein experimentelles Schema für die Implementierung von $\mathrm{U}(N)$ and $\mathrm{SU}(N)$ Gittereichtheorien (i) mit hard-core bosonischer

Materie in ultrakalten polaren Molekülen in optischen Gittern oder Rydberg tweezer arrays sowie (ii) mit fermionischer Materie in ultrakalten Erdalkalimetallen vor.

Die vorgeschlagenen experimentellen Schemen für die Quantensimulation von dotierten Quantenmagneten und Gittereichtheorien in optischen Fallen sowie die Entwicklung analytischer Modelle für Paarung in Hochtemperatursupraleiter ebnen den Weg um Partonphänomene in stark korrelierter Quantenmaterie aus einer mikroskopischen Perspektive zu untersuchen.

Abstract

Strongly correlated electrons exhibit some of the most exotic behaviors, including the fractionalization of their fundamental constituents – the electrons – into smaller components known as partons. The partons can either exists as deconfined particles, as in quantum spin liquids, or become confined into bound states, as in doped antiferromagnetic Mott insulators.

In this thesis, we take into account the microscopic internal structure of the parton bound states in doped quantum magnets, which leads us to the picture of an emergent Feshbach resonance – a concept well-known in particle and atomic physics. For Fermi-Hubbard-type models, we find strong attractive pairing interactions between charge carriers with robust $d_{x^2-y^2}$-wave symmetry, consistent with the phenomenology of cuprate superconductors. This proposed Feshbach pairing mechanism provides a new possible explanation for the long sought pairing glue in high-Tc cuprate compounds.

Furthermore, we establish effective parton models for mixed-dimensional bilayer Hubbard models, and we predict remarkably large binding energies in excellent agreement with numerical simulations. In addition, we discuss potential signatures of emergent Feshbach resonances in mixed-dimensional 1D ladders, and their relevance for the recently discovered high-Tc nickelate compounds.

To probe the emergent parton phenomena, we propose novel schemes for the analog quantum simulation of doped quantum magnets. In particular, we develop a scheme to realize an antiferromagnetic, bosonic t-J-V-W model in three internal states of cold molecules or Rydberg atoms in optical tweezer arrays. The dipolar origin of the magnetic interactions allows us to explore previously experimentally inaccessible parameter regimes, for which we present preliminary experimental results obtained in Rydberg tweezer arrays.

Another common framework to describe parton phenomena are lattice gauge theories (LGTs). Their quantum simulation would not only enable us to directly study low-energy effective theories of strongly correlated electrons, but also topics ranging from particle physics to quantum information. However, achieving large-scale quantum simulations of LGTs with dynamical matter and beyond $(1+1)$D remains elusive. In this thesis, we focus on top-down approaches to simulate LGTs, where the gauge structure emerges from strong energy penalties.

In particular, we theoretically develop a method to stabilize an Abelian $\mathbb{Z}_2$ LGTs with hard-core bosonic matter in $(2+1)$D, which only requires experimentally feasible two-body Ising interactions. This allows us to propose a realistic analog quantum simulation scheme for the large-scale implementation of $\mathbb{Z}_2$ LGTs in Rydberg tweezer arrays. Moreover, we find that antiferromagnetic $SU(N)$ Heisenberg interactions suffice to energetically stabilize non-Abelian gauge constraints. Additionally, we propose experimental schemes to implement $U(N)$ and $SU(N)$ LGTs (i) with hard-core bosonic matter in ultracold polar molecules or Rydberg tweezers, and (ii) with fermionic matter in ultracold alkaline-earth atoms.

The proposed experimental schemes for the quantum simulation of doped quantum magnets and lattice gauge theories in tweezer arrays as well as the development of analytical models for pairing in high-Tc superconductors paves the way to explore parton phenomena in strongly correlated quantum matter from a microscopic perspective.

Acknowledgements

Without any doubts, my deepest gratitude goes to my advisor Prof. Fabian Grusdt. The work and results reported in this thesis are rooted in his outstanding creativity, enthusiasm and curiosity. I could go on and list many more examples ranging from his great intuition about physics to his extraordinary teaching skills. However, I want to highlight one particular thing for which I am especially grateful: Fabian's fulfilling role a mentor. As a graduate student, the most valuable thing I could receive was the constant support and the countless doors Fabian opened for my future. I would like to thank you for the fantastic time in your research group, for your guidance in the past 4.5 years, and your patience to listen to my ideas, thoughts and beyond.

A big gratitude and admiration goes to my co-advisor Prof. Eugene Demler. His deep knowledge, intuition and ability to connect seemingly disconnected phenomena inspires numerous generations of physicists and is the foundation of much of the research underlying my thesis. Discussing physics with Eugene is a very positively intense and stimulating experience, and it fuels my brain with ideas for a long time. I would like to thank you for the numerous things you taught me, for your encouragement, for your support over the past years and for your hospitality at ETH Zurich.

Next, I want to acknowledge and thank my committee members, Prof. Immanuel Bloch and Prof. Dmitri Efetov. Especially, I would like to thank Immanuel, who not only sparked my excitement for this scientific field when I was a young student but also enabled the incredible opportunity to visit the research group of Prof. Monika Schleier-Smith for an extended period after my Bachelor's. This experience has significantly influenced where I am today.

I wish to thank Prof. Annabelle Bohrdt, who fulfilled an equally important role as supervisor during my PhD. When we first started to collaborate, she was about to finish up her PhD and now she is a Professor with her own research group. I think this speaks for itself and I am very impressed about it. Thank you, Annabelle, for the many insights and wonderful physics I was allowed to explore together with you.

I want to thank Dr. Jad. C. Halimeh for our many past and future collaborations, for teaching me a new perspective on quantum simulation of gauge theories, and for constantly pushing his ambitious plans. Jad always guided me back on the track of our projects, which I am thankful about at times when I was lost in details. Your ideas and input has significantly shaped the many exciting projects during my PhD.

Further, I am very happy to have interacted a lot with Prof. Lode Pollet in the past year. I find a real pleasure in collaborating with him and I am really fascinated by his incredible competence. I want to thank you, in the name of many people in our chair, that you are joining our group of students so often for lunch to discuss physics.

Importantly, I would like to express my gratitude to Prof. Ulrich Schollwöck, the head of our chair, who makes many things possible for the students in the background that we

do not even notice and take for granted. I thank Prof. Schollwöck for the many joyful conversations, also beyond physics.

Another important person to talk and to collaborate with, starting during my Master's and throughout my PhD, is Prof. Monika Aidelsburger. I have collected a lot of my knowledge about quantum simulators through discussion with you and it is also really fun to work out theoretical ideas together. In this regard, I also want to acknowledge Dr. Christian Schweizer for his patience and his excellent explanations, when I just started to work in the field of gauge theories – honestly my perspective about gauge theories is very much shaped by our discussions back in my Master's.

Since Matjaž Kebrič and I were the very first members of the Grusdt group, I technically have to acknowledge every single group member who was ever associated with the Grusdt group. First I want to thank everyone for a great time and beers together, for Frühlingsfest and Oktoberfest, for Atzinger and Lindwurmstüberl. I really enjoyed being part of a wonderful team and being among so many talented and ambitious people.

In particular, I wish to thank ...

... Felix Palm for his joyfulness and great helpfulness to everyone in the group. I felt really touched the one time you respectfully acknowledged my skills in drinking beer.

... Gaia De Paciani for collaborating together on new ways to implement non-Abelian gauge theories. It's really wild how Fabian and I are just throwing ideas at you, and I am really impressed how you handle all these vague ideas and make something great out of it.

... Hannah Lange for many, many things in the past 1.5 years. Scientifically, of course, I am really glad to have worked on numerous projects together and it's so helpful to discuss with you. I am happy to have you as an office mate, who is equally excited about coffee. And I am glad to have you as a friend especially during our time at Harvard!

... Henning Schlömer for our common time together at the legendary ITAMP. You are a very brilliant physicist and it's a bummer that we never had the chance to work more closely together.

... Matjaž Kebrič for being my longest companion on this research journey – and who I am glad to have around in Boulder for at least another two years!! It was so helpful to learn together about gauge theories. Beyond physics, I want to thank you for many great common memories starting in our tiny 10-student Master's office in the B-tower.

... Nader Mostaan for the many intriguing discussions and for laughing a lot together in our office. I am thankful to personally know the incarnation of the Bose Polaron.

... Pit Bermes for our collaborations on the Feshbach projects. Because you are so competent in what you are doing, it's just really exciting and productive, and especially fun to discuss with you.

... Simon Linsel for working together on our exciting $\mathbb{Z}_2$ lattice gauge projects – you are my Monte Carlo and personal IT hero. I want to thank you for the many hours we laughed together in the office, or at conferences!

... Tim Harris for sharing so many common interests and I just really appreciate to collaborate with you or just discuss and brainstorm. I am so happy and thankful to have you as a peer and to have someone who is actually excited and so knowledgeable about understanding details of experiments.

... Tizian Blatz for collaborating with you on the bosonic *t-J* model and I am super impressed by the many numerical skills you combine.

In addition, I wish to thank the many current and past members of the Schollwöck chair and Annabelle's group, especially Damiano Aliverti-Piuri, Fabian Pauw, Fabian Döschl, Giovanni Canossa, Hèloïse Albot, Julia Liebert, Lexin Ding, Mattia Moroder, Nicolas Sadoune, Pietro Borchia, Rajah Nutakki, Valentin Schwarz and Zhenjiu Wang. Further, I want to express an extra acknowledgement to Fabian, Matjaž, Tim, Pit and Simon for really helpful feedback on parts of this thesis.

Moreover, I would like to thank the entire MCQST and IMPRS community, from the scientists to the administrators, every single one is such a creative mind. I had the great pleasure to participate in a few outreach projects together with Anca Ionescu and Christoph Hohmann, e.g., in a project together with film making students at the Bauhaus university in Weimar. Thank you for realizing so many great projects and conferences making MCQST and IMPRS a very special place to be.

A big "thank you" is dedicated to the Harvard Physics community, where I ended up spending almost half of my PhD. First, I am really grateful to Prof. Markus Greiner, Prof. Hossein Sadeghpour and Prof. Eugene Demler who supported me to visit for such an extended period of time.

It is hard to put in words how thankful I am to the entire Greiner group for the hospitality, for welcoming us, and for including us in their group. I am grateful about the many discussions we had and about all the physics you taught me. You have no idea how much time I spent with the coffee machine in Greiner lounge during my 6am meetings with Munich. Thanks to Anant Kale, Alexander Douglas, Brice Bakkali-Hassani, Joyce Kwan, Julian Léonard, Lev Kendrick, Lin Su, Martin Lebrat, Markus Greiner, Michal Szurek, Muqing Xu, Ognjen Markovic, Perrin Segura, Sooshin Kim, Vassilios Kaxiras, Yanfei Li and Youqi Gang.

Also, I wish to thank the ITAMP for hosting me for half a year. I have so many positive memories about that time, from laughing together in the office, to scientifically exciting discussions and talks, to drinking beer at Cambridge's #1 roof top bar, to playing soccer or enjoying the Winter school in Arizona. Thanks to Annabelle Bohrdt, Ceren Dag, Francisco Machado, Hossein Sadeghpour, Jaclyn Donahue, Jim Babb, Symeon Mystakidis, Valentin Walther and Vasil Rokaj.

Moreover, I am extremely happy and thankful to have found Simon Hollerith, Sebastian Geier and Neng-Chun (Allen) Chiu from the Atom Array II team as really, really great (theory) collaborators on the bosonic *t-J* project and on many more ideas we are exploring in Rydberg tweezers. There are countless things I learned from you about Rydberg physics

and about experimental platforms. Thanks for the many weekends we were pushing our ideas together.

Another special person and friend during my time at Harvard is Dan Borniga. Dan is not only a brilliant peer, but we were also office mates and later we even became roommates. Thanks for the many fun moments, dinners, coffees and walks we had together!

I really also want to thank Prof. Kang-Kuen Ni and the members of the NaCs molecule lab, Annie Park, Gabriel Patenotte and Lewis Picard, for all the stimulating discussions we are having about implementation of t-J models in your platform.

There are many more people I am grateful to know from my time at Harvard, who made this special time even more special, including Andrea Pizzi, Alex Lukin, Dolev Bluvstein, Erik Knall, Fangli Liu, Harry Zhou, Henry Shackleton, Johannes Feldmeier, Misha Lukin, Nishad Maskara, Rhine Samajdar, Rahul Sahay, Sepehr Ebadi, Simon Evered, Tim Guo, Tout Wang and Zeyu Hao.

I am very thankful about a great on-going collaboration on the t-J-V-W model with the group of Prof. Antoine Browaeys at the Institute d'Optique. Let me take this opportunity to thank the Rubidium Rydberg tweezer team, including Cheng Chen, Gabriel Emperauger, Guillaume Bornet, Mu Qiao and Thierry Lahaye. I am actually very excited about what we are exploring together and how you push this project.

Further, I wish to thank Dr. Johannes Zeiher's Strontium Rydberg team at the MPQ in Munich. From the discussion we are having about implementations of lattice gauge theories, I learnt so many new things. Most importantly, I learnt many new details about the scheme we are actually convincing you to realize, because you are always keep asking the important questions I have not considered before. A big "thanks" to Flavien Gyger, Hendrik Timme, Johannes Zeiher, Maxmilian Ammenwerth and Renhao Tao.

I also want to thank the fantastic people of Prof. Monika Schleier-Smith's group at Stanford, where I spent an extended period of time in the Cavity lab before switching to theory. I know this fact suggest something else, but I truly enjoyed working in the lab! The way I am thinking about quantum simulators and cold atom platforms today is very much shaped by the great physical intuition you all taught me. In addition, I think it is beautiful that I actually had the chance to meet with every single one of you again during my PhD. Thanks to Emily Davis, Gregory Bentsen, Jacob Hines, Monika Schleier-Smith, Ognjen Markovic, Simon Evered, Tori Borish and Tracy Li.

Moreover, I would not even have nearly managed to finish my PhD without the countless administrators who were always helpful. Thank you Bonnie Currier, Cordula Weber, Jaclyn Donahue, Kathrin Higgen and Sonya Gzyl.

As a graduate student, one experiences lots of ups and downs, and therefore I think it's really great to have amazing roommates. Since I moved between Munich and Boston, there are many people I had the pleasure to share my home with. Let me highlight and especially thank Dan Borgnia, Johannes Moser, Romaine Loubes, Robin Groth and Thomas Bezy!

There are so many people I have to thank outside of the physics community. My family and friends from Regensburg who have been with me on that journey for the longest time. When I started my PhD, it was still the first year of the pandemic and certainly not the easiest time. But friends and family made it a bit easier for me. I wish to thank everyone

for patiently listening to my thoughts and boring physics stories, and for all the beautiful memories.

Lastly, I want to express my deep gratitude to my parents and my brother David for their unconditional support – thank you ♡

Author's contributions

In the following, the author's publications and preprints resulting from the doctoral studies are listed. They form the basis of the material presented in this thesis, partially with textual overlap. The research is the result of collaborations with a variety of authors. My contributions to the individual publications are stated below.

Publications in peer-reviewed journals

[P1]   A. Bohrdt, L. Homeier, C. Reinmoser, E. Demler, and F. Grusdt, "Exploration of doped quantum magnets with ultracold atoms", Annals of Physics **435**, 168651 (2021).

> LH contributed to the study of the mixD bilayer Hubbard system and performed the mean-field analysis. AB and FG supervised the project. All authors contributed to the writing of the manuscript.

[P2]   A. Bohrdt, L. Homeier, I. Bloch, E. Demler, and F. Grusdt, "Strong pairing in mixed-dimensional bilayer antiferromagnetic Mott insulators", Nature Physics **18**, 651–656 (2022).

> LH, AB and FG derived the effective parton model. AB performed the DMRG simulations. FG supervised the project. All authors contributed to the writing of the manuscript.

[P3]   J. C. Halimeh, L. Homeier, H. Zhao, A. Bohrdt, F. Grusdt, P. Hauke, and J. Knolle, "Enhancing Disorder-Free Localization through Dynamically Emergent Local Symmetries", PRX Quantum **3**, 020345 (2022).

> LH, JCH and FG proposed the experimental scheme. JCH and JK supervised the project. All authors contributed to the writing of the manuscript.

[P4]   J. C. Halimeh, L. Homeier, C. Schweizer, M. Aidelsburger, P. Hauke, and F. Grusdt, "Stabilizing lattice gauge theories through simplified local pseudogenerators", Physical Review Research **4**, 033120 (2022).

> LH and CS contributed to the conceptual ideas and to the 2D scheme. JCH performed all numerical simulations. FG supervised the project. All authors contributed to the writing of the manuscript.

[P5]   L. Homeier, A. Bohrdt, S. Linsel, E. Demler, J. C. Halimeh, and F. Grusdt, "Realistic scheme for quantum simulation of $\mathbb{Z}_2$ lattice gauge theories with dynamical matter in $(2+1)$D", Communications Physics **6**, 127 (2023).

LH, JCH and FG devised the initial concept. LH proposed the idea for the two-dimensional model, worked out the main analytical calculations and performed the exact diagonalization studies. LH , AB and FG proposed the experimental scheme. SL performed the Monte Carlo simulations. AB conducted the DMRG calculations. All authors contributed substantially to the analysis of the theoretical results and writing of the manuscript.

[P6]   H. Lange, L. Homeier, E. Demler, U. Schollwöck, F. Grusdt, and A. Bohrdt, "Feshbach resonance in a strongly repulsive ladder of mixed dimensionality: a possible scenario for bilayer nickelate superconductors", Physical Review B **109**, 045127 (2024).

HL performed all calculations. LH contributed to the conceptual ideas of the parton and Feshbach model. AB and FG supervised the project. All authors contributed to the writing of the manuscript.

[P7]   L. Homeier, P. Bermes, and F. Grusdt, "Scattering theory of mesons in doped antiferromagnetic Mott insulators: Multichannel perspective and Feshbach resonance", Physical Review B **109**, 125135 (2024).

LH formulated the analytical framework and performed the numerical calculations. PB implemented the truncated basis method. LH and FG proposed the initial concept. FG supervised the project.

[P8]   L. Homeier, T. J. Harris, T. Blatz, S. Geier, S. Hollerith, U. Schollwöck, F. Grusdt, and A. Bohrdt, "Antiferromagnetic Bosonic $t-J$ Models and Their Quantum Simulation in Tweezer Arrays", Phys. Rev. Lett. **132**, 230401 (2024).

LH performed the analytical calculations and developed the experimental schemes. LH, FG and AB proposed the cold molecule setup, with the help of TJH. LH, SG and SH proposed the Rydberg implementation scheme. TJH and TB performed all DMRG calculations. FG and AB supervised the project. All authors contributed to the writing of the manuscript.

Publications submitted to peer-reviewed journals

* These authors contributed equally.

[P9]   J. C. Halimeh∗, L. Homeier∗, A. Bohrdt, and F. Grusdt, "Spin exchange-enabled quantum simulator for large-scale non-Abelian gauge theories", arXiv **2305.06373** (2023).

JCH conceived the idea of dynamical gauge protection. JCH, LH, and FG adapted the idea to experimentally relevant non-Abelian systems. LH devised the experimental proposal for alkaline-earth atoms, with help from FG. LH devised the experimental proposal for ultracold molecules, with help from AB. JCH performed all numerical simulations. LH performed all analytic derivations. JCH and LH wrote the bulk of the manuscript, with all authors contributing to its preparation.

[P10]   H. Lange, L. Homeier, E. Demler, U. Schollwöck, A. Bohrdt, and F. Grusdt, "Pairing dome from an emergent Feshbach resonance in a strongly repulsive bilayer model", arXiv **2309.13040** (2023).

HL performed all calculations. LH contributed to the conceptual ideas of the parton and Feshbach model. AB and FG supervised the project. All authors contributed to the writing of the manuscript.

[P11]   L. Homeier, H. Lange, E. Demler, A. Bohrdt, and F. Grusdt, "Feshbach hypothesis of high-Tc superconductivity in cuprates", arXiv **2312.02982** (2023).

LH performed all calculations. FG supervised the work. LH, AB and FG devised the conceptual idea. All authors jointly analyzed the results and proposed possible experimental tests. LH and FG wrote the manuscript, with input from HL, ED and AB.

[P12]   S. M. Linsel, A. Bohrdt, L. Homeier, L. Pollet, and F. Grusdt, "Percolation as a confinement order parameter in $\mathbb{Z}_2$ lattice gauge theories", arXiv **2401.08770** (2024).

SL performed all numerical simulations. LH contributed to the conceptual ideas. All authors contributed to the writing of the manuscript. LP and FG supervised the work.

Contents

INTRODUCTION

"Whether it be the sweeping eagle in his flight, or the open apple-blossom, the toiling work-horse, the blithe swan, the branching oak, the winding stream at its base, the drifting clouds, over all the coursing sun, form ever follows function, and this is the law. Where function does not change, form does not change."

— Louis Sullivan (1856-1924)

Introduction

ORM FOLLOWS FUNCTION. This concept was coined by Louis Sullivan [1], an architect for skyscrapers in the 19th century, and later became the guiding principle of the Bauhaus, a pioneering design school in Germany. It describes the notion that the form of an object shall naturally follow from its intended function:

All things in nature have a shape, that is to say, a form, an outward semblance, that tells us what they are, that distinguishes them from ourselves and from each other [1].

According to this principle, if we understand the apparent form of an object, this already allows us deduce its characteristic features. This concept can be transferred to the way we formulate theories and approach problems in natural sciences and will serve as the guiding principle in this thesis. Simultaneously, it is accompanied by the idea of "coarse graining" from the perspective that details are neglected and that problems are reduced to their bare phenomenology. Therefore, this thesis is more about *qualitative and phenomenological* features of strongly correlated quantum matter, and less about – equally important – quantitative features relevant to understand details of specific materials or critical phenomena. Specifically, the principle of *form follows function* will be applied bidirectionally. Firstly, we propose simple experimental schemes, where properties such as symmetries are guiding us to develop efficient minimal protocols for the quantum simulation of lattice gauge theories. Secondly, we employ the perspective of quantum gas microscopes [2] to analyze the form of microscopic correlations. This approach enables us to theoretically formulate models capturing phenomena of pairing in cuprate superconductors and other strongly correlated systems.

These systems play a central role in the research of condensed matter and quantum many-body physics [3, 4]. When particles interact very strongly, the prevailing correlations across the system can be so dominating that any theoretically or computationally tractable method reaches its limit [5]. The classes of problems typically involve competing effects, such as strong repulsion and kinetic energy, leading to exotic, sometimes hidden ordering of the particles [6]. Unpacking such hidden structures [7, 8] can give insights into the underlying mechanisms of the emergent phases and help us to comprehend the complexity of strongly correlated quantum matter. From a foundational science perspective, these systems represent an entire class of models, for which no unified approach to treat them has been put forward. At the same time, strongly correlated systems are common in nature such as in materials [9], in the early universe or in neutron stars [10].

Other places, where strongly interacting quantum matter is realized, are quantum simulators. The hardware can be versatile: prominent platforms include cold atoms [11, 12], trapped ions [13] or superconducting qubits [14]. In these experiments, microscopic models are precisely engineered to emulate, e.g., the physics of condensed matter systems or gauge theories [15] in a tunable fashion and with access to in-situ, site-resolved snapshots of the many-body Fock state [P1].

The intimate connection between condensed matter systems and gauge theories can be understood from a projective parton construction [3, 16–20]. One common parton ansatz [21], among many others, fractionalizes the underlying electrons $\hat{c}_{j,\sigma}$ such that

$$\hat{c}_{j,\sigma} = \hat{h}_j^\dagger \hat{f}_{j,\sigma}. \tag{1}$$

I.e., the fermionic electron annihilation operator $\hat{c}_{j,\sigma}$ at site j with spin-1/2 ($\sigma = \downarrow, \uparrow$) is split into two partons: the fermionic, spinless chargon/holon $\hat{h}_j$ and the bosonic spinon $\hat{f}_{j,\sigma}$. In addition, the parton construction imposes the local particle number constraint

$$\hat{h}_j^\dagger \hat{h}_j + \sum_\sigma \hat{f}_{j,\sigma}^\dagger \hat{f}_{j,\sigma} = 1. \tag{2}$$

So far, the original operators were just formally re-written. The power of the parton ansatz manifests when the constraint (2) is lifted, as an approximation. This requires to glue together the partons by introducing a dynamical lattice gauge field [3]. Therefore, similar constructions are also extensively used for mean-field descriptions of quantum spin liquids due to their low-energy emergent gauge structure [22].

Historically, lattice gauge theories (LGTs) were introduced as an ultraviolet regularization of continuum gauge theories in high-energy physics [26]. In parallel, it was discovered by Wegner [27], Fradkin and Shenker [28] that even the simple, discreet gauge group "$\mathbb{Z}_2$" poses an interesting model for statistical physics with a paradigmatic phase diagram featuring phases of matter that are crucial for our modern understanding of correlated systems [4], topological order [29] and non-Abelian gauge theories [26]. While theoretically the $\mathbb{Z}_2$ LGT is appealing to study, from an experimental side their direct implementation in $(2+1)$D is a nightmare: strong four-body interactions.

Here, we arrive at our first example to apply the principle of *form follows function*. In this thesis, we develop theoretical techniques to reduce the experimental complexity for the implementation of a $\mathbb{Z}_2$ LGT in $(2+1)$D with dynamical matter from four-body to two-body interactions [P4, P5]. This yields an experimentally feasible scheme for Rydberg tweezer arrays arranged in a honeycomb geometry, see Chapter 3. This allows to realize a manifestly gauge-invariant effective Hamiltonian, whose exact form is determined by the specific details of the scheme.

From this perspective, LGTs offer a rich playground of models to be explored in current and next-generation quantum simulators [15], see Figure 1. In Part I of this thesis, we cover a variety of quantum simulation applications for LGTs including experimental schemes for the large-scale implementation of Abelian $\mathbb{Z}_2$ and non-Abelian $U(N)$ and $SU(N)$ models [P4, P5, P9, P3]. From the theoretical side, we develop energetic gauge pro-

matter sites
> spin 1/2 = hard-core bosons
> fermions

links (electric/gauge field)
> spin 1/2
> large-S
> fermion double wells

local symmetry constraints
$$\hat{G}_j \left|\psi\right\rangle = g_j \left|\psi\right\rangle$$
> $\mathbb{Z}_2$: local parity
> U(1): local particle number
> SU(2): local total spin

Rydberg tweezers   **ultracold molecules**   **ultracold fermions**
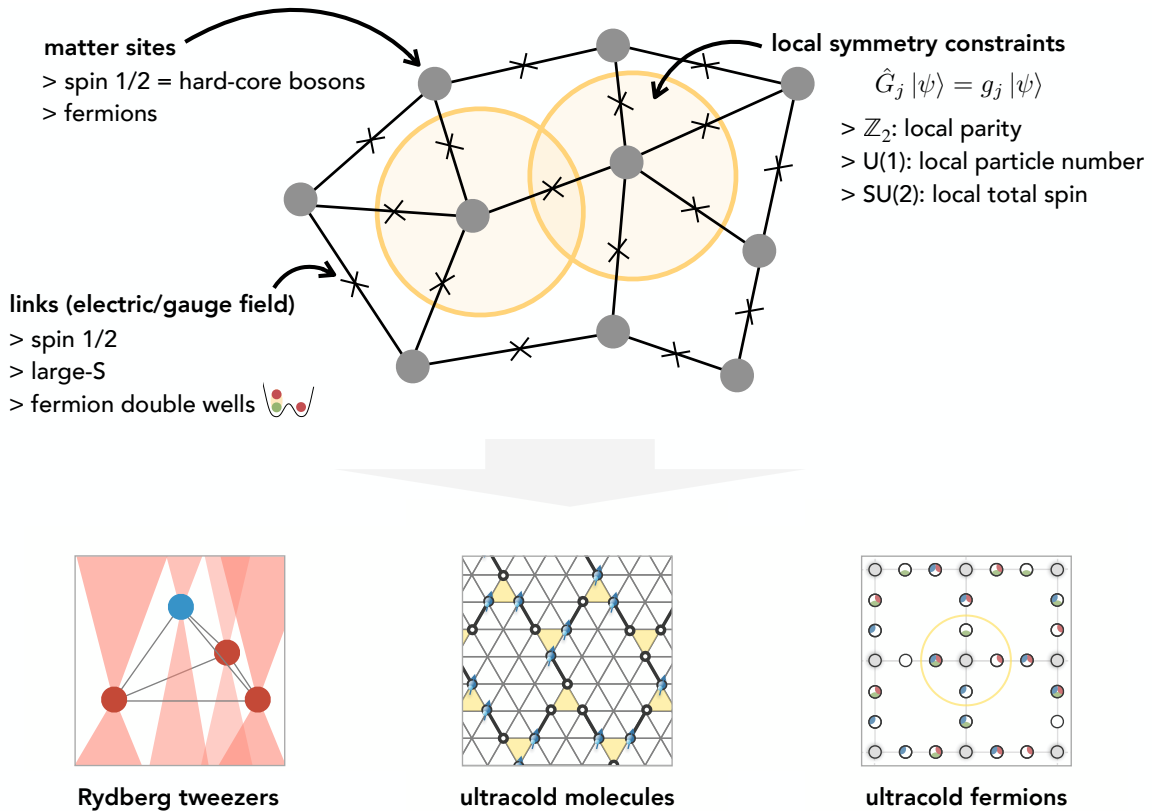
Figure 1: **Lattice gauge theories and their quantum simulation.** Models of lattices gauge theories (LGTs) can be versatile. The sites (links) of the lattice constitute the matter (gauge and electric field) variables. The characteristic feature of LGTs is the local symmetry at each vertex (yellow circle) governed by the Gauss' law operator $\hat{G}_j$. This gives rise to an extensive number of conservation laws, e.g., in a $\mathbb{Z}_2$ LGT the parity is locally conserved. Because neighboring vertices overlap, this yields highly constrained Hilbert spaces. Models with the same local symmetry can have different representations of the gauge group and can be coupled to different matter species, e.g., bosonic or fermionic matter [23–25]. In this thesis, we propose realistic analog quantum simulation schemes to explore Abelian $\mathbb{Z}_2$ and non-Abelian U(N)/SU(N) gauge theories in state-of-the-art experiments with ultracold quantum gases.

tection schemes, where the gauge structure emerges from two-body Ising or spin-exchange interactions [P4, P5, P9, 30]. In emergent gauge theories, there are inevitable gauge breaking errors and thus the goal is to observe *qualitative and phenomenological* features of LGTs that are believed to capture the physics of the ideal gauge theory, and strongly correlated phases of matter [23].

In Part II of this thesis, we will encounter surprising analogies between LGTs and doped quantum magnets: Parton bound states. While parton bound states, such as mesons, naturally appear in LGTs, they have proven as a useful description of hole dopants in antiferromagnetic Mott insulators relevant in the strong-coupling regime of Fermi-Hubbard-type models and cuprate superconductors [21, 31, 32], see Figure 2. Notably, recent state-of-the-art experiments of ultracold atoms in optical lattices find striking signatures of the parton
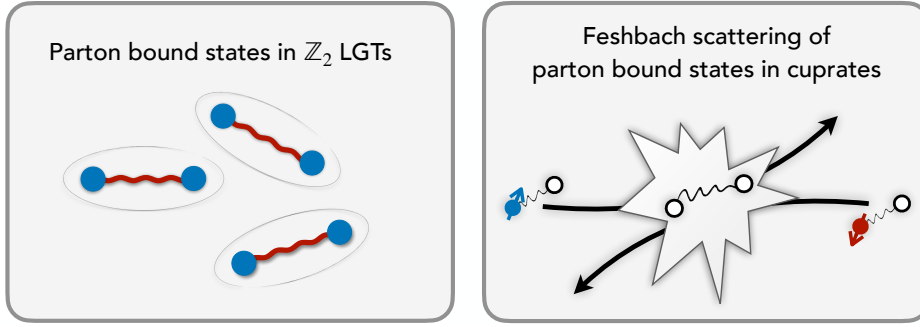
Figure 2: **Parton bound states.** Left: In the confined phase of LGTs, the charged matter particles (blue circles) are bound into mesons by the tension of electric field lines (red lines), familiar from particle physics. We conjecture that these charge-neutral mesons may form a condensate [P5]. Right: We encounter mesonic parton bound states in the one- and two-hole excitation spectrum of doped antiferromagnetic Mott insulators. In analogy to particle physics, we propose a Feshbach perspective on the origin of strong pairing in Fermi-Hubbard-type models and high-Tc cuprate superconductors [P11, P7].

character of magnetic polarons [7, 33].

This analogy to particle physics leads us to a Feshbach perspective of parton bound states in underdoped cuprates [P11, P7]. We suggest that attractive scattering interactions between fermionic spinon-chargon bound states can be induced by a low-lying resonant chargon-chargon bound state [34–37]. We derive an effective parton description of the proposed Feshbach scattering channels and find that the symmetry of the parton bound state manifests as robust, magnetic pairing interactions in the $d_{x^2-y^2}$-wave channel, consistent with the cuprate compounds [38, 39].

Therefore, we take inspiration from new probes in quantum gas microscopes, i.e., signatures of parton bound states in many-body correlations [33], and develop new phenomenological, effective models for strongly correlated electron systems from high-Tc cuprates [P11, P7] to nickelate superconductors [P2, P10, P6]. In this vein, we follow our guiding principle and conclude from the *form* of the parton bound state to their *function* as meson scattering channels.

Outline

This doctoral thesis is structured in two parts, namely in Part I we discuss the quantum simulation of LGTs and in Part II we focus on doped quantum magnets, effective parton models and, one of the main results, the emergent Feshbach resonance in cuprate superconductors.

Each part is accompanied with an extended chapter on the theoretical background: In Part I, Chapter 1-2 we briefly review the basics of cold atom and molecule quantum simulation platforms relevant for this thesis and give an historical introduction into lattice gauge theories and their quantum simulation. In Part II, Chapter 7-8 the broad phenomenology of cuprate superconductors is reviewed with a focus on relevant aspects for this thesis, such as the single-hole problem and proposed magnetic pairing mechanisms. Further, after a block of content is concluded, we give short summaries and outlooks throughout the the-

sis. Lastly, we provide overarching Conclusions & Perspectives of the doctoral thesis.

Part I contains the following content. In Chapter 3, we develop the concept of local pseudogenerators allowing us to propose an analog quantum simulation scheme for $(2+1)\mathrm{D}$ $\mathbb{Z}_2$ LGTs with dynamical matter in Rydberg tweezer arrays (based on Refs. [P4, P5]). In Chapter 4, we discuss experimental equilibrium and out-of-equilibrium probes for $\mathbb{Z}_2$ LGTs (based on Refs. [P5, P3, P12]). In Chapter 5, we derive a gauge protection scheme for non-Abelian gauge theories utilizing spin-exchange interactions and we propose experimental schemes for ultracold alkaline-earth atoms, as well as cold molecules and Rydberg atoms in tweezer arrays (based on Ref. [P9]). In Chapter 6, we briefly conclude with a perspective on the quantum simulation of LGTs.

Part II contains the following content. In Chapter 9, we present the Feshbach hypothesis of high-Tc superconductivity in underdoped cuprate compounds (based on Ref. [P11, P7]). This is followed by Chapter 10, which provides the analytical background of the Feshbach scattering model (based on Ref. [P7]). In Chapter 11, we propose a quantum simulation scheme to implement doped quantum magnets in tweezer arrays with cold molecules and Rydberg tweezers (based on Ref. [P8]). Further we present preliminary experimental results obtained in the Rydberg tweezer platform of Antoine Browaeys at the Institute d'Optique in Palaiseau Cedex, France. In Chapter 12, we derive effective parton models for mixed-dimensional bilayer Hubbard model and elaborate on their relation to high-Tc nickelate superconductors (based on Refs. [P1, P2, P10, P6]).

PART I

Quantum Simulation of Lattice Gauge Theories

1

Summary and Overview

EMERGENT PHENOMENA are deeply linked to gauge theories [3]. One of the most illustrating examples can be found in particle physics. Special relativity enforces microscopic theories to be local in order to comply with causality, i.e., Lagrangians or Hamiltonians are built from local operators. However, this contradicts our empirical observations: two electrical charges interact via a long-ranged Coulomb potential $\propto 1/r$.

The mathematical framework of gauge theories elegantly unifies these pictures by the introduction of additional degrees-of-freedom, namely the gauge bosons, which interact locally with the charged matter particles. The gauge bosons ultimately induce long-range interactions between charges. This construction necessitates local symmetries associated with local conservation laws (Gauss' law). For the example of two U(1) charges, the gauge boson is the massless photon. By applying the construction of gauge theories to a class of Abelian and non-Abelian symmetries, U(1) × SU(2) × SU(3), the quantum field theory for the standard model of particle physics can be obtained [40]. In this framework the *gauge-invariance* is assumed to be a fundamental law of nature.

In contrast, condensed matter systems provide an alternative perspective: emergent gauge theories. Here, the gauge theory itself emerges at low energies from yet another microscopic model, e.g., from strong interactions of electrons in a material [23]. Often, the gauge theory inherits properties of the underlying lattice giving rise to lattice gauge theories (LGTs) [27]. Hereby, the many-body ground state serves as the renormalized vacuum, from which excitations can be created according to Gauss' law [3]. The question about *what kind* of gauge theory may arise from a given microscopic model, however, is extremely challenging and in many cases far from conclusive.

This necessitates to have simple toy models at hand that can be studied both experimentally and theoretically. The Bose-Hubbard model [41, 42] opened the door to explore strongly correlated phases of matter from a microscopic perspective. Similarly, it would be desirable to have an experimental platform that allows us to directly study plain-vanilla

LGTs in a tunable, large-scale fashion in order to probe long-standing theoretical predictions, such as the celebrated Fradkin-Shenker phase diagram [28] discussed in Section 2.2.2.

The relevance of LGTs is even more highlighted by their relation to a variety of fundamental problems in particle physics [26], condensed matter physics [3, 27, 43, 44], biophysics [45] and quantum information [29], to name a few. Notably, the framework of gauge theories captures phenomena ranging from quark confinement to quantum spin liquids and is commonly used in the description of high-Tc superconductors [23, 44]. Their quantum simulation could open the door to a class of questions that are particularly hard to solve numerically, ranging from thermalization dynamics of gauge theories [46] to ground-state phase diagrams [24, 47, 48]. Especially, LGTs with dynamical matter at finite density are proposed to have intimate connections to strongly correlated electrons and high-Tc superconductors [20, 23]. Throughout this thesis, we will encounter intriguing analogies between LGTs and doped quantum magnets, such as meson-like charge excitations that are bound by a fluctuation string object, see e.g. Part I Chapter 3 and Part II Chapter 9. Despite the overarching relevance of strongly coupled gauge theories across various disciplines of physics, experimental realizations beyond $(1+1)$D or non-Abelian gauge theories remain challenging.

One particularly promising approach for the analog quantum simulation of LGTs is built upon the idea of emergent gauge theories [15, 49], analogously to strongly correlated electrons. Hereby, strong energy penalties are utilized to enforce local constraints, e.g., the Rydberg blockade mechanism allows to engineer quantum dimer models on the Kagome lattice [50, 51]. In the language of quantum information, this corresponds to the implementation of stabilizer terms on the level of the Hamiltonian, which energetically favor a particular Gauss' law sector [52, 53], outlined in Section 2.2.5. Thus far, this *gauge protection mechanism* [30] is limited to specific geometries or gauge groups in experiments.

The focal point of this thesis is the development of novel schemes for the analog quantum simulation of emergent lattice gauge theories in AMO platforms[1]. We start with a brief overview about quantum simulators and introduce the concepts of LGTs in Chapter 2. In the subsequent Chapters, we apply a combination of (i) theoretical tricks to simplify the interactions required to implement emergent gauge theories and (ii) propose experimentally feasible schemes for AMO platforms to realize both Abelian $\mathbb{Z}_2$ LGTs in Chapter 3 and non-Abelian U(N) and SU(N) LGTs in Chapter 5. Further, we discuss experimentally relevant probes that can be obtained by single-site resolved snapshots in Chapter 4.

---

[1]AMO = atomic, molecular and optical physics
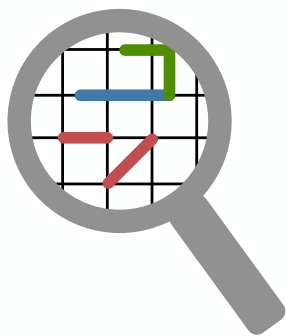
2

Theoretical Background

2.1 Quantum Simulators

DESPITE THE REMARKABLE INCREASE in classical computational power over the past decades, obtaining exact solutions to almost all (interacting) quantum systems poses an unprecedented challenge. Every additional particle comes with an exponential increase in computational cost, which limits state-of-the-art numerical simulations to a few hundred particles - already including clever techniques to reduce the complexity of the problem [54, 55]. At this point, it is convenient to follow the literature [56] and cite Richard Feynman's famous words [57]:

Nature isn't classical, dammit, and if you want to make a simulation of Nature, you'd better make it quantum mechanical, and by golly it's a wonderful problem because it doesn't look so easy.

The key message is to use systems governed by quantum mechanical laws of nature at the level of the computing hardware, thereby allowing us to leverage ubiquitous quantum phenomena, such as superposition and entanglement, as a resource to tackle classically challenging problems in a hardware-efficient way.

Even though there have been many promising advances in the last years in the direction of digital quantum computation, see Ref. [58] and references therein, the focus in this thesis should be on a different route to simulate quantum systems: **analog quantum simulation**. The key difference between the two approaches is that digital machines apply a set of logical operations (gates) serving as building blocks for algorithms, whereas analog machines directly implement (interacting) Hamiltonians [59].

Nowadays, Feynman's visionary idea is becoming a real, useful tool for researchers in the field of quantum sciences. We highlight that currently various platforms and approaches are coexisting offering a rich playground to test quantum many-body physics [11, 59]. While digital quantum computers – proposed by Richard Feynman – are making impressive progress [58], they are not yet serving as a universal machine, e.g., to find the

ground state of the Fermi-Hubbard model. In contrast, analog quantum simulation plat-forms are optimized to compute a specific set of observables for a few specific models, e.g., Hubbard models [41, 60]. Another exciting route is provided by hybrid analog-digital machines, which may play a significant role in the study of fermionic problems in the near future [61, 62].

In the following, we briefly review various features of state-of-the-art analog quantum simulation platforms. It should be considered as an overview of available tools in the toolbox of experimental AMO platforms. Subsets of tools can be compatible, for example tweezer arrays can be combined with Rydberg atoms [12], cold molecules [63–65] or optical lattices [66]. The purpose is to summarize and compare which models can be realized in different platforms; for details we will refer to specialized reviews.

In this thesis, we focus on tools that can be found in (ultra)cold AMO experiments [11], where vast technological developments in the past decade enable experimental physicists to control and manipulate individual degrees-of-freedom on the single-particle level. The microscopic Hamiltonians, that can be realized, are determined by the atomic or molecular species and its internal states (quantum statistics, spins, scattering, electric dipole moments). We note that there are many other promising quantum simulation platforms not covered in this thesis, including superconducting qubits [14], optical nanofibers [67], Cavity QED [68, 69], trapped ions [13] or hybrid combinations [70] of them.

2.1.1 Interactions

One of the key ingredients to realize strongly correlated phases of matter are controllable, strong and coherent interactions. Inducing strong interactions, i.e., *strong* compared to other energy scales such as the kinetic energy, between charge neutral objects is challenging but a various methods are now established in the AMO toolbox.

Scattering interactions

One elegant technique to induce interactions between neutral atoms is based on the idea of Fano-Feshbach resonances[1]; an idea that was initially developed in the context of particle physics [71, 72]. Let us first give a phenomenological explanation. The Fano-Feshbach resonance describes the consequence of a bound state that approaches a free particle continuum [73]. The bound state influences the scattering properties of the individual particles and can lead to a divergent scattering length. This scattering length a can directly be related to a point-like pseudo-potential at low energies [74].

The following situation can occur in an AMO setup [73]: two atoms can form a bound state, i.e., a molecular state, with a magnetically tunable binding energy ΔE. In some cases, an external magnetic field B can tune the molecular state into and out-of-resonance giving rise to strong and tunable attractive or repulsive interactions, see Figure 2.1a. The existence and the properties of such resonances are determined by the atomic species and isotopes. If the closed channel can be integrated out, the scattering length is captured by a simple

---

[1]In the AMO context, it is often just called *Feshbach resonance*.
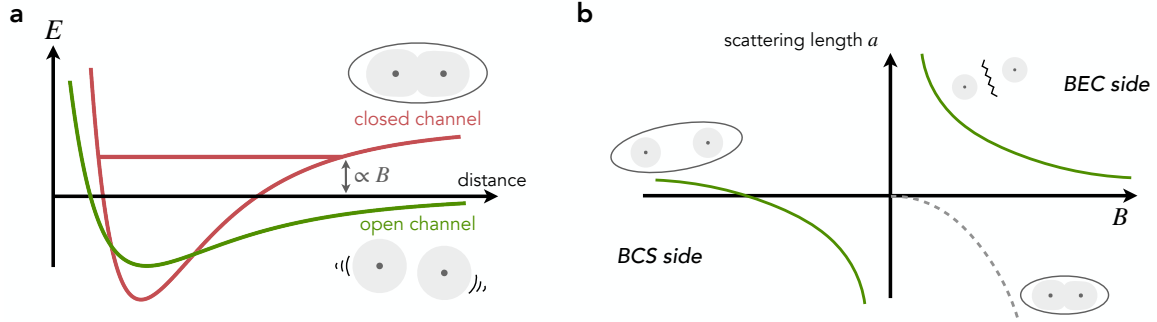
Figure 2.1: **Two-channel model of a Feshbach resonance. a** We consider a model with constituents in two different configurations: free particles in the open channel and molecules in the closed channel. In cold atom experiments, the energy difference ΔE between the two channels can be tuned via an external magnetic field B. **b** By integrating out the closed channel, we obtain a Feshbach-induced scattering length a between open channel particles with the unitary $1/a = 0$ at $B = B_0$. The vertical offset corresponds to a background scattering length a_0 originating from the open channel potential shown in **a**. The attractive (repulsive) side of the two-particle resonance is associated with the BCS (BEC) regime of the many-particle ground state.

effective description given by

$$a(B) = a_0 \left(1 - \frac{\Delta}{B - B_0} \right) \tag{2.1}$$

with the background scattering length a_0, the resonance position B_0 and resonance width Δ. Conveniently, for low-energy scattering (or long-wavelength behaviour) the scattering length is proportional to the strength $g \propto a$ of a contact interaction $V(x) = g\delta(x)$ obtained in Born approximation [74].

A simple description of the Feshbach resonance is derived from a two-channel model. Hereby, the individual particles (or atoms) in the continuum form an open scattering channel with asymptotically free particle states at times $t \to \pm\infty$ [75] described by $\hat{\mathcal{H}}_{\text{open}}$. Moreover, we introduce a closed scattering channel (the molecule) described by $\hat{\mathcal{H}}_{\text{cl}}$; it is called *closed* because scattering into this channel in energetically forbidden. Further, we denote states in the open (closed) channel as $|\psi_{\text{open}}\rangle \in \mathscr{H}_{\text{open}}$ ($|\psi_{\text{cl}}\rangle \in \mathscr{H}_{\text{cl}}$), and we define a Hamiltonian $\hat{H}_{\text{oc}}$ coupling the open and closed channel.

Formally, one can solve the scattering problem of the simplified two-channel model [73]; here we want to provide an intuitive picture. Let us start by considering a pair of particles in the open channel, that lies energetically below the closed channel. When the particles start to spatially overlap, they can couple into the closed channel via $\hat{\mathcal{H}}_{\text{cl}}$. In a simple two level picture, the open channel states can lower their energy by this process leading to an attractive interaction, see Figure 2.1b. In Born approximation, we can compute the Feshbach scattering length by a second-order perturbative coupling

$$a(\Delta E) \propto \sum_{|\psi_{\text{cl}}\rangle} \frac{|\langle \psi_{\text{cl}} | \hat{H}_{\text{oc}} | \psi_{\text{open}}\rangle|^2}{\Delta E}, \tag{2.2}$$

where ΔE describes the energy difference between the particle pair $|\psi_{\text{open}}\rangle = |\psi_{\text{open}}(k_1, k_2)\rangle$ in the open channel with momenta k_1, k_2 and the closed channel molecular state. This illustrates that the sign of the interaction can be inverted if the molecule becomes the two-particle ground state, see Figure 2.1b. At $\Delta E = 0$, the system reaches unitary under which condition a strong-coupling description of the two-channel model is required [10]. Here, we have neglected important details of Feshbach resonances, such as dispersion of the closed channel states. Those can play a significant role for validity of the Born approximation.

We highlight that Feshbach resonances provided a game changer in the field of ultra-cold atoms [76]. The mechanism allows to engineer strong, tunable interactions in neutral atoms, and thus to realize a variety of strongly-interacting phases of matter from the Fermi-Hubbard model to the BEC-BCS crossover [10, 73, 77]. In Part II, Chapter 9, we study an emergent Feshbach resonance in the context of charge carriers in strongly correlated cuprate superconductors and find a dominating d-wave scattering resonance.

Rydberg interactions

The electric and magnetic coupling dipole moments of neutral atoms in their ground state configuration are small. They are so small that the resulting dipole-dipole interactions are typically too weak to harness for many-body simulations[2]. To our advantage, atoms offer a rich internal structure of electronic states, which can be used to dramatically increase their interaction strength. Specifically, the Rydberg series [79, 80] describes a class of highly-excited atomic states with large principle quantum number $n \gg 1$. If a single electron in an atom is excited to a Rydberg state, its binding energy is well-described by hydrogen-like atom

$$E_{n,I} = -\frac{\text{Ry}}{\bar{n}^2}, \tag{2.3}$$

where $\{n, I\}$ are a set of quantum numbers, Ry is the mass-renormalized Rydberg constant and $\bar{n}$ is the effective principle quantum number, which depends on $\{n, I\}$. Thus, the Rydberg series can be explained by a single electron that binds to the screened charge $(Z-1)e$ of the ionic core, where Z is the atomic number and e is the unit of electric charge. The corrections to this simplified picture are captured by quantum defect theory [81] and absorbed in the effective principle quantum number $\bar{n} \approx n - \delta_{n,I}$, where $\delta_{n,I}$ is the quantum defect. An excellent overview can be found in Ref. [82].

The hydrogen-like wavefunctions of the Rydberg states allow us to easily obtain the scaling behaviour of matrix elements known from the exact solution of the hydrogen atoms [83]. Here, we use these scaling relations to review the most important, qualitative properties of Rydberg states. We note that it requires more sophisticated methods to calculate the necessary quantitative properties [84].

The first observation is that the energy spacing of nearby Rydberg states decreases as $\Delta E \propto \bar{n}^{-3}$. At the same time, the transition dipole moments $\mathbf{d} = \langle nI'|e\hat{\mathbf{r}}|nI\rangle \propto \bar{n}^2$ between two electronic states $|nI'\rangle$ and $|nI\rangle$ are enhanced for states in the Rydberg series [80]; here $\hat{\mathbf{r}}$ is the position operator.

---

[2]We highlight that with recent experimental advances, it was achieved to stabilize ordered phases of the extended Bose-Hubbard model using magnetic Erbium atoms [78].

The fundamental interaction between two dipoles $\hat{\mathbf{d}}_1$ and $\hat{\mathbf{d}}_2$ is given by the Hamiltonian

$$\hat{\mathcal{H}}_{\mathrm{dd}} \propto \frac{\hat{\mathbf{d}}_1 \cdot \hat{\mathbf{d}}_2 - 3\left(\hat{\mathbf{d}}_1 \cdot e_{\mathbf{R}}\right)\left(\hat{\mathbf{d}}_2 \cdot e_{\mathbf{R}}\right)}{|\mathbf{R}|^3}, \tag{2.4}$$

where $\mathbf{R}$ is the vector connecting the two atoms with unit vector $e_{\mathbf{R}} = \mathbf{R}/|\mathbf{R}|$. Now, we focus on the Rydberg-enabled models relevant for quantum simulation of many-body problems [12]. We distinguish two scenarios that can occur from the dipole-dipole interaction:

(1) Direct exchange. Two Rydberg states are connected by a non-vanishing dipole matrix element leading to an exchange interaction between two atoms in dipole coupled Rydberg states. Typically, two neighbouring Rydberg states $|nS\rangle = |\downarrow\rangle$ and $|nP\rangle = |\uparrow\rangle$ with $n \approx 60$ are identified with a spin-1/2 subspace. The direct dipolar coupling between a pair of atoms [85–88] is given by

$$\langle nP_i, nS_j | \hat{\mathcal{H}}_{\mathrm{dd}} | nS_i, nP_j \rangle = \frac{C_3}{|\mathbf{R}|^3} \left(1 - 3\cos^2\theta\right) \tag{2.5}$$

with coupling strength C_3, and can be written in operator form as

$$\hat{\mathcal{H}}_{\mathrm{XY}} = \frac{J_\perp}{2} \sum_{i<j} \frac{1}{r_{ij}^3} \left(\hat{S}_i^+ \hat{S}_j^- + \mathrm{h.c.}\right) + \Omega \sum_j \hat{S}_j^x + \sum_j \Delta_j \hat{S}_j^z, \tag{2.6}$$

with the spin-1/2 operators $\hat{S}_j^\alpha$ ($\alpha = x, y, z$) and $\hat{S}_j^\pm = \hat{S}_j^x \pm i\hat{S}_j^y$ for atoms at site j. Here the transverse field Ω (longitudinal field Δ_j) describes the ability to experimentally couple the two Rydberg states with a microwave (apply local light shifts) [89, 90].

(2) Van-der-Waals interactions. The next leading order term enabled by dipolar exchange are second-order van-der-Waals interactions. Without loss of generality, we consider a pair of atoms in the same Rydberg state $|nS_i, nS_j\rangle$. The dipole-dipole interactions couples this state to all other Rydberg states $|n'I_i, n''J_j\rangle$ allowed by dipole selection rules giving rise to van-der-Waals-type interactions

$$\hat{\mathcal{H}}_{\mathrm{vdW}} = \sum_{n'I, n''J} \frac{|\langle n'I_i, n''J_j | \hat{\mathcal{H}}_{\mathrm{dd}} | nS_i, nS_j \rangle|^2}{\Delta E_{n'I, n''J}} |nS_i, nS_j\rangle\langle nS_i, nS_j|. \tag{2.7}$$

The Förster defect describes the energy difference between the pair states $\Delta E_{n'I, n''J} = 2E_{nS} - (E_{n'I} + E_{n''J})$; for nearby Rydberg states with $n \approx n' \approx n''$ the Förster defect scales as $\Delta E_{n'I, n''J} \propto n^3$, where we have used the energy scaling of hydrogen-like Rydberg states Eq. (2.3). The sum over virtual Rydberg states is often summarized in the coupling constant $C_6/|R|^6 \propto n^{11}$; in the last step we have combined the scaling relations discussed above.

By identifying the atomic ground state with $|g\rangle = |\downarrow\rangle$ and the Rydberg state with $|nS\rangle = |\uparrow\rangle$, the van-der-Waals interactions enables to quantum simulate the Ising model in transverse and longitudinal fields. Using this mapping, the Hamiltonian of van-der-Waals inter-

acting Rydberg state becomes [91, 92]

$$\hat{\mathcal{H}}_{ZZ} = J_z \sum_{i<j} \frac{1}{r_{ij}^6} \hat{S}_i^z \hat{S}_j^z + \Omega \sum_j \hat{S}_j^x + \sum_j \Delta_j \hat{S}_j^z,$$ (2.8)

where the transverse field Ω is given by the Rabi drive between $|\downarrow\rangle$ and $|\uparrow\rangle$. The local longitudinal field Δ_j contains contributions from both the mapping of Eq. (2.7) to spins and from local detunings of the Rabi drive.

Positional disorder in the experimental setups translates into strong disorder of the interaction potential due to the power-law dependence of the interaction $\propto R^{-6}$. Therefore, an appealing regime is the so-called blockaded regime, which is insensitive to positional disorder. This regime is determined by the interaction shift of the pair state $|nS, nS\rangle$ such that only *one* atom within the blockade radius R_b can be excited by the drive Ω; this radius is given by $C_6/R_b^6 = \Omega$. Formally, the blockade constraint can be enforced by a projector $\hat{\mathcal{P}}$, which removes the energetically forbidden multi-excited states within a blockade radius [93]. In the blockaded Hilbert space, the Ising model (2.8) reduces to the so-called PXP-model

$$\hat{\mathcal{H}}_{PXP} = \Omega \sum_j \hat{\mathcal{P}} \hat{S}_j^x \hat{\mathcal{P}} + \sum_j \Delta_j \hat{S}_j^z + \hat{\mathcal{H}}_{tails},$$ (2.9)

where $\hat{\mathcal{H}}_{tails}$ contains the long-range tails of the Rydberg interaction outside the blockade radius.

The realization of the model has led to numerous studies of quantum magnets in both the ground state, e.g., Refs. [92, 94], or quench dynamics, e.g., Refs. [91, 95]. In particular, deep in the blockaded regime new phenomena such as quantum many-body scarring have been discovered [96] or signatures of a $\mathbb{Z}_2$ spin liquid have been reported [50, 51]. Moreover, the Rydberg blockade mechanism forms the basis of digital quantum computing with neutral atoms [58, 97–100].

In Part II, Chapter 11 we will discuss a new model combining both types of interactions, i.e., direct exchange and van-der-Waals interactions, to realize a bosonic t-J model in Rydberg tweezer arrays.

Polar molecules

The dipole-dipole interaction (2.4) is only useful in the presence of non-vanishing dipole moments $|\mathbf{d}|$. To obtain sufficiently strong interactions (compared to the timescales of an experiment), large dipole moments are required. In the previous section, we have discussed how highly excited electronic states have large dipole moments. Another way to leverage dipolar interactions in quantum simulators is to use particles, which naturally exhibit a strong net dipole moment in the electronic ground state, e.g., polar molecules [101–104].

Here, we briefly review di-atomic, polar molecules. To understand the dipolar interactions between two molecules, we first need to consider the degrees-of-freedom and their hierarchy of energy scales [105]. A simple understanding about the level structure of molecules can be obtained from a Born-Oppenheimer ansatz, where we factorize the molecular wavefunction into the electronic and nuclear parts, $|\Psi\rangle = |\Psi\rangle_{el} \otimes |\Psi\rangle_{nuc}$. For

two atoms at far distance, the electronic wavefunctions of the atoms are independent. By moving the atoms closer together, the electronic wavefunctions start to overlap and the ground-state energy $E(R)$ will depend on the distance R between the two atoms in our Born-Oppenheimer description. For orbitals in a binding configuration, this potential has a minimum energy of $E(R)$ at $R = R_0$ and a Pauli blockade at very short distances. The corresponding potential $E(R)$ can be expanded around its minimum leading to harmonic oscillator modes of the nuclei: the vibrational spectrum. In cold molecules, we assume that individual molecules are in its electronic ($\sim 100\,\text{THz}$) and vibrational ($\sim 100\,\text{GHz}$) ground state.

The next smaller energy scale are the rotational modes ($\sim 1\,\text{GHz}$), which can be approximated by a rigid rotor [105] with an energy spectrum $E_N \propto N(N+1)$; here N is the quantum number of rotational quanta. The rotational (sub)levels $\{N, m_n\}$ form the subspace relevant for quantum simulation. In the rotational frame, the dipole of the molecule is steady. However in the lab frame, the dipoles are rotating and its the rotation of the dipoles, which induces pair interactions between rotational levels of two molecules. If we map the rotational states $|N = 0, m_N = 0\rangle = |\downarrow\rangle$ and $|N = 1, m_N = 0\rangle = |\uparrow\rangle$ on a qubit, the resulting spin-1/2 interaction is given by

$$\hat{\mathcal{H}}_{\text{XY}} = \frac{J_\perp}{2} \sum_{i<j} \frac{1}{r_{ij}^3} \left(\hat{S}_i^+ \hat{S}_j^- + \text{h.c.} \right) + \Omega \sum_j \hat{S}_j^x. \tag{2.10}$$

Since the qubits are implemented in rotational levels of the molecules with energy spacing in the microwave spectrum, their rate of spontaneous emission is very slow compared to the interaction scale ($\sim 1\,\text{kHz}$ in the optical lattice [106]). Indeed, T_2 times of several seconds have been reported [107]. Further, the Hamiltonian (2.10) includes coherent Rabi oscillations $\propto \Omega$ from a drive implemented with microwaves; note that the intrinsically strong dipole moments between rotational states give rise to large Rabi frequencies of several hundred kHz [106].

Altogether, the separation of energy scales in cold, polar molecules provide an ideal platform for Floquet engineering of spin models [106, 108]. Moreover, while we have restricted our discussion to two rotational levels, in principle an entire ladder of internal rotational states are available suitable to implement synthetic dimensions [109] or *t-J* models [P8].

2.1.2 Optical lattices

One discipline in condensed matter physics deals with the description of electrons in a solid, crystalline material [110]. Hereby, the ionic cores of atoms form a Bravais lattice structure, which is experienced as a periodic potential for the underlying electrons. If the electrons are tightly bound to the ionic cores, they are well described by localized Wannier functions, such that the overlap between neighboring Wannier functions gives rise to kinetic delocalization of the electrons across the lattice: the tight-binding model. Similarly, a retro reflected optical laser beam (standing wave) can induce an optical potential landscape experienced as a periodic cosine potential for atoms or molecules [11]. For deep optical lattices and at

ultracold temperatures, the particles are well described by a tight-binding model.

It was proposed by Jaksch et al. [41] that bosonic atoms at sufficiently low temperatures can occupy the lowest Bloch band of an optical lattice. By tuning the lattice parameters the localized Wannier functions can be modified such that an interplay between kinetic energy, i.e., overlap between neighbouring Wannier functions, and potential energy, i.e., localization of the on-site Wannier function, enables to drive the ground state from the Mott insulating to superfluid regime[3]. Soon after, this was experimentally realized by Greiner et al. [42] in Munich.

Thus, optical lattice experiments typically realize Hamiltonians of the form

$$\hat{H} = -t \sum_{\langle i,j \rangle} \left(\hat{a}_i^\dagger \hat{a}_j + \text{h.c.} \right) + \frac{1}{2} U \sum_j \hat{n}_j \left(\hat{n}_j - 1 \right) - \sum_j \mu_j \hat{n}_j, \qquad (2.11)$$

where the first term describes a tight-binding hopping t of bosonic/fermionic particles $\hat{a}_j^\dagger$ on nearest-neighbour sites i and j on the lattice; the second term is the density-dependent on-site Hubbard interaction U with $\hat{n}_j = \hat{a}_j^\dagger \hat{a}_j$. Both parameters depend on the lattice depth [41], where the tunneling t scales inversely exponential in the lattice depth. A local chemical potential term $\propto \mu_j$ is introduced to model disorder and harmonic confinement of the trap [55, 111]. The Hubbard interaction arises from low-energy two-particle scattering and is proportional to the scattering length $U \propto a$. If the atomic species used in an experiment hosts a useful Feshbach resonance, the tunability of the Hubbard interaction is dramatically increased and allows to switch from attractive to repulsive Hubbard interactions [73].

We highlight that Hamiltonian (2.11) can be generalized to, e.g., spinful particles, molecules [106] or magnetic atoms [78] by modifying the interaction term accordingly. In the case of spin-1/2 fermions the model describes the paradigmatic Fermi-Hubbard model

$$\hat{H}_{\text{FH}} = -t \sum_{\langle i,j \rangle, \sigma} \left(\hat{c}_{i,\sigma}^\dagger \hat{c}_{j,\sigma} + \text{h.c.} \right) + U \sum_j \hat{n}_{j,\uparrow} \hat{n}_{j,\downarrow}, \qquad (2.12)$$

where the operator $\hat{c}_{j,\sigma}^\dagger$ ($\hat{c}_{j,\sigma}$) creates (annihilates) a fermion with spin $\sigma = \downarrow, \uparrow$ at site j, and $\hat{n}_{j,\sigma} = \hat{c}_{j,\sigma}^\dagger \hat{c}_{j,\sigma}$ is the number operator. It was realized by Duan et al. [60] that in the limit of strong Hubbard interactions $U \gg t$, the antiferromagnetic superexchange mechanism allows to engineer spin model with interaction strength $J = 4t^2/U$ [112], see Chapter 7.

2.1.3 Tweezer arrays

Viruses and bacteria are macroscopic objects in the world of quantum physics. Yet, light-mediated forces are strong enough to trap living organisms in individual optical tweezers with a few milliwatts of laser power [113]. This demonstration lead to technological advancements and opened new research directions in the field of biology, for which Arthur Ashkin was awarded the 2018 Nobel prize [114].

To use this application for quantum simulation purposes, such as simulating spin mod-

---

[3]Strictly speaking, the atoms in the lattice are in a metastable state and eventually decay into free space.

els in Rydberg atoms or polar molecules, one needs to trap cold, individual particles in a defect-free array. Hereby, each optical tweezer is constituted by a tightly focused, high-power laser beam modelled by a harmonic, confining potential. Thus, a cold, defect-free array refers to multiple optical tweezers each filled with a single atom close to the motional ground state of the tweezer. Several technological developments over the past two decades allows us to create such arrays with up to thousands of atoms [115, 116] with high fidelity. Cold molecule platforms are demonstrating impressive progress [63, 65, 117] towards unity filled arrays in the motional ground state.

Let us highlight a few key aspects of creating deterministic, defect-free arrays [118]. Probabilistic loading of atoms in tweezers, i.e., by adiabatically turning on the tweezer light overlapped with a cloud of atoms, is only able to reach *single*-atom-per-tweezer fidelity of less than 40% because the number of atoms in the tweezers follow Poisson's distribution. Exploiting light-assisted collision, where atoms are pairwise lost from the tweezers, enables us to create tweezer arrays with 50% filling ("collisional blockade mechanmism") [119]. While this probability can be drastically enhanced using different collision channels [120], defect-free arrays are nowadays assembled using reconfigurable arrays pioneered by Endres et al. [121]. In this technique, atoms are first loaded using the collisional blockade mechanism and then subsequently, non-destructively imaged and rearranged into deterministically filled arrays.

The tweezer array platforms have revolutionized the quantum simulation of spin models [12], the field of neutral atom quantum computing [58, 122] and state preparation in optical lattices [66] within less than 10 years. A few advantages include ability to generate almost arbitrary geometries [123], fast cycle times [115], and in-situ reconfigurable arrays [122]. In the context of doped quantum magnets, new possibilities are emerging including the implementation of physical tunneling between tweezers [124], e.g., to build tunneling gates with fermionic statistics [61].

Using the resorting algorithm [121] to assemble defect-free arrays of cold molecules, requires efficient non-destructive imaging and cooling techniques for molecules trapped in tweezers. This may be enabled by novel promising techniques such as detection of molecules via nearby Rydberg atoms [125]. In combination with Floquet engineering, this would allows us to realize an entire new class of XYZ spin systems with high precision in arbitrary 2D geometries [103, 106].

As we progress through this thesis, we make use of the toolbox introduced above. For example, we will use Ising interactions between Rydberg atoms in combination with the liberty to create arbitrary geometries with tweezer technology. This allows us to propose a scheme for the implementation of an emergent $\mathbb{Z}_2$ lattice gauge theory with dynamical matter in $(2+1)$D [Chapter 3]. Moreover, we use the technique of Floquet engineering in ultracold molecules in optical lattices to propose a realistic scheme for the implementation of an emergent non-Abelian $U(N)$ lattice gauge theory in $(2+1)$D. Further, we envisage future digital-analog experiments with coherent control over fermionic degrees-of-freedom in optical tweezers and lattices [62] to implement non-Abelian $SU(N)$ lattice gauge theories

with fermionic matter beyond $(2+1)$D [Chapter 5]. In Part II of this thesis, we present preliminary experimental results extending the currently available toolbox to study *doped* quantum magnets in Rydberg tweezer arrays utilizing their naturally strong dipolar interactions.

2.2   Lattice gauge theories

SELF-DUALITY is a powerful concept in the study of statistical physics. A few years before Onsager provided an analytical solution to the 2D classical Ising model in 1944 [126], Kramers and Wannier predicted the critical temperature $T_c = 2.23J$ ($k_B = 1$) of the square lattice Ising model by mapping the low- to the high temperature behaviour [127]; J is the Ising coupling.

Intrigued by the simplicity of their argument [128], Franz Wegner studied similar mappings in higher dimensional Ising models in 1971 [27], and found that the 3D cubic lattice Ising model is dual to a model, where the original global $\mathbb{Z}_2$ symmetry is promoted to a local $\mathbb{Z}_2$ gauge symmetry: the Ising lattice gauge theory. Following the argument of duality, Wegner predicted that the dual model must have a phase transition: the Ising* transition. However, any local observable probing $\mathbb{Z}_2$ symmetry breaking must vanish identically due to the gauge symmetry. Therefore, it cannot be classified by the Ginzburg-Landau theory of continuous phase transitions [129] – the paradigm of phase transitions at the time – and Wegner anticipated to have discovered a *"phase transitions without local order parameters"* [27]. From a modern physics perspectives, we have a clear understanding and classification of the Ising* transition in terms of topological order and condensation of topological defects [4, 130]. In particular, the disordered phase of the Ising model corresponds to a gapped, $\mathbb{Z}_2$ quantum spin liquid in the dual model [3] motivating the topicality of LGTs in modern quantum many-body physics.

Soon after Wegner's discovery, LGTs have sparked interest in various different fields. In 1974, Wilson independently formulated a non-Abelian lattice gauge theory allowing for a strong coupling analysis of lattice quantum chromodynamics (lattice QCD), where confined quarks are found [26, 131]. This has opened an entire field in particle physics since the models provide a natural high-energy cutoff and allow us to apply established computational methods, such as Monte Carlo algorithms.

Initiated by Wegner and Wilson, LGTs were soon realized to provide a rich class of models interesting to be studied from the perspective of statistical and low-energy physics. Notably, Kogut, Susskind and Fradkin derived a *d*-dimensional quantum Hamiltonian formulation of the corresponding $(d + 1)$-dimensional classical LGT [132, 133]. By equipping Wegner's Ising LGT with $\mathbb{Z}_2$ matter fields, they were able to establish self-duality in the $(2 + 1)$D Ising LGT. In 1979, Fradkin and Shenker [28] proved analytically that the phase diagram of this model is constituted by only two phases: a deconfined phase and a confined/Higgs phase. In particular, from this result it follows that (1) simple, discrete gauge groups contain the confinement phenomenon known from non-Abelian gauge theories and (2) the spectrum of the Higgs phase is smoothly connected to the confined phase in $\mathbb{Z}_2$ LGTs.

With the discovery of the fractional quantum Hall effect [134] and high-Tc superconductivity in copper oxide compounds [135] in the 1980s, strongly interacting electron systems came to the fore. For most of these systems, the strong correlations resist to be efficiently captured by any available theoretical and numerical method. This necessitated the development of new theoretical tools, such as parton formulations [17, 136, 137] giving rise to gauge degrees-of-freedom [3]. Since then intimate theoretical connections between LGTs

and strongly correlated electrons, e.g., high-Tc superconductivity, have been reported [20, 23, 138].

Today, LGTs provide a fundamental framework in many topics of modern quantum many-body physics. Introduced by Alexei Kitaev [29], an exactly solvable model – the toric code – with a $\mathbb{Z}_2$ spin liquid ground state has been found, which nowadays serves as a textbook example for $\mathbb{Z}_2$ LGTs. The model plays a fundamental role in the context of fault-tolerant quantum computation due to its topological protected ground state degeneracy suitable to encode quantum information. Further, the model has gained noticeable attention in analog quantum simulation [50, 51, 139] since it is one of the few well-understood examples to host a gapped quantum spin liquid phase.

One of the long-term goals in the field is the large-scale quantum simulation of non-Abelian gauge theories with dynamical matter. This would allow us to probe gauge theories from an entirely new perspective in a regime inaccessible for numerical studies. For example, particle colliders are essentially restricted to probe the physics of gauge theories at infinity times after the collision. Observing the collision process in real-time adds a new dimension to the study of particle physics [140–144]. Moreover, the direct observation of confinement of dynamical charges, in both Abelian and non-Abelian gauge theories, would provide an experimental toy model to test suitable (non-local) order parameters proposed to capture confinement. This goes hand in hand with questions in condensed-matter physics, namely to understand the ground-state phase diagrams of a variety of LGTs. In the context of quantum many-body physics and quantum information, the observation of quasiparticles with non-Abelian statistics, that can be hosted in quantum spin liquids and lattice gauge theories [52], would be a major achievement.

Despite the relevance of LGTs in many disciplines of theoretical physics, the large-scale experimental realization in $(2 + 1)\mathrm{D}$ and with dynamical matter remains elusive. This is attributed to the complicated structure of interactions and the challenge to impose gauge invariance in an experimental setup, see Chapter 2.2.5. In the following, we use a historical approach but modern formulation to introduce the framework of LGTs on the example of the Ising $\mathbb{Z}_2$ LGT.

2.2.1   The Ising lattice gauge theory

Now, we want to add formalism to LGTs and describe Kramers and Wannier's, and Wegner's construction in terms of a Hamiltonian formulation, i.e., our starting point is a $(d - 1)$-dimensional transverse field Ising model instead of a d-dimensional classical Ising model used in their original works [27, 127].

Kramers-Wannier duality   The 1D transverse field Ising model,

$$\hat{\mathcal{H}}_{\mathrm{TFIM}} = -J \sum_{\langle i,j \rangle} \hat{\tau}_i^z \hat{\tau}_j^z - \sum_j \hat{\tau}_j^x, \tag{2.13}$$

describes Ising couplings of neighbouring spins $\hat{\tau}^z$ along the Pauli z-direction with (unit less) coupling strength $J > 0$, in a transverse field $\hat{\tau}^x$ along the Pauli x-direction. At the crit-

a Kramers-Wannier self-duality
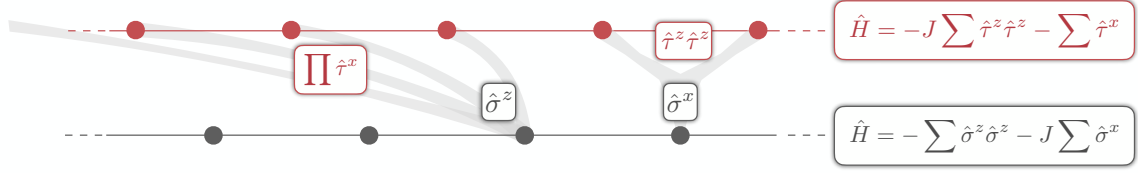
b Wegner duality
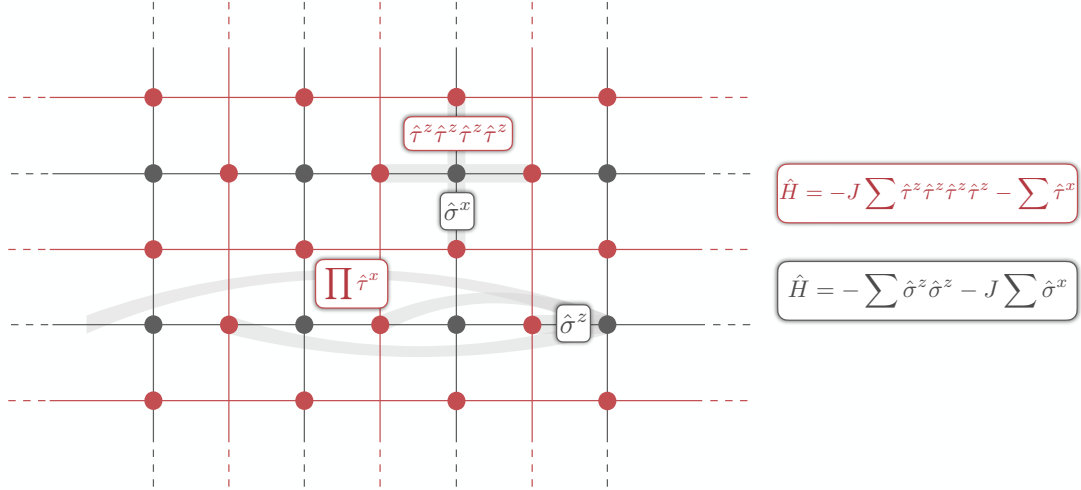
Figure 2.2: **Ising dualities. a** The Kramers-Wannier duality maps the strong to the weak coupling behaviour of the 1D transverse field Ising model [127]. **b** The 2D transverse field Ising model (gray) is dual to a $\mathbb{Z}_2$ Ising LGT (red). The known phase transition in the Ising model implies a phase transition with non-local order parameters in the LGT [27].

ical coupling $J_c = 1$, the ground state of the model exhibits a quantum phase transition [145] from a disordered paramagnetic phase at $J < J_c$ to an ordered ferromagnet at $J > J_c$. The ordered phase breaks the global $\mathbb{Z}_2$ symmetry associated with the unitary, parity operator

$$\hat{U} = \prod_j \hat{\tau}_j^x, \tag{2.14}$$

i.e. $[\hat{\mathcal{H}}_{\text{TFIM}}, \hat{U}] = 0$. The magnetization $\langle \hat{\tau}_j^z \rangle$ is the local order parameter distinguishing the disordered ($\langle \hat{\tau}_j^z \rangle = 0$) from the symmetry broken phase ($\langle \hat{\tau}_j^z \rangle \neq 0$).

The existence of the critical point can be derived from the self-duality of the 1D transverse field Ising model, see Figure 2.2a. To this end, we introduce the dual operators as

$$\hat{\sigma}_j^x = \hat{\tau}_{j-1}^z \hat{\tau}_j^z \tag{2.15a}$$

$$\hat{\sigma}_j^z = \prod_{i<j} \hat{\tau}_i^x. \tag{2.15b}$$

These operators satisfy the algebra of Pauli matrices, and re-writing Hamiltonian (2.13) in

terms of Eq. (2.15), gives the self-dual model

$$\hat{\mathcal{H}}_{\text{TFIM}} = -J \sum_{\langle i,j \rangle} \hat{\tau}_i^z \hat{\tau}_j^z - \sum_j \hat{\tau}_j^x = J \left[-\sum_j \hat{\sigma}_j^x - \frac{1}{J} \sum_{\langle i,j \rangle} \hat{\sigma}_i^z \hat{\sigma}_j^z \right]. \tag{2.16}$$

We conclude that the spectra of the 1D transverse field Ising model must obey the scaling relation $E(J) = J \cdot E(J^{-1})$ [43]. If the excitation gap vanishes at the critical point $J_c \neq 0$, it likewise must vanish for J_c^{-1} assuming the critical point to be unique. Thus, self-duality allows us to find the quantum phase transition at $J_c = 1$.

Wegner duality   Having reviewed the Kramers-Wannier self-duality, we continue with Wegner's Ising lattice gauge theory. We start with the pure $\mathbb{Z}_2$ LGT in $(2+1)$D, where spins are defined only on the links $\langle i,j \rangle$ connecting sites i and j of a square lattice, see Figure 2.2b:

$$\hat{\mathcal{H}}_{\mathbb{Z}_2} = -J \sum_P \prod_{\langle i,j \rangle \in P} \hat{\tau}_{\langle i,j \rangle}^z - \sum_{\langle i,j \rangle} \hat{\tau}_{\langle i,j \rangle}^x \tag{2.17}$$

with the plaquette interaction summing over all plaquettes P. This is our first example of a LGT: The Hamiltonian (2.17) commutes with the generators $\hat{G}_j$ of a local $\mathbb{Z}_2$ symmetry,

$$[\hat{\mathcal{H}}_{\mathbb{Z}_2}, \hat{G}_j] = 0 \quad \text{for all } j, \tag{2.18}$$

with

$$\hat{G}_j = \prod_{\langle i,j \rangle \in +_j} \hat{\tau}_{\langle i,j \rangle}^x, \tag{2.19}$$

where the symmetry generators are the product of Pauli $\hat{\tau}^x$ operators over all links adjacent to vertex j. The $\mathbb{Z}_2$ structure refers to the group structure of the generators, i.e., $(\hat{G}_j)^2 = 1$. The eigenvalues of $\hat{G}_j$ are $g_j = \pm 1$. Because the model (2.17) is only constituted by link variables, it is called *pure* LGT; in Section 2.2.2 we add matter variables on the sites of the lattice, and provide physical interpretation in terms of electric fields, gauge fields and Gauss' law.

The local symmetries give rise to an extensive set of local conservation laws, such that $\mathbf{g} = (g_1, ..., g_n)$ are a set of good quantum numbers often denoted as *superselection sectors*. The physics of different superselection sectors can be very different, e.g., typical choices are (i) the toric code, which is an even $\mathbb{Z}_2$ LGT with $g_j \equiv 1$ for all j, or (ii) dimer models, which is an odd $\mathbb{Z}_2$ LGT with $g_j \equiv -1$ for all j.

Similar to the 1D case, we perform a duality transformation by mapping

$$\hat{\sigma}_j^x = \prod_{\langle i,j \rangle \in P} \hat{\tau}_{\langle i,j \rangle}^z, \tag{2.20a}$$

$$\hat{\sigma}_j^z = \prod_{\langle i,j \rangle \in \Sigma_j} \hat{\tau}_{\langle i,j \rangle}^x \tag{2.20b}$$

as illustrated in Figure 2.2b; the string Σ_j labels all links to the left of dual site j. The mapping is not one-to-one due to the gauge invariance of the $\mathbb{Z}_2$ LGT. In particular, the mapping

uses the superselection sector $g_j \equiv 1$ to remove half of the degrees-of-freedom, see Refs. [4, 43] for a detailed discussion. Re-writing Hamiltonian (2.17) in terms of the dual operators yields the 2D transverse field Ising model

$$\hat{\mathcal{H}}_{\text{TFIM}} = -\sum_{\langle i,j \rangle} \hat{\sigma}_i^z \hat{\sigma}_j^z - J \sum_j \hat{\sigma}_j^x. \tag{2.21}$$

Phases of the pure Ising $\mathbb{Z}_2$ LGT Since the transverse field Ising model (2.21) exhibits a continuous phase transition, it was concluded by Wegner that the Ising LGT must have two phases. But what is the order parameter of the Ising LGT? The transverse field Ising model spontaneously breaks the global $\mathbb{Z}_2$ symmetry giving rise to a local order parameter $\langle \hat{\sigma}_j^z \rangle$. In contrast, the Ising LGT only has a local $\mathbb{Z}_2$ symmetry, which cannot be broken. In fact, **Elitzur's theorem** [146] prevents any gauge-noninvariant operator, i.e., operators $\hat{\mathcal{O}}$ with $[\hat{\mathcal{O}}, \hat{G}_j] \neq 0$, to have a finite expectation value. To show this on the example of the local magnetization, we consider the gauge-noninvariant operator $\langle \hat{\sigma}_j^z \rangle$ with $\hat{G}_j \hat{\sigma}_j^z = -\hat{\sigma}_j^z \hat{G}_j$. Then, it follows from Eq. (2.18) that for any physical state $|\psi\rangle$, the expectation value is

$$\langle \psi | \hat{\sigma}_j^z | \psi \rangle \propto \langle \psi | \hat{G}_j^{-1} \hat{\sigma}_j^z \hat{G}_j | \psi \rangle = -\langle \psi | \hat{\sigma}_j^z | \psi \rangle, \tag{2.22}$$

and thus $\langle \hat{\sigma}_j^z \rangle \equiv 0$.

If spontaneous symmetry breaking does not characterize the two phases, what order parameters could distinguish between the weak and strong coupling regime? By considering the mapping in Eqs. (2.20), we realize that the local magnetization in the transverse field Ising model corresponds to a non-local string object, where the length of the string scales with system size. This non-local string creates excitations of the plaquette operator at its end, which can be interpreted as $\mathbb{Z}_2$ magnetic monopoles; the ordered phase is therefore a condensate of $\mathbb{Z}_2$ monopoles. But can we nonetheless find a proxy to a local observable distinguishing the two phases?

Indeed, Wegner [27] and Wilson [26] have shown that the correlation length of loop order parameters, so-called Wegner-Wilson loops, are suitable to probe the phase transition. The Wegner-Wilson loops

$$\hat{W}(\mathcal{L}) = \prod_{\langle i,j \rangle \in \partial \mathcal{L}} \hat{\tau}_{\langle i,j \rangle}^z \tag{2.23}$$

are generalizations of the plaquette operator, Eq. (2.17), and characterized by their perimeter $L_{\mathcal{L}}$ and the area $A_{\mathcal{L}}$ of the closed loop $\mathcal{L}$. Thus, the operators $\hat{W}(\mathcal{L})$ are gauge invariant by construction and can admit non-zero expectation values consistent with Elitzur's theorem. The characteristic behaviour of the Wegner-Wilson loop is an area law decay $\langle \hat{W}(\mathcal{L}) \rangle \propto \exp(-A_{\mathcal{L}})$ in regime $J < J_c$ and a perimeter law decay $\langle \hat{W}(\mathcal{L}) \rangle \propto \exp(-L_{\mathcal{L}})$ in regime $J > J_c$.

2.2.2 Ising lattice gauge theory with matter

In the previous section, we have encountered a duality transformation that maps the $(2 + 1)$D transverse field Ising model onto the $(2 + 1)$D Ising lattice gauge theory – thus the
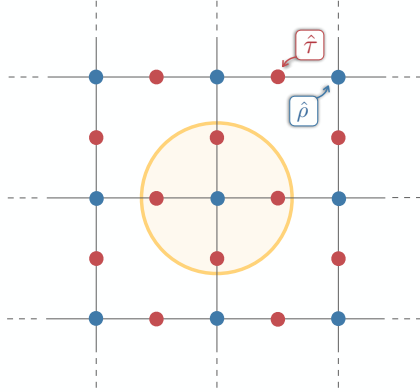
a Ising lattice gauge theory with matter   **b** Gauss' law
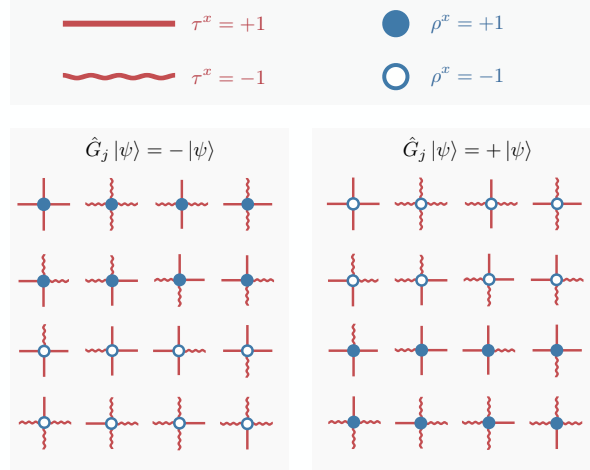
Figure 2.3: $\mathbb{Z}_2$ **LGT with matter. a** Self-duality of the $(2+1)$D Ising LGT is obtained by including matter degrees-of-freedom on the site of the lattice. The minimal coupling $\propto \hat{\rho}_i^z \hat{\tau}_{\langle i,j \rangle}^z \hat{\rho}_j^z$ between matter $\hat{\rho}$ (blue) and gauge $\hat{\tau}$ (red) fields gives rise to local conservation laws associated with the $\mathbb{Z}_2$ Gauss' law with matter illustrated in **b**. In the electric field τ^x and matter occupation ρ^z basis, Gauss' law in the sector without static background charges (right panel) implies that $\mathbb{Z}_2$ electric field lines can only terminate at $\mathbb{Z}_2$ charges.

model is not self-dual. As realized by Fradkin and Shenker in 1979 [28], self-duality can be established by extending the model in Eq. (2.17) with *matter* degrees-of-freedom $\hat{\rho}_j^x$ on the sites j of the lattice, where $\hat{\rho}^x = +1$ is the presence ($\hat{\rho}^x = -1$ is the absence) of a matter excitation, see Figure 2.3a.

The Fradkin-Shenker Hamiltonian [28, 133] of the $(2+1)$D $\mathbb{Z}_2$ Ising LGT with dynamical matter is given by

$$\hat{\mathcal{H}}_{\text{FS}} = -t \sum_{\langle i,j \rangle} \hat{\rho}_i^z \hat{\tau}_{\langle i,j \rangle}^z \hat{\rho}_j^z - J \sum_P \prod_{\langle i,j \rangle \in P} \hat{\tau}_{\langle i,j \rangle}^z - h \sum_{\langle i,j \rangle} \hat{\tau}_{\langle i,j \rangle}^x - \mu \sum_j \hat{\rho}_j^x, \qquad (2.24)$$

with the dimensional couplings for the minimal coupling term t, the plaquette interaction J, the string tension h and chemical potential μ. The Hamiltonian (2.24) commutes with the generalized local symmetry generators

$$\hat{G}_j = -\hat{\rho}_j^x \prod_{i:\langle i,j \rangle} \hat{\tau}_{\langle i,j \rangle}^x, \qquad (2.25)$$

and physical states are eigenstates $\hat{G}_j |\psi\rangle = g_j |\psi\rangle$ of a specific superselection sector $\mathbf{g} = (g_1, ..., g_n)$. As illustrated in Figure 2.3b, the eigenstates can be represented in the $\hat{\tau}_{\langle i,j \rangle}^x$-basis of the link variables ($\mathbb{Z}_2$ electric field) and the $\hat{\rho}^x$-basis of the matter variables ($\mathbb{Z}_2$ gauge charge). Thus, the matter and electric fields of a physical state are related via the $\mathbb{Z}_2$ **Gauss' law**

$$\prod_{i:\langle i,j \rangle} \hat{\tau}_{\langle i,j \rangle}^x = -g_j \hat{\rho}_j^x, \qquad (2.26)$$

which can be considered as a discretized version of Maxwell's first equation, $\nabla \cdot \mathbf{E} = \rho$, relating the flux of the electric field $\mathbf{E}$ to the charge distribution ρ. In Eq. (2.26), the choice of the superselection sector enters as a distribution of *static* background charges g_j. For the sector with no background charges ($g_j = +1$ for all j) $\mathbb{Z}_2$ charges at site i and j are connected by an electric string, which is a path of flipped strings $\tau^x_{\langle i,j \rangle} = -1$ from site i to site j.

Then, the $\mathbb{Z}_2$ gauge field $\hat{\tau}^z_{\langle i,j \rangle}$ is the conjugate variable, i.e., $[\hat{\tau}^z_{\langle i,j \rangle}, \hat{\tau}^x_{\langle i,j \rangle}] = 2i\hat{\tau}^y_{\langle i,j \rangle}$, of the electric field. Since the gauge field operator does not commute with the symmetry generator, it is not an observable in the LGT. However, closed loops such as Wilson loop or plaquette operator can admit expectation values, which we interpret as (divergent free) $\mathbb{Z}_2$ magnetic flux.

Phases of the Ising $\mathbb{Z}_2$ LGT with matter   The model (2.24) is dual to itself. To study the ground state phase diagram [28], we consider the limiting cases $t/\mu = 0$ and $J/h = \infty$, see Figure 2.4. In the latter case, the gauge field dynamics is frozen (pure matter theory) and we can fix the gauge $\hat{\tau}^z_{\langle i,j \rangle} \equiv 1$, such that we obtain the transverse field model with continuous phase transition. In fact, this reflects the Wegner duality and, likewise, we obtain the Ising* transition for the pure gauge theory ($t = 0$). Thus, the transitions of the pure matter and pure gauge theory are captured by the Ising magnetization and the Wegner-Wilson loops, respectively.

To understand the effect of dynamical matter in the gauge theory, we start in the limit of the pure gauge theory and deep in the plaquette phase ($t = 0$, $J/h \to \infty$). Here, the Hamiltonian reduces to

$$\hat{\mathcal{H}} = -J \sum_P \prod_{\langle i,j \rangle \in P} \hat{\tau}^z_{\langle i,j \rangle} - \mu \sum_j \hat{\rho}^x_j. \tag{2.27}$$

Let the state $|0\rangle$ describe a state without matter excitations. Then, by applying a non-local string operator $\hat{b}^\dagger_x = (\prod_{j<x} \hat{\tau}^z_j)\hat{\rho}^z_x$, we can create a $\mathbb{Z}_2$ charged state $|x\rangle = \hat{b}^\dagger_x|0\rangle$ at finite energy cost. Thus, the phase contains free $\mathbb{Z}_2$ charge excitations. In Ref. [28] they show that this *deconfined* phase is stable for small perturbations $t, h \ll J, \mu$, see Figure 2.4, before the string tension h confines $\mathbb{Z}_2$ charges.

Similarly, in the limit $h/J \to \infty$ we can construct a state with two static test charges at position x and x', i.e., we choose $g_x = g'_x = -1$ and $g_j = +1$ elsewhere. Because of Gauss' law, the two static charges have to be connected by an electric field line with an energy cost $V(\ell) = h \cdot \ell$, where ℓ is the length of the string. The linearly increasing potential $V(\ell)$ causes confinement of $\mathbb{Z}_2$ charges. As J is increased, the electric strings start to fluctuate until infinitely large electric loops proliferate and charges become deconfined [4, P5, P12].

In fact, in the limit of two test charges, the perimeter and area law is suitable to distinguish between the different regimes, and the Wilson loops give direct access to the effective potential between charges [4]. However, once we include finite matter density this order parameters breaks down and Wilson loops obey perimeter law away from the axis in Figure 2.4. Since the Wilson loops are related to the effective potential, the perimeter law decay in the presence of dynamical charges indicates screening of the $\mathbb{Z}_2$ charge and string breaking.

In their seminal 1979 paper [28], Fradkin and Shenker were able to map out the full
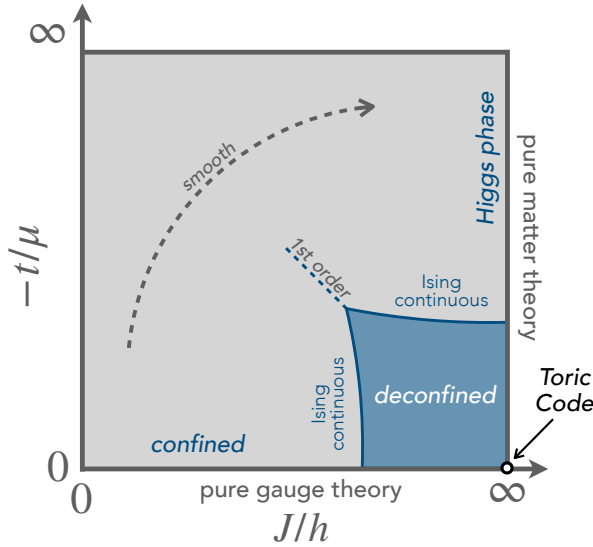
Figure 2.4: **Fradkin-Shenker model.** The ground-state phase diagram of the $\mathbb{Z}_2$ LGT with matter, Eq. (2.24), consists of only two phases: the deconfined/topologically-ordered phase and the confined-Higgs phase. As shown in Ref. [28], the confinement and Higgs mechanism are smoothly connected in this model. The figure was adapted from Ref. [P5].

phase diagram of the Ising LGT with matter, which was later also confirmed in Monte Carlo simulations [130]. Their most important finding is about the inside of the phase diagram shown in Figure 2.4. By constructing a path (dotted line) between the confined phase and the corresponding phase mirrored at the self-duality line (the Higgs phase), they concluded that the two regions are smoothly connected without any discontinuity in the partition function. This is surprising: in the Higgs phase the gauge charges "condense" and the gauge field acquires a mass; in the confined phase no free charges can exist. Despite the physically very different mechanisms, the spectrum of the confined and Higgs phase is smoothly connected, similar to a BEC-BCS crossover scenario.

We highlight that a bulk of the results discussed above can be obtained using symmetries and self-duality. This allowed us to show the rich structure of models with local symmetries, e.g., phases of matter with connections to charge (de)confinement. However, these arguments are limited to very fine tuned systems and, in fact, phase diagrams for general classes of gauge theories with dynamical matter remain elusive [23]. This has various reasons: Numerical simulations in $(2+1)$D and beyond are limited to extremely small systems. Further, the interplay between charge and gauge degrees-of-freedom can lead to new emergent phenomena, such as condensation of confined charge pairs [P5] necessitating to develop new order parameters. Moreover, experimental toy models with access to non-local observables, e.g., in quantum simulators, remain challenging to be implemented for large system sizes, see Section 2.2.5.

2.2.3 Constructing LGTs

In the previous section, we covered a very explicit example of a LGT with the purpose of introducing notation, terminology and lines of arguments typically used in the study of LGTs. In the literature, a few models such as the Fradkin-Shenker model [28], Wilson's lattice QCD [26], or the quantum link model [147], are considered. In contrast, for near-future experimental applications it may be more important to focus on the defining features of LGTs, which can be readily implemented, instead of exactly engineering the Hamiltonians

of the above examples (*we take what we can get*).

For example, in optical lattice experiments the particle number is conserved and therefore the model will have an additional global U(1) symmetry that is present on top of the local gauge symmetry. Therefore, the model may not be a LGT in the traditional sense of gauging a global symmetry. Instead, the additional global symmetry can indeed be spontaneously broken with substantial consequences for the phase diagram [P5].

In this thesis, we define LGTs using the following ingredients:

Geometry — LGTs can be defined on arbitrary geometries, see Figure 1. Here, we focus on Bravais lattices in d spatial dimension; for historical reasons, we write $(d + 1)$-dimensional LGT.

Link variables — We define degrees-of-freedom on the links $\langle i, j \rangle$ between site i and j. The links can be constituted by different microscopic objects, such as spins or bosonic/fermionic particles, depending on the symmetry group and its representation. The electric and gauge fields are a set of conjugate operators acting on the link Hilbert space, and they are charged under the gauge symmetry.

Matter sites — We define dynamical matter degrees-of-freedom on the sites j of the lattice, which can be (hard core) bosons, fermions, spin-S, spin polarized, etc. The matter is charged under the gauge field, e.g., in SU(3) the matter has a color charge.

Local symmetries — A set of local symmetry generators $\hat{G}_j^\alpha$ ($\alpha = 1, .., M$) are defined on vertices of a lattice, which include the matter sites and its adjacent links. A set of non-commuting generators give rise to a non-Abelian gauge symmetry, e.g., the Lie group SU(N) is constituted by $M = N^2 - 1$ generators. Various local symmetries can be combined, e.g., U(N) = SU(N) × U(1). The corresponding conservation laws are the Gauss' laws of the LGT.

Hamiltonian — We call a Hamiltonian $\hat{\mathcal{H}}$ a LGT, if it obeys the above structure and commutes with all local symmetry generators $[\hat{\mathcal{H}}, \hat{G}_j^\alpha] = 0$. The Hamiltonian should be non-trivial in the sense that it is an interacting Hamiltonian[4].

Global symmetries — The Hamiltonian $\hat{\mathcal{H}}$ may have additional global symmetries, such as particle number conservation of matter excitations.

2.2.4 Non-Abelian gauge theories and the rishon construction

In the beginning of the Chapter, we have constructed a LGT with the discreet gauge group $\mathbb{Z}_2$. For the purpose of numerical or quantum simulations, a discreet group structure is advantageous because it comes with a finite dimensional link Hilbert space. In contrast, continuous gauge groups, e.g., U(1) or SU(N), require an infinitely dimensional Hilbert space at every link. For all practical purposes, the link Hilbert space has to be truncated, for which efficient descriptions in terms of *quantum link models* were put forward by D.

---

[4]One can construct trivial Hamiltonians with local symmetries, e.g., N-independent spins in a field $\hat{\mathcal{H}} = \sum_j \hat{\tau}_{\langle i,j \rangle}^z$. Since they are non-interacting, local magnetization is trivially conserved.
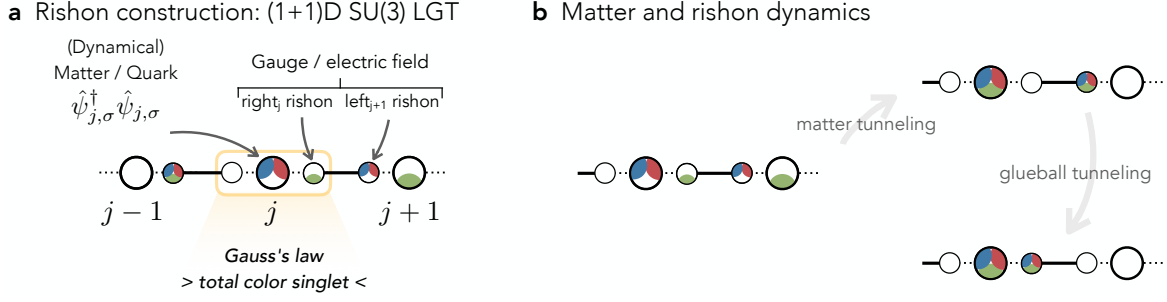
a Rishon construction: (1+1)D SU(3) LGT   **b** Matter and rishon dynamics

Figure 2.5: **Non-Abelian quantum link models. a** In the rishon construction, fermionic particles are introduced carrying the color charges $\sigma = $ red, blue, green. This formulation provides a finite dimensional representation of the link Hilbert space useful for quantum simulation [P9, 148, 149]. The Gauss' law enforces physical states to be a total color singlet on each vertex. Additionally, the rishon particle number per link $\mathcal{N}$ is strictly conserved; here we show $\mathcal{N} = 3$. Note that the notations 'left' and 'right' rishon are relative to a vertex j, which the rishon site is adjacent to. **b** We show tunneling processes consistent with the Gauss' law and rishon number constraint. Understanding the formation and properties of glueballs is one of the open questions in non-Abelian gauge theories: Indeed, proving the mass gap of a glueball excitation is part of the Millennium prize problem on the quantum Yang-Mills theory [150].

Horn [151], U. J. Wiese and co-workers [147, 148]. In the following, we provide a brief overview of a non-Abelian quantum link formulation: the rishon construction [152].

In the quantum link formulation of SU(N) gauge theories, the link is constituted by two sites with exactly $\mathcal{N}$ color charges fermions (= rishons) per link, see Figure 2.5a. In $(1+1)$D, we can label the two sites 'left' and 'right' with respect to the vertex j and define fermionic rishon creation operators $\hat{c}^\dagger_{j,\sigma,L}$ and $\hat{c}^\dagger_{j,\sigma,R}$ with color σ. The color charged electric fields $\hat{E}^\sigma_{\langle i,j\rangle}$ (gauge fields $\hat{U}^{\sigma\sigma'}_{\langle i,j\rangle}$) are defined as the imbalance (off-diagonal order) between the the two rishon sites on link $\langle i,j\rangle$,

$$\hat{E}^\sigma_{\langle i,j\rangle} = \frac{1}{2}\left(\hat{c}^\dagger_{j,\sigma,L}\hat{c}_{j,\sigma,L} - \hat{c}^\dagger_{i,\sigma,R}\hat{c}_{i,\sigma,R}\right) \tag{2.28a}$$

$$\hat{U}^{\sigma\sigma'}_{\langle i,j\rangle} = \hat{c}_{i,\sigma,R}\hat{c}^\dagger_{j,\sigma',L}\ , \tag{2.28b}$$

which correctly satisfy (almost all) commutation relations of a SU(N) LGT [148, 152]. The advantage of the rishon formulation is that the Hamiltonian of Wilson's lattice QCD can be used one-to-one, with the only difference that gauge fields on the same link become non-commuting objects, $[\hat{U}^{\sigma\sigma'}, \hat{U}^{\alpha\alpha'}] \neq 0$. Moreover, different rishon numbers $\mathcal{N} = \hat{c}^\dagger_{i,\sigma,R}\hat{c}_{i,\sigma,R} + \hat{c}^\dagger_{j,\sigma,L}\hat{c}_{j,\sigma,L}$ correspond to a different truncation of the gauge group, where $\mathcal{N} = 1$ provides the simplest case of one-rishon models and $\mathcal{N} = N$ are multirishon models with richer phenomenology [153].

On the sites of the lattice, we introduce the color charged matter excitations $\hat{\psi}^\dagger_{j,\sigma}$, which are the quarks in a SU(3) LGT. The color spin is defined using Schwinger fermions with $\hat{\mathbf{S}}_j = \hat{\psi}^\dagger_{j,\sigma}\mathbf{T}^{\sigma\sigma'}\hat{\psi}_{j,\sigma'}$; here $\mathbf{T} = (T^1, ..., T^M)$ are the generators of the SU(N) Lie algebra. Analogously, the color spin for the rishons is defined.

The non-Abelian gauge theory is characterized by multiple Gauss' laws for each gener-
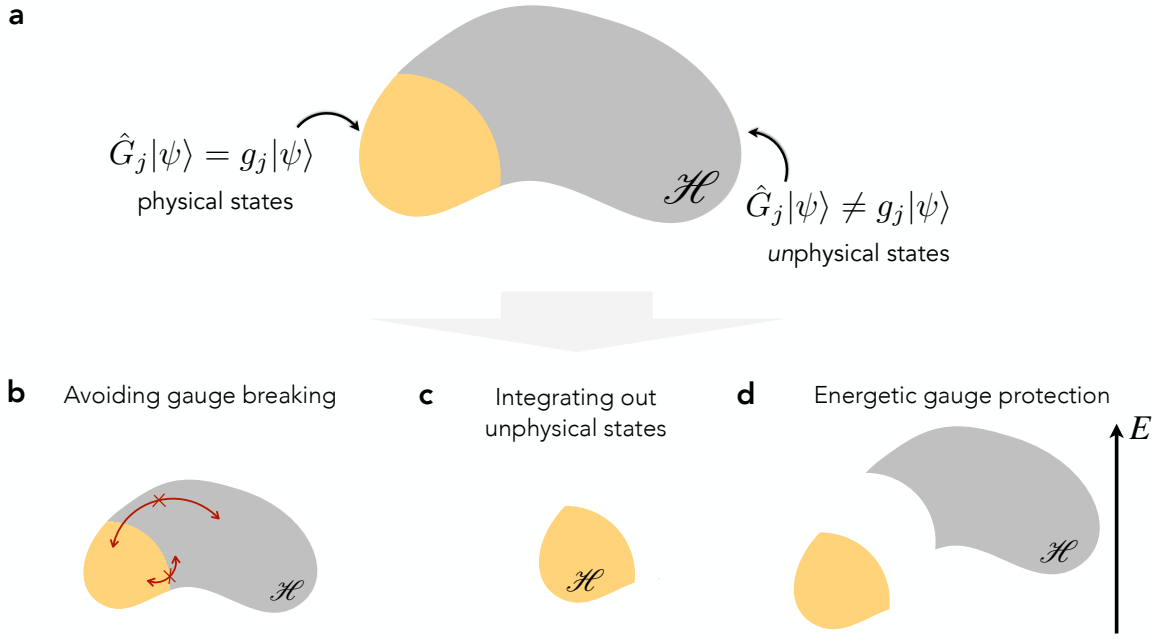
Figure 2.6: **Implementing Gauss' law. a** Gauge theories are highly constrained models with an extensive number of local conservation laws (Gauss' laws/superselection sectors) that have to be simultaneously fulfilled across the entire system. States in the correct (incorrect) Gauss' law sector are called physical (unphysical) states. One of the major challenges for the quantum simulation of LGTs is to enforce the Gauss' law constraints. **b-d** Various approaches have successfully demonstrated the experimental realization of a LGT; in Table 2.1 the different methods are compared.

ator $\alpha = 1, ..., M$, which mutually do not commute on the same vertex:

$$\hat{G}_j^\alpha = \hat{\psi}_{j,\sigma}^\dagger (T^\alpha)^{\sigma\sigma'} \hat{\psi}_{j,\sigma'} + \sum_{I=L,R} \hat{c}_{j,I,\sigma}^\dagger (T^\alpha)^{\sigma\sigma'} \hat{c}_{j,I,\sigma'}. \qquad (2.29)$$

For rishon models without static background charges, the Gauss' laws enforces that physical states $|\psi\rangle$ are a total color singlet at each vertex, such that

$$\hat{G}_j^\alpha |\psi\rangle = 0. \qquad (2.30)$$

Additionally, it may occur that the total number of particles (matter+rishon) is conserved on each vertex. This gives rise to an extra local U(1) symmetry, which in combination with the non-Abelian model yields a non-Abelian U(N) = SU(N) × U(1) LGT.

In summary, the rishon formulation of non-Abelian LGTs requires two constraints: (1) The non-Abelian Gauss' laws and (2) the rishon number constraint. In Figure 2.5b processes consistent with these constraints are illustrated. The tunneling of an entire glueball is only allowed in SU(N) LGTs but not in U(N) LGTs because it does not conserve particle number locally.

	Avoiding gauge breaking	Integrating out unphysical states	Energetic gauge protection
Hilbert space	$\mathcal{H}_{\mathrm{phys}} \cup \overline{\mathcal{H}}_{\mathrm{phys}}$	$\mathcal{H}_{\mathrm{phys}}$	$\mathcal{H}_{\mathrm{phys}} \cup \overline{\mathcal{H}}_{\mathrm{phys}}$
➕	accurate Hamiltonian engineering	No gauge violation	Experimental feasibility
➖	limited to building blocks	complicated many-particle interactions	no accurate Hamiltonian engineering
scalable	not yet	yes	yes
superselection sectors	accessible	not accessible	accessible
Experiments	e.g. Ref. [154]	e.g. Refs. [96, 155–158]	e.g. Refs. [51, 53, 159]

Table 2.1: **Strategies in the quantum simulation of LGTs.** Various strategies to realize LGTs in quantum simulation platforms have been developed and experimentally demonstrated.

2.2.5   LGTs in quantum simulators

The phenomenology of gauge theories emerges from the highly constrained Hilbert space $\mathcal{H}_{\mathrm{phys}} = \{|\psi\rangle \mid \hat{G}_j|\psi\rangle = g_j|\psi\rangle\} \subset \mathcal{H}$, see Figure 2.6a. Any coupling of physical, gauge-invariant states $|\psi\rangle \in \mathcal{H}_{\mathrm{phys}}$ to unphysical, gauge-variant states can cause thermalization of the system with the unconstrained Hilbert space $\mathcal{H}$. While in high-energy physics and in most theoretical studies gauge violations are conjectured to be zero, these gauge violating processes are crucial to understand and control in the context of quantum simulation, where imperfections in the engineering of Hamiltonians cannot be avoided [46].

In the field, various approaches to realize LGTs have been put forward, which currently all co-exist with their own advantages and disadvantages, summarized in Table 2.1 and illustrated in Figure 2.6b-d. Broadly, they can be categorized in *bottom-up* and *top-down* approaches:

Bottom-up   Given a Hamiltonian of a LGT, the goal is to engineer this exact Hamiltonian in a quantum simulator with high accuracy. Typically, digital simulators, where logical gates enable to time evolve under any Hamiltonian, use bottom-up approaches, see e.g. Ref. [160, 161]. Further, perturbative schemes for analog quantum simulation were developed and led to the first experimental demonstration of a $\mathbb{Z}_2$ LGT building block in Munich in 2019 [154, 162], realizing the Hamiltonian

$$\hat{\mathcal{H}} = -t \sum_{\langle i,j \rangle} \left(\hat{a}_i^\dagger \hat{\tau}_{\langle i,j \rangle}^z \hat{a}_j + \mathrm{h.c.} \right) + h \sum_{\langle i,j \rangle} \hat{\tau}_{\langle i,j \rangle}^x, \tag{2.31}$$

where $\hat{a}_j^\dagger$ ($\hat{a}_j$) is the creation (annihilation) operator of hardcore bosonic matter on site j; see also Ref. [139] for a superconducting qubit implementation scheme. In a LGT, the minimal coupling term, which describes the gauge-invariant tunneling of matter, is already a three-body interaction; since most natural interactions are between two bodies, see Section 2.1, higher-order interactions only arise in perturbation theory. While the leading-order term in the perturbative expansion may accurately be described by, e.g., Eq. (2.31), higher-order terms and external error sources may not be gauge invariant.

An experimental sequence consists of preparing an initial state in the physical Hilbert space with subsequent time evolution under the leading-order gauge-invariant Hamiltonian. Inevitably, the gauge breaking terms cause thermalization with the non-physical states, see Figure 2.6b. Without additional protection mechanism, such as energetic protection of the physical subspace, a large-scale experimental realization is only possible under highly controlled conditions.

Another approach is to integrate out the unphysical states of the Hilbert space, see Figure 2.6c. In the $\mathbb{Z}_2$ LGT with hardcore bosonic matter, this is easily achieved by using Gauss' law to derive the operator identity in Eq. (2.26). While this completely removes the unphysical states, and thus the undesired gauge breaking terms, it comes with other challenges. The resulting new effective Hamiltonian is typically long-ranged [155] or at least contains many-body interactions that have to be engineered. In specific circumstances, however, the process of integrating out either matter or gauge degrees-of-freedom can be advantageous [158]. For example, the dynamics of a chain of Rydberg atoms under the PXP model can be directly mapped to a U(1) quantum link model [96, 156]. We note that eliminating degrees-of-freedom can be non-trivial for gauge theories beyond $\mathbb{Z}_2$ LGT, but procedures for non-Abelian LGTs have been developed in the literature [163].

Top-down   Another approach is motivated by condensed-matter physics, where gauge constraints emerge at low energies. Given the Hamiltonian $\hat{\mathcal{H}}_{\text{LGT}}$ and the symmetry generator $\hat{G}_j$ of a LGT, we add a stabilizer term $\hat{\mathcal{H}}_V$ to the Hamiltonian given by

$$V\hat{\mathcal{H}}_V = -V \sum_j \left(\hat{G}_j - g_j\right)^2, \tag{2.32}$$

which acts as a Lagrange multiplier. We assume the symmetry generator has a discrete spectrum, which is true for $\mathbb{Z}_2$ LGTs or quantum link models. As illustrated in Figure 2.6c, the full Hamiltonian $\hat{\mathcal{H}} = \hat{\mathcal{H}}_{\text{LGT}} + V\hat{\mathcal{H}}_V$ has a low-energy manifold with states in the physical subspace associated with the superselection sector $\mathbf{g} = (g_1, ..., g_n)$; the protection term V has to be larger than any other energy scale in the system. For the gauge-invariant Hamiltonian, the stabilizer term trivially divides the spectrum into manifolds of physical and unphysical states. However, the stabilizer term becomes crucial when we include gauge-noninvariant error terms $\varepsilon\hat{\mathcal{H}}_\varepsilon$ with $[\hat{G}_j, \hat{\mathcal{H}}_\varepsilon] \neq 0$, e.g., external error sources in experiments or errors arising from the engineering of $\hat{\mathcal{H}}_{\text{LGT}}$ [154]. It has been shown that for sufficiently large V/ε gauge breaking errors are efficiently suppressed up to exponentially long times relevant for experiments [30, 164].

One interpretation of the energetic gauge protection can be obtained from the quantum

Zeno effect [165, 166]. The *strong* stabilizer term acts as a projector into the eigenspace of $\hat{\mathcal{H}}_V$, which can be seen, e.g., by trotterizing the time evolution under a Hamiltonian $\hat{\mathcal{H}} + \hat{\mathcal{H}}_\varepsilon$. If the eigenspace of $\hat{\mathcal{H}}_V$ is spanned by the superselection sectors, the system remains gauge-invariant throughout the time evolution.

The top-down method to realize gauge theories is based on the following idea [167]: We start with a LGT and its symmetry generators $\hat{G}_j$ and we define the unperturbed Hamiltonian $\hat{\mathcal{H}}_V$, which energetically singles out a specific superselection sector of physical states, see Figure 2.6c. The unperturbed Hamiltonian has manifolds with exponentially large degeneracy associated with the Gauss' law constraints. Next, we add a (coherent) perturbation $\varepsilon\hat{\mathcal{H}}_\varepsilon$ with $\varepsilon \ll V$, such that perturbative dynamics is induced [P5, P9, 51, 53]. Due to the energetic protection of gauge-invariant subspaces, the induced effective dynamics $\hat{\mathcal{H}}_{\text{eff}}$ is – per construction – gauge-invariant in the target Hilbert space of physical states. The effective, low-energy Hamiltonian $\hat{\mathcal{H}}_{\text{eff}}$ can be obtained by the Schrieffer-Wolff transformation [168]

$$\hat{\mathcal{H}}_{\text{eff}} = \hat{\mathcal{P}}_{\text{phys}} e^{\hat{S}} \hat{\mathcal{H}} e^{-\hat{S}} \hat{\mathcal{P}}_{\text{phys}}, \tag{2.33a}$$

$$\hat{\mathcal{H}} = V\hat{\mathcal{H}}_V + \varepsilon\hat{\mathcal{H}}_\varepsilon, \tag{2.33b}$$

where $\hat{\mathcal{P}}_{\text{phys}}$ is a projector onto the target Hilbert space and $\hat{S}$ is the generator of the transformation defined by $\varepsilon\hat{\mathcal{H}}_\varepsilon + [\hat{S}, V\hat{\mathcal{H}}_V] = 0$.

The top-down approach has the advantage that gauge-breaking errors are well controlled by the strength of the perturbation ε/V, which has to be chosen such that (i) gauge-breaking errors are sufficiently small and (ii) effective dynamics is sufficiently large on experimental time scales. While this can be fulfilled for lowest order perturbative processes, e.g., the minimal coupling term can arise in second or third-order perturbation theory [P5, P9], the method does not solve the problem of generating strong, nonperturbative plaquette terms [139].

Moreover, since the top-down approach does not integrate out degrees-of-freedom, one has straightforward access to all superselection sectors important in the study of gauge theories. In condensed-matter physics, gauge theories emerge at low-energies with the ground state serving as a renormalized vacuum $|0\rangle$, e.g., the topological phase of the toric code is characterized by fluctuating loops [3, 4]. Then, the charge and magnetic excitations on top of the renormalized vacuum are characteristic of the underlying phase of matter. In the topological phase, the excitations are anyons with mutual braiding statistics [29]; the confined phase has no free charge excitations. Having direct access to all those degrees-of-freedom is an advantage over schemes, where matter or link variables are integrated out.

The top-down method has enabled the first large-scale implementation of a (1+1)D $U(1)$ quantum link model with dynamical matter. The scheme starts from a Bose-Hubbard model in a superlattice with a tilted chemical potential [53, 159]. The latter is a simple scheme to energetically protect the target Gauss' law sector, while on-site Hubbard interactions U together with the superlattice structure and tunneling gives rise to second-order gauge-invariant tunneling processes.

In this thesis, we discuss two top-down schemes for the implementation of $\mathbb{Z}_2$ LGTs and

for SU(N) LGTs with dynamical matter beyond $(1+1)$D. In particular, we develop new methods that simplify the experimentally required interactions to two-body interactions and we propose concrete experimental schemes for Rydberg tweezer arrays, cold molecules and ultracold fermions.
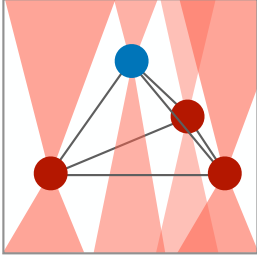
3

Large-scale implementation of $\mathbb{Z}_2$ lattice gauge theories with dynamical matter

THE LARGE-SCALE IMPLEMENTATION of LGTs necessitates to control gauge-violating processes, which do not conserve Gauss' law and break the local symmetries. Hereby, $\mathbb{Z}_2$ LGTs with dynamical matter pose a surprisingly difficult challenge because of the structure of Gauss' law, which preserves local parity. Let us re-write Eq. (2.26) as

$$\hat{G}_j = (-1)^{\hat{n}_j} \prod_{i:\langle i,j \rangle} \hat{\tau}^x_{\langle i,j \rangle}, \tag{3.1}$$

where $\hat{n}_j = \hat{a}^\dagger_j \hat{a}_j$ is the number operator for hardcore bosonic matter $\hat{a}^\dagger_j$ at site j. Therefore, a top-down approach, see Chapter 1, where the stabilizer term is explicitly implement experimentally requires strong $(z+1)$-body terms; z is the coordination number of the underlying lattice.

In this Chapter, we discuss a theoretical trick that enables us to reduce the experimental complexity from $(z+1)$-body to two-body terms for lattices with $z \leq 3$ by using so-called *local pseudogenerators* (LPGs). Further, experimentally realistic schemes for Rydberg tweezer arrays are presented including the resulting effective $\mathbb{Z}_2$ gauge-invariant Hamiltonian. We discuss the phase diagram and find intimate relations to the Fradkin-Shenker phase diagram in Figure 2.4.

The following Chapter is based on publication [P4] and [P5]. The text and figures are rearranged, adapted and supplemented. Moreover, preliminary results are presented in Section 3.7 and 3.8. Those preliminary results are obtained from discussions with Johannes Zeiher and his Strontium tweezer team as well as in collaboration with Andrea Pizzi, Fabian Grusdt, Jad C. Halimeh and Hongzheng Zhao, respectively.
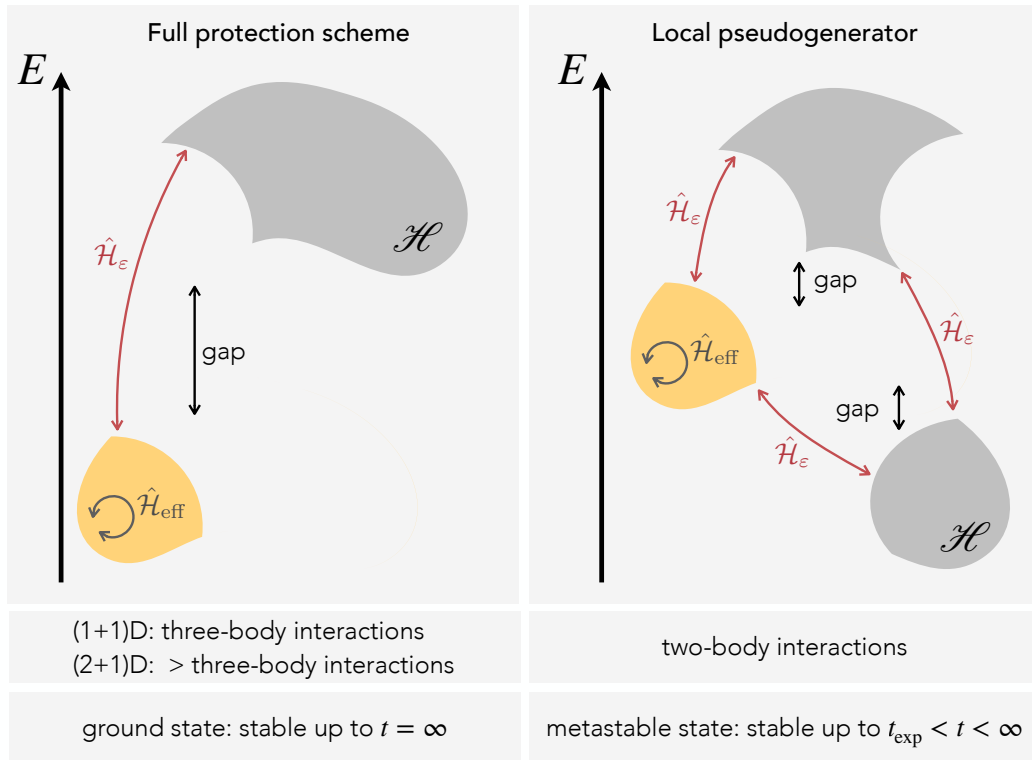
Figure 3.1: **Energetic gauge protection** introduces an energy gap between a target sector of physical states (yellow) and undesired unphysical states (gray). The full protection scheme is able to protect gauge-invariance up to infinite times t, but requires experimentally challenging many-body interactions as the largest energy scale in the system. In contrast, the novel local pseudogenerator (LPG) protection scheme replaces the ground-state protection scheme by a metastable manifold of physical states. This reduces the experimental complexity to two-body Ising interactions, while maintaining gauge invariance for all experimentally relevant times t_{exp}. In both cases, the perturbation $\hat{\mathcal{H}}_\varepsilon$ can be used to generate manifestly gauge-invariant dynamics described by $\hat{\mathcal{H}}_{\mathrm{eff}}$ within the physical subsector.

3.1   Local pseudogenerators in $(1+1)\mathbf{D}$

The key idea of local pseudogenerators, see Figure 3.1, is as follows: The full protection scheme has a low-energy sector associated with physical states fulfilling Gauss' law. If we prepare a physical state in a quantum simulator, it will remain in the sector for infinite times because it cannot decay into unphysical states. However, this requires to experimentally implement the $(z + 1)$-body stabilizer terms described above. In contrast, the local pseudogenerator (LPG) has a *metastable* manifold, which is protected up to times relevant for the experiment, and only requires two-body Ising interactions; eventually a physical state will decay and thermalize with the unphysical states. Therefore, the LPG is ideally suited for quantum simulation purposes: it is based on experimentally feasible interactions and single-site control allows to prepare initial states in the physical subspace protected up to all relevant times.

While the LPG method provides a conceptual idea, we need to show that LPGs can

exists for $\mathbb{Z}_2$ LGTs with dynamical matter. In $(1+1)$D, this can be easily shown using algebraic transformations. In the physical subspace, the Gauss' law becomes an operator identity

$$\hat{G}_j = (-1)^{\hat{n}_j} \hat{\tau}^x_{\langle j-1,j \rangle} \hat{\tau}^x_{\langle j,j+1 \rangle} = g_j \mathbb{1}. \tag{3.2}$$

For hardcore bosons/fermions, we use $\hat{n}_j \leq 1$ to define the LPG as [P4]

$$\hat{W}^{1D}_j = \hat{\tau}^x_{\langle j-1,j \rangle} \hat{\tau}^x_{\langle j,j+1 \rangle} + g_j(2\hat{n}_j - 1), \tag{3.3}$$

where we have neglected a constant energy offset. The spectrum of the LPG term consists of three manifolds with eigenenergies $w^{1D}_j = -2, 0, +2$, which energetically separates the Hilbert into physical and unphysical states, see Figure 3.1:

$$\hat{W}^{1D}_j |\psi_{\text{phys}}\rangle = 0|\psi_{\text{phys}}\rangle, \qquad \hat{W}^{1D}_j |\psi_{\text{unphys}}\rangle = \begin{cases} +2|\psi_{\text{unphys}}\rangle \\ -2|\psi_{\text{unphys}}\rangle \end{cases}. \tag{3.4}$$

To show that the LPG allows us to protect the Gauss' law for experimentally relevant time scales, we introduce a general protection scheme based on LPGs described by the Hamiltonian

$$\hat{\mathcal{H}} = \hat{\mathcal{H}}_{\text{LGT}} + \hat{\mathcal{H}}_\varepsilon + \hat{H}_V \tag{3.5}$$

with

$$\hat{\mathcal{H}}_{\text{LGT}} = J \sum_{\langle i,j \rangle} \left(\hat{a}^\dagger_i \hat{\tau}^z_{\langle i,j \rangle} \hat{a}_j + \text{h.c.} \right) - h \sum_{\langle i,j \rangle} \hat{\tau}^x_{\langle i,j \rangle}, \tag{3.6a}$$

$$\hat{\mathcal{H}}_\varepsilon = \lambda \sum_j \hat{\mathcal{H}}^{\text{err}}_{\text{loc}}, \tag{3.6b}$$

$$\hat{H}_V = V \sum_j c_j \hat{W}^{1D}_j. \tag{3.6c}$$

Here, $\hat{\mathcal{H}}_{\text{LGT}}$ is a $(1+1)$D$\mathbb{Z}_2$ LGT with dynamical, hardcore bosonic matter $\hat{a}^\dagger_j$ including the minimal coupling $\propto J$ and confining term $\propto h$. The error term $\hat{\mathcal{H}}_\varepsilon$ contains experimentally relevant, local errors obtained from Ref. [154, 162] (see Ref. [P4] for an explicit expression).

The protection term $\propto V$ contains local coefficients $c_j \in [-1,1]$, which are needed to suppress remaining, undesired resonances between physical and unphysical states. Suppose the system is initialized in a physical state, then states with Gauss' law errors on two vertices i and j may be on resonance if the vertex i (j) goes up (down) in energy, or vice versa, according to Eq. (3.4). If the errors are local, which have assumed above, then those undesired resonances can be efficiently suppressed by choosing a staggered sequence, e.g., $c_j = [6(-1)^j + 5]/11$.

In Figure 3.2, we show results of an exact time-evolution study of the Hamiltonian (3.5) in a small system with $L = 6$ sites. The system is initialized in the physical subspace with $g_j = +1$ for all j, in particular in a state $|\psi_0\rangle$ with staggered matter occupation, and evolved up to times $t \cdot J$ for various protection strengths V/J; the error term is kept constant
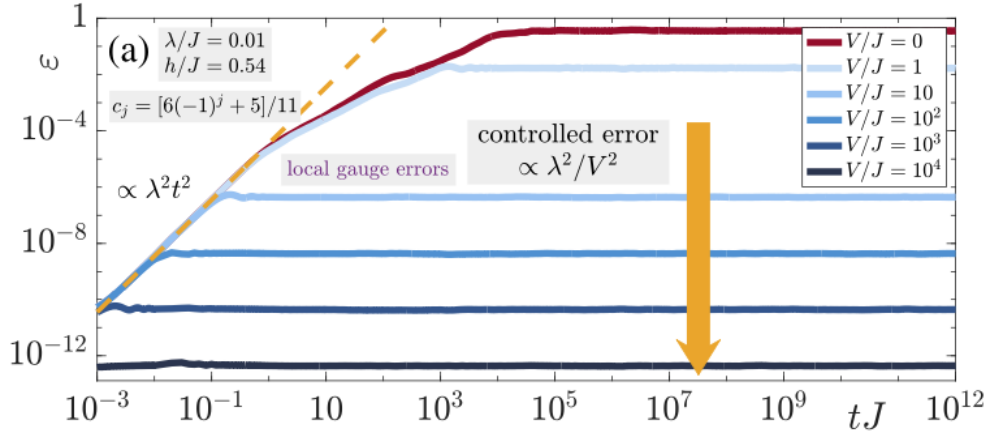
Figure 3.2: **LPG gauge protection in** $(1+1)$**D** $\mathbb{Z}_2$ **LGT.** We show the time evolution of an initial gauge-invariant state under a $(1+1)$D $\mathbb{Z}_2$ LGT with dynamical hardcore bosonic matter in the presence of errors $\propto \lambda$ and protection terms $\propto V$ using exact diagonalization. After an initial growth of the gauge breaking error $\varepsilon(t)$, Eq. (3.7), the error plateaus and remains finite for all numerically accessible times. The ED simulations were performed by Jad C. Halimeh.

with $\lambda/J = 0.01$. We define a measure for the gauge violation $\varepsilon(t)$ with

$$\varepsilon(t) = 1 - \frac{1}{Lt} \int_0^t ds \sum_j \langle \psi(s) | \hat{G}_j | \psi(s) \rangle, \tag{3.7}$$

where $\psi(t) = e^{-i\hat{H}t} |\psi_0\rangle$ is the time evolved state. For local errors and a staggered sequence, we find strong suppression of the gauge violation up to all accessible times in the small system and for various initial states. For early times, the gauge violation grows polynomially with $\epsilon(t) \propto \lambda^2 t^2$, which can be obtained from time-dependent perturbation theory [P4, 30]. For later time, the error remains constant and settles to a plateau with a height $\propto \lambda^2/V^2$.

While the LPG stabilizer in Eq. (3.6c) is able to stabilize the gauge constraints with only two-body interactions, it is not suitable as a starting point to perturbatively induce gauge-invariant dynamics in a top-down approach, see Chapter 2.2.5. Instead, we have assumed that a gauge-invariant Hamiltonian $\hat{\mathcal{H}}_{\text{LGT}}$ can be engineered, see e.g. Refs. [139, 154, 162]. To perturbatively generate a $\mathbb{Z}_2$ invariant Hamiltonian including a minimal coupling term, we need to introduce some interaction between gauge and matter degrees-of-freedom; otherwise those degrees-of-freedom are completely independent. In the next section, we find that there exists a LPG for $(2+1)$D, where matter and gauge are fully coupled and which cannot be derived as above. By cookie-cutting a $(1+1)$D chain, an alternative LPG term in $(1+1)$D is derived.

Lastly, we briefly discuss the validity of the LPG stabilizer. As we show in Figure 3.2, the gauge errors are controlled and can be suppressed by increasing the protection strength V. Nevertheless, there are remaining gauge breaking errors with – in principle – detrimental consequences for the phenomenology of LGTs. Let us draw an analogy with numerical methods: Using approximate numerical methods, such as tensor product states or Monte

Carlo techniques, to determine the ground or thermal state of an interacting many-body system is a challenging problem. In particular, the result can look converged by looking at "simple" observables, e.g., the local density, whereas higher-order correlation function may not be converged yet. Similarly, the suppressed gauge violation may suggest that the dynamics is completely governed by the gauge-invariant Hamiltonian $\hat{\mathcal{H}}_{\mathrm{LGT}}$. Thus, we emphasize the importance to compare the dynamics of various observables between the ideal LGT and LPG protected model. For the LPG in $(1+1)$D, it was shown to be able to stabilize ubiquitous phenomena of $\mathbb{Z}_2$ LGTs such as quantum many-body scarring [169] and disorder-free localization [30].

3.2   Local pseudogenerators in $(2+1)$D

We introduce a local pseudogenerator (LPG) method for a $(2+1)$D $\mathbb{Z}_2$ gauge theory with dynamical matter ($\mathbb{Z}_2$ mLGT) on the honeycomb lattice [P5] with the Gauss' law in Eq. (3.2). For the honeycomb lattice with coordination number $z = 3$, one can find a LPG term constituted by only two-body Ising interactions and single-body chemical potential terms, which enables to stabilize the Gauss' law constraint in Rydberg tweezer quantum simulators on timescales relevant to experiments. This allows us to propose a conceptually novel and feasible scheme to engineer $\mathbb{Z}_2$ gauge-invariant Hamiltonians, inherently protected from gauge-symmetry breaking imperfections and including dynamical matter. We study the phase diagrams of the derived effective models and suggest experimental probes to explore their rich physics. Our scheme allows to explore physics beyond numerically accessible regimes in state-of-the-art analog quantum simulators.

We propose to realize matter and link variables as qubits, implementable by the ground $|g\rangle$ and Rydberg $|r\rangle$ states of atoms in optical tweezers [12, 51, 91, 92, 96, 170], see Figure 3.3a and b. Thus, the product in Eq. (3.2) measures the parity of qubit excitations of matter and links around vertex j. In the following we concentrate on $g_j = +1$, which is called an even $\mathbb{Z}_2$ LGT, but as shown in Ref. [P5] the sector $g_j = -1$ can also be experimentally realized. Within the sector $g_j = +1$ and at full filling, i.e., $\hat{n}_j = +1 \; \forall j$, the matter is static and the system is equivalent to an odd $\mathbb{Z}_2$ LGT without matter [44], i.e., $\hat{n}_j = 0$ but $g_j = -1$.

3.2.1   Local pseudogenerator on the honeycomb lattice

The main ingredient of the experimental scheme is the LPG interaction term $V\hat{W}_j$. As shown in Figure 3.3a, $V\hat{W}_j$ consists of equal-strength $2V$ interactions among all qubits (matter and gauge) around vertex j, taking the form

$$V\hat{W}_j = \frac{V}{4}\left[(2\hat{n}_j - 1) + \sum_{i:\langle i,j\rangle} \hat{\tau}^x_{\langle i,j\rangle}\right]^2. \tag{3.8}$$

We assume that V defines the largest energy scale in the problem, which separates the Hilbert space into constrained subspaces. This overcomes the most challenging step, im-
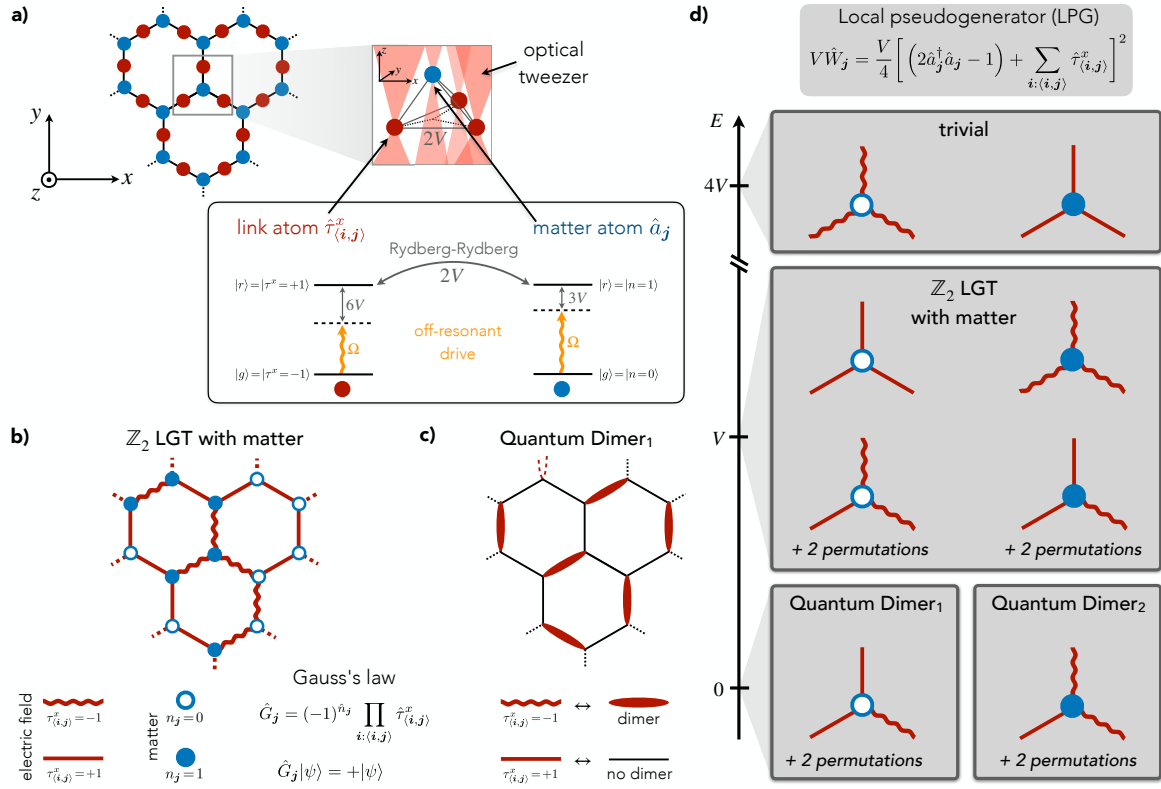
Figure 3.3: **Constraint-based scheme. a)** The $\mathbb{Z}_2$ gauge structure emerges from the dominant local-pseudogenerator (LPG) interaction on the honeycomb lattice. A vertex contains matter $\hat{a}_j$ qubits (blue) and shares link $\hat{\tau}^x_{\langle i,j \rangle}$ qubits (red) with neighboring vertices. All qubits connected to a vertex interact pairwise with strength $2V$. In a Rydberg atom array experiment the qubits are implemented by individual atoms in optical tweezers, which are assigned the role of matter or link depending on the position in the lattice. Here, the ground- and Rydberg state of the atoms, $|g\rangle$ and $|r\rangle$, encode qubit states, which are coupled by an off-resonant drive Ω to induce effective interactions. To realize equal strength nearest neighbor, two-body Rydberg-Rydberg interactions, the matter atoms can be elevated out of plane. **b)** We introduce the notation for the QDM subspace with exactly one dimer per vertex and for the $\mathbb{Z}_2$ mLGT, for which the Hilbert space constraint is given by Gauss's law $\hat{G}_j = +1$. **c)** We show how the distinct subspaces are energetically separated by the LPG term $V\hat{W}_j$. The two quantum dimer subspaces are disconnected when the matter is static, which can be exactly realized by the absence of matter atoms in panel **a)** and setting $(2\hat{a}_j^\dagger \hat{a}_j - 1) = \pm 1$ in $V\hat{W}_j$.

posing different gauge constraints in the emerging subspaces, see Chapter 2.2.5 and Figure 3.1.

We obtain three distinct eigenspaces of the LPG term: 1) Two (distinct) quantum dimer model (QDM) subspaces at low-energy, 2) physical states of a $\mathbb{Z}_2$ mLGT at intermediate energies, and 3) trivial, polarized states at high energy, see Figure 3.3b and c.

Experimentally, we propose to implement strong LPG terms in the Hamiltonian such that quantum dynamics are constrained to remain in LPG eigenspaces by large energy barriers enabling the large-scale quantum simulation of $\mathbb{Z}_2$ mLGTs in (2+1)D. To introduce

Figure 3.4: **Disorder-based protection scheme.** We calculate the spectrum of the minimal model (inset) and plot all eigenstates of the LPG protection term, Eq. (3.8), around energy $E = 4V$. Green (red) dots are states that fulfil (break) Gauss' law as illustrated with two examples in the inset of panel **a)**. Without disorder, i.e. $V_j = V$ for all j, the physical and unphysical states are on resonance. In panel **b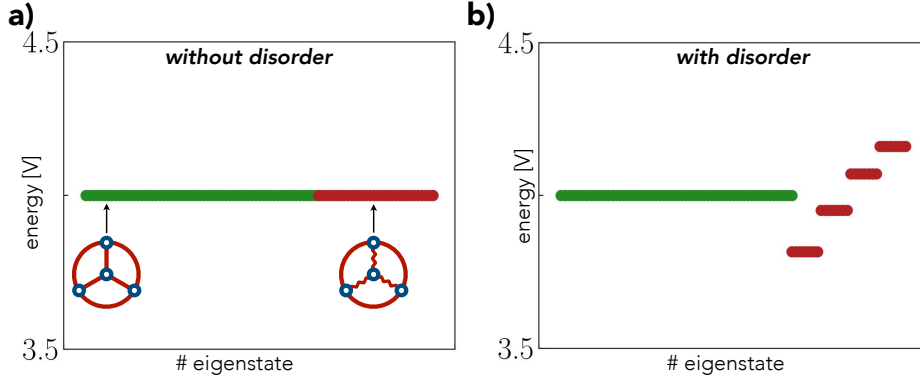)**, we show the effect of disordered protection terms $V_j = V + \delta V_j$, which only shifts the unphysical states out of resonance and hence fully stabilizes the gauge theory. We note that even without disorder, the emergent gauge structure is remarkably robust.

constraint-preserving dynamics within the LPG subspaces, the latter are coupled by weak on-site driving terms of strength $\Omega \ll V$ as discussed below. Through the constrained dynamics, a $\mathbb{Z}_2$ mLGT emerges in an intermediate-energy eigenspace of $V\hat{W}_j$, which is accessible in quantum simulation platforms and which distinguishes our work from previous studies on emergent gauge symmetries, e.g. [171–173].

The LPG method is built upon stabilizing a high-energy sector of the spectrum, which comes with the caveat that a few unphysical states are resonantly coupled when considering the entire lattice. Let us first consider the spectrum of the LPG term

$$V\hat{W}_j|\psi^{\mathrm{phys}}\rangle = +V|\psi^{\mathrm{phys}}\rangle, \qquad V\hat{W}_j|\psi^{\mathrm{unphys}}\rangle = \begin{cases} +4V|\psi^{\mathrm{unphys}}\rangle \\ 0V|\psi^{\mathrm{unphys}}\rangle \end{cases}, \qquad (3.9)$$

which has eigenenergies $w_j = (0, V, 4V)$. If the interaction strength V is equally strong at each vertex gauge-symmetry breaking can occur. Most notable are an important class of unphysical states that violate Gauss' law on four vertices with energy lowered on three vertices and raised on one vertex; hence these states are on resonance with physical states. For example, by exciting vertex j_0 and simultaneously de-exciting three vertices j_1, j_2 and j_3. This process has a net energy difference of $\Delta E = +3V - 3 \cdot V = 0$ and the resonance between the two states can lead to an instability towards unphysical states, hence gauge-symmetry breaking. However, numerical simulations in small systems suggest that these gauge-breaking terms only play a subdominant role and gauge-invariance remains intact.

Therefore, the LPG method without disorder cannot energetically protect against *some* states that break Gauss' law on four vertices. An efficient way to stabilize the gauge theory even against such scenarios is to introduce disorder in the coupling strengths by $\hat{W} = \sum_j V_j \hat{W}_j$ with $V_j = V + \delta V_j$. The couplings δV_j are random and form a so-called com-

pliant sequence [P4, 30]. In $(1+1)$D systems, this has been shown to faithfully protect $\mathbb{Z}_2$ LGTs also for extremely long times, see Section 3.1 and Ref. [P4] for a detailed discussion of (non)compliant sequences. Moreover, we note that numerical simulations in small systems suggest that these gauge-breaking terms only play a subdominant role and gauge-invariance remains intact.

For our $(2+1)$D model, we illustrate the effect of disordered protection terms in Figure 3.4, which shows that only the gauge non-invariant states are shifted out of resonance. In particular, we propose to use weak disorder such that the overall perturbative couplings remain unchanged in leading order. We emphasize that the disorder scheme does not require any additional experimental capabilities but only arbitrary control over the geometry as well as local detuning patterns. Even more, an experimental realization will always encounter slight disorder, i.e., the gauge non-invariant processes might already be sufficiently suppressed in experiment.

We further note that the example above, where Gauss's law is violated on four vertices, yields gauge-breaking terms in third-order perturbation theory. Ensuring that none of the protection terms V_j have gauge-breaking resonances within such a nearest-neighbour cluster, these terms can be suppressed. However, now it remains space for fifth-order breaking terms on next-nearest neighbour vertices. Hence, the non-resonance condition is now desired on a larger cluster and so forth. Therefore, systematically choosing the disorder potentials can suppress gauge-breaking terms to arbitrary finite order and stabilize gauge invariance up to exponential times. Its fate in the thermodynamic limit, however, is an open question and will be briefly discussed in a classical spin system in Section 3.8.

3.2.2　Experimental realization in Rydberg tweezer arrays

In the following, we introduce the microscopic model $\hat{\mathcal{H}}^{\mathrm{mic}}$ which can be directly implemented in state-of-the-art Rydberg atom arrays in optical tweezers, see Figure 3.3a. From the microscopic model, effective Hamiltonians for the $\mathbb{Z}_2$ mLGT and QDM subspaces can be derived by a Schrieffer-Wolff transformation, see Sections 3.3 and 3.5. On realistic timescales of experiments, the effective models are gauge-invariant by construction and studied further below.

The constituents are qubits, which can be modeled by the ground $|g\rangle$ and Rydberg $|r\rangle$ states of individual atoms. As shown in Figure 3.3a, we label the atoms as *matter atom* or *link atom* depending on their position on the lattice. The $\mathbb{Z}_2$ gauge structure then emerges from nearest-neighbor Ising interactions V realized by Rydberg-Rydberg interactions and hence the real space geometric arrangement plays a key role. The dynamics is induced by a weak transverse field Ω_m (Ω_l), which corresponds to a homogeneous drive between the ground and Rydberg states of the matter (link) atoms. Moreover, tunability of parameters defining the phase diagram is achieved by a longitudinal field or detuning Δ_m (Δ_l) of the weak drive.

The interesting physics emerges in different energy subsectors of the LPG protection term $\propto V\hat{W}_j$ in Eq. (3.8); in particular the $\mathbb{Z}_2$ mLGT is a sector in the middle of the spectrum of $\hat{\mathcal{H}}^{\mathrm{mic}}$. The suitability for Rydberg atom arrays comes from the flexibility in geometric arrangement required for the LPG term as well as from the natural energy scales $V \gg \Omega$ in

the system, which we use to derive the effective models below, see Eqs. (3.11) and (3.18).

Matter atoms $\hat{a}_j$ form the sites of a honeycomb lattice and we map the empty $|n_j = 0\rangle$ (occupied $|n_j = 1\rangle$) state on the ground state $|g\rangle_j$ (Rydberg state $|r\rangle_j$) of the atoms. Link atoms $\hat{\tau}^x_{\langle i,j\rangle}$ are located on the links of the honeycomb lattice, i.e., a Kagome lattice, and analogously we map the $\tau^x_{\langle i,j\rangle} = +1$ ($\tau^x_{\langle i,j\rangle} = -1$) state on the atomic state $|g\rangle_{\langle i,j\rangle}$ ($|r\rangle_{\langle i,j\rangle} = \hat{a}^\dagger_{\langle i,j\rangle} |g\rangle_{\langle i,j\rangle}$). Moreover, we want the matter and link atoms to be in different layers and those layers should be vertically slightly apart in real space to ensure equal two-body interactions between matter and link atoms. Using the out-of-plane direction has the advantage that it only requires atoms of the same species and with the same internal states. However, the equal strength interaction can also be achieved in-plane by using e.g. two atomic species [174–176] or different (suitable) internal Rydberg states for the matter and link atoms.

We first propose a non gauge-invariant microscopic Hamiltonian from which we later derive an effective model with only gauge-invariant terms. To lowest order in perturbation theory and on experimentally relevant timescales, the system evolves under an emergent gauge-invariant Hamiltonian. The microscopic Hamiltonian is given by

$$\hat{\mathcal{H}}^{\text{mic}} = \hat{\mathcal{H}}^{\text{LPG}} + \hat{\mathcal{H}}^{\text{detuning}} + \hat{\mathcal{H}}^{\text{drive}}, \tag{3.10a}$$

$$\hat{\mathcal{H}}^{\text{LPG}} = V \sum_j \hat{W}_j, \tag{3.10b}$$

$$\hat{\mathcal{H}}^{\text{detuning}} = -\Delta_m \sum_j \hat{n}_j - \frac{\Delta_l}{2} \sum_{\langle i,j\rangle} \hat{\tau}^x_{\langle i,j\rangle}, \tag{3.10c}$$

$$\hat{\mathcal{H}}^{\text{drive}} = \Omega_m \sum_j \left(\hat{a}_j + \hat{a}^\dagger_j \right) + \Omega_l \sum_{\langle i,j\rangle} \left(\hat{a}_{\langle i,j\rangle} + \hat{a}^\dagger_{\langle i,j\rangle} \right), \tag{3.10d}$$

where bosonic operators $\hat{a}^{(\dagger)}_j$ and $\hat{a}^{(\dagger)}_{\langle i,j\rangle}$ annihilate (create) excitations on the matter and link atoms, respectively; $\hat{W}_j$ is the LPG term introduced in Eq. (3.8). The last two terms describe driving of matter ($|g\rangle_j \leftrightarrow |r\rangle_j$) and link atoms ($|g\rangle_{\langle i,j\rangle} \leftrightarrow |r\rangle_{\langle i,j\rangle}$) in the rotating frame. Rewriting (3.10) in the atomic basis yields Rydberg-Rydberg interactions of strength $2V$ and renormalized, large detunings $\tilde{\Delta}_m = -3V + \Delta_m$ and $\tilde{\Delta}_l = -3V + \Delta_l$. In a Rydberg setup the driving terms can be realized by an external laser, which couples $|g\rangle \leftrightarrow |r\rangle$, while the detunings Δ_m, Δ_l of the laser relative to the resonance frequency controls the electric field Δ_l and chemical potential Δ_m in the rotating frame.

In the limit $\Omega_m, \Omega_l \ll V$, the energy subspaces defined by the LPG term $V\hat{W}_j$, Eq. (3.8), are weakly coupled by the drive to induce effective interactions and it is convenient but not required to choose $\Omega_m = \Omega_l = \Omega$. The $\mathbb{Z}_2$ mLGT emerges as an intermediate-energy eigenspace of the LPG term $V\hat{W}_j$. The effective interactions in the constrained $\mathbb{Z}_2$ mLGT and QDM subspaces of $\hat{W}_j$ can be derived by a Schrieffer-Wolff transformation yielding the models discussed in the next sections.

In the experiment we propose, the Rydberg-Rydberg interactions are not only restricted to nearest neighbours but are long ranged. We emphasize that beyond nearest neighbour interactions are inherently gauge invariant and hence do neither influence the LPG gauge protection scheme nor the Schrieffer-Wolff transformation. However, the long-range in-

teractions can have strong influence on the $\mathbb{Z}_2$ invariant dynamics. While the interaction strength decreases as $1/R^6$, where R is the distance between atoms, the interaction is still comparable to the effective perturbative dynamics, see Supplementary Information in Ref. [P5]. We note that the dynamics might be slowed down but the qualitative features of the $\mathbb{Z}_2$ mLGT remain intact.

3.3   Effective $\mathbb{Z}_2$ mLGT model

A model is locally $\mathbb{Z}_2$ invariant if its Hamiltonian $\hat{\mathcal{H}}$ commutes with all symmetry generators $\hat{G}_j$, i.e., $[\hat{\mathcal{H}}, \hat{G}_j] = 0$ for all j. This ensures that all dynamics is constrained to the physical subspace without leaking into unphysical states. In Eq. (3.8), the target sector is $g_j = +1$ for all j but our scheme can be easily adapted for any $\{g_j\}_j$.

In the presence of strong LPG protection, the system is energetically enforced to remain in a target gauge sector and unphysical states are only virtually occupied by the drive Ω, see Figure 3.1. To be precise, resonant couplings to unphysical sectors are suppressed by the (experimentally feasible) disorder protection scheme discussed above. Otherwise emergent gauge-breaking terms appear in third-order perturbation theory. However, in small systems we have numerically confirmed that even without disorder in the LPG terms Gauss's law is well conserved, which in larger systems we expect to crossover to an *approximate* gauge invariance. In the following we assume disorder protection or small systems, where leading order gauge-breaking terms are absent or can be neglect, respectively.

For the proposed on-site driving terms discussed above and shown in Figure 3.3a, we derive the following effective Hamiltonian from the microscopic model (3.10) in the intermediate-energy LPG eigenspace:

$$\hat{\mathcal{H}}_{\mathbb{Z}_2}^{\text{eff}} = \sum_{\langle i,j \rangle} \left(t \hat{a}_i^\dagger \hat{\tau}_{\langle i,j \rangle}^z \hat{a}_j + \Delta_1 \hat{a}_i^\dagger \hat{\tau}_{\langle i,j \rangle}^z \hat{a}_j^\dagger + \Delta_2 \hat{a}_i^\dagger \hat{\tau}_{\langle i,j \rangle}^x \hat{\tau}_{\langle i,j \rangle}^z \hat{a}_j^\dagger + \text{H.c.} \right)$$
$$- J \sum_{\bigcirc} \prod_{\langle i,j \rangle \in \bigcirc} \hat{\tau}_{\langle i,j \rangle}^z - h \sum_{\langle i,j \rangle} \hat{\tau}_{\langle i,j \rangle}^x - \mu \sum_j \hat{n}_j. \tag{3.11}$$

The first terms in Eq. (3.11) describe gauge-invariant hopping of matter excitations with amplitude t and (anomalous) pairing $\propto \Delta_1$ ($\propto \Delta_2$). The term $\propto J$ is the magnetic plaquette interaction on the honeycomb lattice. The last two terms are referred to as electric field term h and chemical potential μ, respectively. Note that deriving Hamiltonian (3.11) from the microscopic model in Eq. (3.10) yields additional higher-order terms, see below, $\propto \hat{\tau}^x \hat{\tau}^x$, $\hat{\tau}^x \hat{n}$, etc. In the effective model $\hat{\mathcal{H}}_{\mathbb{Z}_2}^{\text{eff}}$ we treat these higher-order terms on a mean-field level of the electric field and matter density. Moreover, we emphasize that the effective model is solely derived from the microscopic Hamiltonian, which only requires a simple set of one- and two-body interactions between the constituents.

Schrieffer-Wolff transformation   In this section, we explain the derivation of the effective Hamiltonian (3.11) in terms of a Schrieffer-Wolff transformation [168]. Starting point is the experimentally motivated microscopic Hamiltonian (3.10), where identify the unperturbed, diagonal part (in the Fock basis) with $\hat{\mathcal{H}}_0 = \hat{\mathcal{H}}^{\text{LPG}} + \hat{\mathcal{H}}^{\text{detuning}}$ and the off-diagonal

perturbation with $\hat{\mathcal{H}}^{\text{drive}}$. Note that the perturbation is a gauge-symmetry breaking term, $[\hat{\mathcal{H}}^{\text{drive}}, \hat{G}_j] \neq 0 \,\forall j$. However a state prepared in the physical subspace, $g_j = +1 \,\forall j$, will only virtually occupy unphysical states under $\hat{\mathcal{H}}^{\text{mic}}$ because of the large energy gap V between the sectors in the limit of weak driving, $\Omega_m, \Omega_l \ll V$.

Hamiltonian $\hat{\mathcal{H}}_0$ is diagonal in the matter density and electric field basis and hence the unperturbed eigenstates are product states $|\alpha\rangle = \bigotimes_j |n_j\rangle \bigotimes_{\langle i,j \rangle} |\tau^x_{\langle i,j \rangle}\rangle$. Since $\hat{\mathcal{H}}^{\text{drive}}$ only contains off-diagonal elements, there are no first-order contributions, $\langle \alpha | \hat{\mathcal{H}}^{\text{drive}} | \alpha \rangle = 0$. The derivation of the second- and third-order terms are explained in the following.

The second-order terms are given by

$$\langle \beta | \hat{\mathcal{H}}^{\text{eff}}_{\text{2nd}} | \alpha \rangle = \frac{1}{2} \sum_\delta \langle \beta | \hat{\mathcal{H}}^{\text{drive}} | \delta \rangle \langle \delta | \hat{\mathcal{H}}^{\text{drive}} | \alpha \rangle \left(\frac{1}{E_\beta - E_\delta} + \frac{1}{E_\alpha - E_\delta} \right), \qquad (3.12)$$

where $|\alpha\rangle$ ($|\beta\rangle$) are the initial (final) state and $|\delta\rangle$ are virtual states. Because $\hat{\mathcal{H}}^{\text{drive}}$ has only off-diagonal elements, it always couples to states outside the physical energy sector and hence in second-order the initial and final state coincide, $|\alpha\rangle = |\beta\rangle$, in order to remain within the same energy subspace.

In third-order perturbation theory, coupling between different states, $|\alpha\rangle \neq |\beta\rangle$, occurs, which yields interesting dynamical hopping and pairing terms. The coupling elements in the effective Hamiltonian can be calculated by evaluating

$$\langle \beta | \hat{\mathcal{H}}^{\text{eff}}_{\text{3rd}} | \alpha \rangle = \frac{1}{3} \sum_{\delta, \delta'} \langle \beta | \hat{\mathcal{H}}^{\text{drive}} | \delta \rangle \langle \delta | \hat{\mathcal{H}}^{\text{drive}} | \delta' \rangle \langle \delta' | \hat{\mathcal{H}}^{\text{drive}} | \alpha \rangle$$
$$\times \left[\frac{1}{(E_\delta - E_{\delta'})(E_{\delta'} - E_\alpha)} + \frac{1}{(E_\beta - E_\delta)(E_\delta - E_{\delta'})} - \frac{2}{(E_\beta - E_\delta)(E_{\delta'} - E_\alpha)} \right], \qquad (3.13)$$

where the sum runs over two virtual states $|\delta\rangle$, $|\delta'\rangle$.

Calculating the above matrix elements in the target energy subspace yield the effective Hamiltonian (3.11). Note that the plaquette terms are not appearing directly in third-order perturbation but would require to go to sixth-order perturbation theory; the plaquette terms are discussed separately in Ref. [P5]. First, we want to give an explicit expression of the effective Hamiltonian up to third-order perturbation theory and distinguish the cases with and without global U(1) symmetry.

3.3.1 Global U(1) symmetry for matter

To enforce conservation of matter excitations, we introduce an additional energy gap between different particle number sectors by choosing $|\Delta_m| = V/2 \gg \Delta_l, \Omega_m, \Omega_l$. This strong chemical potential term suppresses creation and annihilation of matter excitations induced by $\hat{\mathcal{H}}^{\text{drive}}$.

The effective model for U(1) matter coupled to a $\mathbb{Z}_2$ gauge field in the sector $g_j = +1 \,\forall j$

ampl.	$\hat{\mathcal{H}}^{\text{eff}}$		$U(1)$ matter	Quantum $\mathbb{Z}_2$ matter
t	$\sum_{\langle i,j\rangle}\left(\hat{a}_i^\dagger \hat{\tau}_{\langle i,j\rangle}^z \hat{a}_j + \text{H.c.}\right)$		$\dfrac{4\Omega_l\Omega_m^2\left(3+\Delta_m^2/V^2\right)}{(9V^2-\Delta_m^2)(1-\Delta_m^2/V^2)^2}$	$\dfrac{4\Omega_l\Omega_m^2}{3V^2}$
Δ_1	$\sum_{\langle i,j\rangle}\left(\hat{a}_i^\dagger \hat{\tau}_{\langle i,j\rangle}^z \hat{a}_j^\dagger + \text{H.c.}\right)$		–	$\dfrac{20\Omega_l\Omega_m^2}{9V^2}$
Δ_2	$\sum_{\langle i,j\rangle}\left(\hat{a}_i^\dagger \hat{\tau}_{\langle i,j\rangle}^x \hat{\tau}_{\langle i,j\rangle}^z \hat{a}_j^\dagger + \text{H.c.}\right)$		–	$\dfrac{16\Omega_l\Omega_m^2}{9V^2}$
h	$\sum_{\langle i,j\rangle}\hat{\tau}_{\langle i,j\rangle}^x$		$\dfrac{2\Omega_m^2}{3V-2\Delta_m-\Delta_m^2/V}+\dfrac{\Delta_l}{2}$	$\dfrac{2\Omega_m^2}{3V}+\dfrac{\Delta_l}{2}$
μ	$\sum_j \hat{n}_j$		$\Delta_m+\dfrac{2\Omega_m^2\left(-7\Delta_m-\Delta_m^3/V^2\right)}{9V^2-10\Delta_m^3/V+\Delta_m^3/V^2}$	$\dfrac{\Omega_l^2}{2V}+\Delta_m$
M	$\sum_{\langle i,j\rangle}\hat{n}_i\hat{n}_j$		$\dfrac{\Omega_l^2}{3V}$	$\dfrac{\Omega_l^2}{3V}$
χ_1	$\sum_{j_1}\hat{n}_{j_1}\left(\hat{\tau}_{\langle j_2,j_1+x\rangle}^x+\hat{\tau}_{\langle j_2,j_1+y\rangle}^x\right)$ $+\sum_{j_2}\hat{n}_{j_2}\left(\hat{\tau}_{\langle j_2-x,j_1\rangle}^x+\hat{\tau}_{\langle j_2-y,j_1\rangle}^x\right)$		$\dfrac{\Omega_l^2}{6V}$	$\dfrac{\Omega_l^2}{6V}$
χ_2	$\sum_{j_1}\left(\hat{\tau}_{\langle j_2-x,j_1\rangle}^x+\hat{\tau}_{\langle j_2-y,j_1\rangle}^x\right)$ $\times\left(\hat{\tau}_{\langle j_2,j_1+x\rangle}^x+\hat{\tau}_{\langle j_2,j_1-y\rangle}^x\right)$		$\dfrac{\Omega_l^2}{12V}$	$\dfrac{\Omega_l^2}{12V}$
χ_3	$\sum_{j_1}\hat{n}_{j_1}\left(\hat{\tau}_{\langle j_1,j_2\rangle}^x+\hat{\tau}_{\langle j_2-y,j_1\rangle}^x+\hat{\tau}_{\langle j_2-x,j_1\rangle}^x\right)$ $+\sum_{j_2}\hat{n}_{j_2}\left(\hat{\tau}_{\langle j_1,j_2\rangle}^x+\hat{\tau}_{\langle j_2,j_1+y\rangle}^x+\hat{\tau}_{\langle j_2,j_1+x\rangle}^x\right)$		$-\dfrac{\Omega_l^2}{3V}+\dfrac{2\Omega_m^2(3-\Delta_m^2/V^2)}{9V-10\Delta_m^2/V+\Delta_m^3/V^2}$	$-\dfrac{\Omega_l^2}{3V}+\dfrac{2\Omega_m^2}{3V}$
const.	$\mathbb{1}$		$\dfrac{\Omega_l^2}{6V}$ (# links) $+\dfrac{\Omega_m^2\left(2V-\Delta_m\right)}{\left(3V-\Delta_m\right)\left(V+\Delta_m\right)}$ (# sites)	$\dfrac{\Omega_l^2}{6V}$ (# links) $+\dfrac{2\Omega_m^2}{3V}$ (# sites)

Table 3.1: **Effective couplings derived from perturbation theory.** The LPG term defines energy subspaces, which can be weakly coupled by a drive, see Eq. (3.10). The effective couplings are derived in terms of a Schrieffer-Wolff transformation, yielding Hamiltonians Eqs. (3.14) and (3.16).

is given by

$$
\begin{aligned}
\hat{H}^{\text{eff}}_{\text{U(1) matter}} = {}& t \sum_{\langle i,j \rangle} \text{⧓} - J \sum_{\bigcirc} \text{⬡} - h \sum_{\langle i,j \rangle} \text{⊳⊲} - \mu \sum_{j} \text{⊱} + M \sum_{\langle i,j \rangle} \text{⊳⊲} \\
& + \chi_1 \sum_{\langle i,j \rangle} \left(\text{⊱⊲} + \text{⊳⊲} + \text{⊳⊱} + \text{⊳⊲} \right) \\
& + \chi_2 \sum_{\langle i,j \rangle} \left(\text{⊳⊲} + \text{⊳⊲} + \text{⊳⊲} + \text{⊳⊲} \right) \\
& + \chi_3 \sum_{j} \left(\text{⊱−} + \text{⊱−} + \text{⊱−} \right) + \text{const.}
\end{aligned}
\tag{3.14}
$$

The operator form and its corresponding coupling amplitudes for the second- and third order processes can be found in the fourth column of Table 3.1. Note that Gauss' law, $\hat{G}_j = +1$ has been used to simplify, collect and eliminate higher-order terms.

The terms $\propto M$, $\propto \chi_1$, $\propto \chi_2$ and $\propto \chi_3$ are (nearest neighbor density-density), (next-nearest neighbor density-electric field), (next-nearest neighbor electric field-electric field) and (nearest neighbor density-electric field) interactions, respectively. In the effective Hamiltonian, Eq. (3.11), we treat these terms on mean-field level in the electric field $\hat{\tau}^x_{\langle i,j \rangle}$ and matter density $\hat{n}_j$, which is well-defined since both quantities are gauge invariant. To be explicit, we perform for example a mean-field decoupling of $M \sum_{\langle i,j \rangle} \hat{n}_i \hat{n}_j \to M \langle \hat{n}_i \rangle \sum_j \hat{n}_j$, which simplifies the effective Hamiltonian.

3.3.2 Quantum-$\mathbb{Z}_2$ matter

Here, we discuss the derivation of the effective Hamiltonian (3.11) with quantum-$\mathbb{Z}_2$ matter coupled to a $\mathbb{Z}_2$ gauge field. In contrast to the previous paragraph, we do not enforce a global U(1) symmetry for the matter but otherwise the derivation is completely analogous. This leads to the additional pairing terms Δ_1, Δ_2 in Eq. (3.11). The effective model we find is invariant under the local transformation

$$
\hat{a}_j \longrightarrow -\hat{a}_j \qquad \hat{\tau}^z_{\langle i,j \rangle} \longrightarrow -\hat{\tau}^z_{\langle i,j \rangle} \ \forall i : \langle i,j \rangle.
\tag{3.15}
$$

However, the 2D quantum Hamiltonian cannot be mapped exactly on a classical 3D Ising LGT in the sense of Ref. [28], which is origin of the term "quantum-$\mathbb{Z}_2$ mLGT".

In the gauge sector $g_j = +1 \; \forall j$, the effective model reads

$$
\begin{aligned}
\hat{H}^{\text{eff},(3)}_{\mathbb{Z}_2} = {}& t \sum_{\langle i,j \rangle} \text{⧓} + \Delta_1 \sum_{\langle i,j \rangle} \text{⧓} + \Delta_2 \sum_{\langle i,j \rangle} \text{⧓} - J \sum_{\bigcirc} \text{⬡} \\
& - h \sum_{\langle i,j \rangle} \text{⧓} - \mu \sum_j \text{⊱} + M \sum_{\langle i,j \rangle} \text{⧓} \\
& + \chi_1 \sum_{\langle i,j \rangle} \left(\text{⧓} + \text{⧓} + \text{⧓} + \text{⧓} \right) \\
& + \chi_2 \sum_{\langle i,j \rangle} \left(\text{⧓} + \text{⧓} + \text{⧓} + \text{⧓} \right) \\
& + \chi_3 \sum_j \left(\text{⊱} + \text{⊱} + \text{⊱} \right) + \text{const.}
\end{aligned}
\tag{3.16}
$$

The operator form and its corresponding second- and third-order coupling amplitudes can be found in the fifth column of Table 3.1. Compared to (3.14), we now find pairing terms Δ_1 and Δ_2, which also appear in Fradkin & Shenker's Ising $\mathbb{Z}_2$ mLGT in a similar fashion, see Chapter 1. Again, the terms $\propto M$, $\propto \chi_1$, $\propto \chi_2$ and $\propto \chi_3$ can be treated on mean-field level yielding the effective model (3.11).

In particular, the electric field term $-h \sum_{\langle i,j \rangle} \hat{\tau}^x_{\langle i,j \rangle}$ can be fine-tuned by changing the detuning Δ_l, which in the limit $\Delta_l \ll V$ does not alter the results obtained from perturbation theory. On mean-field level, this allows to tune the expectation value to $\langle \hat{\tau}^x_{\langle i,j \rangle} \rangle = -1/2$. Then, the effective coupling renormalizes to $\tilde{\Delta}_1 = \Delta_1 - \langle \hat{\tau}^x_{\langle i,j \rangle} \rangle \Delta_2 = \Delta_1 - \Delta_2/2 = t$. At this particular point, we retrieve the $(2+1)$D model studied by Fradkin & Shenker [28], where it is known to map on a classical 3D $\mathbb{Z}_2$ mLGT with continuous phase transitions in the Ising universality class as discussed in Chapter 1. Note that our model is defined on the honeycomb and not square lattice. For a detailed discussion of the duality between a $\mathbb{Z}_2$ mLGT on a honeycomb and triangular lattice, we refer to the Supplementary Information of Ref. [173]. Because of this duality, the results obtained in Ref. [28] should be still valid, however the phase diagram might not be symmetric across the diagonal as in Figure 2.4.

3.4 Ground-state phase diagrams

We return to the effective model for the $\mathbb{Z}_2$ mLGT in Eq. (3.11). For any site j, one can take $\hat{a}_j \to -\hat{a}_j$ and $\hat{\tau}^z_{\langle i,j \rangle} \to -\hat{\tau}^z_{\langle i,j \rangle}$; hence the effective Hamiltonian (3.11) has a local $\mathbb{Z}_2$ symmetry, $[\hat{\mathcal{H}}^{\text{eff}}_{\mathbb{Z}_2}, \hat{G}_j] = 0 \; \forall j$, qualifying it as $\mathbb{Z}_2$ mLGT in $(2+1)$D. In particular, in our proposed scheme we do not have to apply involved steps to engineer $\mathbb{Z}_2$-invariant interactions but rather we exploit the intrinsic gauge protection by dominant LPG terms, which enforces any weak perturbation to yield an effective $\mathbb{Z}_2$ mLGT. This approach also inherently implies robustness against gauge-symmetry breaking terms in experimental realizations.

In the following, we discuss the rich physics of the effective model (3.11). However, due to the complexity of the system, it is challenging to conduct faithful numerical studies in extended systems. As a first step, we examine well-known limits of the model and
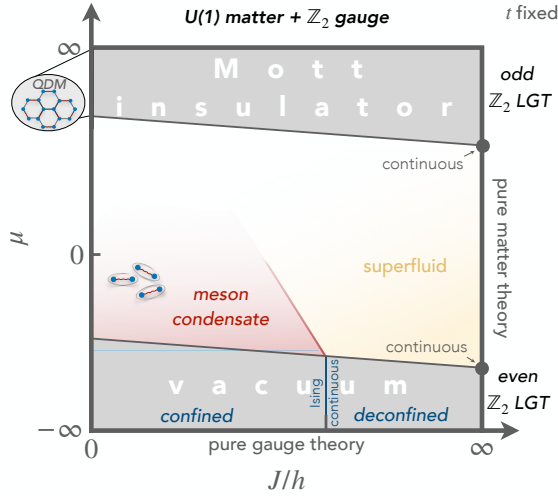
Figure 3.5: **Conjectured ground-state phase diagram.** We show a qualitative sketch of the phase diagrams for the effective model 3.11 with $\Delta_1 = \Delta_2 = 0$, i.e., with a global $U(1)$ symmetry for the matter. Along the vertical direction the filling is tuned, which yields an even (odd) $\mathbb{Z}_2$ pure gauge theory in the vacuum (Mott insulator). In between the matter and gauge degrees-of-freedom interplay, for which we examined the limiting cases.

conjecture $T = 0$ phase diagrams of the effective Hamiltonian when the $\mathbb{Z}_2$ gauge field is coupled to U(1) or quantum-$\mathbb{Z}_2$ dynamical matter, respectively. We note that the strength of the plaquette interaction can only be estimated, see Ref. [P5] for a detailed discussion, and competes with the long-range Rydberg interactions. Moreover, the disorder protection scheme underlying the derivation of the effective Hamiltonian ensures gauge-invariance of the leading order contributions but higher-order gauge breaking terms can in principle appear and affect the physics at very long timescales.

Our effective model describes the physics of experimental system sizes and timescales; the efficiency of the LPG gauge protection in the thermodynamic limit is a subtle but important open question, which we address in Section 3.8. Hence, in the following we discuss phases of the effective model (3.11) that may (or may not) emerge from the microscopic model (3.10).

3.4.1   Global U(1) symmetry for matter

By fixing the number of matter excitations in the system, i.e., $\Delta_1 = \Delta_2 = 0$ in Hamiltonian (3.11), the model has a global U(1) symmetry of the matter (hard-core) bosons, which can be achieved by choosing the detuning at the matter sites Δ_m comparable to V in our proposed experimental scheme Eq. (3.10). Here, we consider the phase diagram when the filling of matter excitations is controlled by the chemical potential μ. To map out different possible phases, we fix the hopping t and study limiting cases.

First, we consider the pure gauge theory with no matter excitations ($\mu \to -\infty$), see Figure 3.5 (bottom). The Hamiltonian then reduces to the Wegner's pure Ising LGT [27] with matter vacuum - an even $\mathbb{Z}_2$ LGT. As discussed in Chapter 1, the dual of this model exhibits a continuous (2+1)D Ising phase transition, corresponding to a confined (deconfined) phase below (above) a critical $(J/h)_c$, respectively [27, 43]. At the toric code point ($J/h = \infty$) the system is exactly solvable [177] and the gapped ground state has topological order.

Because for $J/h = \infty$ the gauge field has no fluctuations, we can fix the gauge by setting $\hat{\tau}^z_{\langle i,j \rangle} = +1$ and map out the pure matter theory in Figure 3.5 (right). For finite μ we find a model with free hopping of hard-core bosons, for which the filling can be tuned

by changing the chemical potential μ. Hence, for increasing μ and results based on the square lattice [178, 179] we expect two continuous phase transitions: vacuum-to-superfluid and superfluid-to-Mott insulator. The Mott insulator phase is an odd $\mathbb{Z}_2$ LGT because the matter is static and acts as background charge and thus can be treated as a pure gauge theory with $g_j = -1$ [44]. In the opposite limit $J/h = 0$, the same Mott state gives rise to a hard-core quantum dimer constraint for the $\mathbb{Z}_2$ electric field lines. On the square lattice, the quantum dimer model and odd $\mathbb{Z}_2$ LGT exhibit a phase transition from a confined to deconfined phase [47]. The honeycomb lattice and next-nearest neighbor Rydberg-Rydberg interactions might feature additional symmetry-broken phases. Hence it requires a sophisticated analysis to map out the substructure of the Mott insulating phase in Figure 3.5.

In the limit of low fillings and small but finite $J/h \ll 1$, the matter excitations form two-body mesonic bound states [47], which are $\mathbb{Z}_2$-charge neutral and can be considered as point-like particles. Below, we derive an effective meson model yielding hard-core bosons on the sites of a Kagome lattice.

At $T = 0$ and sufficiently low densities, the mesons can condense and spontaneously break the emergent global U(1) symmetry associated with meson number conservation. To determine the phase boundary of the meson condensate, we consider a single pair of matter excitations doped into the vacuum. This pair cannot alter the pure gauge phases and thus the two charges can be considered as probes for the (de)confined regime. For the latter, the matter excitations are bound into mesons, in contrast to free excitations above the deconfined regime. Hence, the effective description of bound mesonic pairs breaks down at the phase transition of the pure gauge theory indicating the phase boundary of the meson condensate phase at small filling.

At higher densities, dimer-dimer interactions and fluctuations of the gauge field play a role, requiring a more sophisticated analysis to predict the ground state. We emphasize that the rich physics in this model emerges from the gauge constraint generated by the LPG terms. Moreover, we note that by lifting the hard-core boson constraint, which is beyond our experimental scheme, the model maps onto a classical XY model coupled to a $\mathbb{Z}_2$ gauge field [44]. This model has been studied on the square lattice in the context of topological phases of matter [44] and high-Tc superconductivity [20, 180, 181], to name a few.

3.4.2 Effective meson model

As discussed above, deep in the confined regime and at low-density we expect a meson condensate phase. Here, we want to derive an effective meson model, which captures the condensate phase.

In the limit $J/h, t/h \to 0$ and dilute U(1) matter in the ground state, electric field strings are minimized under the constraints imposed by Gauss's law, i.e., number of links with $\tau^x_{\langle i,j \rangle} = -1$ is minimized. To fulfill Gauss' law $g_j = +1 \; \forall j$ matter excitations are bound into pairs connected by an electric field string, see Fig. 3.6a. Gauge-invariant hopping of matter excitations prolongs the string and thus kinetic energy t competes with the string tension h. Since $h \gg t$ it is unfavourable for single matter excitations to be mobile, which justifies to describe the constituents as tightly bound mesons.
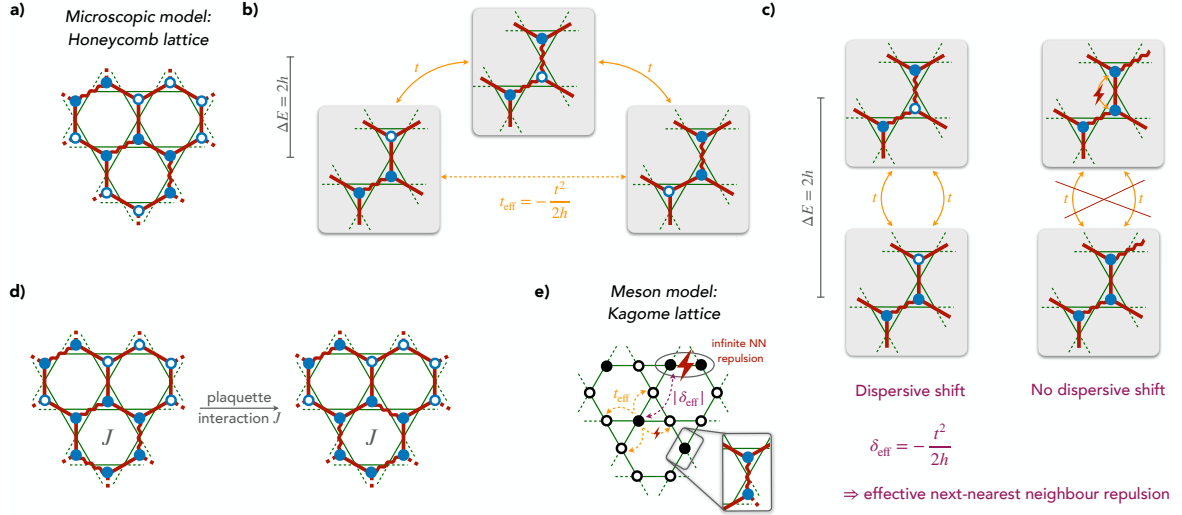
Figure 3.6: **Effective meson model. a)** For $J/h, t/h \to 0$, the matter excitations are tightly bound into mesonic pairs $\hat{b}$ on the honeycomb lattice. These mesons are again hard-core bosons and $\mathbb{Z}_2$ charge neutral. In **b)** and **c)**, we describe the leading order second-order processes derived from the $\mathbb{Z}_2$ mLGT, which gives rise to hopping t_{eff} of mesons as well as repulsive interactions $|\delta_{\text{eff}}|$ due to the absence of dispersive shifts for next-nearest neighbor mesons. Moreover, the plaquette interaction of the $\mathbb{Z}_2$ mLGT yields to fluctuating mesons for plaquettes with exactly three mesons as depicted in panel **d)**. Panel **e)** summarizes the effective meson model. The model is described by hopping $\propto t_{\text{eff}}$ of hard-core bosons $\hat{b}$ (black circles) on a Kagome lattice with infinitely strong nearest-neighbor repulsion (from the hard-core constraint on the honeycomb lattice), finite NNN repulsive interactions $\propto |\delta_{\text{eff}}|$ and plaquette interactions $\propto J$.

Nevertheless, the mesons can gain kinetic energy in two distinct processes: 1) a second-order hopping process $t_{\text{eff}} = -t^2/2h$, in which the entire pair moves from one link to a neighboring link as shown in Figure 3.6b and 2) plaquette interactions $\propto J$ induce fluctuations between the two different meson configurations on a plaquette as illustrated in Figure 3.6d. Additionally, the mesons gain dispersive energy shifts $\delta_{\text{eff}} = -t^2/2h$ if the matter excitation hops back and forth on neighboring sites, see Figure 3.6c. However, this process is only allowed for an empty neighboring site and therefore the dispersive energy shift leads to repulsive interactions between mesons. To summarize, we find an effective model of $\mathbb{Z}_2$ neutral, hard-core bosonic mesons $\hat{b}_n$ hopping on the sites of a Kagome lattice, with infinitely strong nearest neighbor (NN) repulsion, finite next-nearest neighbor (NNN) repulsion and plaquette interactions, see Figure 3.6e. The infinite repulsive term comes from the hard-core boson constraint of single matter excitations. Therefore, the effective meson model is given by

$$\hat{\mathcal{H}}_{\text{meson}} = t_{\text{eff}} \sum_{\langle n,m \rangle} \hat{P}_{\text{NN}} \left(\hat{b}_n^\dagger \hat{b}_m + \text{H.c.} \right) \hat{P}_{\text{NN}} - J \sum_P \hat{P}_{\text{NN}} \left(|\hexagon\rangle\langle\hexagon| + \text{H.c.} \right) \hat{P}_{\text{NN}}$$
$$+ |\delta_{\text{eff}}| \sum_{\langle\langle n,m \rangle\rangle} \hat{b}_n^\dagger \hat{b}_n \hat{b}_m^\dagger \hat{b}_m$$

(3.17)

where n, m denote sites of the Kagome lattice as shown in Figure 3.6e and the projector $\hat{P}_{\text{NN}}$ ensures the constraint that no nearest neighbor mesons can exist. Here, the notation $\langle \cdot, \cdot \rangle$ ($\langle\langle \cdot, \cdot \rangle\rangle$) describes (next-)nearest neighbors on the Kagome lattice.

For experimentally relevant parameters, we can choose $J/t \ll t/h$ and $J/h \ll 1$ and thus neglect the plaquette interaction term. In the limit of dilute mesons $\langle \hat{b}^\dagger \hat{b} \rangle \approx 0$, we can treat $\hat{P}_{\text{NN}}$ on a mean-field level yielding free hard-core bosons on the Kagome lattice. In the ground state the mesons $\hat{b}$ condense as conjectured in Figure 3.5.

Taking the plaquette interactions into account, i.e., $J/t \approx t/h$, phase separation by clustering of mesons has been discussed in Ref. [47] for spinless fermions on the square lattice. However, the NNN repulsive interaction should suppress clustering and hence a more sophisticated analysis is required.

Away from the above discussed limit $J/h \ll 1$, the meson pairs have some finite extend ℓ^2, which alters the effective model (3.17). However, for a sufficiently dilute gas of matter excitations, i.e., $\ell^2 \ll 1/\langle \hat{b}^\dagger \hat{b} \rangle$, we expect the description of free hard-core bosons to be still valid which we indicate by the finite extend of the meson condensate phase in Figure 3.5. We note that the phase boundary is expected to end at the deconfinement-confinement transition of the vacuum since in the deconfined phase the picture of bound mesonic pairs breaks down.

3.4.3   Quantum $\mathbb{Z}_2$ mLGT

Now, we consider the full effective Hamiltonian (3.11), where hopping and pairing are anisotropic $t \neq \Delta_1$ and the pairing strength can depend on the electric field configuration $\Delta_2 \neq 0$, and relate it to the phenomenology of the Fradkin and Shenker model described in Chapter 1 and Figure 2.4. In our model, the pure matter theory can no longer be mapped on the classical 3D Ising model. Hence, we introduce the term quantum-$\mathbb{Z}_2$ matter, which emphasizes the matter's $\mathbb{Z}_2$ symmetry group but points out that a mapping to a known classical model is lacking.

We note that close to the toric code point ($J/h = \infty$ and $t/\mu = 0$) in Figure 2.4, the expectation value of the electric field vanishes, $\langle \hat{\tau}^x_{\langle i,j \rangle} \rangle = 0$, and thus in mean-field approximation the anomalous terms should be negligible and renormalize the pairing $\Delta_1 \to \tilde{\Delta}_1$. For the pure gauge theory it has been shown in Ref. [182] that the expectation value $\langle \hat{\tau}^x_{\langle i,j \rangle} \rangle$ continuously changes by tuning the electric field term h. Hence, by performing a mean-field approximation in the electric field, the quantum-$\mathbb{Z}_2$ mLGT maps onto the classical Ising $\mathbb{Z}_2$ mLGT, see Section 3.3.

Due to its proximity to the Ising $\mathbb{Z}_2$ mLGT and its common symmetries generated by the proposed LPG term, we anticipate that the phase diagram of the quantum-$\mathbb{Z}_2$ mLGT shares all essential features of the Ising $\mathbb{Z}_2$ mLGT as shown in Figure 2.4.

3.5   Quantum dimer model (QDM)

Rokhsar and Kivelson introduced the QDM in the context of high-T_c superconductivity, which has the constraint that exactly one dimer is attached to each vertex [138, 183]. The

QDM is an odd $\mathbb{Z}_2$ LGT, i.e., a pure gauge theory with $g_j = +1$ replaced by $g_j = -1\ \forall j$, with $h \to \infty$, and its fundamental monomer excitations are gapped and can only be created in pairs.

Our proposed scheme allows to directly implement the gauge constraint of the QDM experimentally by preparing the system in the ground-state manifold of the LPG term as shown in Fig. 3.3b and d. Note that the LPG term splits the ground-state manifold into two distinct subspaces, QDM$_1$ and QDM$_2$, which can be seen by entirely removing the matter atoms and setting $\hat{n}_j = 0, 1$ in Eq. (3.8), such that only the link atom Kagome lattice remains; hence it can be implemented in-plane. A dimer then corresponds to either $\tau^x_{\langle i,j \rangle} = -1$ (QDM$_1$) or $\tau^x_{\langle i,j \rangle} = +1$ (QDM$_2$). Due to the LPG protection the QDM subspaces are energetically protected and monomer excitations cost a finite energy $2V$.

By weakly driving the system, the motion of virtual, gapped monomer pairs perturbatively induces plaquette terms of strength J_{QDM}, and we can derive an effective model (see below) given by

$$\hat{\mathcal{H}}^{\text{eff}}_{\text{QDM}} = -J_{\text{QDM}} \sum_{\bigcirc} \prod_{\langle i,j \rangle \in \bigcirc} \hat{\tau}^z_{\langle i,j \rangle} + K \sum_{\text{NNN}} \hat{\tau}^x_{\langle i,j \rangle} \hat{\tau}^x_{\langle m,n \rangle}. \tag{3.18}$$

Here, the NNN link-link interaction K can be tuned by the blockade radius of the Rydberg-Rydberg interactions.

Experimental [51] and theoretical [50, 173, 184, 185] studies of QDMs in Rydberg atom arrays for different geometries and parameters regimes have shown to be an interesting playground to probe $\mathbb{Z}_2$ spin liquids. Our proposed setup is a promising candidate to further study QDMs due to its versatility and its inherent protection by the LPG term and the phase diagram of Hamiltonian (3.18) remains to be explored.

Here, we examine two limiting cases of Hamiltonian (3.18). For $J_{\text{QDM}}/K \gg 1$, the system is in the so-called plaquette phase [186], which is characterized by a maximal number of flippable plaquettes and resonating dimers. On the other hand, for $J_{\text{QDM}}/K \ll 1$ we find a classical Ising antiferromagnet on the Kagome lattice with NN and NNN interactions from the hard-core dimer constraint and K-term, respectively.

Derivation of effective quantum dimer model Since the derivation of the effective model (3.18) is distinctly different from the perturbation theory used for Rydberg blockaded models, see e.g., Refs. [50, 187], we will elaborate in more detail in the following.

For the QDM, the physical subspace is given by the QDM$_1$ low-energy subspace of the LPG term, see Figure 3.3; analogously we could consider the QDM$_2$ subspace. Hence, for strong protection $V \gg \Omega_m, \Omega_l$ states in the non-physical sectors are only virtually occupied and we can derive the effective model perturbatively, which yields the plaquette terms $\propto J_{\text{QDM}}$.

Let us first consider the simpler terms $\propto K$. These terms are introduced to drive potential quantum phase transitions in J/K. In our proposed scheme, the strong LPG terms arise from nearest-neighbor interactions. However, the Rydberg-Rydberg interactions decay as R^{-6}, where R is the distance between two atoms in optical tweezers. Hence, there are small but finite next-nearest neighbor interactions between links of the honeycomb lattice (next-nearest neighbors on the Kagome lattice), which give rise to the term $\propto K$ in Eq. (3.18).
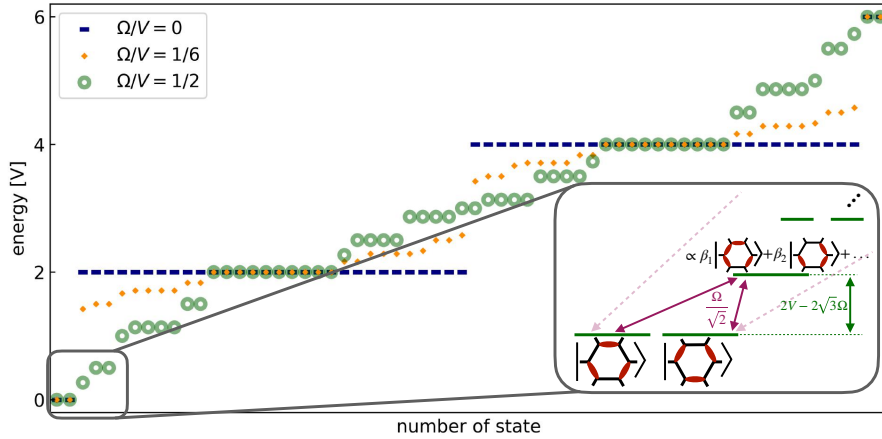
Figure 3.7: **Derivation of plaquette terms for the QDM.** We show the spectrum of the microscopic model (3.10) on one plaquette for different driving strengths in the flippable plaquette subspace. The blue dashes show the unperturbed system. The two low-energy states are the two flippable plaquette configurations in the QDM sector. The first (second) excited manifold has two (four) monomers and the two high-energy states contain a maximum number of six monomers. To perform perturbation theory, we first need to diagonalize the degenerate subspaces because the drive couples within the two and four monomer excitation blocks, i.e. the drive can move around the monomer excitations without energy cost, thus making them mobile. The orange and green dots show the spectrum for different driving strength, where the blocks are diagonalized. However, there are still off-diagonal couplings between the blocks. These couplings are the starting point for the second step, which is the actual Schrieffer-Wolff perturbation theory. The inset illustrates the smallest energy gap and its renormalized coupling after the first step. This allows to compare the effective driving strength to the energy gap in order to determine a regime of validity for the perturbation theory.

Now, we want to elaborate on the degenerate perturbation theory to derive the plaquette terms in sixth order. In the QDM subspace there are only two resonating ("flippable") configurations that can be coupled by plaquette terms and hence we can rewrite the interaction by

$$-J_{\text{QDM}} \sum_{\bigcirc} \prod_{\langle i,j \rangle \in \bigcirc} \hat{\tau}^z_{\langle i,j \rangle} = -J_{\text{QDM}} \sum_{\bigcirc} \left(|\hexagon\rangle\langle\hexagon| + \text{H.c.} \right), \qquad (3.19)$$

where we have used the electric field string $\leftrightarrow$ dimer mapping shown in Figure 3.3b. The two configurations shown in (3.19) now span the low-energy manifold and are the starting point for our perturbation theory. Above the low-energy manifold, we have three high-energy subspaces with energies $2V$, $4V$ and $6V$ since excitations (=monomers) can only be created in pairs. The unperturbed subspaces are shown as blue dashes in Figure 3.7.

We perturb the system by a weak drive $\hat{\mathcal{H}}^{\text{drive}}$, Eq. (3.10), coupling not only states between subsectors but also within the highly-degenerate manifolds with energy $2V$ and $4V$. Since these processes at the same time break and restore Gauss's law at different vertices, they are all degenerate and the denominators of the perturbative expansion vanish. To circumvent this non-physical divergence, we first need to diagonalize the degenerate sub-

spaces, which renormalizes all couplings and energy gaps.

Diagonalization of the degenerate subspaces, with respect to the perturbation, yields the transformed Hamiltonian $\hat{\tilde{H}}^{\text{mic}} = \hat{U}^\dagger \hat{H}^{\text{mic}} \hat{U}$ that is diagonal within the energy blocks but couples states from different blocks in a non-trivial way. The off-diagonal terms in $\hat{\tilde{H}}^{\text{mic}}$ now become the perturbation $\hat{\tilde{H}}^{\text{drive}}$ in the new basis. Note that the states have also transformed and should be denoted by $|\tilde{\alpha}\rangle = \hat{U}|\alpha\rangle$ in the new basis.

Since we have access to the full one-plaquette spectrum, we can now explicitly construct the unitary operator $\hat{S}$ of the Schrieffer-Wolff transformation by calculating the matrix elements

$$\langle \tilde{\beta}|\hat{S}|\tilde{\alpha}\rangle = \frac{\langle \tilde{\beta}|\hat{\tilde{H}}^{\text{drive}}|\tilde{\alpha}\rangle}{E_{\tilde{\beta}} - E_{\tilde{\alpha}}}, \tag{3.20}$$

where $\hat{\tilde{H}}^{\text{drive}} = \hat{U}^\dagger \hat{H}^{\text{drive}} \hat{U}$ and $E_{\tilde{\alpha}}$, $E_{\tilde{\beta}}$ are the unperturbed energies in the transformed basis. Because we completely diagonalized the degenerate subspace, divergences of the denominator only appear for uncoupled states, i.e., the nominator vanishes, for which we define the matrix element of $\hat{S}$ to be zero. In the Schrieffer-Wolff formalism we can now write down a well-defined expansion in Ω/V:

$$\hat{\mathcal{H}}^{\text{eff}}_{\bigcirc,U(1)} = \sum_n \hat{\mathcal{H}}^{(n)} \tag{3.21a}$$

$$\hat{\mathcal{H}}^{(0)} = \hat{\tilde{H}}^{\text{mic}} - \hat{\tilde{H}}^{\text{drive}} \tag{3.21b}$$

$$\hat{\mathcal{H}}^{(1)} = 0 \tag{3.21c}$$

$$\vdots$$

$$\hat{\mathcal{H}}^{(n)} = \frac{n-1}{n!} \underbrace{\left[\hat{S}, \left[\hat{S}, ..., [\hat{S}, \hat{\tilde{H}}^{\text{drive}}]... \right] \right]}_{(n-1)\text{-commutators}} \tag{3.21d}$$

Note that in the transformed basis the energy denominator in Eq. (3.20) can depend on V and Ω. Since we require $\Omega \ll V$, we can expand the expressions and find in leading order sixth-order contributions for any $2 \leq n \leq 6$.

In Figure 3.7, we show the full spectrum for different driving strengths Ω/V ($\Omega_m = \Omega_l = \Omega$). In general, the validity of a perturbation theory is determined by the coupling strength divided by the energy gap in the unperturbed system. In degenerate perturbation theory, this quantity has to be evaluated after the transformation $\hat{U}$. As shown in the inset of Figure 3.7, the gap between the low-energy manifold and the first excited states becomes $\tilde{V} = 2V - 2\sqrt{3}\Omega$ and the matrix element between the two states is $\tilde{\Omega} = \Omega/\sqrt{2}$. Hence, we find

$$\frac{\tilde{\Omega}}{\tilde{V}} = \frac{\Omega}{2\sqrt{2}V - 2\sqrt{6}\Omega} \tag{3.22}$$

and, e.g., $\tilde{\Omega}/\tilde{V} = 1/4$ for $\Omega/V \approx 1/3$, which allows to have relatively strong driving strength in the lab frame.

From $\hat{\tilde{H}}^{\text{mic}}$, we can now calculate the Schrieffer-Wolff transformation, see Eqs. (3.21a)-

(3.21d). To summarize, by evaluating (3.21a) we can derive the leading-order contribution of the plaquette interaction in the quantum dimer subspace and find

$$J_{\text{QDM}} = \frac{917}{120} \frac{\Omega^6}{V^5},$$

(3.23)

which yields $J_{\text{QDM}}/V \approx 0.01$ for $\Omega/V = 1/3$. The effective coupling is surprisingly strong despite the small prefactor $1/144$ in the perturbative expansion, Eq. (3.21d). Intuitively, we can understand these strong many-body interactions to be induced by the highly mobile and gapped monomer excitations. While this observation is interesting in the context of interacting spins in solids, the plaquette interaction is too small ofr current Rydberg tweezer platforms.

3.6   Experimental challenges and perspectives

The experimental LPG scheme to realize the $\mathbb{Z}_2$ LGT with dynamical matter in $(2+1)$D is founded on equal strength interactions between the atoms in one vertex and works for coordination numbers $z \leq 3$. Thus, in $(2+1)$D the coordination number $z = 3$ is in our favour, because it naturally realizes the equal strength interaction between links, see Figure 3.3a. To engineer equal strength interactions between link and matter atoms, we propose to elevate the matter atoms out-of-plane to form a tetrahedron structure at each vertex [123]. Further, to minimize matter-matter interactions of strength $V_{\text{matter}-\text{matter}} \approx 0.43V$, we suggest to arrange the tetrahedrons in a staggered configuration with matter atoms on sublattice A (B) above (below) the plane of link atoms. Additionally, our scheme requires *strong* local detuning of strength $\Delta_m = 3V$ ($\Delta_l = 6V$) for matter (link) atoms; the factor of 2 arises because a matter (link) atom is member of one vertex (two vertices). Those detunings arise from the mapping of Ising interactions to Rydberg density-density interactions, see Section 3.2.1.

We have performed careful analysis with actual parameters of state-of-the-art platforms, see Section 4.2.1, and find that even in the presence of experimental imperfections the Gauss' law is well-conserved and dynamics appears on experimentally realistic time scales. Currently, we recognize the greatest challenge in the experimental development of efficient tweezer resorting schemes for 3D structures, which can presumably be solved in the near future.

Nevertheless, any scheme implementing equal strength density-density interactions is suitable to engineer the LPG terms in $(2+1)$D. To this end, we propose to use internal degrees-of-freedom accessible in novel Rydberg tweezer platforms based on alkaline-earth(-like) atoms [98, 100, 188] or two atomic species [174–176]. In the former case, two different Rydberg states $|r_1\rangle$ and $|r_2\rangle$ have to be addressed on matter and link atoms, respectively, with mutual interactions yielding the equal strength interactions for in-plane atoms. For the latter case, different atomic species, and thus Rydberg states, are used for matter and link atoms.

Moreover, there follows an immediate corollary of our $(2+1)$D scheme: A $(1+1)$D zig-zag chain[1] Here, a one-dimensional chain is cookie cut from the tetrahedron structure

---

[1]We note that the LPG term introduced in Section 3.1 is not sufficient to perturbatively generate $\mathbb{Z}_2$ invariant
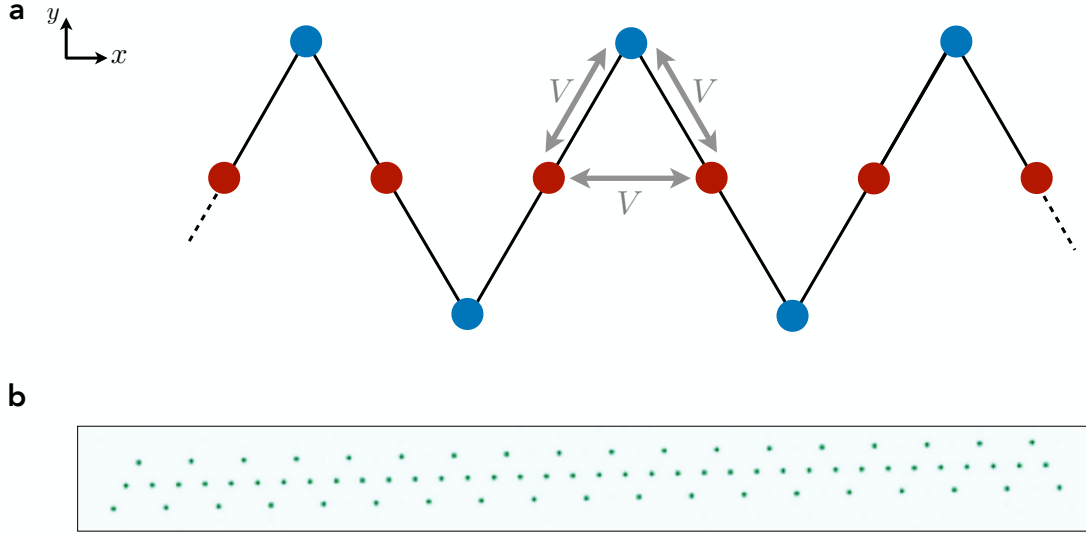
a

b

Figure 3.8: $(1+1)$**D Zig-Zag ladder. a** We illustrate the geometry of atoms in a Rydberg tweezer experiment: A combination of Rydberg interactions, local detunings and global drive yields an emergent $\mathbb{Z}_2$ LGT with dynamical matter in $(1+1)$D. **b** We show an averaged image of Strontium atoms in optical tweezers arranged in the zig-zag geometry with nearest-neighbour distance $a = 3.5\,\mu$m, obtained from the Strontium tweezer lab of Johannes Zeiher and Immanuel Bloch at the Max-Planck Institute for Quantum Optics in Garching.

followed by a tilt such that all atoms (matter and link) are located in the x-y plane.

3.7 Effective $\mathbb{Z}_2$ LGT in a Zig-Zag chain

In the following section, we derive the effective $\mathbb{Z}_2$ LGT Hamiltonian for the $(1+1)$D zig-zag ladder and fully include the van-der-Waals Rydberg tails; the $(1+1)$D zig-zag ladder is illustrated in Figure 3.8. By cutting the chain from the $(2+1)$D geometry, we have the liberty to choose a boundary condition, i.e., we pick a frozen configuration $\tau^x_{\langle i,j \rangle}$ of the links perpendicular to the chain. Here, we consider the superselection sector with $g_j = +1 \,\forall j$ and set the (physically absent) boundary links to $\tau^x_{\langle i,j \rangle} = +1$; if the chain start and ends with a matter site, we also assume the (physically absent) boundary link to be $\tau^x_{\langle i,j \rangle} = +1$. This reduces the LPG term to

$$V\hat{W}_j = \frac{V}{8}\left[(2\hat{n}_j - 1) + \hat{\tau}^x_{\langle j-1,j \rangle} + \hat{\tau}^x_{\langle j,j+1 \rangle} + 1\right]^2 \tag{3.24a}$$

$$= V\left[\hat{n}_{\langle j-1,j \rangle}\hat{n}_j + \hat{n}_j\hat{n}_{\langle j,j+1 \rangle} + \hat{n}_{\langle j-1,j \rangle}\hat{n}_{\langle j,j+1 \rangle}\right] - \frac{V}{2}\left[\hat{n}_{\langle j-1,j \rangle} + \hat{n}_j + \hat{n}_{\langle j,j+1 \rangle}\right] + \text{const.} \tag{3.24b}$$

In comparison to Eq. (3.8), we have changed the pre-factor of the LPG term such that V directly corresponds to the Rydberg density-density interaction; however the smallest gap between physical and unphysical states is now $V/2$. In the second line, we have used the

---

dynamics, and we refer to the discussion in the corresponding section.

identity $\hat{\tau}^x = 2\hat{n} - 1$.

The microscopic Hamiltonian including Rydberg tails, see Section 2.1, is given by

$$\hat{\mathcal{H}}_{\text{mic}} = \sum_{I<J} \frac{C_6}{r_{IJ}^6} \hat{n}_I \hat{n}_J - \left(\frac{V}{2} + \Delta_m\right) \sum_{J \in \text{matter}} \hat{n}_J - (V + \Delta_l) \sum_{J \in \text{link}} \hat{n}_J + \frac{\Omega}{2} \sum_J \left(\hat{a}_J + \hat{a}_J^\dagger\right), \quad (3.25)$$

where the indices I and J label sites on the tweezer array, and the link (matter) sites are the red (blue) sites shown in Figure 3.8. The coefficient C_6 describes the van-der-Waals interaction between two Rydberg states generating the required $\propto \hat{n}\hat{n}$ interaction of Eq. (3.24). In the following, we define the protection strength to be $V = C_6/a$, where a is the the nearest-neighbour distance on the zig-zag array, and include the tails as small diagonal terms. We highlight, once again, that the diagonal basis is the basis of electric field strings and matter occupation, see Figure 3.3, and thus the Rydberg tails are inherently $\mathbb{Z}_2$ gauge invariant.

We follow the derivation of the effective Schrieffer-Wolff Hamiltonian in Section 3.3, and find the effective model for the $(1 + 1)$D zig-zag chain with fixed boundaries in the sector $g_j = 1$:

$$\begin{aligned}
\hat{\mathcal{H}}_{\text{eff,zigzag}} = &+ t \sum_{\langle i,j \rangle} \left(\hat{a}_i^\dagger \hat{\tau}_{\langle i,j \rangle}^z \hat{a}_j + \text{h.c.}\right) \\
&+ \Delta_1 \sum_{\langle i,j \rangle} \left(\hat{a}_i^\dagger \hat{\tau}_{\langle i,j \rangle}^z \hat{a}_j^\dagger + \text{h.c.}\right) + \Delta_2 \sum_{\langle i,j \rangle} \left(\hat{a}_i^\dagger \hat{\tau}_{\langle i,j \rangle}^x \hat{\tau}_{\langle i,j \rangle}^z \hat{a}_j^\dagger + \text{h.c.}\right) \\
&+ \sum_{\langle i,j \rangle} (h + \xi_{\langle i,j \rangle}) \hat{\tau}_{\langle i,j \rangle}^x - \mu \sum_j \hat{n}_j \\
&+ \gamma \sum_{\langle i,j \rangle} \hat{n}_i \hat{\tau}_{\langle i,j \rangle}^x \hat{n}_j + M \sum_{\langle i,j \rangle} \hat{n}_i \hat{n}_j \\
&+ \epsilon_l \left(\hat{\tau}_{\langle 1,2 \rangle}^x + \hat{\tau}_{\langle L-1,L \rangle}^x\right) + \epsilon_{\text{m}} \left(\hat{n}_1 + \hat{n}_L\right) \\
&+ V \sum_{i<j} \frac{1}{|i-j|^6} \hat{n}_i \hat{n}_j + \frac{V}{4} \sum_{j=1}^{L-1} \sum_{d=2}^{L-1-j} \frac{1}{d^6} \hat{\tau}_{\langle j,j+1 \rangle}^x \hat{\tau}_{\langle j+d,j+1+d \rangle}^x.
\end{aligned} \quad (3.26)$$

Here, the two terms $\propto \epsilon_l, \epsilon_{\text{m}}$ are dispersive shifts on the boundary of a chain of length L starting and ending with a matter site at $j = 1, L$. The last line describes the tails of the Rydberg interactions leading to a shift of the string tension given by $\xi_{\langle i,j \rangle} = \frac{V}{4} \sum_{|i-k| \geq 2} \frac{1}{|i-k|^6}$. In the thermodynamic limit, we find $\xi_{\langle i,j \rangle} = \frac{V}{4}[\zeta(6) - 1] \approx 4.33V \cdot 10^{-3}$, where $\zeta(x)$ is the Riemann zeta function. The perturbative couplings are summarized in the following table:

t	Δ_1	Δ_2	h	μ	$M = -\gamma$	$\epsilon_{\text{m}} = 2\epsilon_l$
$\frac{2}{3}\frac{\Omega^3}{V^2}$	$\frac{10}{9}\frac{\Omega^3}{V^2}$	$\frac{8}{9}\frac{\Omega^3}{V^2}$	$-\frac{1}{3}\frac{\Omega^2}{V} - \frac{\Delta_1}{2}$	$-\frac{1}{6}\frac{\Omega^2}{V} + \Delta_{\text{m}}$	$\frac{1}{3}\frac{\Omega^2}{V}$	$\frac{1}{4}\frac{\Omega^2}{V}$

In the next Chapter 4, we will compare the dynamics between the microscopic and effective model, and show the excellent agreement between the two models. We refer the reader to Section 4.2.1 for more details.

3.8 Stability of gauge structure in classical spin systems

In the following Section, we present preliminary results that are obtained in collaboration with Andrea Pizzi, Fabian Grusdt, Jad C. Halimeh and Hongzheng Zhao.

The advantage of the LPG method is its experimental feasibility, i.e., the $\mathbb{Z}_2$ Gauss' law constraints are stabilized by two-body Ising interactions. The cost of reducing the experimental complexity is that the emergent gauge structure is only metastable. In Section 3.1, we present exact numerical simulations in $(1+1)$D suggesting that gauge invariance remain intact even up to infinite times using LPG protection terms. In Section 3.2, we argue that the LPG method is sufficient to stabilize the gauge constraints up to times relevant for experiments. This has been confirmed in small exact numerical simulations in Ref. [P5].

Here, we address the efficiency of the LPG gauge protection scheme in $(2+1)$D using large-scale simulations of classical spins [189, 190]. In particular, we simulate the dynamics of a system of rotors (classical spins) under a classical $\mathbb{Z}_2$ LGT Hamiltonian introduced below. This allows us to study much larger system sizes and times exceeding any simulation possible for the quantum system. While the model cannot capture the correct gauge-invariant physics of the $\mathbb{Z}_2$ LGT, it is sensitive to gauge breaking errors and can describe the breakdown of the emergent gauge structure.

Let us consider a 2D honeycomb lattice with spins $\sigma_j = (\sigma_j^x, \sigma_j^y, \sigma_j^z)$ on sites j and spins $\sigma_{\langle i,j \rangle} = (\sigma_{\langle i,j \rangle}^x, \sigma_{\langle i,j \rangle}^y, \sigma_{\langle i,j \rangle}^z)$ on the links $\langle i,j \rangle$, where each spin is a vector of unit length pointing on a 3D sphere. The σ_j^z component describes the excitation of a matter field and $\sigma_{\langle i,j \rangle}^x$ $(\sigma_{\langle i,j \rangle}^z)$ is the electric field (gauge field). We can define a $\mathbb{Z}_2$ Gauss' law as the functional

$$G_j = -\sigma_j^x \prod_{i:\langle i,j \rangle} \sigma_{\langle i,j \rangle}^x. \tag{3.27}$$

Now, this functional can take any value $G_j[\{\sigma_i\}] \in [-1,1]$ for all j. In the following, we target for a Gauss' law value of $G_j[\{\sigma_i\}] = +1$ and take its deviation as a measure for the emergent gauge structure.

The dynamics is governed by the classical Hamiltonian $H = H_0 + H_V + H_\lambda$ with

$$H_0 = J \sum_{\langle i,j \rangle} \sigma_i^z \sigma_{\langle i,j \rangle}^z \sigma_j^z \tag{3.28}$$

$$H_V = \frac{V}{4} \sum_j c_j \left(\sigma_j^x + \sum_{i:\langle i,j \rangle} \sigma_i^x \right)^2 \tag{3.29}$$

$$H_\lambda = \lambda \sum_j \sigma_j^z. \tag{3.30}$$

The first term describes the dynamical propagation of matter and gauge fields and is a classical variant of the kinetic term in the Fradkin-Shenker model, see Chapter 2. The second term corresponds to the LPG stabilizer term, which energetically favours the spins to point in a direction such that $G_j \approx 1$ for all j, see Eq. (3.8) in Section 3.2. Further, we introduce a disorder coefficient c_j in the protection term. The last term describes local gauge violation of strength λ. As we have discussed in Section 3.2, the LPG term energetically allows for spe-

cial resonant configurations, where $G_j = -1$ on four vertices. While we can construct such gauge breaking configurations and simultaneously conserve energy, it is unclear if there is a classical trajectory connecting the gauge-invariant and gauge-noninvariant configurations.

In the classical spin model the dynamics is strictly restricted to energy conserving trajectories. In contrast, quantum fluctuations allow to tunnel through the energy barrier imposed by the LPG term, which are increasingly suppress for increasing V/λ. Moreover, the classical model provides a much larger phase space and thus is believed to be an upper boundary for gauge breaking dynamics, in the sense that e.g. the LPG term is not quantized but can admit continuous values.

The equations of motion for classical spins are related to the Poisson bracket [189, 191, 192],

$$\frac{d\sigma_j(t)}{dt} = \{\sigma_j(t), H\} \tag{3.31}$$

with

$$\{\sigma_i^\alpha, \sigma_j^\beta\} = \delta_{ij}\varepsilon_{\alpha\beta\gamma}\sigma_i^\gamma. \tag{3.32}$$

For the Hamiltonian in Eq. (3.28), this defines a set of coupled non-linear differential equations, which can be solved numerically. Here we apply a trotterization procedure [189] and set the time steps sufficiently short. We ensure proper convergence by comparing the trotterized dynamics to exact solutions obtained from an ordinary differential equation solver at short times and for small systems.

To measure the efficiency of gauge protection in the classical system of spins, we define an observable for the Gauss' law errors $\epsilon(T)$ at time T as

$$\epsilon(T) = \frac{1}{VT}\int_0^T dt \sum_{j=1}^L \left[1 - G_j(t)\right], \tag{3.33}$$

where V denotes the number of vertices and the quantity $\epsilon(T)$ can admit the values $\epsilon = 0$ ($\epsilon = 2$) corresponding to minimal (maximal) violation of the Gauss' law constraints; here we evaluate the $\mathbb{Z}_2$ Gauss' law with the time evolved spin configurations according to Eq. (3.31). Note that at infinite temperature, the error is given by $\epsilon = 1$ and hence we have chosen a meaningful normalization of $\epsilon(T)$.

For the numerical simulations, we initialize the spins in a configuration pointing along the x-direction such that $G_j(t = 0) = +1$ for all j. Further, we average over an ensemble of $N_{\text{ens}} = 200$ random initial states. The system has 10×10 honeycomb plaquettes corresponding to a total of $N = 500$ spins (matter and link spins). As discussed around Figure 3.4, we expect the efficiency of the LPG protection to be enhanced by introducing disorder in the local protection terms in order to suppress undesired resonances. This is incorporated in the coefficients c_j in Eq. (3.28) and we choose coefficients drawn from a normal distribution with mean $\mu = 1$ and standard deviation $\sigma = 0.1$; hence the local protection term Vc_j is centered around V. To be precise about our numerical simulation, we start with a random initial state and random coefficients c_j, and then time evolve with various protection strengths V. This is repeated for $N_{\text{ens}} = 200$ realizations.

In the following, we set the coupling strength $J = \lambda = 1$ and vary the protection
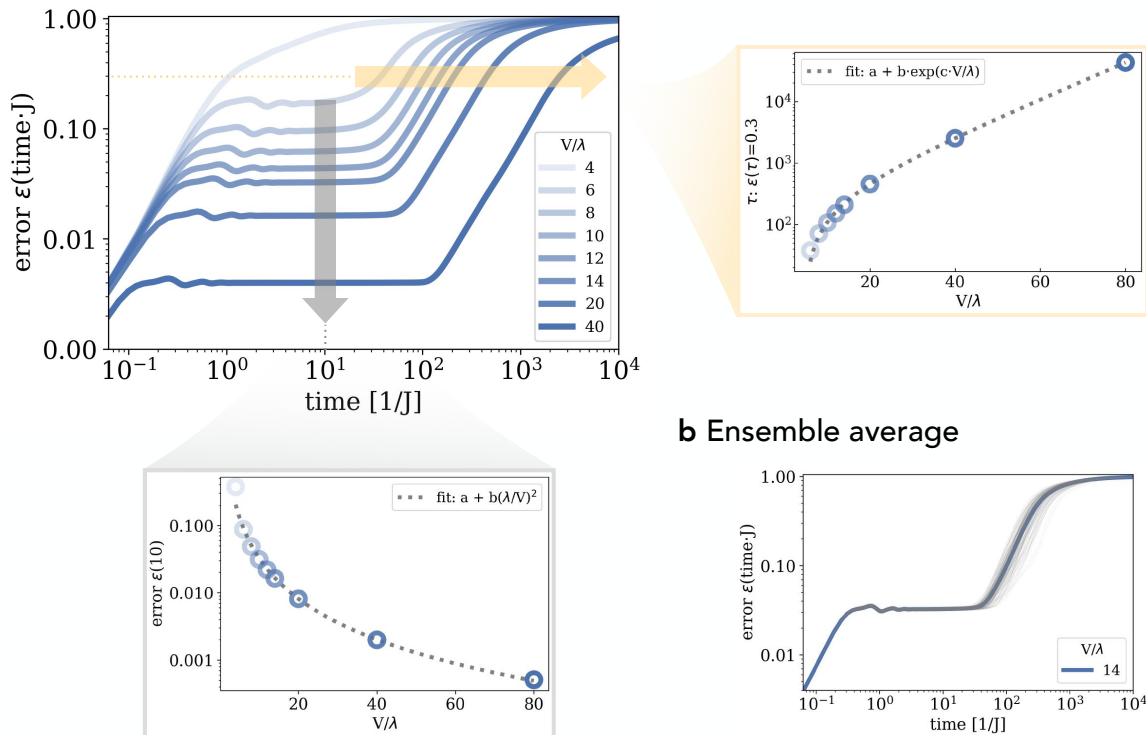
a Gauss' law violation

b Ensemble average

Figure 3.9: **Dynamical gauge protection in classical spins.** We numerically solve the equation of motion of classical spins for a honeycomb $\mathbb{Z}_2$ LGT with $N = 500$ spins, i.e., a system with 10×10 plaquettes. **a** We plot the dynamics of the Gauss' law violation for various protection strengths V/λ; here λ is the gauge violation. We find a metastable plateau with (i) a height that is controlled by $(\lambda/V)^2$ [bottom] and (ii) a duration that scales exponentially in V/λ [right]. **b** The results in panel **a** show the average (blue line) over an ensemble of $N_{\mathrm{ens}} = 200$ realizations each with a random gauge-invariant initial state. The grey lines are the individual trajectories. For each realization a random sequence c_j is drawn from a normal distribution.

strength V/λ. In Figure 3.9a, we show the Gauss' law errors $\epsilon(t)$ obtained from the sequence described above. In Figure 3.9b, we further show the individual trajectories of the $N_{\mathrm{ens}} = 200$ realizations, which average to the blue curves shown in Figure 3.9a.

We observe four different regimes: (i) At short times, the error grows polynomially with $\epsilon(t) \propto t^2$ showing the universal behavior of dynamical gauge protection schemes [30]. In the quantum regime, this can be understood from time-dependent perturbation theory. The error grows until (ii) it enters a plateau with a height that scales with $(\lambda/V)^2$ [P4, 30], see Figure 3.9a (bottom left). The time the system remains in the plateau grows exponentially with $\propto \exp V/\lambda$; a signature of a prethermal phase with $\mathbb{Z}_2$ gauge structure. This plateau demonstrates the efficiency of the LPG scheme in large-scale 2D systems of classical spins. (iii) Afterwards, the Gauss' law violations grows again polynomially with $\epsilon(t) \propto t^2$. (iv) At late times, the system reaches an equilibrium with infinite-temperature Gauss' law violation.

The prethermal phase (iii) is of significant importance for the experimental realization
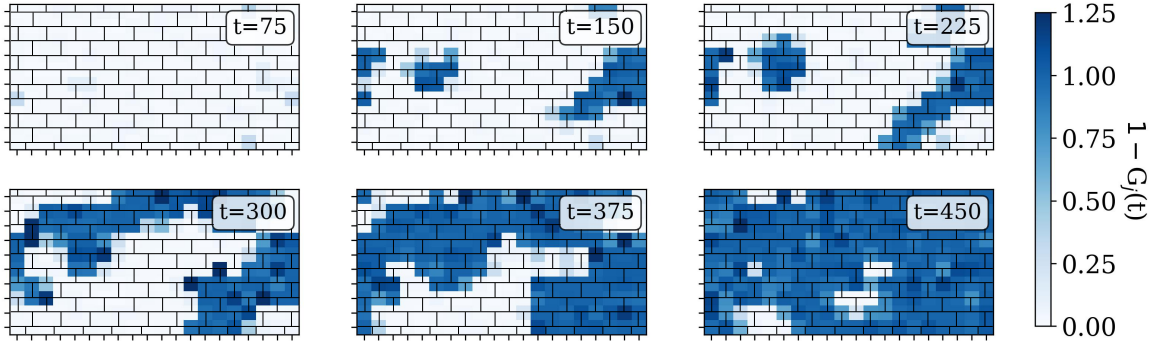
Figure 3.10: **Spreading of Gauss' law violations.** We time evolve a representative random initial state with $V/\lambda = 20$ and plot the local Gauss' laws $[1 - G_j(t)]$ at times t (in units of $J = \lambda = 1$). The grid lines correspond to the honeycomb lattice illustrated in a brick wall geometry. At the end of the plateau phase ($t = 100$), see Figure 3.9a, local nucleation regions appear. These regions start to proliferate and eventually percolate across the entire system.

of the LPG scheme. It allows to maintain gauge invariance despite the presence of experimental errors. Further, gauge violation errors and the accessible timescale can be controlled by the LPG protection strength V allowing for exponentially long $\mathbb{Z}_2$ gauge-invariant simulations.

Now, we examine the thermalization dynamics in phase (iv) more closely. In particular, we consider a representative trajectory of a random initial state evolved under the Hamiltonian (3.28) with $V/\lambda = 20$. In Figure 3.10, we plot the Gauss' law violation for times starting at the end of the plateau phase and onwards. We observe that the vertices with Gauss' law values different from $G_j = +1$ begin to form a local nucleation region, from which the Gauss' law violation proliferates across the system. Therefore, the thermalization dynamics seems to happen in a correlated way throughout the system. The pattern formation shown in Figure 3.10 further shares great similarities with critical, scale invariant behavior and percolation pattern [P12]. Further, we note that even at late time, we observe substantial local fluctuations of the Gauss' law violation.

Therefore, we find a non-trivial thermalization behavior, which by itself is an interesting future topic to study. Further, we recognize the universal shape of the thermalization dynamics, see Figure 3.9a. The investigation of the scaling relation, and the potential collapse of the curves, may give additional insights into the universality of the thermalization dynamics discovered in this classical spin system and into the thermalization of gauge theories [15]. Studying the quantum version of Hamiltonian (3.28) for large systems and long times is impossible with current numerical techniques. Eventually, the realization of our proposed experiment in a quantum simulation device could explore the thermalization of the quantum $\mathbb{Z}_2$ LGT in $(2+1)$D.
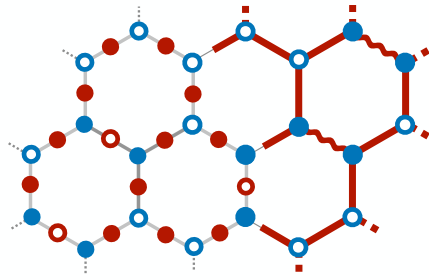
4

Equilibrium and Out-of-Equilibrium probes of $\mathbb{Z}_2$ lattice gauge theories with matter

$\mathbf{W}$HAT CAN WE LEARN from the quantum simulation of lattice gauge theories? And, how do we test the faithful implementation of a gauge theory in experiment? In this Chapter, we discuss experimental probes that give insight into the ubiquitous behaviour of gauge theories. Therein, we briefly elaborate on ground-state properties, however, the focal point are experimentally accessible out-of-equilibrium probes.

In particular, we consider quench experiments with the following protocol:

(1) State preparation: At time $t = 0$ an initial product state $|\psi_0\rangle = \otimes_j |n_j^\sigma\rangle$ in the Fock basis is prepared. Here, we assume that at site j a state with n_j^σ particles of spin σ can be prepared. The spin is measured in an arbitrary basis.

(2) Time evolution: The system is exposed to the microscopic Hamiltonian $\hat{\mathcal{H}}_{\mathrm{mic}}$ for a time $t > 0$, such that the system evolves under the unitary transformation $|\psi(t)\rangle = \exp(-i\hat{\mathcal{H}}_{\mathrm{mic}}t)|\psi_0\rangle$; we set $\hbar \equiv 1$ throughout. Entanglement is built up during the time evolution and, in general, $|\psi(t)\rangle$ is not a product state anymore.

(3) Readout: We measure the system instantaneously at time t in the spin-resolved Fock state basis [193].

We emphasize that experimentally the most feasible protocols only require to prepare and to readout all spins in the same basis; however local control techniques become increasingly accessible, see e.g. Refs. [90, 194].

The following Chapter is based on publication [P3], [P5] and [P12]. The text and figures are rearranged, adapted and supplemented. Moreover, preliminary results are presented in Section 4.2.1.

4.1　Gauss' law conservation

The most direct signature in the quantum simulation of a LGT is the measurement of Gauss' law constraints. The Gauss' law expectation values, or conversely the gauge breaking errors [Eq. (3.7)], quantifies whether gauge constraints emerge from an underlying microscopic model. Emergent gauge theories always contain inevitable gauge breaking errors: by increasing the protection strength V the errors are suppressed and it is in the limit of $V \to \infty$ to retrieve the ideal gauge theory. Therefore, for top-down methods, see Section 2.2.5, the Gauss' law constraints have to be monitored and it has to be checked whether the system is well within the limit of a controlled emergent gauge theory, i.e., whether perturbation theory is valid. In Chapter 3, Sections 3.1 and 3.8 the Gauss' law errors are discussed from a theoretical and numerical perspective.

Depending on the experimental scheme, the Gauss' law may or may not be directly accessible. The experimental proposal presented in Chapter 3 implements the electric field and matter occupation in the ground and Rydberg state and thus a projective measurement in this basis allows to directly evaluate the Gauss' law (3.1) in each snapshot. In contrast, non-Abelian gauge theories with their separate Gauss' laws for each generator, see Section 2.2.4, do not allow to extract the Gauss' law conservation in an individual snapshot but only on average.

We conclude that monitoring Gauss' law constraints constitutes one of the necessary probes for emergent gauge theories. It directly indicates the amount of gauge violation and it can be used to test if a system is a controlled, gauge protected regime by varying the small perturbative parameters Ω/V. There are well-known scaling laws $\propto \Omega^2/V^2$ for gauge breaking error at infinite time [30].

4.2　Schwinger effect

The Schwinger effect [195] is a non-perturbative result obtained from quantum electrodynamics (QED), which describes the rate under which electron-positron pairs are created. Due to its weak coupling constant $\alpha = 1/137$, extremely high electric field strengths are required to observe the Schwinger pair production in QED. In contrast, the goal of the quantum simulation of LGTs is to explicitly probe models with strong coupling between matter and gauge fields.

Here, we discuss a Schwinger-like phenomenon for strongly coupled $\mathbb{Z}_2$ LGTs with dynamical matter in the presence of global $U(1)$ symmetry breaking terms ("pairing terms"). First, we explain the conceptual idea by considering a simple $(1+1)$D toy model, similar to Eq. (3.26), in a weak coupling limit:

$$\hat{\mathcal{H}}_{\text{toy}} = +t \sum_{\langle i,j \rangle} \left(\hat{a}_i^\dagger \hat{\tau}_{\langle i,j \rangle}^z \hat{a}_j + \text{h.c.} \right) + \Delta \sum_{\langle i,j \rangle} \left(\hat{a}_i^\dagger \hat{\tau}_{\langle i,j \rangle}^z \hat{a}_j^\dagger + \text{h.c.} \right) + h \sum_{\langle i,j \rangle} \hat{\tau}_{\langle i,j \rangle}^x - \mu \sum_j \hat{n}_j. \qquad (4.1)$$

We start from an initial state close to Schwinger's model, i.e., a vacuum and an electric field configuration with high energy density. In the $(1+1)$D setup, we choose an initial product state $|\psi_0\rangle$ with matter sites in $|n_j = 0\rangle$ and the links in $|\tau_{\langle i,j \rangle}^x = -1\rangle$; hence the Gauss' law
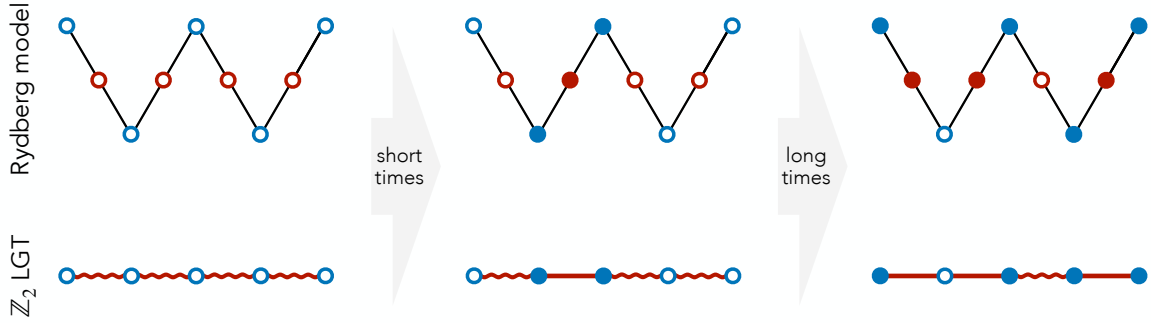
Figure 4.1: **Schwinger effect in** $(1+1)$**D** $\mathbb{Z}_2$ **LGT.** We propose to initialize a product state with all atoms in their atomic ground state. In our $\mathbb{Z}_2$ LGT mapping, see Figure 3.3, this maps onto a matter vacuum with an electric field line penetrating the entire system. After time evolution under the Rydberg Hamiltonian (3.25), snapshots in the ground or Rydberg basis are taken (top: empty and full circles). The Schwinger effect is characterized by $\mathbb{Z}_2$ charge pairs created from the electric string. In the late time dynamics, those charges start to fluctuate and correlations between $\mathbb{Z}_2$ charges and strings may contain information about a finite temperature phase of a $\mathbb{Z}_2$ LGT at high densities.

sector is $g_j = +1$ for all j.

In the unperturbed limit of $t, \Delta = 0$, the energy E_{init} of the initial state is fully determined by the string tension $h < 0$ with $E_{\text{init}} = -h \cdot (L-1)$; we assume a chain with L matter sites sharing $L-1$ links. By applying the Hamiltonian (4.1) to the initial state, we find a degenerate subspace of states $\{|n\rangle\}$ that have non-zero matrix elements of amplitude Δ and that contain exactly one pair of neighbouring $\mathbb{Z}_2$ charges at sites j and $j+1$ with a reversed electric field line $\tau^x_{\langle j,j+1\rangle} = +1$, see Figure 4.1. The energy of states $|n\rangle$ is given by $E_n = -h \cdot (L-3) - 2\mu$. This yields the resonance condition $E_{\text{init}} = E_n \Leftrightarrow h = -\mu$, for which we expect an enhanced rate of pair production.

Away from the resonance and in the perturbative limit, i.e., $\Delta \ll \delta E = |E_n - E_{\text{init}}|$, we use time-dependent perturbation theory to estimate the $\mathbb{Z}_2$ charge production at short times t with $\delta E \cdot t \ll 1$. In this limit, the matter density $n(t) = N(t)/L$ at time t for model (4.1) is then given by

$$n(t) = 2 \left| \frac{\Delta}{h - \mu} \right|^2 \sin^2 \left[(h - \mu) \cdot t \right], \tag{4.2}$$

where we have neglected boundary terms of order $\mathcal{O}(1/L)$. We comment that this time-dependent perturbation theory gives an easy insight into the phenomenology of the $\mathbb{Z}_2$ toy model. In Schwinger's original work, infinitely many terms were summed up leading to a non-perturbative result.

4.2.1 $(1+1)$**D Zig-Zag chain**

Next, we probe the above described dynamics in the microscopic model (3.25) and compare it to the effective dynamics (3.26). Thus, we want to study the emergent $\mathbb{Z}_2$ gauge theory, which contains additional terms not included in the toy model above. Nevertheless, the

phenomenology of Schwinger pair production remains the same.

Here, we use a set of experimentally relevant parameters for the example of Strontium [98, 115, 188, 196] tweezer arrays to demonstrate the feasibility of our scheme. To be precise, we consider Strontium-88 and implement the qubit in $|g\rangle = |5s5p\,^3P_0\rangle$ and $|r\rangle = |5s61s\,^3S_0, m_J = 0\rangle$ with van-der-Waals coefficient $C_6 = 2\pi \cdot 254\,\mathrm{GHz} \times \mu\mathrm{m}^6$ [196]. We set the Rabi frequency $\Omega = 2\pi \cdot 3\,\mathrm{MHz}$ between the two states using the definition in Eq. (3.25). Thus, we vary the distance a between neighbour atoms to tune the ratio V/Ω. In the following, we set $V/\Omega = 6$ or $a = 4.92\,\mu\mathrm{m}$, which is a typical distance used in Rydberg tweezer array platforms. Note that we want to avoid to operate at too short distances because the system becomes more sensitive to distance fluctuations of atoms in the tweezers. Moreover, we choose the detunings on matter sites $\Delta_m = -2\pi \cdot 72\,\mathrm{kHz}$ and link sites $\Delta_l = 2\pi \cdot 252\,\mathrm{kHz}$.

Using the parameters above, we predicted the following effective couplings for the $\mathbb{Z}_2$ LGT in Eq. (3.26):

t	Δ_1/t	Δ_2/t	h/t	$\xi_{\langle i,j\rangle}/t$	μ/t	$M/t =$ $-\gamma/t$	$\epsilon_{\mathrm{m}}/t =$ $2\epsilon_{\mathrm{l}}/t$	V_{NNN}/t
$2\pi \cdot 444.4\,\mathrm{kHz}$	1.7	1.3	-5.27	2.81	0.2	3	-2.25	5.06

Here, V_{NNN} is the repulsive matter-matter interaction due to the long-range Rydberg tails. We emphasize that the detunings Δ_m and Δ_l allows us to freely tune the string tension and chemical potential. In this setting, we choose a regime where the Schwinger pair production is slightly off-resonant.

We propose to initialize all atoms in the ground state $|\psi_0\rangle = \otimes|g\rangle$ and quench the system with Hamiltonian (3.25) at time $t = 0$; the initial state is gauge invariant with $\hat{G}_j|\psi_0\rangle = +|\psi_0\rangle$. After time $t > 0$, we measure the expectation value of atoms in the Rydberg state $|r\rangle$ (or ground state $|g\rangle$). In this basis, we can locally extract the $\mathbb{Z}_2$ matter occupation $\langle \hat{n}_j\rangle_t$ and $\mathbb{Z}_2$ electric string $\langle \hat{\tau}^x_{\langle i,j\rangle}\rangle_t$, which are manifestly gauge-invariant observables. The expectation value $\langle \cdot \rangle_t$ is evaluated with respect to $|\psi(t)\rangle$. This allows us to evaluate the following quantities, see Figure 4.1:

1. Matter density $n(t) = \frac{1}{L}\sum_j \langle \hat{n}_j\rangle_t$

2. Gauss' law errors $\epsilon(t) = \frac{1}{L}\sum_j \left(1 - \langle \hat{G}_j\rangle_t\right)$

3. Projected matter density $n(t) = \frac{1}{L}\sum_j \langle \hat{\mathcal{P}}_G \hat{n}_j(t) \hat{\mathcal{P}}_G\rangle_t$ with $\hat{\mathcal{P}}_G = 2^{-L}\prod_j(\mathbb{1} + \hat{G}_j)$

In our theoretical analysis, we assume perfect state preparation, unitary dynamics, and perfect readout. Further, we assume atoms in the motional ground state of a tweezer with infinitely large trap frequency.

We use exact diagonalization techniques to simulate the above protocol in a small system of length $L = 9$ (9 matter sites and 8 links). The parameter regime provides an excellent trade-off between gauge protection and accessible gauge-invariant dynamics, see Figure 4.2. Importantly, the Gauss' law error $\epsilon(t)$ remains stable at approximately 15%.
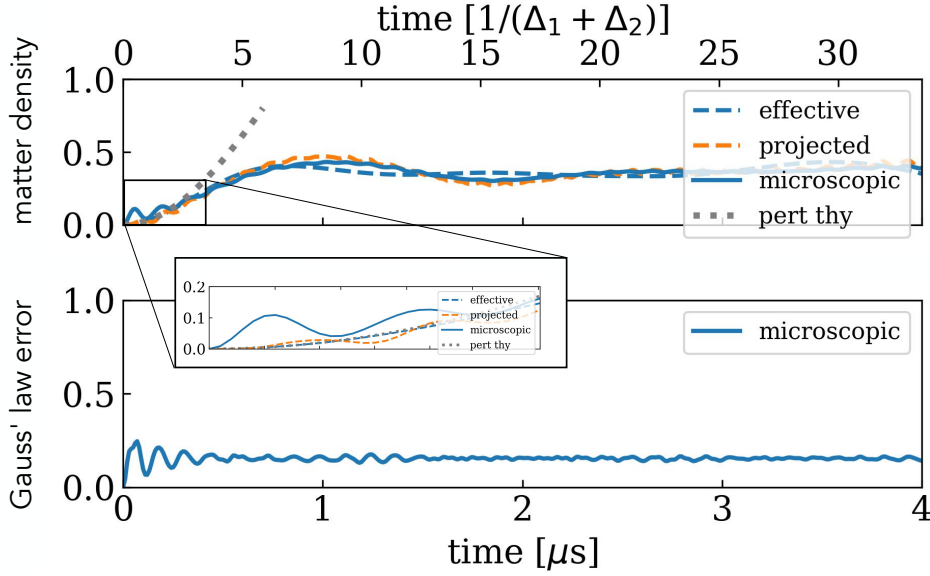
Figure 4.2: **Quench dynamics.** We use exact diagonalization to simulate the quench protocol with experimentally realistic parameters described in the main text for a chain of length $L = 9$ (9 matter sites and 8 links). The initial state is shown in Figure 4.1 (left) and we time evolve under the microscopic Hamiltonian (3.25) (solid blue) and effective Hamiltonian (3.26) (dashed blue). In the top panel, we show the matter density and predict the short time Schwinger pair production from time-dependent perturbation theory without any fit parameters (dashed gray). At late times the system equilibrates to a finite density state. In the lower panel, we demonstrate that the LPG term allows us to control Gauss' law error (here about 15% for $V/\Omega = 6$); ultimately the LPG term is responsible for the dynamically emerging gauge constraints. By post selecting on snapshots consistent with the target Gauss' law sector, $\hat{G}_j = +1$ for all j, we obtain the projected matter density (dashed orange), which shows that the observed features are governed by the $\mathbb{Z}_2$ gauge invariant processes.

Moreover, we find evidence for Schwinger pair production on experimentally accessible time scales based on the following observations shown in Figure 4.2 (top). First, the matter density $n(t)$ shows the production of $\mathbb{Z}_2$ charges, which thermalizes to a high-density soup with about 40% filling. Second, we post select on configurations consistent with Gauss' law to demonstrate that the dynamics is governed by $\mathbb{Z}_2$ gauge-invariant processes. Third, we compare the microscopic dynamics to the effective Schrieffer-Wolff model, Eq. (3.26), showing excellent between the microscopic model and the emergent $\mathbb{Z}_2$ gauge theory at all accessible time scales. Last, we apply time-dependent perturbation theory to the effective $\mathbb{Z}_2$ model to describe the rate of Schwinger pair production, see Section 4.2, at early times. Our calculation predicts the creation of pairs from a decaying electric field line without any fit parameters. In this context, we point out that the Schwinger pair resonance is determined by the constructively interfering pairing terms $\Delta = \Delta_1 + \Delta_2$. In contrast, if we would start from the opposite electric string state $|\tau^x\rangle = +1$, the two terms destructively interfere.

We conclude that the numerical simulation demonstrates emergent $\mathbb{Z}_2$ gauge dynamics obtained from our experimentally realistic proposed model. The early time dynamics can be described by the Schwinger effect. At intermediate to late times, the system equilibrates

to a strongly correlated finite density regime of $\mathbb{Z}_2$ pairs. A comprehensive study of those correlations is subject of future studies [197]. We emphasize that accessing this regime, i.e., long times and large systems, is becoming increasingly challenging for numerical simulation; especially starting from the microscopic model with the energy scale $\propto V$.

4.2.2 $(2+1)$D minimal toy model

In the full $(2+1)$D model introduced in Section 3.2, numerical time evolution methods are limited to small system sizes and short times. Additionally our model (3.10) describes an emergent gauge theory and therefore the energy scale is determined by the large protection V while the dynamics emerges on a time scale $\propto \Omega^3/V^2$, which poses a challenge to simulate long times up to a few hundred interaction times t in units of $1/V$.

Therefore, we will focus on small-scale exact numerical simulations and artificial geometries with coordination number $z = 3$: the Mercedes star geometry shown in the inset of Figure 4.3. While this geometry cannot be implemented in Rydberg tweezer platforms, since the distances do not give the correct interaction strength, it provides a conceptually interesting model because it gives rise to stronger plaquette interactions $\propto \Omega^3/V^2$ emerging from the LPG method.

Here, we numerically probe similar Schwinger dynamics as describes in the beginning of Section 4.2. However, in this study we consider the opposite vacuum, i.e., an initial product state $|\psi_0\rangle$ with matter sites in $|n_j = 0\rangle$ and the links in $|\tau^x_{\langle i,j \rangle} = +1\rangle$; the Gauss' law sector is $g_j = +1$ for all j. The goal is to probe the resonant features of Schwinger pair production discussed for the $(1+1)$D toy model.

To this end, we simulate the microscopic model (3.10) for $\Omega_m/V = \Omega_l/V = 1/8$ ($V = 2\pi \cdot 40\,\text{MHz}$) and vary the detunings Δ_l and Δ_m, which effectively tunes the string tension h and chemical potential μ, see Eq. (3.3). We calculate the time evolution staring from the initial state $|\psi_0\rangle$ and calculate the expectation value of the total number of matter excitations $N_{\text{tot}}(t)$. Then, we extract the point of maximum $\mathbb{Z}_2$ matter defined as $N_{\text{max}} = \max_{t \in [0, 6000/V]} N_{\text{tot}}(t)$. In Figure 4.3, we plot N_{max} for the various detunings Δ_m, Δ_l and find strong resonant features associated with resonances described in Section 4.2. The exact position of these resonant features remains challenging to predict due to finite-size effects and strong gauge field fluctuations.

Moreover, we have carefully evaluated that the observed matter production is inherently $\mathbb{Z}_2$ gauge invariant. In particular, we have projected the time evolved state $|\psi(t)\rangle$ onto the target superselection subspace given by $\hat{G}_j = \mathbb{1}$, which allows us to distinguish between gauge invariant and gauge-noninvariant dynamics, see Ref. [P5].

4.3   Disorder-free localization

The thermalization of quantum systems in the presence of interactions is an active field of research and one of the many promising applications of quantum simulators [198]. The thermalization dynamics of LGTs, which is dominated by both strong interactions and local constraints, poses theoretical and numerical challenges and remains mostly elusive [159,
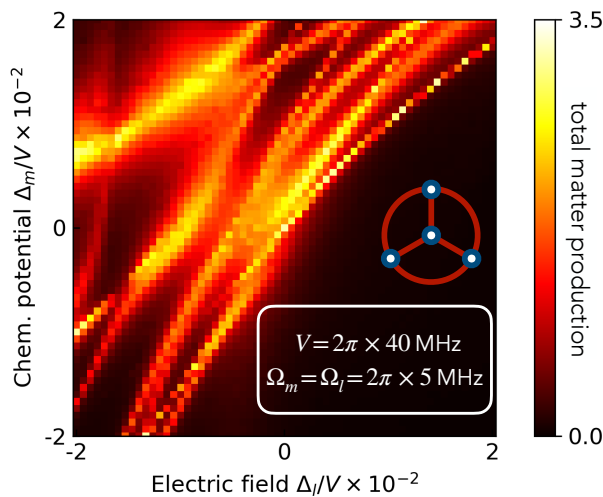
Figure 4.3: **Schwinger pair resonances.** We probe the Schwinger effect by quenching the vacuum state with the microscopic model for different experimentally relevant parameters: matter detuning Δ_m (chemical potential) and link detuning Δ_l (electric field). We find lines of resonance, where the production of matter excitations out of the vacuum is large.

199]. At the same time, thermalization of LGTs may be relevant to understand the dynamics of the early universe.

Here, we discuss a non-thermalization behaviour of LGTs, which can be understood from disorder in the internal, superselection sectors but without spatial disorder. This phenomenon was first described by Smith et al. [200, 201] under the name *disorder-free localization*. The idea is as follows: Each superselection sector $\{g_j\}_j$ corresponds to a distribution of static $\mathbb{Z}_2$ charges. Suppose we prepare an initial state in an equal superposition between all superselection sectors, i.e., a gauge noninvariant state, and time evolve under gauge-invariant Hamiltonian $\hat{\mathcal{H}}_{\mathbb{Z}_2}$. Then, each sector evolves independently since we have $[\hat{\mathcal{H}}_{\mathbb{Z}_2}, \hat{G}_j] = 0$ for all j. After time t, we perform a measurement projecting the system into one superselection sector; hence we randomly sample system with different distribution of background charges. It is the averaging over random distribution of charges, which induces disorder despite starting from an underlying translationally invariant Hamiltonian. It has been shown in Refs. [200–203] that in $\mathbb{Z}_2$ LGTs and $U(1)$ quantum link models sufficiently strong mixture between superselection sectors can lead to a new type of localization ubiquitous to gauge theories.

Let us highlight that the phenomenon of *disorder-free localization* necessitates to have access to all Gauss' law sectors and thus it cannot be experimentally realized in models, where either gauge or matter degrees-of-freedom are integrated out [96, 155–158], see Section 2.2.5. While this suggests to use schemes based on gauge protection mechanism, it is a priori not clear if the localization survives under experimental errors. Here, we want to address the questions whether disorder-free localization (DFL) may exist in emergent gauge theories and in the presence of small but finite Gauss' law errors [P5, P3, 204].

Here, we study the $(2 + 1)$D gauge theory in the minimal "Mercedes star" setup, see Section 4.2.2. We use the microscopic model (3.10) and show DFL behaviour in a small-scale exact diagonalization simulation for the case of $U(1)$ matter using the parameters shown in the inset of Figure 4.4. In particular, the observation of DFL would be an accessible experimental probe since it only requires to prepare the system in two different initial product states and time-evolve them under the microscopic Hamiltonian.
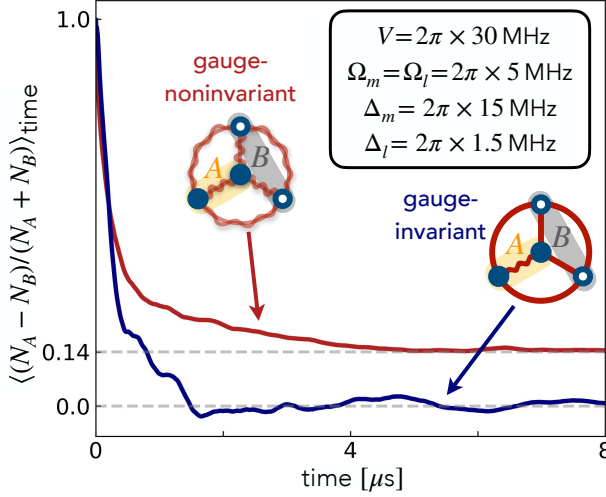
Figure 4.4: **Disorder-free localization.** We show numerical results obtained from exact diagonalization of the time-evolution of the microscopic model (3.10) with experimentally realistic parameters in a system with coordination number $z = 3$ (see inset). We observe disorder-free localization by initializing the system in a gauge-(non)invariant initial product state with two matter excitations localized in subsystem A and calculating the time-averaged imbalance between subsystem A and B as shown.

Consider a system with two subsytems A and B and an initial state, where all matter sites in subsystem A (B) are occupied (empty). We time evolve the initial state for a time t and probe whether the matter excitations stay localized in subsystem A or delocalize equally across subsystem A and B. Hence, the quantity of interest is the time-averaged imbalance $\mathcal{I}(t)$ of matter excitations at time t between the subsystems given by

$$\mathcal{I}(t) = \frac{1}{Lt} \int_0^t \left[\langle \hat{n}_A(\tau) \rangle - \langle \hat{n}_B(\tau) \rangle \right] d\tau, \tag{4.3}$$

where $\langle \hat{n}_{A(B)}(\tau) \rangle$ is the expectation value of total matter excitations in subsystem A (B) at time τ and L denotes the system size.

The eigenstate thermalization hypothesis (ETH) claims that $\mathcal{I}(t)$ eventually approaches its thermal equilibrium value. In DFL, this hypothesis is believed to be broken for gauge-noninvariant initial states $|\psi^{\text{ninv}}\rangle$ as discussed above.

Now, we numerically examine this behaviour on the example of "Mercedes star" geometry with coordination number $z = 3$. To this end, we consider the gauge-invariant initial state $|\psi^{\text{inv}}\rangle$ with $\hat{G}_j|\psi^{\text{inv}}\rangle = +|\psi^{\text{inv}}\rangle$ and matter excitations being distributed as described above. The Mercedes star model with four matter sites and six links is illustrated in the inset of Figure 4.4. For this initial state, we can compute the imbalance from the thermal ensemble as predicted by ETH (see also Ref. [P3]) and find that the system indeed fully delocalizes $\langle \mathcal{I} \rangle_{\text{thermal}} = 0$. Comparing this to the numerical results in Figure 4.4, we find that the time-averaged imbalance quickly vanishes as expected.

The situation changes for the gauge-noninvariant initial state $|\psi^{\text{ninv}}\rangle$. For this state the matter excitations are again initially located only in subsystem A but now the links are in $\tau_\langle^z i, j\rangle = +1$ as indicated in Figure 4.4. Therefore, $|\psi^{\text{ninv}}\rangle$ is an equal superposition of all possible gauge sectors $g_j = \pm 1$. While still $\langle \mathcal{I} \rangle_{\text{thermal}} = 0$, as we have verified numerically, we find that the state does not thermalize under time-evolution with $\hat{\mathcal{H}}_{\text{mic}}$ as shown in Figure 4.4.

In our proposed scheme, where the gauge invariance emerges due to energetic con-
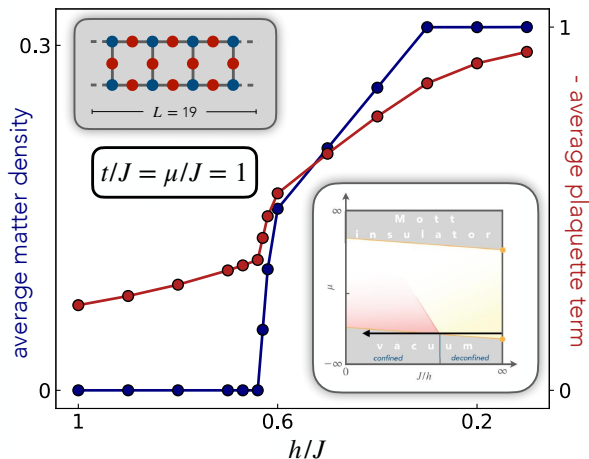
Figure 4.5: **Quantum phase transition.** We plot the average $U(1)$ matter density obtained from DMRG calculations on a ladder of length $L = 19$ and with $J < 0$. We can qualitatively understand the sharp decay of matter as a transition into the vacuum phase as discussed in Figure 3.5 (inset). The DMRG simulations were performed by Annabelle Bohrdt.

straints, we inevitability have Gauss' law errors induced by the weak drive Ω[1]. Thus, in the long time limit, the weak drive eventually leads to thermalization of the system discussed in Ref. [P5]. However, at experimentally relevant timescales we find a clear pre-thermal plateau indicating DFL as shown in Figure 4.4.

4.4 Signature of phase transition in a ladder

Our proposed scheme introduced in Chapter 3 is suitable for any geometry with coordination number $z = 3$; hence one can experimentally study square ladders of coupled $(1+1)$D chains. Here, we have examined the ground state of a $\mathbb{Z}_2$ LGT with $U(1)$ matter using the density matrix renormalization group (DMRG) technique [54] on a ladder and we find signatures of a quantum phase transition. Details on the numerical simulation are presented in Ref. [P5].

For our numerical simulations, we use Hamiltonian (3.11) with $\Delta_1 = \Delta_2 = 0$, i.e., we enforce a global $U(1)$ symmetry for the matter, and we tune the electric field h and chemical potential μ for fixed tunneling and plaquette interactions $t = 1$ and $J = -1$. Using the DMRG technique, we calculate the ground state of the above described Hamiltonian on a ladder with $L = 19$ plaquettes.

From the ground state calculated in DMRG, we obtain the average matter excitation density – an experimentally directly accessible quantity, e.g. by taking snapshots in the atomic ground state and Rydberg basis. As shown in Figure 4.5, the system is in a matter vacuum for large h/J similar to the $(2+1)$D case. For decreasing h/J, we find a abrupt increase of matter excitations indicating a phase transition. At the same critical electric field value, the plaquette term shows a sharp feature; note that $J < 0$ and thus the plaquette expectation value is negative indicated by the reversed sign on the plot label in Figure 4.5.

As shown in Figure 4.5, both the average density of matter excitations and the plaquette terms, which are experimentally directly accessible by projective measurements, change abruptly by tuning the electric field h indicating a transition into the vacuum phase. We emphasize that the ladder geometry is different from the $(2+1)$D honeycomb model studied

---

[1]In the top-down approach, the weak drive also enables us to generate $\mathbb{Z}_2$ invariant dynamics.

in Figure 3.5, however numerical simulations suggest the presence of a phase transition. To characterize the different phases and its phase transitions requires more elaborate studies of our effective model on the ladder. We emphasize that due to its numerical accessibility and experimental feasibility, the ladder model is an interesting playground to probe $\mathbb{Z}_2$ lattice gauge theories coupled to dynamical matter beyond $(1+1)$D.

4.5   Percolation order parameter

Defining order parameters for confinement is a challenging task, since it is a statement about the entire spectrum of a model instead of a symmetry breaking order parameter. In Chapter 2, we have seen that the scaling of Wilson loops can be used to distinguish the confined from the deconfined phase, but this is restricted to strictly zero matter density. Alternatively, the Fredenhagen-Marcu order parameter [205, 206], which measures open versus closed loops, was successfully applied in the context of frustrated dimer models [50, 51]. However, the Fredenhagen-Marcu order parameter is not capable of efficiently mapping out the entire Fradkin-Shenker phase diagram [P12, 207]. For finite temperature numerical simulations, Wilson loops in imaginary time – the Polyakov loops [206, 208] – are used to probe confinement. However, the Polyakov loops are numerically extremely challenging to probe and experimentally not accessible.

With the possibly to implement $(2+1)$D LGTs in state-of-the-art cold atoms experiments, new type of order parameters have to be developed that are easily accessible and are applicable at finite temperature. Even more, quantum simulators give access to new observables and thus it triggers the search for novel probes.

Here, we propose a non-local order parameter for (de)confinement in $\mathbb{Z}_2$ LGTs with dynamical matter using percolating clusters of electric field lines; hence the order parameter is manifestly gauge invariant. First, this order parameter was explored in a classical variant of the $\mathbb{Z}_2$ LGT in Ref. [P5]. Later, the order parameter was generalized to the quantum domain by Linsel et al. [P12]. In the following, we discuss the classical model.

In particular, we examine a temperature-induced deconfinement transition [209] in a classical limit of our effective model (3.16), which neglects charge and gauge dynamics $t = \Delta_{1,2} = J = 0$. Hence, the resulting matter-excitation conserving Hamiltonian is purely classical and a configuration is fully determined by the distribution of matter and electric field lines under the Gauss's law constraint, i.e. $\{(n_j, \tau^x_{\langle i,j \rangle}) \mid (-1)^{n_j} = g_j \prod_{i:\langle i,j \rangle} \tau^x_{\langle i,j \rangle} \ \forall j\}$ and we consider the sector with $g_j = +1 \ \forall j$.

To study thermal deconfinement, we consider exactly two matter excitations which, due to Gauss's law, have to be connected by a string Σ of electric field lines; i.e. Σ is a path of links with electric fields $\tau^x_{\langle i,j \rangle} = -1$ for $\langle i,j \rangle \in \Sigma$. This setting can be used as a probe of a deconfined (confined) phase, in which the $\mathbb{Z}_2$ matter is free (bound) [210].

To determine the classical equilibrium state, we note the following: 1) Due to the electric field term h in the Hamiltonian, a string of flipped electric fields $\tau^x_{\langle i,j \rangle} = -1$ costs an energy $2h \cdot \ell$, where ℓ is the length of the string. 2) Gauss's law enforces that at least one string is connected to each matter excitation.

Hence, in the classical ground state the two matter excitations form a mesonic bound
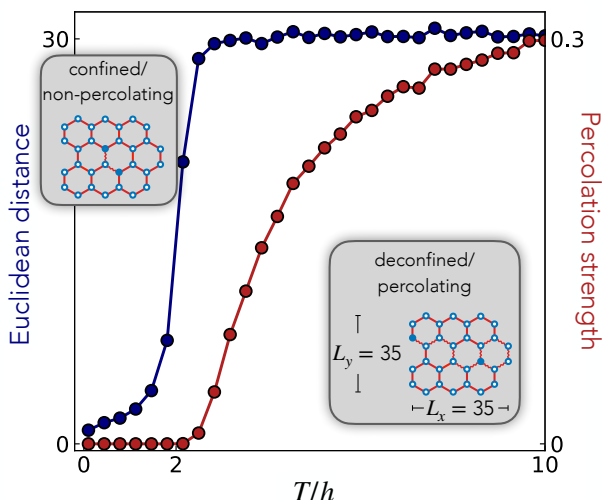
Figure 4.6: **Finite-T phase transition.** We use two fluctuating test charges to probe a temperature-induced deconfinement transition in a classical limit of our effective model using Monte Carlo simulations. Both in the percolation strength and the Euclidean distance of two matter excitations, we find that above a certain temperature T/h the system undergoes a percolation transition. The Monte Carlo simulations were performed by Simon Linsel.

state on nearest neighbor lattice sites, see e.g. Section 3.4.2. Therefore, the matter excitations are confined by a linear string potential. In the co-moving frame of one matter excitation, this model can approximately be described as a particle in a linear confining potential.

At non-zero temperature $T > 0$, the entropy contribution to the free energy $F = E - TS$ must also be considered. Even though the electric field term h yields an approximately linear string tension, the two charges can separate infinitely in thermal equilibrium provided that $E(\ell) < T \log(N_\ell)$ for $\ell \to \infty$, where $\log(N_\ell) = S$ denotes the entropy S of all the string states N_ℓ with length ℓ (setting $k_B = 1$) and $E(\ell)$ is their typical energy [210]. This happens beyond a critical temperature $T > T_c$, when a percolating net of $\mathbb{Z}_2$ electric strings forms.

At the critical temperature T_c we anticipate a thermal deconfinement transition, where matter excitations become free $\mathbb{Z}_2$ charges (bound mesons) for $T > T_c$ ($T < T_c$). To study this transition we use the percolation strength – a measure for the spatial extend of a global string net – as an order parameter for the deconfined phase. The percolation strength is defined as the number of strings in the largest percolating cluster of $\mathbb{Z}_2$ electric strings, normalized to the system size. Furthermore, we consider the Euclidean distance between two matter excitation and show that an abrupt change of behaviour in this quantity indicates the disappearance of the bound state.

We perform Monte Carlo simulations on a 35×35 honeycomb lattice (in units of lattice spacing) using classical Metropolis-Hastings sampling, see Ref. [P5] for details. To be precise, we consider a classical model that is motivated by the microscopic Hamiltonian (3.10) - in particular we used the precise effective model as derived in Eq. (3.16) of Section 3.3 for experimentally realistic parameters $\Omega/V = 1/8$, $\Delta_m = V/2$ and $\Delta_l/V \approx 0.044$.

We find a sharp transition for both the percolation strength and Euclidean distance between two matter excitations around $(T/h)_c \approx 2$ as shown in Figure 4.6: At a critical temperature $(T/h)_c \approx 2$, the percolation strength abruptly increases, i.e. the string net percolates. Moreover, at the same critical temperature $(T/h)_c \approx 2$ the Euclidean distance shows a drastic change of behavior and saturates at about 30 for high temperatures. This saturation can be explained by the finite system size.

For a finite density of matter excitations in the system, the Euclidean distance is not

a reasonable measure anymore. However, the percolation transition can be related to (de)confinement at finite densities as has been numerically confirmed in Ref. [P12]. Indeed, the percolation order parameter is able to capture the Fradkin-Shenker phase diagram, see Figure 2.4, and thus provides a suitable observable to probe confinement in quantum simulators.
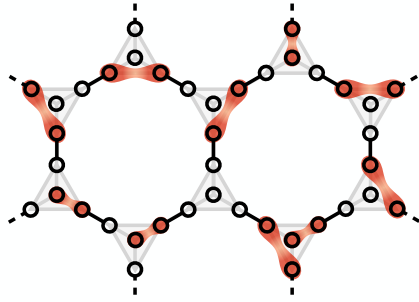
5

Large-scale implementation of non-Abelian quantum link models

THE LONG-SOUGHT GOAL in the quantum simulation of LGTs is the realization of non-Abelian gauge theories beyond $(1+1)$D, and ultimately simulate Wilson's lattice QCD, which is believed to capture quark confinement [26]. This would allow us to probe gauge theories and the consequence of non-Abelian symmetries from an entirely new perspective enabled by the tunability of parameters, by the access to non-local quantities and by observing real-time dynamics.

There are various different approached toward realizing non-Abelian gauge theories even at the level of the constituents of the theory. In particular, there exist different truncation methods of the infinite dimensional link Hilbert space. Here, we will present a method based on a rishon formulation of LGTs, see Section 2.2.4: In this formulation the link is represented as a double well with exactly $\mathcal{N}$ particle carrying N colors, the so-called rishons [147, 148, 152]. In the simplest model, the link consists of a single spin-1/2 particle tunneling back and forth on a link. As we will show below, the rishons can be enforced to fulfill $\mathrm{SU}(N)$ Gauss' law constraints by using readily available Hubbard or dipolar interactions. We propose concrete schemes and architectures to realize $\mathrm{SU}(N)$ and $\mathrm{U}(N)$ LGTs with hardcore bosonic or fermionic matter in $(2+1)$D in cold molecule tweezer arrays or optical lattices, respectively. The following Chapter is based on publication [P9]. The text and figures are rearranged, adapted and supplemented.

5.1 Non-Abelian gauge protection

Until now, almost all quantum-simulation experiments of gauge theories have been performed in one spatial dimension, have been restricted to a small number of degrees of freedom, or focused on Abelian gauge groups, with most non-Abelian proposals restricted to building blocks [154, 157, 159, 211–221]. Partly, this is due to current technical limitations,
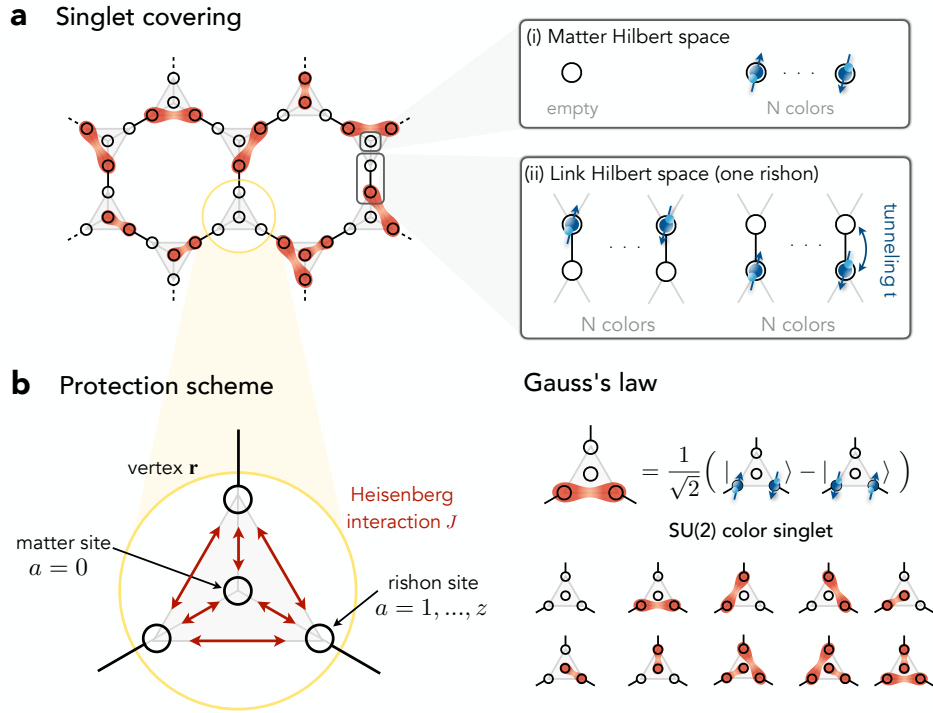
a Singlet covering

(i) Matter Hilbert space

empty   N colors

(ii) Link Hilbert space (one rishon)

N colors   N colors

tunneling t

b Protection scheme

Gauss's law

vertex **r**

Heisenberg
interaction J

matter site
$a = 0$

rishon site
$a = 1, ..., z$

$$ = \frac{1}{\sqrt{2}} \left(| \, \rangle - | \, \rangle \right)$$

SU(2) color singlet

Figure 5.1: SU(N) **gauge protection. a** The rishon formulation of non-Abelian LGTs contains (i) matter on lattice sites and (ii) rishons on links connecting two sites. The links are composed of two separate rishon sites and in the simplest description we enforce to have exactly one rishon per link. The matter particles and rishons have N colors; here we illustrate $N = 2$. Gauge-invariant configurations in a SU(2) LGT have to cover the lattice with spin singlets while fulfilling the rishon number constraint. **b** Gauss's law enforces that the sites around a vertex have to form a total color singlet, with the physical allowed states on a vertex depicted on the right. The Gauss's law constraint can be energetically enforced by antiferromagnetic SU(N) gauge-invariant Heisenberg interactions between all sites adjacent to a vertex, as depicted on the left. We propose to implement the SU(2) LGT using ultracold atoms or molecules (blue dots). The honeycomb lattice is an appealing geometry to realize the required interaction strengths.

but more importantly, extended systems are intrinsically vulnerable to gauge-breaking errors unless explicit gauge protection schemes are implemented, see Section 2.2.5. Indeed, the only large-scale experiments so far have relied either on the complete elimination of gauge-noninvariant subspaces [96, 155, 156], or on linear Stark gauge protection [53, 159]. Likewise, the recent realization of a $\mathbb{Z}_2$ topological spin liquid in Rydberg atom arrays [51] have relied on an energetically protected emergent gauge structure.

In particular, gauge protection schemes for non-Abelian gauge theories have been few and with limited experimental feasibility [222–224]. Experimental proposals have mostly adopted a *bottom-up* approach focusing on the realization of an exact non-Abelian target gauge theory in some perturbative regime of a mapped model [149, 221, 225, 226], without an explicit gauge protection scheme in place. In order to further advance the quantum simulation of gauge theories, it is crucial to propose experimentally feasible realizations of large-scale non-Abelian gauge theories where gauge invariance is directly stabilized by

an explicit gauge protection term that should appear naturally in experimentally relevant settings.

Here, we propose realistic implementations of non-Abelian SU(N) LGTs using a *top-down* approach in which the focus is on realizing the gauge protection terms locally, with the gauge-invariant dynamics induced perturbatively. We demonstrate how non-Abelian gauge constraints can be energetically enforced in current and near-term quantum simulation setups based on ultracold atoms and polar molecules in optical lattices or optical tweezer arrays. Provided that these gauge protection terms define the largest energy scale in the system, the low-energy subspace is guaranteed to be described by an effective (or emergent) non-Abelian LGT. By tuning the strength or form of subdominant gauge-noninvariant terms—e.g., through tunneling or simple local spin-flip processes—the terms in the effective low-energy Hamiltonian can be conveniently controlled. Therefore, our scheme offers a realistic pathway towards large-scale implementations of non-Abelian SU(N) and U(N) lattice gauge theories, including dynamical matter and plaquette terms, and with an inherent robustness of the emergent gauge symmetry.

In our proposal, we use the rishon construction [147, 148, 152] of non-Abelian LGTs introduced in Section 2.5. We propose to directly implement rishon and matter sites, and energetically enforce SU(N) [or U(N)] gauge invariance by a proper choice of intra-vertex interactions, where in the following we shall define a vertex. Consider a lattice with matter sites denoted by indices $\mathbf{r}$ and links $\langle \mathbf{r}, \mathbf{r}' \rangle$ between nearest-neighbor sites $\mathbf{r}$ and $\mathbf{r}'$. Each link hosts two rishon sites; see Figure 5.1a. A vertex represented by the index $\mathbf{r}$ is then comprised of the matter site $\mathbf{r}$ and the nearest rishon sites on the links connecting to it, as illustrated in Figure 5.1b.

The generators of the SU(N) symmetry can be written in vector form as [152]

$$\hat{\mathbf{G}}_{\mathbf{r}} = \sum_{a=0}^{z} \hat{\mathbf{S}}_{(\mathbf{r},a)} = \sum_{a=0}^{z} \sum_{\alpha,\beta=1}^{N} \hat{c}^{\dagger}_{(\mathbf{r},a),\alpha} \hat{\mathbf{T}}^{\alpha\beta} \hat{c}_{(\mathbf{r},a),\beta}, \tag{5.1}$$

where $\hat{\mathbf{T}} = (\hat{T}_1, \ldots, \hat{T}_{N^2-1})$ are the $N^2 - 1$ elements of the SU(N) Lie algebra, each of which is an $N \times N$ matrix [152], $\alpha, \beta \in \{1, \ldots, N\}$ are indices representing the N colors, $\hat{c}_{(\mathbf{r},a),\alpha}$ is a rishon ($a \neq 0$) or matter ($a = 0$) annihilation operator on vertex $\mathbf{r}$; the index $a \in \{0, \ldots, z\}$ indicates a matter site when $a = 0$, and a "nearest" rishon site when $a = 1, \ldots, z$ with lattice coordination number z; see Figure 5.1b. Note that the hallmark of a non-Abelian gauge symmetry is that the $N^2 - 1$ components of $\hat{\mathbf{G}}_{\mathbf{r}}$ generally do not commute with each other. This significantly contributes to the difficulty in realizing large-scale non-Abelian gauge theories on quantum simulators using a bottom-up approach.

For a faithful gauge-theory quantum simulation, it is necessary to work in the *target* or *physical* gauge superselection sector $\hat{\mathbf{G}}_{\mathbf{r}} |\psi\rangle = 0$, $\forall \mathbf{r}$. Any dynamics initialized in this sector can be restricted to remain in this sector by employing the *gauge protection term* $\hat{H}_J = \frac{J}{2} \sum_{\mathbf{r}} \hat{\mathbf{G}}_{\mathbf{r}}^2$, which for $J > 0$ enforces a color singlet as the ground state at each vertex as discussed in Section 2.2.5, see Figure 5.1. The essence of our approach is to rewrite this gauge protection term in a convenient form that contains Heisenberg and Hubbard interactions, which usually naturally occur in experimental setups, thereby making it amenable

for experimental implementation using ultracold molecules and atoms in an optical lattice, as we will demonstrate through concrete experimental proposals below.

In this vein, we utilize Eq. (5.1) in order to rewrite the gauge protection term as

$$\hat{H}_J = J \sum_{\mathbf{r}} \left[\sum_{\langle a,b \rangle} \hat{\mathbf{S}}_{(\mathbf{r},a)} \cdot \hat{\mathbf{S}}_{(\mathbf{r},b)} + \frac{1}{2} \sum_a \hat{\mathbf{S}}^2_{(\mathbf{r},a)} \right]. \tag{5.2}$$

The first term on the right-hand side is a Heisenberg-interaction term, while the second the second term enforces on-site spin singlets. We reformulate the latter as a two-body on-site Hubbard term using identities of the SU(N) algebra [227] yielding (we suppress the site index here)

$$\begin{aligned}
\hat{\mathbf{S}}^2 &= \sum_{\alpha,\beta} \sum_{\gamma,\delta} \hat{c}^\dagger_\alpha \hat{c}_\beta \hat{c}^\dagger_\gamma \hat{c}_\delta \left(\vec{T}_{\alpha,\beta} \cdot \vec{T}_{\gamma,\delta} \right) \\
&= \sum_{\alpha,\beta} \sum_{\gamma,\delta} \hat{c}^\dagger_\alpha \hat{c}_\beta \hat{c}^\dagger_\gamma \hat{c}_\delta \frac{1}{2} \left(\delta_{\alpha,\delta} \delta_{\beta,\gamma} - \frac{1}{N} \delta_{\alpha\beta} \delta_{\gamma,\delta} \right) \\
&= \frac{1}{2} \sum_{\alpha,\beta} \left(\hat{c}^\dagger_\alpha \hat{c}_\beta \hat{c}^\dagger_\beta \hat{c}_\alpha - \frac{1}{N} \hat{c}^\dagger_\alpha \hat{c}_\alpha \hat{c}^\dagger_\beta \hat{c}_\beta \right) \\
&= \frac{N^2 - 1}{2N} \hat{n} - \frac{1 - \xi N}{N} \sum_{\beta > \alpha} \hat{n}_\alpha \hat{n}_\beta
\end{aligned} \tag{5.3}$$

with $\hat{n} = \sum_\alpha \hat{n}_\alpha$. Further, we have used the hard-core constraint of fermions ($\xi = -1$) or hard-core bosons ($\xi = +1$), i.e. $\hat{n}_\alpha^2 = \hat{n}_\alpha$. We find that the on-site spin singlets are enforced by an (unimportant) chemical potential and Hubbard interactions with $U = -\frac{1-\xi N}{N} J$. The sign of the interaction for fermions with $N > 1$ is negative and thus attractive.

In summary, the gauge protection term (5.2) can be reformulated as

$$\hat{H}_J = \sum_{\mathbf{r},a} \left[J \sum_{b > a} \hat{\mathbf{S}}_{(\mathbf{r},a)} \cdot \hat{\mathbf{S}}_{(\mathbf{r},b)} + U \sum_{\beta > \alpha} \hat{n}_{(\mathbf{r},a),\alpha} \hat{n}_{(\mathbf{r},a),\beta} \right] \tag{5.4}$$

with all-to-all antiferromagnetic Heisenberg interactions J and on-site Hubbard interactions U.

Next, we place the emphasis on experimentally realizing the protection term (5.4), along with the required rishon-number conservation per link. In its general form, such a gauge protection term has been shown analytically and numerically to enable large-scale quantum simulations of (non-)Abelian lattice gauge theories [164, 222, 223]. Dynamics can then be induced perturbatively by a term $\hat{H}_t$, in part gauge-invariant and in part not, but the gauge protection term (5.2) will ensure the reliable suppression of gauge-breaking errors up to times exponential in J [164], see Section 2.2.5 and Section 3.1.

5.2 Effective lattice gauge theory

Similar to the $\mathbb{Z}_2$ LGT discussed in Chapter 3, the effective (gauge-invariant) Hamiltonian emerges from the microscopic Hamiltonian $\hat{H} = \hat{H}_J + \hat{H}_t$, which we will further discuss
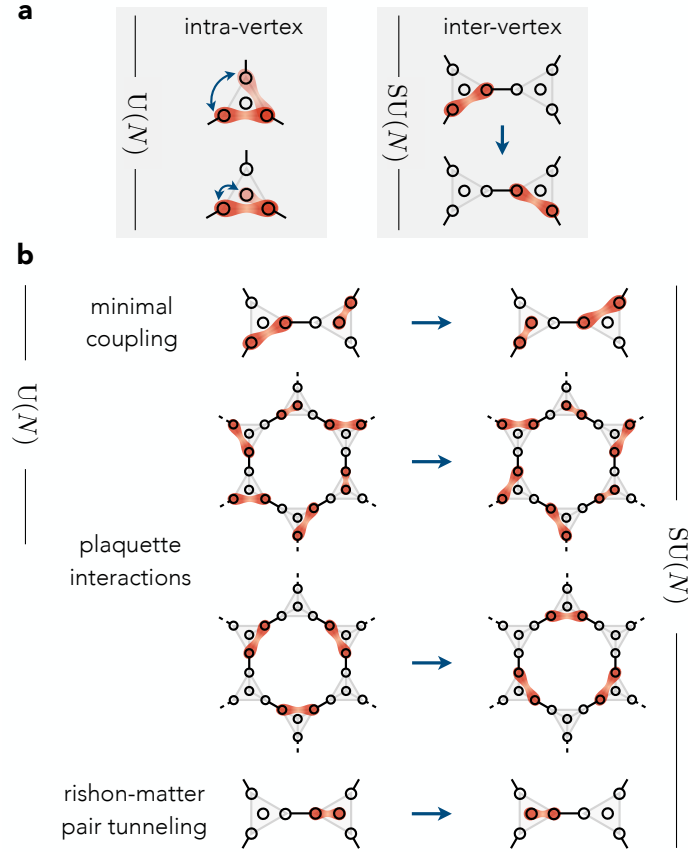
Figure 5.2: **Effective lattice gauge theory.** We illustrate the terms contained in the effective Hamiltonian for a one-rishon-per-link model on the honeycomb lattice, which can be realized in our proposed scheme. **(a)** U(N) and SU(N) LGTs are generated by terms that rearrange color singlets within a vertex (intra-vertex) or between neighbouring vertices (inter-vertex) involving both matter and rishon particles. The former additionally conserves a local U(1) symmetry. **(b)** The terms in the effective model contain the minimal gauge-matter and plaquette couplings, i.e., the kinetic and magnetic interactions of lattice gauge models.

below in experimentally relevant settings. To recap, our method is based on a separation of energy scales with (i) strong protection terms (5.2) of strength J and (ii) weak tunneling perturbation t, allowing us to treat the latter perturbatively and to derive the effective gauge-invariant model, see Appendix in Ref. [P9]. The perturbation describes the tunneling of rishons within links as well as tunneling of matter between vertices.

For sufficiently weak perturbations, $|t| \ll |J|$, the system approaches a controlled-violation regime, where the occupation of gauge-noninvariant sectors is strongly suppressed. Hence, the low-energy effective theory is inherently gauge-invariant, which we confirm by numerical simulations of small systems, see Appendix in Ref. [P9]. This allows us to determine the dominant terms of the effective Hamiltonian, which are gauge-invariant and conserve the rishon number constraint. In our model, we identify two types of processes:

Firstly, the simultaneous rearrangement of color singlets within a vertex (intra-vertex) while maintaining the rishon and matter number constraint is manifestly gauge-invariant,

see Figure 5.2a. Since the total number of particles around a given vertex is maintained, the terms generated by intra-vertex processes host an additional local U(1) symmetry, which yields an effective $U(N) = U(1) \times SU(N)$ LGT [152].

Secondly, our method induces terms that are $SU(N)$ gauge-invariant but break the local U(1) symmetry. Thus, the local symmetry structure is reduced to $SU(N)$. The relevant $SU(N)$ gauge-invariant terms involve inter-vertex tunneling of matter and rishons, in which whole color singlets tunnel between vertices; see Figure 5.2a.

By constructing the effective model as described above, we can in principle obtain the form of the effective Hamiltonian with the typical minimal gauge-matter couplings and magnetic plaquette interactions. The amplitudes of these terms can have a functional dependence on the matter and rishon distribution, as well as on the particle statistics and can be computed perturbatively. The leading minimal coupling and rishon-matter tunneling terms occur in second-order processes with strength $\propto t^2/J$; hence our proposal enables a feasible implementation of non-Abelian LGT with sizable effective interactions as we will show numerically below.

In general, the leading-order contributions are generated by perturbatively coupling the energetically-resonant gauge-invariant states. The protection term (5.2) enforces the color singlet constraint on each vertex, and in its simplest form in Eq. (5.2), all singlets are energetically equally favoured. On the other hand, by introducing disordered protection strengths, $J \to J_{\mathbf{r}}$, transporting color singlets between vertices is energetically costly, which efficiently suppresses inter-vertex processes, see Figure 5.2a. Therefore an additional local U(1) symmetry is protected for a proper choice of $J_{\mathbf{r}}$. We emphasize, however, that in multi-rishon models, the $SU(N)$ gauge-invariant model further contains terms that transport glueballs, i.e., bound states of rishon color singlets [148], see Section 2.2.4.

5.3   One-rishon models: ultracold molecules.

In order to demonstrate our approach, we shall first focus on the case of large-scale $(2+1)$D SU(2) LGTs. For the purpose of most realistic and immediate experimental relevance, we further employ a hard-core constraint on the matter and rishon sites, while fixing the rishon number per link to unity, $\mathcal{N} = 1$. This allows us to drop the second term in Eq. (5.4), and only focus on proposing an experimentally feasible scheme for the realization of the Heisenberg term. The latter involves equal-strength magnetic interactions at magnitude J around a vertex, and a rishon per link that can tunnel between the two sites on any given rishon link. This tunneling, along with a similar term for the matter, does not commute with $\hat{H}_J$ and will take the role of the gauge-breaking perturbation with strength $|t| \ll |J|$.

For models with exactly one rishon per site, the statistics of the rishon has no effect as long as we assume that rishons cannot tunnel between different rishon links. In this case, we can replace the fermionic rishons by bosons.

Ultracold polar molecules are a new powerful tool [65, 101, 107, 117, 228–232] to implement and control SU(2)-invariant Heisenberg interactions by Floquet-driving the intrinsic dipole-dipole interactions [106]. So far, coherent tunneling of molecules has not been demonstrated, but it should be experimentally feasible. Therefore, we suggest two different
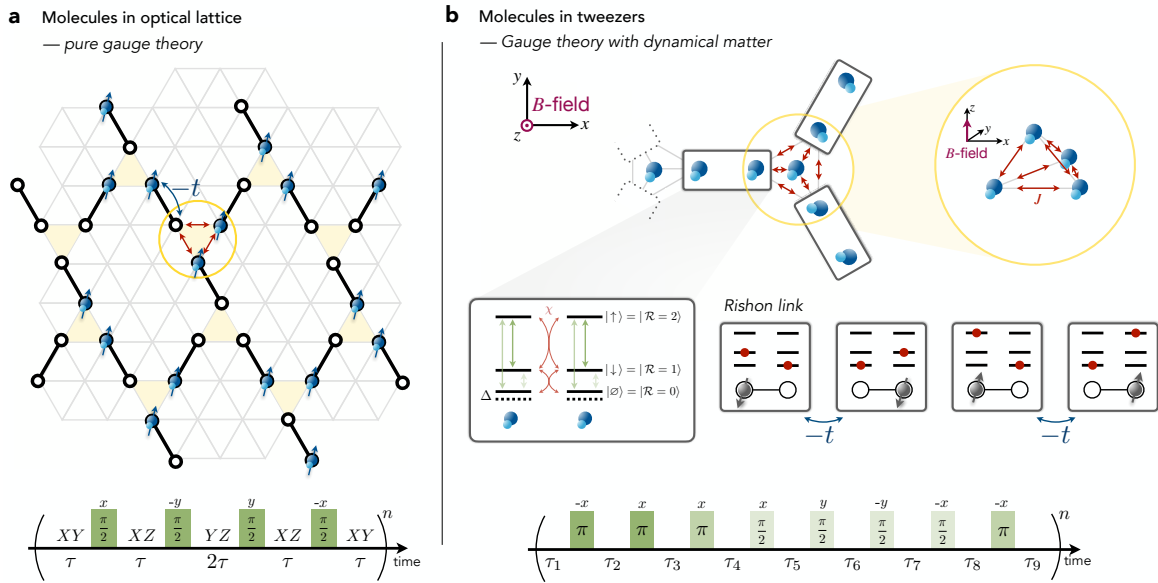
Figure 5.3: **Implementation with ultracold polar molecules. (a)** Pure SU(2) LGT (without dynamical matter): Ultracold molecules in optical lattices directly implement the desired microscopic Hamiltonian with gauge protection terms of strength J and weak (perturbative) tunneling t. We propose to imprint a potential landscape on a triangular lattice that enables molecule tunneling only within double wells (solid black); hence the rishon number constraint is exactly fulfilled. Moreover, by using an isolated qubit subspace of internal rotational states, the dipole-dipole interaction can be used to Floquet engineer Heisenberg interactions between molecules by repeatedly applying a sequence of rotations in the qubit subspace combined with time evolution of the microscopic molecular Hamiltonian (bottom). **(b)** SU(2) LGT with dynamical matter: Alternatively, we propose a scheme for molecules in tweezers arrays, where the tunneling is implemented by flip-flop processes and which allows to include dynamical matter. Each link is built from two molecules and the molecule on the matter site is located in a second plane such that the interaction strength around molecules adjacent to a vertex have equal strength J. We encode the states $|\varnothing\rangle$, $|\downarrow\rangle$, and $|\uparrow\rangle$ in each molecule's internal rotational states $|\mathcal{R} = 0\rangle$, $|\mathcal{R} = 1\rangle$, and $|\mathcal{R} = 2\rangle$, respectively. By applying a Floquet sequence which rotates within the molecular rotational states, both rishon tunneling as well as the Heisenberg interactions can be realized efficiently. To avoid tunneling between different rishon links or between matter and rishon sites, we require local detunings Δ for the $|\mathcal{R} = 0\rangle$ states by local AC stark shifts.

schemes below: with and without physical tunneling of molecules. Furthermore, we note that molecules currently face problems to reach high fillings of tweezers/optical lattices, and deterministic filling is not (yet) possible, but we expect that such technical challenges can soon be overcome.

5.3.1 Optical lattice: Tunneling scheme

Let us first consider an SU(2) LGT *without* dynamical matter, and with one rishon per link. The use of ultracold molecules in optical lattices has the advantage that the local Hilbert space structure and hence the rishon-number constraint can be exactly fulfilled by simply suppressing tunneling outside the links for all experimentally relevant times. To this end,

we propose to implement an optical landscape with double-well potentials on links between vertices either by a superlattice or by removing lattice sites from an optical lattice using a digital mirror device ("cookie-cutting method"), see Figure 5.3a. Each double well should be loaded with exactly one molecule, and we restrict the molecular internal states to a qubit subspace to encode the two colors $\downarrow$ and $\uparrow$.

Thus, the microscopic Hamiltonian we suggest to implement is given by $\hat{H} = \hat{H}_J + \hat{H}_t$ with the (weak) rishon-tunneling perturbation

$$\hat{H}_t = -t \sum_{\langle \mathbf{r}, \mathbf{r}' \rangle} \sum_{\alpha = \downarrow, \uparrow} \left[\hat{c}^\dagger_{(\mathbf{r},a),\alpha} \hat{c}_{(\mathbf{r}',b),\alpha} + \text{h.c.} \right], \tag{5.5}$$

where the indices a, b defining the rishon link are uniquely determined by the link $\langle \mathbf{r}, \mathbf{r}' \rangle$. The geometry has to be chosen such that the sites around a vertex are pairwise equally distanced. A chain in $(1+1)$D trivially fulfills this constraint; in $(2+1)$D, this can be achieved in, e.g., a honeycomb lattice as shown in Figure 5.1a, i.e., the rishon links form a kagome lattice. Other lattices would be feasible by either exploiting out-of-plane geometries or anisotropic interactions.

In our proposed setup in $(2+1)$D, the Gauss's law constraint yields a covering of singlets on the kagome lattice, which is a highly degenerate ground-state manifold. In the ground-state, this particular model can be re-written in terms of a quantum dimer model on a non-bipartite lattice [153] hosting a $\mathbb{Z}_2$ spin liquid phase in the deconfined regime [50, 51]. We emphasize, however, that our model features distinctly different vertex excitations associated with the stabilizer term $\hat{H}_J$ if we allow individual gauge-breaking excitations that carry well-defined SU(2) charges.

The gauge protection (5.4) can be implemented by using strong nearest-neighbor dipole-dipole interactions as follows: molecules located around the same vertex interact with resonant dipole-dipole interactions of strength χ between two rotational states of molecules giving rise to XY spin interactions. In order to engineer the SU(2) gauge-invariant Heisenberg interactions, which energetically enforce the low-energy manifold to fulfill the Gauss's law constraint, see Figure 5.1b, we propose to use Floquet-driving of the system [86, 87, 106]: Consecutive $\pi/2$-rotations around the Pauli $(x, -y, y, x)$-direction yield an effective isotropic Heisenberg Hamiltonian in the limit of high frequencies $1/T \gg \chi$, where T is the Floquet cycle time, see Figure 5.3a.

To induce dynamics within the gauge-invariant subspace, we propose to weakly perturb the system with gauge-breaking terms. Due to the energetic constraints, the system evolves under an SU(2) gauge-invariant Hamiltonian and undesired gauge sectors remain only virtually occupied [30]. In our scheme, the tunneling $|t| \ll |J|$ between neighboring rishon sites is a sufficient perturbation to induce the desired dynamics, which we numerically benchmark below.

We remark that the dipolar interactions decay with the cube of the distance between two molecules giving rise to long-range interactions. Thus, beyond nearest-neighbor, interactions can be treated as another gauge-breaking perturbation with a strength much smaller than $|J|$; in the presence of Floquet driving the perturbation is long-range Heisenberg-type. In our proposed scheme with built-in gauge protection, the extra perturbation yields an

additional source to induce dynamics within the gauge-invariant subspace.

Dynamical matter can be included in principle by introducing an additional lattice, e.g., in a bilayer geometry, on which matter molecules of the same species interact with rishon molecules around a vertex with Heisenberg interactions at strength J. Tunneling $|t| \ll |J|$ allows the molecules to move between matter sites. While the tunneling scheme is conceptually the simplest model, realizing it with dynamical matter in current setups is challenging.

5.3.2 Tweezer arrays: Bosonic tunneling scheme

We propose a second scheme that implements tunneling through flip-flop processes of bosonic (spin-flip) excitations by including a third rotational molecular state to encode an empty site. Here, we assume a fully filled lattice with one molecule on each matter/rishon site. To engineer both tunneling and magnetic interactions, we adapt a Floquet driving scheme that is based on resonant dipole-dipole interactions combined with rotations within the subspace of three internal states, see also Chapter 11.

For concreteness, we also assume that the matter sites form a honeycomb lattice with adjacent rishon links. Since we do not require physical tunneling between any sites on the lattice, the geometry can be realized with optical tweezers. The link building block, i.e., two sites occupied by one bosonic rishon, is constructed from two molecules: For the left and right molecule, we identify the internal rotational molecular states $|\mathcal{R}\rangle$ with: an empty site $|\varnothing\rangle$ ($\mathcal{R} = 0$), a $\downarrow$-rishon ($\mathcal{R} = 1$), and a $\uparrow$-rishon ($\mathcal{R} = 2$). We will describe below how the effective dynamics can be restricted to a subspace that fulfills the rishon number constraint; see Figure 5.2b. Additionally, we place molecules on matter sites and identify the internal states with bosonic matter fields as in the rishon case. To obtain equal-strength interactions around a vertex on, e.g., the honeycomb lattice, we propose to elevate the molecules on matter sites adequately out-of-plane [123].

Using this mapping, the Heisenberg interaction term J required for gauge protection is engineered with the same Floquet driving sequence as proposed for the optical lattice implementation. Additionally, the tunneling within a rishon link corresponds to an exchange processes $|\mathcal{R} = 0, \mathcal{R} = 1\rangle \leftrightarrow |\mathcal{R} = 1, \mathcal{R} = 0\rangle$ ($|\mathcal{R} = 0, \mathcal{R} = 2\rangle \leftrightarrow |\mathcal{R} = 2, \mathcal{R} = 0\rangle$) for tunneling of a $\downarrow$-rishon ($\uparrow$-rishon). The $\downarrow$-rishon tunneling is conveniently implemented by the resonant dipole-dipole interaction. In order to obtain the same tunneling strength for the $\uparrow$-rishon, an extra rotation within the Floquet sequence has to be included. We refer to Chapter 11 for details.

To suppress hopping of rishon excitations between *different* links or onto matter sites, local AC stark shifts $|\Delta_j| \gg 1/T$ can be applied to the $|\mathcal{R} = 0\rangle$ states, such that resonant tunneling t only occurs if $\Delta_i = \Delta_j$, where i and j are indices distinguishing between the different links or matter sites. In the effective Floquet model, the coupling ratio t/J can be tuned by adjusting the distance between molecules around a vertex and between the two rishon sites. Hence, the tunneling rate between matter sites t_m and between rishon sites t is determined by the geometry, see Ref. [P9] for details. Concretely, the microscopic
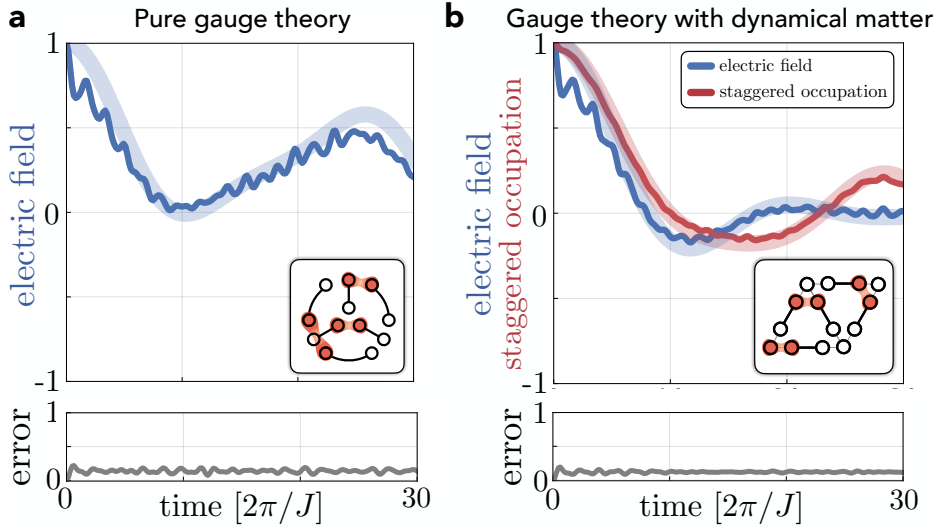
Figure 5.4: **Exact diagonalization study. (a)** Quench dynamics of the electric field in the SU(2) pure LGT without dynamical matter on a Mercedes star geometry for $t/J = 0.075$. The initial state is illustrated in the inset. Throughout the entire dynamics, the gauge violation is always below 22% of the infinite-temperature violation (which corresponds to an error of 1 in our plot), settling into a stable plateau $\propto t^2/J^2$, see Figure 5.5. **(b)** Quench dynamics of the electric field in the SU(2) LGT with dynamical matter on a double-triangle geometry with four matter sites at the corners for $t = 4t_m = 0.15J$. The initial state is illustrated in the inset. Throughout the entire dynamics, the gauge violation is always below 20% of the infinite-temperature violation, settling into a stable plateau $\propto t^2/J^2$, see Figure 5.5. Shaded lines in (a) and (b) correspond to dynamics of the corresponding gauge-invariant effective Hamiltonian, which agree well with our exact prediction for the microscopic model. In both cases, the microscopic model exhibits rich gauge-invariant dynamics in a controlled-violation regime. The ED simulations were performed by Jad C. Halimeh.

Hamiltonian is now $\hat{H} = \hat{H}_J + \hat{H}_t + \hat{H}_{t_m}$, where

$$\hat{H}_{t_m} = -t_m \sum_{\langle \mathbf{r}, \mathbf{r}' \rangle} \sum_{\alpha = \downarrow, \uparrow} \left[\hat{c}^\dagger_{(\mathbf{r},0),\alpha} \hat{c}_{(\mathbf{r}',0),\alpha} + \text{h.c.} \right]. \tag{5.6}$$

5.3.3 Numerical benchmarks.

We now validate our scheme by considering the two aforementioned SU(2) LGTs (the one with dynamical matter and the one without) on geometries amenable for exact diagonalization. The quench dynamics of the electric field, defined as the local staggered rishon occupation on links, is shown in Figure 5.4 for the SU(2) LGT without matter on a *Mercedes star* geometry with $t = 0.075J$ and for the SU(2) LGT with dynamical matter on a double-triangle geometry with four matter sites at the corners and with $t = 4t_m = 0.15J$. In both cases, the initial state is shown as an inset. For the case with dynamical matter in Figure 5.3.3b, we additionally show the difference in matter occupation between matter sites on the long diagonal and those on the short diagonal, with only one matter site on the long diagonal initially occupied. For all local observables, we find rich fast dynamics within ex-
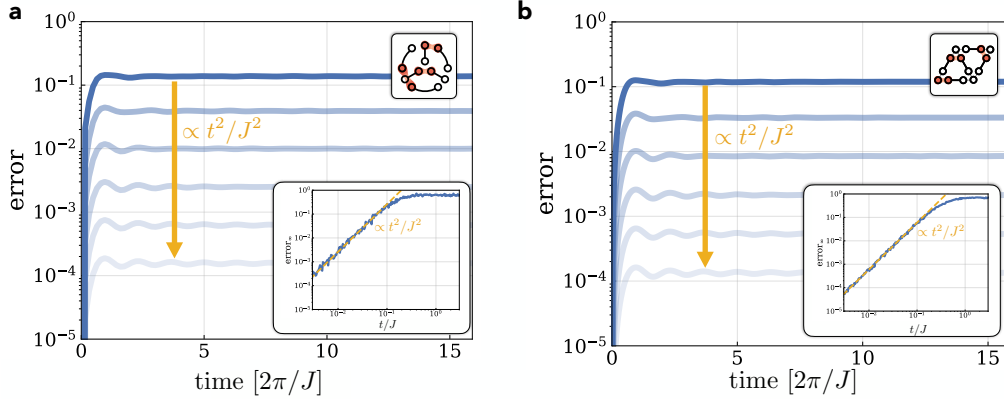
Figure 5.5: **Controlled gauge violation regime.** Using the same initial states as in Figure 5.4, we repeat the corresponding quenches for **(a)** the Mercedes star geometry at $t = 0.075 \times 2^{-k}J$ and **(b)** the double-triangle geometry at $t = 4t_m = 0.15 \times 2^{-k}J$ with $k = 0, 1, \ldots, 5$ (dark to bright blue). In all cases, we find that the gauge violation settles into a plateau of value $\propto t^2/J^2$ for all investigated evolution times, a hallmark of the controlled-violation regime [164]. In the insets, we show the "infinite"-time gauge violation as a function of t/J. In exact diagonalization, we chose various times $t \gtrsim 10^4/J$ to extract this quantity. For sufficiently small t/J, stabilized gauge invariance is guaranteed. The ED simulations were performed by Jad C. Halimeh.

perimentally realistic evolution times. Crucially, the parameters used for the tunneling are in a controlled-violation regime, guaranteeing faithful gauge-theory dynamics up to times exponential in J [164]. We define the gauge violation error as

$$\sum_{\mathbf{r}} \langle \hat{\mathbf{G}}_{\mathbf{r}}^2 \rangle \, / \sum_{\mathbf{r}} \langle \hat{\mathbf{G}}_{\mathbf{r}}^2 \rangle_{\infty}, \tag{5.7}$$

where $\langle \cdot \rangle_{\infty}$ denotes the infinite-temperature state. Indeed, for both models we find the gauge violation to be suppressed into a plateau $\propto t^2/J^2$ for all investigated late times, see Figure 5.5, and is always below 22% for the parameters employed in Figure 5.4.

The dynamics from the microscopic model $\hat{H}$ for the parameters employed in Figure 5.4 is faithfully reproduced by an effective gauge-invariant Hamiltonian $\hat{H}_{\text{eff}}$. The latter is extracted numerically by projecting the time-evolution unitary propagated by $\hat{H}$, for some evolution interval $\delta\tau$, onto the gauge-invariant color-singlet subspace, $\hat{\mathcal{P}}_G e^{-i\hat{H}\delta\tau}\hat{\mathcal{P}}_G \approx e^{-i\hat{H}_{\text{eff}}\delta\tau}$, where $\hat{\mathcal{P}}_G$ is the corresponding projector. An optimal value for $\delta\tau$ is then found in the range $1/J \ll \delta\tau \ll J/t^2$ at which the dynamics of both models show very good quantitative agreement, which allows constructing the matrix elements of $\hat{H}_{\text{eff}}$. We find that $\hat{H}_{\text{eff}}$ contains minimal coupling and plaquette terms, see Ref. [P9] for details, which is a very significant result given that the implementation of plaquette terms in proposals of large-scale quantum simulators of gauge theories face severe experimental limitations [233, 234].
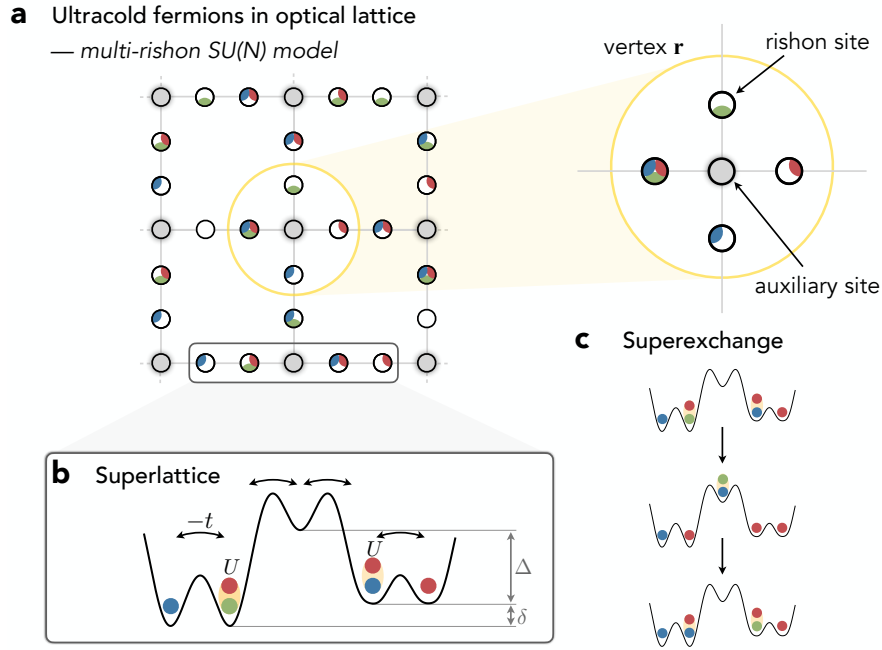
Figure 5.6: **Multi-rishon model. (a)** An arbitrary number of rishons encoded in fermionic alkaline-earth atoms are placed on rishon links formed by double-well potentials; here we illustrate an SU(3) case with colors red, blue and green, and three rishons per link. **(b)** The atoms can tunnel between neighboring sites with amplitude t and interact with on-site attractive Hubbard interactions $U < 0$. An optical superlattice prevents direct tunneling of rishons between different links by applying a potential offset $|\delta| \gg |t|, |U|$. Each rishon link is connected to an auxiliary site with large potential offset $|\Delta| \gg |t|, |U|$. **(c)** Fourth-order processes, in which atoms of neighboring links virtually occupy the auxiliary site and interact with Hubbard interactions, yield the desired equal-strength antiferromagnetic interaction between all sites connected to a vertex $\mathbf{r}$. Together with the on-site Hubbard interactions, the effective model includes all required building blocks to gauge-stabilize a multi-rishon-per-link SU(N) LGT, in which the dynamics is perturbatively induced by tunneling t within rishon links.

5.4   Multi-rishon-per-link models: SU(N) with alkaline-earth atoms.

The long-sought goal is the realization of SU(N) LGTs beyond one rishon per link and with fermionic matter. Now, we propose a possible scheme to implement the required gauge protection, which in principle enables the large-scale simulation of lattice QCD. In the multi-rishon regime, we cannot neglect the second term in Eq. (5.4) nor the fermionic statistics on rishon links. Hence, gauge protection requires a combination of on-site attractive Hubbard interactions $U < 0$ and antiferromagnetic interactions $J > 0$ around all sites adjacent to a vertex.

(i) We envision a scheme based on an SU(N) Fermi-Hubbard model of alkaline-earth atoms [235, 236] in an optical superlattice combined with tweezer arrays. As illustrated in Figure 5.6a, the rishon links are built from double-well potentials attached to an auxiliary

central site with potential offset Δ. The potential landscape with additional offsets δ be-between rishon links shown in Figure 5.6b, ensures the conservation of rishon number per link.

A fourth-order superexchange mechanism, where atoms can virtually occupy the auxiliary site, yields the desired SU(N)-invariant antiferromagnetic interactions around a vertex mediated by Hubbard interactions, see Figure 5.6c. Moreover, attractive Hubbard interactions $U < 0$ accommodate for the required on-site term in Eq. (5.4) and their strength is tunable via a Feshbach resonance. We note that the detuning Δ between the rishon and auxiliary sites allows to tune the sign of the superexchange J to obtain antiferromagnetic couplings.

To be precise, for the setup shown in Figure 5.6b we find effective fourth-order vertex terms given by

$$\hat{H}_{\text{eff}}^{(4)} = \hat{H}_{\text{AFM}} + \hat{H}_{\text{nn}}, \tag{5.8}$$

with

$$\hat{H}_{\text{AFM}} = \sum_{\mathbf{r},a} \sum_{b<a} J\left[\hat{n}_{(\mathbf{r},a)}, \hat{n}_{(\mathbf{r},b)}\right] \hat{\mathbf{S}}_{\mathbf{r},a} \cdot \hat{\mathbf{S}}_{\mathbf{r},b}, \tag{5.9}$$

$$\hat{H}_{\text{nn}} = \sum_{\mathbf{r},a} \sum_{b<a} V\left[\hat{n}_{(\mathbf{r},a)}, \hat{n}_{(\mathbf{r},b)}\right] \hat{n}_{(\mathbf{r},a)}\hat{n}_{(\mathbf{r},b)}. \tag{5.10}$$

The amplitudes J and V are weakly density-dependent because the energy difference to the virtual states depends on the number of rishons at a given rishon site through the interaction U. Nevertheless, all terms in Eq. (5.9) are SU(N) invariant.

The amplitudes are related by

$$V\left[\hat{n}_{(\mathbf{r},a)}, \hat{n}_{(\mathbf{r},b)}\right] = \frac{1}{2}J\left[\hat{n}_{(\mathbf{r},a)}, \hat{n}_{(\mathbf{r},b)}\right]\left(\frac{1}{N} - 1\right), \tag{5.11}$$

which gives the well-known $V = -J/4$ density-density term of the $t-J$ model for $N = 2$ [112]. The strength J scales as $\propto t^4/\Delta^3$, and we require that

$$J = -2NU/(1+N) \tag{5.12}$$

for the on-site Hubbard interaction, Eq. (5.4). Therefore, we require the Hubbard interaction to be small $|U| \ll |\delta|, |\Delta|$. In this limit, we can expand the AFM interaction $J\left[\hat{n}_{(\mathbf{r},a)}, \hat{n}_{(\mathbf{r},b)}\right]$ in the small $|U|$ and obtain the density-independent coupling strength

$$J = \frac{16t^4\left(36\Delta^2 - 5\delta^2\right)}{\left(\delta^2 - 4\Delta^2\right)^3}U + \mathcal{O}\left(U^2\right). \tag{5.13}$$

The desired gauge protection term can be constructed by choosing a set of parameters (t, U, δ) and finding Δ such that Eq. (5.12) is fulfilled.

Therefore, the gauge protection term (5.4) can be engineered using a fourth-order superexchange mechanism. Additionally, the gauge invariant dynamics is again induced by weak perturbations given by the tunneling between rishon and matter sites in the optical

lattice. We emphasize that the proposed scheme is independent of the coordination number or geometry since the interactions are mediated through the on-site Hubbard interaction on the auxiliary site in contrast to the long-range dipole-dipole interactions described above. Moreover, $SU(N)$ color charges can be conceptually easily included in this scheme by introducing a second layer, where atoms are located on matter sites connected to the auxiliary site of its corresponding vertex.

(ii) Another approach to realize multi-rishon models are hybrid analog-digital fermionic quantum processors [61, 62, 237], which potentially allow for much stronger interaction scales than the superexchange-based scheme [238]. In these platforms, fermionic atoms are trapped in optical tweezers that are spatially rearranged throughout the quantum simulation. A combination of interaction and tunneling gates can then realize the desired Hamiltonian we propose here with protection and perturbation terms, respectively. The arbitrary connectivity enables to include fermionic, dynamical matter or implement models beyond $(2+1)$D.
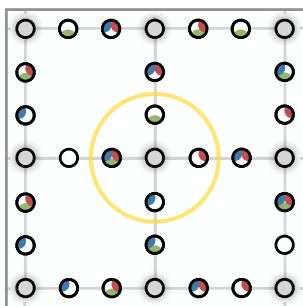
6

Perspectives for quantum simulation of LGTs

Phase diagrams of strongly correlated gauge theories remain elusive. With experimental large-scale implementations of LGTs in $(2+1)$D coming into reach, there is a need for new theoretical and numerical tools. This includes to rigorously map out ground-state phase diagrams, to develop phenomenological models of bound states and their excitations, and to propose new experimentally accessible observables. It is worth highlighting that the phases of gauge theories typically refuse to be described through local order parameters. Instead, to distinguish the phases tools such as Wilson loops [26], string order parameters [51, 197] or percolation [P12] are used. Consequently, the utilization of single-site resolved quantum simulators is anticipated to be of particular advantage in this context.

The advent of tuneable realizations of LGTs with dynamical matter holds promise to address long-standing questions, such as confinement of gauge charges in Abelian and non-Abelian settings. Most likely, first experimental realizations will focus on the application of quench protocols [15] necessitating to develop dynamical observables capable of capturing phenomena such as charge confinement. In addition, in a high-energy quench the entire spectrum is accessed, which may contain useful information yet to be harnessed.

For the bigger picture, it is important to understand whether one specific approach to simulate gauge theories proves to be more feasible than others, see Section 2.2.5. This knowledge is crucial for the development of experimental schemes with fermionic matter and in $(3+1)$D. In particular, it remains challenging to engineer strong plaquette interaction terms in a non-perturbative fashion. One promising route is to induce strong plaquette terms by the motion of dynamical matter, which has been shown to give rise to plaquette interactions on the scale of tunneling t in a specific setting [139]. The strong plaquette terms are necessary to stabilize exotic, quantum spin liquid phases with technological relevance in the field of topological quantum computation [29, 239].

In conclusion, the quantum simulation of LGTs is significant for both foundational science as well as for technological applications, ranging from particle physics [26] to high-

Tc superconductivity [20]. The forthcoming exploration of LGT building blocks, and the subsequent scaling to larger systems, opens up a new frontier in both experimental and theoretical quantum many-body physics. This effort promises to bridge the gap to other cutting-edge technologies, including particle colliders.

PART II

EMERGENT PAIRING MECHANISMS IN FERMI-HUBBARD MODELS

7

Summary and Overview

THE OBSERVATION of high-temperature (high-Tc) superconductivity by Georg Bednorz and Karl Müller in 1986 [135] was the discovery of a class of materials – the cuprates compounds – which resisted and still resist any type of conventional modelling in many ways until today [39]. The cuprates exhibit a sequence of strongly correlated phases as the chemical composition of the material is changed, which modifies the electron density in the two-dimensional copper-oxide layers. At half filling a well-understood antiferromagnetic (AFM) Mott insulator with one electron per lattice site is realized [31], see Figure 7.1. As the system is doped away from the Mott insulator, experiments have revealed uncommon signatures, whose microscopic origin is still controversially discussed in the theoretical community [31, 39, 44, 240].

The paradigmatic phase diagram of these materials has a dome-like region of superconductivity across a doping range of about 20%, as shown in Figure 7.1; here doping $\delta > 0$ ($\delta < 0$) refers to additional holes (electrons) relative to half filling. Remarkably, cuprate compounds with critical Tc's well-above the boiling point of liquid nitrogen have been synthesized [39]. Measurements of the Knight shift [241] and on the flux quantization [242] corroborate the picture of Cooper pair (charge 2e) condensation familiar from the Bardeen-Cooper-Schrieffer (BCS) theory of superconductivity [243]. In contrast to conventional electron-phonon BCS superconductors, however, measurements on phase sensitive superconducting quantum interference devices (SQUID) observe a superconducting order parameter with nodal $d_{x^2-y^2}$ symmetry [38] resulting in a vanishing superconducting gap at the *nodal* points $\vec{k} = (\pm \pi/2, \pm \pi/2)$ [244]. These experimental facts suggest an unconventional pairing symmetry with a condensation of Cooper pairs in the $d_{x^2-y^2}$ spin singlet channel [245].

The electron-phonon interaction is believed to be too weak to explain the high critical Tc's [251]. Approaching the dome from the overdoped side, see Figure 7.1 (right), weak-coupling BCS mean-field descriptions are able to explain the *d*-wave attractive in-
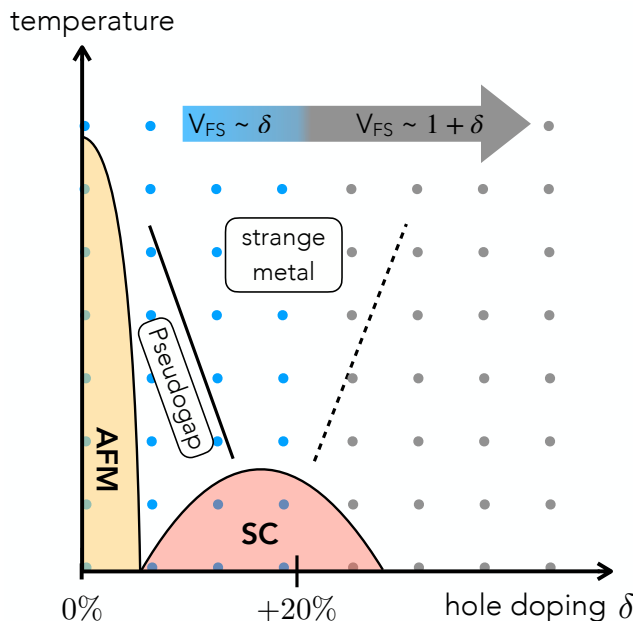
Figure 7.1: **Sketch of the cuprate phase diagram.** By changing the chemical composition of the material, the number of hole dopants δ is varied. At optimal doping, a nodal d-wave superconductor with remarkably large critical Tc's is experimentally observed. One of the many controversies in the cuprate community is about the nature of the parent state under which superconductivity emerges in the underdoped regime, i.e., its interplay with the pseudogap and antiferromagnetism (there are more phases such as a charge-density wave or a stripe phase not illustrated here [31, 39, 246]). In the underdoped regime, the Fermi surface is distinctly different from the electron-like Fermi surface in the overdoped regime (gray dots). At very low doping (blue dots), small hole pockets with volume $\propto \delta$ are observed in ARPES experiments [247, 248]. Further, quantum oscillation [249] and Hall coefficient [250] measurements suggest a Fermi surface of holes between half filling and optimal doping. In this thesis we develop a phenomenological model for Cooper pairing starting from magnetic polarons consistent with the hole-like constituents [P11, P7].

teractions [245, 252–254], where the AFM spin interactions give rise to pairing between the underlying electrons. This establishes the picture that magnetic pairing is responsible for nodal $d_{x^2-y^2}$-wave superconductivity in the limit of weak interactions [245, 252, 255–258].

In contrast, the underdoped side remains considerably less understood [31], yet it is widely believed that magnetic interactions similarly play a central role [259], see Figure 7.1 (left). In underdoped cuprates, we recognize strong deviations to BCS mean-field theory, e.g., in measurements of the specific heat [260]. Most notably, finding an explanation for the absence of a conventional Fermi Liquid (FL) above the critical Tc – known as the pseudogap phase with its apparent violation of Luttinger's theorem – is likely to be one of the key missing pieces [244, 247, 261–265].

It was observed by Uemura [266], Emery and Kivelson [267] that preformed pairs may exist above Tc suggesting a phase ordering transition of those pairs. While this scenario is appealing because it is consistent with the phenomenology of the BEC-BCS crossover [10, 77, 268–272], the question about the microscopic origin of strong attractive interactions,

causing the preformed pairs to begin with, remains unanswered as Philip Anderson noted in his late years [251]:

Is there a glue in cuprate superconductors?

The difficulty to find a concise model for the origin of strong pairing is rooted in the controversy about the normal state. Therefore, the main focus of research is on the properties of the normal state, from which superconductivity emerges in the underdoped regime. Strong-couplings descriptions are needed with impressive contributions over the past decades. These contributions include fascinating and creative theoretical ideas that have not only opened entirely new fields of physics [262] but also established potential connections to emergent gauge theories [20, 44, 138, 273].

Quantum oscillation and Hall coefficient measurements shed light on the enigmatic dichotomy between under- and overdoped cuprates [249, 250]: the volume of the Fermi surface undergoes an abrupt change around optimal doping $\delta \approx 18\%$. This change in Fermi surface volume indicates a metamorphosis in the nature of charge carriers from an electron-like Fermi surface $V_{FS} \propto 1 + \delta$ (overdoped regime) to a hole-like Fermi surface $V_{FS} \propto \delta$ (underdoped regime) [247–250]. This suggests a picture of emergent hole-like charge carriers – the magnetic/spin polaron – in the low-doping regime, where the polaron is described by the properties of a single mobile hole impurity in the AFM Mott insulator. In Section 8.3, we briefly review the properties and formulations of the single-hole problem. One of the major achievements of this thesis is the proposal of a novel pairing mechanism based on emergent Feshbach resonances between polaron-type charge carriers, i.e., we propose a genuine strong-coupling pairing mechanism for underdoped cuprates. In our Feshbach model, we find robust $d_{x^2-y^2}$ pairing mediated by AFM magnetic interactions $J_\perp$ and next-nearest neighbour tunneling t'. Our study includes the analytical development of a two-channel formulation including the full structure of emergent meson-like parton bound states, see Chapter 9-10, consistent with a small Fermi surface volume.

The paradigmatic model, which is the starting point of many theoretical studies of strongly correlated electrons including the studies in this thesis, is the single-band Fermi-Hubbard model [112, 274] with nearest-neighbour tunneling t and on-site Hubbard interactions U. In the strong-coupling description, $U \gg t$, the model reduces to the t-J model described by a quantum Heisenberg antiferromagnet doped with mobile charge carriers, see Sections 8.1-8.2. The relevance of the Hubbard model in the description of cuprates was highlighted one year after the discovery of high-Tc superconductivity in the cuprate compounds, when Philip Anderson suggested his celebrated resonating valence bound (RVB) picture of superconductivity [31, 275]: Anderson argued that doping a quantum Heisenberg AFM gives rise to a quantum spin liquid [276] with deconfined spinon and chargon excitations naturally explaining the d-wave superconductivity. While numerical and experimental evidences for this picture are lacking [1] [279], it has been an inspiring perspective to study high-Tc superconductivity starting from doped quantum magnets [P1, P11, P7, 264].

---

[1] In the 1D system, spin-charge separation with deconfined excitations of mass $\propto t^{-1}$ (chargon) and $\propto J^{-1}$ (spinon) does exist [277, 278].

Indeed, countless studies on the Fermi-Hubbard model and its strong-coupling limit, the *t-J* model, have revealed to capture much of the phenomenology of the cuprate phase diagram [5, 280], see Figure 7.1, such as the antiferromagnetism [281, 282] or the weak-coupling nodal *d*-wave superconductor [245, 253, 254]. Recent state-of-the-art numerical studies, however, give valuable new insights into the plain-vanilla Hubbard model [283]: At parameters relevant for cuprate compounds, the ground state has charge-density wave order and superconductivity at commensurate fillings is found to be absent. This is challenged by a follow-up study [284] showing *d*-wave superconducting order by slight modifications of the band structure upon including next-nearest tunneling t'.

These findings not only demonstrate the sensitivity of the ground state with respect to model parameters, but suggest that the plain-vanilla single-band Hubbard model may not be sufficient as a theoretical model to describe the cuprates [285]. From a microscopic perspective, these materials are assembled by (weakly coupled) two-dimensional Cu-O layers with a three site unit cell and copper (oxygen) atoms on sites (links) of a Lieb lattice. It was argued by Zhang and Rice [286], that the electrons form local spin singlets effectively reducing the three-band to a single-band Hubbard model, further corroborating the approach by Anderson [275]. The extent to which additional terms, such as density-assisted or next-nearest neighbor tunneling, contribute is currently under active investigation [287]. Despite open controversies about the correct description of the cuprate superconductors, the fact that the Hubbard model captures the broad phenomenology of many strongly correlated phases of matter cannot be overstated. Because of its importance in condensed matter physics, the Hubbard model is often called the "Ising model of interacting electrons" [285].

Soon after the first optical lattice experiments with ultracold bosons [41, 42], the relevance of analog quantum simulation of the Fermi-Hubbard model was pointed out by Duan, Demler and Lukin [60]. Impressive experimental advances in the field of ultracold atoms achieved to prepare systems at temperatures below the magnetic interaction scale $J = 4t^2/U$ allowing to enter the antiferromagnetic regime [288, 289] and opening the door to explore doped quantum magnets [P1]. Especially, the technique of quantum gas microscopy [290, 291] offers access to single-site and spin-resolved snapshots [2] of the many-body wavefunction in the Fock state basis. Over the past decade, analog quantum simulators have made unaccountable, significant contributions to our modern understanding of the Hubbard model.

It is this quantum simulation perspective that is the guiding principle of the studies underlying this thesis. (1) The two-channel model of Feshbach-induced pairing is motivated by the internal structure of charge carriers in the very low-doping regime. This internal meson-like structure of parton bound states was directly imaged by quantum gas microscopes for the first time [33]. In Chapter 9 and 10, we formulate the Feshbach hypothesis for high-Tc in cuprate superconductors [P5] and develop the theoretical framework for meson scattering [P7]. (2) In order to enhance the pair binding energy, we have proposed cold-atom motivated schemes based on mixed-dimensional settings [P2] and analyzed their finite doping mean-field phase diagram [P1]. The developed, theoretical formalism now appears to potentially play a significant role for recently discovered pressurized nickelate superconductors [P10, P6], summarized in Chapter 12. (3) Lastly, we extend the exploration

of doped quantum magnetism to a new platform [P8]: tweezer arrays. By leveraging three internal levels, it allows us to propose schemes to implement antiferromagnetic, bosonic t-J models in either cold molecules or Rydberg atoms. Preliminary experimental results of our proposed scheme realized in Rydberg tweezer arrays are presented in Chapter 11.
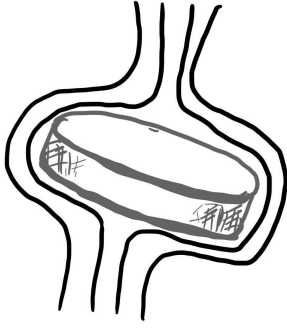
8
Theoretical Background

8.1 The Fermi-Hubbard model

With the experimental discovery of high-temperature superconductivity in cuprates [135], theoretical physicists needed to find a suitable model that would capture the observed phases of electrons. The paradigmatic model, which is believed to contain the phenomenology of a variety of strongly correlated electron systems, is the Fermi-Hubbard model [274]. The Hubbard model is a tight-binding description of electrons in a lattice with "narrow bands" [274]. If the electronic wavefunction is strongly localized in the orbitals of the crystal atoms, as it appears to occur in d- and f-orbital systems, the Coulomb repulsion $\propto U$ plays a dominant role with respect to the kinetic energy $\propto t$. While this Coulomb interaction is long-ranged $\propto r^{-1}$, the screening of the electromagnetic potential due to mobile charge carriers leads to an exponential decay in the Coulomb potential, and thus Coulomb interactions are typically neglected beyond the on-site term. This results in a seemingly innocent mathematical description of the Hubbard model given by

$$\hat{H}_{\mathrm{FH}} = -t \sum_{\langle i,j \rangle, \sigma} \left(\hat{c}^{\dagger}_{i,\sigma} \hat{c}_{j,\sigma} + \mathrm{h.c.} \right) + U \sum_{j} \hat{n}_{j,\uparrow} \hat{n}_{j,\downarrow}, \tag{8.1}$$

where $\hat{c}^{\dagger}_{j,\sigma}$ ($\hat{c}_{j,\sigma}$) creates (annihilates) a fermion with spin $\sigma = \downarrow, \uparrow$ at site j. The kinetic energy $\propto t$ is described by a tight-binding model with tunneling on nearest-neighbour sites $\langle i,j \rangle$. The Hubbard interaction $\propto U$ describes the on-site repulsive (attractive) interaction $U > 0$ ($U < 0$) and $\hat{n}_{j,\sigma} = \hat{c}^{\dagger}_{j,\sigma} \hat{c}_{j,\sigma}$ is the number operator. Extensions of the Hubbard model include modifications of the band structure, e.g., next-nearest neighbour (NNN) tunnelings t' [284], or beyond on-site Hubbard interactions (extended Hubbard models) [78].

In the strong-coupling limit $U \gg t$ relevant for cuprate superconductors, the Hubbard interaction cannot be treated perturbatively. A plethora of studies is dedicated to determine the ground state of the 2D square lattice Fermi-Hubbard model for different hole

dopings δ [240, 292], see Figure 7.1. In general, the ground-state phase diagram for a typical coupling strength $U/t = 8$ and away from half filling remains debated [240].

The Hubbard model features various symmetries, such as a U(1) symmetry for each spin species, a SU(2) symmetry generated by the Pauli spin-1/2 algebra and a particle-hole symmetry, among other symmetries. The success of the Hubbard model is due to the many physical phenomena it contains including the interplay between charge order and quantum magnetism, relevant for a variety of condensed matter systems. A few examples are the following: (i) A weak-coupling Random Phase Approximation (RPA) captures the charge and AFM spin ordering of fermions [282] observed in experiments [289]. (ii) In the limit of $U \to \infty$, Nagaoka proved that the ground state close to half filling is ferromagnetic [293–295]. (iii) Lieb's theorem states that the ground state of the repulsive Hubbard model at half filling is a total spin singlet [296]. (iv) Ultracold atom emulators of the Fermi-Hubbard model observe unconventional transport properties at relatively high temperatures [297].

Notably, many of the qualitative aspects of the phase diagram of cuprates, such as the AFM Mott insulator close to half filling, is captured by the Fermi-Hubbard model. Even more, at large doping or weak coupling a BCS mean-field analysis finds a $d_{x^2-y^2}$ nodal superconductor [254], and numerical simulations at commensurate low filling and strong coupling report a competition between stripe phases and d-wave superconducting order [283, 284]. Nevertheless, the region of small but finite doping remains a controversy in the strong-coupling limit $U \gg t$. In this limit, the effective low-energy properties are described by the t-J model introduced in the next section.

8.2   Strong-coupling description: t-J model

Let us consider the classical energy landscape of the Hubbard model for $t = 0$. The lowest energy manifold is given by the configurations, which fulfill $\sum_\sigma \hat{n}_{j,\sigma} \leq 1$ for all j. Above this energy $E = 0$ manifold, we find an extensive number of so-called Hubbard bands separated by the Hubbard energy U corresponding to the number of doublons (= doubly occupied sites) in the system. At strong coupling $U \gg t$, it is convenient to derive an effective low-energy theory in the subspace with no doublons. To this end, we define the Gutzwiller projector $\hat{\mathcal{P}}_G$ to be the projector onto the subspace constituted by states with $\sum_\sigma \hat{n}_{j,\sigma} \leq 1$ for all j.

The goal is to derive a low-energy effective theory by treating the tunneling t perturbatively and by applying a Schrieffer-Wolff transformation [168]. This unitary transformation $e^{\hat{S}}$ rotates the basis into a new "dressed" basis, in which all first order couplings between manifolds are removed, allowing for a controlled approximation in t/U. In the dressed basis, the interacting Hamiltonian is given by

$$\hat{H} = e^{\hat{S}} \left(\hat{H}_U + \hat{H}_t \right) e^{-\hat{S}} \tag{8.2}$$

$$= \hat{H}_U + \hat{H}_t + [\hat{S}, \hat{H}_U] + \frac{1}{2}[\hat{S}, [\hat{S}, \hat{H}_U]] + \frac{1}{2}[\hat{S}, [\hat{S}, \hat{H}_t]] + ..., \tag{8.3}$$

where we have separated the Hubbard model (8.1) into its kinetic $\hat{H}_t$ and interacting $\hat{H}_U$ part. In the second line, we have used the Baker-Campbell-Hausdorff identity. The re-

quirement that first order couplings between manifolds have to vanish, yields an defining equation for $\hat{S}$ of the form

$$\langle\delta|\hat{S}|\gamma\rangle = \frac{\langle\delta|\hat{H}_t|\gamma\rangle}{E_\delta - E_\gamma} \tag{8.4}$$

with states γ, δ in different energy subspaces. Importantly, the generator $\hat{S}$ scales as t/U making it suitable as a perturbative expansion coefficient in Eq. (8.3). Here, we want to derive the effective Hamiltonian in the low-energy subspace including terms of order $\mathcal{O}(t^2/U^2)$. To this end, we truncate the expansion as in Eq. (8.3) and use the Gutzwiller projectors $\hat{\mathcal{P}}_G$, such that

$$\hat{H}_{t-J} = \hat{\mathcal{P}}_G\hat{H}_t\hat{\mathcal{P}}_G + \frac{1}{2}\sum_\delta \hat{\mathcal{P}}_G \frac{\hat{H}_t|\delta\rangle\langle\delta|\hat{H}_t}{E_\delta - E_\gamma}\hat{\mathcal{P}}_G. \tag{8.5}$$

The first term describes tunneling of particles, if and only if the tunneling does not create doublons. The second term has to be evaluated [112] in second-order perturbation theory and contains information about the low-energy effective spin interactions. In particular, we find

$$\hat{H}_{t-J} = \hat{H}_t + \hat{H}_J + \hat{H}_{3-s} \tag{8.6}$$

$$\hat{H}_t = -t\sum_{\langle i,j\rangle,\sigma} \hat{\mathcal{P}}_G\left(\hat{c}^\dagger_{i,\sigma}\hat{c}_{j,\sigma} + \text{h.c.}\right)\hat{\mathcal{P}}_G \tag{8.7}$$

$$\hat{H}_J = J\sum_{\langle i,j\rangle}\left(\hat{\mathbf{S}}_i\cdot\hat{\mathbf{S}}_j - \frac{1}{4}\hat{n}_i\hat{n}_j\right) \tag{8.8}$$

$$\hat{H}_{3-s} = -t_{3s}\sum_{\substack{\langle i,j\rangle,\langle i,j'\rangle \\ j\neq j',\sigma}}\left(\hat{c}^\dagger_{j',\sigma}\hat{n}_{i,\bar{\sigma}}\hat{c}_{j,\sigma} + \hat{c}^\dagger_{j',\sigma}\hat{c}^\dagger_{i,\bar{\sigma}}\hat{c}_{i,\sigma}\hat{c}_{j,\bar{\sigma}} + \text{h.c.}\right) \tag{8.9}$$

with the SU(2) symmetric AFM superexchange $J = 4t^2/U$ and the 3-site tunneling term $t_{3s} = t^2/U$ [112, 298].

Therefore, we have derived a low-energy effective theory that captures the antiferromagnetism in the Fermi-Hubbard model. Intuitively, we can understand this by comparing configurations with aligned and anti-aligned spins. If two spins on adjacent sites are aligned, the Pauli blocking of fermions quenches the kinetic energy. In contrast, if two spins on adjacent sites are anti-aligned, the system can gain kinetic energy by virtual tunneling processes into doublons.

The 3-site term introduces density- and spin-exchange-assisted tunneling between NNN sites. However, it is often neglected in the study of the *t-J* model and its effect on the ground state is unclear and receives little attention [5]. Previous studies have indicated tendency for nematic $s + id$ superconducting order in the presence of the 3-site term [299]. With recent numerical studies indicating the importance of NNN tunneling terms [283, 284] for superconducting correlations in the Fermi-Hubbard model, the study of the three-site term may experience a renaissance.

For the purpose of theoretical and numerical studies of doped quantum magnets, the

t-J model serves as a useful effective model with a reduced local Hilbert space dimension because the doublons have been integrated out. In the strong-coupling limit ($U/t \gg 1$), the perturbative expansion gives rise to a separation of coupling strengths with $t \gg J, t_{3s}$. For cuprate compounds, a representative set of parameters is given by $t \approx 3J$ [300, 301]. Beyond that, the *t-J* model is often used as one of *the* paradigmatic models in the study of strongly correlated electrons and couplings are often arbitrarily modified. For example, in the regime $J/t \gg 1$ there is conclusive numerical evidence of phase separation between holes and spins [302]. Further, it can be useful to study the *t-XXZ* model, where the Heisenberg interaction $\hat{H}_J$ is replaced by an AFM XXZ Hamiltonian, in order to investigate the role of spin fluctuations [21, 303]. Very recently, the realization of a tunable fermionic *t-J* model in ultracold molecules trapped in an optical lattices was reported in Ref. [304]. In Chapter 11, we propose a scheme for the analog quantum simulation of an antiferromagnetic, *bosonic t-J* model in three-internal levels of cold molecules or Rydberg tweezers with tunable interactions [P8].

8.3 Single-hole problem

Superconductivity in the cuprate compounds arises upon doping the AFM Mott insulator away from half filling [31] with either holes or electrons[1]. On the hole doped side, it was observed that approximately 4% of dopants are sufficient to open a superconducting gap [248]. The critical Tc follows a dome shaped curve as doping is increased with an optimal doping at about $15 - 20\%$ [39]. It is therefore of fundamental importance to understand the properties of charge carriers (dopants) and their interplay with AFM order in the strong-coupling regime [31]. At very low doping, the quasi particle associated with the mobile charge carrier in the AFM background is called a magnetic polaron [21, 35, 36, 305–308]. The spin correlations play a crucial role for the properties of the polaron: for a ferromagnetic background, the dopant can move freely without disturbing the spin order, while for the antiferromagnetic background the motion of holes disturbs and frustrates the AFM order, see Figure 8.1.

However, a microscopic theoretical and numerical study of this question at finite doping is yet too challenging. Therefore, microscopic studies have almost exclusively focused on the single-hole problem and its phenomenological extension to finite doping, but it remains hard to conclude at which level of doping the single-hole description of the magnetic polaron breaks down [309]. This is further obstructed by the difficulty to make clean samples of cuprates in the ultra low doping regime, but with recent progress in layered $Ba_2Ca_5Cu_6O_{12}(F, O)_2$ precise measurements in this regime are coming within reach [248]. Moreover, a new perspective emerges with the advances in ultracold atom experiments, see Chapter 2.1. These experiments can directly probe a single hole doped into a Mott insulator with single site resolution [7, 33]. Studies of the Fermi-Hubbard model across the doping regime have reported that the magnetic polaron description may be valid over a larger range of dopings than previously anticipated [309] by evaluating higher-order correlators

---

[1]In the plain vanilla square lattice Hubbard model, it follows from particle-hole symmetry that electron and hole doping is equivalent.
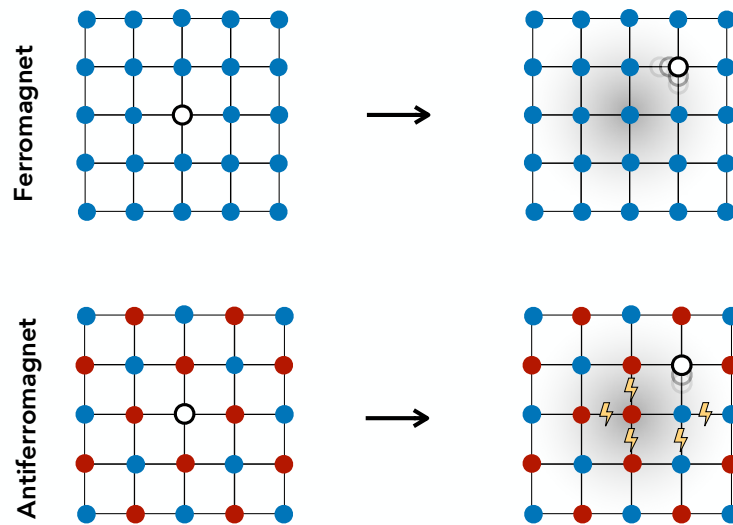
Figure 8.1: **Doped quantum magnets.** The interplay between mobile hole dopants and spin interactions is a highly complex problem. Here, we sketch the effect of introducing a single hole into a quantum magnet. In the ferromagnetic background (top), the hole motion is described by a quantum walk and it propagates ballistically. This is in stark contrast to the antiferromagnet (bottom): The properties of the motion of a single hole is highly correlated with the spin background. The hole's motion rearranges the spin background and introduces frustration, as studied first by Bulaevskii et al. [305].

characteristic of the magnetic polaron [21, 310].

Numerous analytical and numerical studies have contributed to our today's understanding of a single hole doped in an AFM Mott insulator [31]. Here, we want to give a crisp overview and highlight a few out of many excellent studies on the topic. The single-hole problem was studied as early as 1968 by **Bulaevskii et al.** [305]:

As the electron moves away from the center, flipped spins appear on its trajectory, and the exchange energy increased with lengthening of the trajectory. This can be interpreted as the existence of a quasi-elastic force that tends to return the extra electron to the center.

From our modern perspective, this phenomenology had already correctly described the core of problem. The dopant's motion leaves behind a *trajectory* of flipped spins and thus a history of its path is encoded in the disturbed spin background, see Figure 8.1 (bottom). The AFM spin interactions, responsible for the spin order to begin with, induce a *quasi-elastic force* between both ends of the trajectory. The object associated with the trajectory shall be called a *string* in consensus with modern literature. Around the same time, **Brinkman and Rice** likewise formulated an effective model based on string states on a Bethe lattice [306] leading to the picture of localized holes due to the confining string. In their picture, the hole retrieves mobility by a Brownian motion induced by scattering off the background electrons. An approximate evaluation of the single-particle Green's function showed the reduced bandwidth of the hole.

Trugman then generalized the string picture and included previously neglected loop effects [311, 312]. When the hole traverses the AFM background one and a half times around

a square plaquette, the spin background is restored but the hole has moved along the diagonal of the lattice restoring its mobility in a higher order process. This is in contrast to the localization effect due to the string's tension. Therefore, in his conclusions he states *that contrary to expectations, a hole in an antiferromagnet is not bound by a string* [311]. Nevertheless, in later studies Trugman identifies the excitation spectrum of the single hole with excitations of the string [312].

Simultaneously, theoretical and numerical studies on the single-hole problem were performed starting from a spin-wave analysis, where the hole's motion is coupled to the spin waves. Thus, this ansatz is unbiased with respect to the string picture. **Kane, Lee, Read** [313] and **Sachdev** [314] find that the single hole has a dispersion minimum at $\vec{k} = (\pi/2, \pi/2)$, which is an important results in the context of solid state experiments. The minimum of the dispersion is consistent with the later detected hole pockets observed in ARPES measurements on the cuprates [247, 248]. Theoretical studies further find the bandwidth of the hole to scale with the magnetic spin interaction, $J \ll t$, suggesting the picture of a spin polaron. Within this thesis, we use the dispersion relation obtained by **Martínez and Horsch**,

$$\varepsilon_{1\text{hole}}(\vec{k}) = A[\cos(2k_x) + \cos(2k_y)] + B[\cos(k_x + k_y) + \cos(k_x - k_y)], \qquad (8.10)$$

where $\vec{k} = (k_x, k_y)$ is the momentum of the hole and A, B are fit parameters; for realistic parameters in cuprates compounds $t/J = 10/3$, the fit parameters are $A = 0.31J$ and $B = 0.44J$ [315].

In addition, in the limit $J_\perp \to 0$ the spin-wave ansatz predicts long-lived spectral excitation peaks gapped by $t(t/J_z)^{2/3}$, which is consistently reported in the study of the single hole [313]. These findings have been confirmed by numerous numerical studies in the 1990s and we refer to Refs. [21, P11, 316] for more detailed discussions. The relation between the excitation spectrum and the string picture was formally established by **Liu and Manousakis** [317, 318]. By describing the hole as a particle confined by a linear string potential, they find bound states with energy

$$E_n/t = -2\sqrt{3} + a_n(J_z/t)^{2/3} \qquad (8.11)$$

in the t-J_z model; a_n is a geometry dependent constant. Therefore the string picture correctly captures the scaling relation of the energy spacing between quasiparticle excitation peaks reported in numerical studies [313], and interprets the excitations as vibrational excitations in the linear confining potential.

It was **Béran, Poilblanc and Laughlin** who recognized and resolved an apparent dichotomy [32]: while some properties scale with J – e.g. the dispersion relation – others scale with t – e.g. the Drude conductivity. This is not consistent with the spin polaron picture, where the hole is completely described by its dressing with the spin waves. This led them to the **parton picture** of the single hole. In this scenario, the hole with quantum numbers spin and charge decays into its fractional constituents, the spinon (s) and chargon (c), which form a bound state as a consequence of the confining string potential. Thus, the composite (sc) particle maintains both characteristic energy scales of the chargon tunnel-

ing $\propto t$ and spinon motion $\propto J$. Even more, they interpreted the string excitation spectrum as excitation of the bound state in analogy to meson excitations.

The string picture of bound partons [32] is challenged by **Anderson**'s RVB paper [275]. In stark contrast, Anderson proposed a scenario of deconfined spinons and chargons. He argued that upon doping the Heisenberg AFM the system's ground state evolves into a quantum spin liquid of resonating singlets with the deconfined, fractionalized excitations. Further, he derived that the Gutzwiller projected wavefunction gives rise to a BCS wavefunction of the chargons. Can these two extreme pictures of either spin-charge separation or spin-charge bound states be brought together? In fact, it is the parton picture, which naturally draws the intriguing connection between doped quantum magnets and gauge theories with their confined and deconfined phases [32], see Part I Chapter 1.

A phenomenological model with predictive power – combining both the parton and string picture – was developed by **Grusdt and Demler** and co-workers [21, 36, 303, 319]. In this picture the two partons, i.e., spinons (s) and chargons (c), are connected to the two ends of a geometric string, which encodes the history of the chargon's path through the AFM. In the limit of $t \gg J$, the confining string potential gives rise to a bound state between a light chargon and heavy spinon. In the $t\text{-}J_z$ model, the string description becomes exact and the motion of the bound state is only determined by the Trugman loops [311]. When spin flip-flop interactions $J_\perp$ are increased [303], the composite object disperses with the spinon motion $\propto J_\perp$ and numerical simulation of the the $t\text{-}J$ model confirmed the validity of the (sc) bound state, or magnetic polaron [316].

Further striking evidence of the parton theory of the magnetic polaron has been reported in quantum gas microscope experiments of ultracold fermions in optical lattices emulating the Fermi-Hubbard model [33]. **Koepsell et al.** measured the spin correlations in the vicinity of a mobile dopant at relatively high temperatures $k_B T = 0.45t$ and compared their data to theoretical predictions obtained from the geometric string model finding good agreement. In addition, signatures of the magnetic polarons are found up to about 30% hole doping [309].

Beyond ground-state correlations, the geometric string framework allows to predict the excitation spectrum of the (sc) bound state, i.e., the magnetic polaron acquires an *internal* structure. In the co-moving frame with the heavy spinon, the chargon's motion is described by a particle hopping on a Bethe lattice with corresponding C4 symmetry of the underlying square lattice and emergent C3 symmetries of the string description. These angular symmetries manifest in the bound state's wavefunction facilitating the calculation of the ro-vibrational meson excitation spectrum [21] envisaged by Beran et al [32]. Significantly, angular momentum-resolved ARPES spectra obtained from time-dependent DMRG studies of the $t\text{-}J$ model have revealed the presence of Regge-like trajectories [320] as predicted from the meson spectrum. Notably, the ARPES spectra within the parton framework is equivalent to the spectra of the underlying "c" electrons [316]. We emphasize that it is within the parton picture that properties such as rotational spectra find a particularly natural description. We refer to Section 10.1.2 for a formal semi-analytical description of the parton string theory.

Lastly, we emphasize that after the discovery of high-Tc superconductivity in the

cuprates, **Trugman** [311] and **Manousakis** [35] have studied a potential pairing mechanism of holes in the string picture, where two holes are connected by a confining string of flipped spins. In the d-wave pairing channel this leads to a tightly-bound, bosonic bi-polaron [36, 37]. In Chapter 9, we argue that the cuprate's fermionic ground state does not suggest tightly-bound BEC pairs to constitute the superconducting state. Instead, we propose the tightly-bound pairs to exist as a long-lived, low-lying resonant state. We find that the internal, mesonic structure of different parton bound states gives rise to an emergent Feshbach resonance with pairing of charge carriers in the $d_{x^2-y^2}$ channel. We propose the emergent Feshbach resonance as a scenario for strong pairing in cuprates [P11].

8.4   Pairing mechanisms in underdoped cuprates

The mechanism behind text book BCS-type superconductors is the electron-phonon interaction causing an instability of the Fermi surface [243]. **Fröhlich** derived a model for electron-electron interaction mediated by exchange bosons, i.e., the phonon, which can lead to an attraction of electrons [321]. However, it was not apparent how this attraction could overcome the repulsive Coulomb interactions. It was **Bardeen and Pines** who treated both the screened Coulomb and the electron-phonon interaction on equal footing [322]. The resulting Bardeen-Pines effective electron-electron interaction [254],

$$V(\vec{q}, \nu) \propto \frac{1}{\vec{q}^2 + \kappa^2} \left[1 + \frac{\omega_{\vec{q}^2}}{\nu^2 - \omega_{\vec{q}^2}} \right], \tag{8.12}$$

is frequency ν and momentum $\vec{q}$ dependent. The Coulomb interactions are screened on the scale of the Thomas-Fermi length κ^{-1}. The electron-phonon interaction is highly retarded and, in fact, at low energies $\nu < \omega_{\vec{q}}$ the Coulomb repulsion is overscreened and the interaction $V(\vec{q}, \nu)$ becomes attractive; the energy scale is determined by the phonon dispersion $\omega_{\vec{q}}$. Ultimately, **Bardeen, Cooper and Schrieffer** (BCS) formulated a theory of superconductivity, which describes the consequence of attraction at low energies leading to pairing of electrons at the Fermi surface [243]. They received the 1971 Nobel prize for the development of their theory.

The theory of superconductivity heralded in a paradigm shift by unifying well-established facts into a phenomenological model and by putting forward a variational wavefunction of Cooper pairs. **Morel and Anderson** even predicted that *all metals should be superconductors, although those not observed to do so would have remarkably low transition temperatures* [323]. Importantly, the BCS mechanism is not dependent on the type of interaction; instead any attractive interaction can cause a BCS instability of the Fermi surface. For example, **Kohn and Luttinger** formulated a theory of unconventional superconductivity, where Friedel oscillations induce attractive interactions between electrons in purely repulsive models [324], however the expected critical temperatures from this effect do not explain the high critical Tc's observed in cuprates.

For models with strong repulsive interactions, such as the Hubbard model at strong coupling $U \gg t$, the situation is different to conventional BCS superconductors. The repulsive

core U for electrons at the same site cannot be screened, and electron-phonon interactions are believed to be too weak to overscreen the Coulomb repulsion [251]. Rather, the d-wave symmetry of the superconducting state suggests a different type of mechanism: The node in the relative wavefunction between charge carriers is another effective way to suppress repulsive Hubbard interactions U without dynamical screening.

The cuprate problem addresses the origin of the attractive interactions in the under-doped cuprate compounds [39], see Chapter 7. Hereby, a fundamental challenge is to formulate a genuine strong-coupling description of the normal state in the underdoped cuprates, and to complement it with a strong pairing mechanism of magnetic origin [259]. One such strong-coupling description starts by doping the AFM Mott insulator [31] and studying the properties of the single hole, see Section 8.3. Other strong coupling treatments include Anderson's RVB picture [275] or fractionalized Fermi Liquids (FL*) [44, 262–264]. Here, we give a very brief overview of magnetic pairing mechanisms, that we believe are most relevant to compare to our proposed two-channel Feshbach model, see Chapter 9.

Before the discovery of the cuprates, **Scalapino et al.** have suggested an exchange mechanism of paramagnons for the three-dimensional Hubbard model using a diagrammatic random phase approximation (RPA) at $U/t = 4$ [252, 255]. In the vicinity of an antiferromagnetic instability, the coupling to the paramagnon diverges leading to a strong pairing interaction in the $d_{x^2-y^2}$ channel rooted in the perfect nesting property of the square lattice Hubbard model. Simultaneously, the RPA approach shows the sensitivity of paramagnon exchange towards modifications in the band structure and away from half filling. **Monthoux, Balatsky and Pines** described the paramagnon exchange from a more phenomenological perspective of experimentally accessible spin fluctuations to describe superconductivity in the 2D square lattice. Similarly, they find attractive magnetic pairing interactions with $d_{x^2-y^2}$ symmetry [256].

Alternatively, a more microscopic picture of "spin bags" was developed by **Schrieffer, Wen and Zhang** [325]. In this model, the single dopant is argued to deplete the AFM order parameter locally creating a "bag" in which the hole is self-trapped. While the spin bag is advantageous for the energy of the hole, it has to be balanced to the energy cost of reducing the AFM order. Thus, it can be energetically favorable for two holes to populate the same spin bag leading to an effective attractive interaction that overcomes Coulomb repulsion. In Ref. [326] the pairing interaction with respect to the Fermi surface topology is studied, which can result in both nodal and nodeless d-wave superconductors.

Starting from the $SU(2)$ symmetry broken phase, **U. J. Wiese** and collaborators constructed a systematic low-energy effective theory for holes and magnons [327]. Their effective theory correctly describes the location of hole pockets centered around the nodal points $\vec{k} = (\pi/2, \pi/2)$ giving rise to two pockets in the magnetic Brillouin zone. For the case of two hole dopants, the effective potential mediated by one-magnon exchange is derived [328]. For intra-pocket bound states, i.e., zero center-of-mass pairs, the pairing interaction is found to have d_{xy} symmetry, while for inter-pocket magnon exchange $d_{x^2-y^2}$-wave pairing is found.

Despite numerous proposals for magnetic pairing in cuprate superconductors, the origin of strong pairing of charge carriers remains debated. The difficulty to find a phe-

nomenological model of pairing, similar to the Bardeen-Pines interaction (8.12) in conventional BCS superconductors, is rooted in the controversy about the enigmatic normal state above Tc in underdoped cuprates. In the following, we present a novel pairing mechanism for magnetic polarons by including the internal structure of meson-like parton bound states, see Section 8.3. The existence of a long-lived low-energy meson excitation found in numerical simulations of the t-J model [36, 37] leads us to the picture of emergent Feshbach resonances of parton bound states [P11, P7].
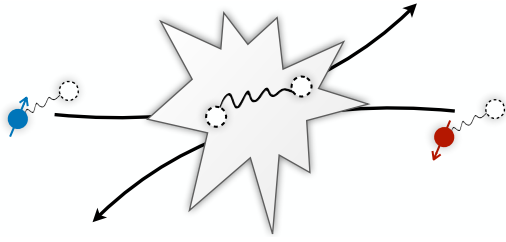
9

Feshbach hypothesis of high-Tc superconductivity in cuprates

THE ORIGIN OF STRONG PAIRING of charge carriers and the enigmatic relation between the various phases observed in underdoped cuprate superconductors remains highly debated [31, 39], see Chapters 7 and 8. While the electron-phonon mediated attraction alone is too weak to explain the high critical Tc's [251], there is a consensus about the magnetic origin of pairing confirmed by numerous theoretical and numerical studies [245, 255–258, 325, 328–330]. Recent scanning tunneling microscopy experiments further confirm the picture of magnetic pairing [259].

Nevertheless, a microscopic theory for pairing in underdoped cuprates is missing. Promising candidates for such a microscopic theory are demanded to be consistent with the common phenomenology of underdoped cuprates, such as the well-established $d_{x^2-y^2}$ pairing symmetry [38] or the pseudogap [244]. It is believed that the attractive interactions are *strong* compared to typical energy scales in conventional BCS superconductors. Not only the high critical Tc's indicate strong pairing, but rather the existence of two distinct energy gaps [331, 332] associate with two temperature scales T^* and T_c suggests that pairing of charge carriers appears above the critical temperature $T^* > T_c$. This is further corroborated by Uemura's [266], Emery's and Kivelson's [267] observation that incoherent pairs may form above T_c, which become phase coherent as the temperature is decreased. At the same time, this is familiar from the phenomenology in the BEC-BCS crossover [10, 77, 268–270]: As the attractive scattering length between fermionic constituents approaches the unitary regime, pre-formed pairs exist above the critical Tc. However, the scattering length is introduced as a phenomenological parameter to model the crossover from weak to strong pairing.

In this Chapter, we propose a novel microscopic mechanism for the origin of the strong attractive scattering length between charge carriers in Hubbard-type models at strong coupling: emergent Feshbach resonance. We start from the AFM Mott insulating state with

correlation length $\zeta_{\text{AFM}} \gg a$, where $a = 1$ is the lattice spacing. In the limit of very low-doping, it was found in theoretical [21, 35, 36, 303, 311], numerical [32, 34, 37, 320, 333] and experimental [33, 334] studies that the fundamental one- and two-hole excitations can be described as extended meson-like excitations with rich internal structure, see Chapter 7. The parton constituents, i.e., the chargon (c) and spinon (s), give rise to fermionic (sc) [magnetic polaron] and bosonic (cc) meson bound states. Eventually, the existence of such meson bound states leads us to the description of a Feshbach resonance between the an open channel $(\text{sc})^2$ and a tightly-bound (cc) meson.

A Fano-Feshbach resonance [71–73, 76], see Chapter 2.1, was introduced in the context of particle physics and describes the consequence of a bound state embedded in a particle continuum. A characteristic quantity, which determines whether the induced two-particle effective interaction is attractive (BCS side) or repulsive (BEC side), is the energy difference ΔE between the open and closed scattering channels. From the two particle perspective, a low-lying tightly-bound (cc) meson above the scattering threshold $\Delta E > 0$ gives rise to attractive interaction between a pair of magnetic polarons $(\text{sc})^2$. We argue that cuprate superconductors are clearly located on the BCS side of the Feshbach resonance but in the vicinity of a $d_{x^2-y^2}$ scattering resonance: The ground state of the underdoped cuprates is characterized by Fermi surface excitations [247], even in the very low-doping regime [248, 335]. Further, a Fermi surface of volume $\propto \delta$, is observed in quantum oscillations measurements [249, 250] consistent with our picture of fermionic, magnetic polarons (sc) in the ground state. It is the existence of the low-lying tightly-bound (cc) meson above but in the vicinity of the Fermi surface, which induces the strong pairing between fermionic constituents as discussed in the remained of this Chapter.

We highlight that Feshbach resonances, beyond particle and atomic physics, have sparked great attention over the past decade. In solid state materials a Feshbach resonance between excitons and trions was observed [336, 337] with recent proposals to utilize such Feshbach resonances for quantum simulation [338, 339]. Likewise, Feshbach resonances have been proposed to underlie the pairing mechanism in a broader class of strongly correlated materials [340, 341], including the recently discovered pressurized nickelate superconductors [P10, P6, 342]. In this vein, the goal of this chapter is to identify potential Feshbach scattering channels in underdoped cuprates, starting from a microscopic theory of the charge carriers. Using a semi-analytical description of the open and closed scattering channels, we derive selection rules for the scattering processes and find that the dominant scattering channel has $d_{x^2-y^2}$ symmetry. Importantly, we suggest experimental probes for solid state materials to search for the low-lying closed scattering channel, constituted by the charge 2e boson, in cuprate compounds.

The Chapter is based on publications [P11, P7]. The text and figures are rearranged, adapted and supplemented. While this Chapter introduces the **Feshbach hypothesis** and puts it in the perspective of cuprate superconductors, the subsequent Chapter 10 elaborates on the mathematical formulation of a two-particle, multichannel description of Feshbach resonances between magnetic polarons.

9.1   Single-hole and two-hole excitations

Our starting point is a weakly hole-doped parent state with strong local antiferromagnetism and a sufficiently large AFM correlation length $\xi_{AFM} \gg a$. In cuprates, this regime is believed to be realized below the pseudogap temperature, $T < T^*$ [330]. Charge carriers in this regime correspond to mobile holes and give rise to hole pockets, smoothly developing into Fermi-arcs [247], observed around the nodal points, $\mathbf{k} = (\pm\pi/2, \pm\pi/2)$, in angle-resolved photoemission spectroscopy (ARPES) [248] and by quantum oscillations [248, 250]. At low doping in the square lattice Hubbard model with large on-site interaction $U \gg t$, the individual holes are well described by magnetic polarons, as revealed by analytical [305, 306, 311, 313, 314, 343] and numerical studies [312, 317, 344–349], as well as experiments in solids [334] and recently in ultracold atoms [33], see Chapter 8.

In contrast, the two-hole excitation spectrum of the doped AFM is much harder to access experimentally and less understood theoretically. On the one hand, weak attraction between magnetic polarons, such as phonon- or magnon-exchange would suggest, could give rise to loosely bound Cooper-like pairs and would naturally lead to a BCS-type instability. On the other hand, numerical studies based on Hubbard and t-J models have indicated the existence of much more tightly bound pairs of holes [34, 307, 311, 350–352] with only small energy differences between different pairing channels [37, 308, 351]. Moreover, recent density matrix renormalization group (DMRG) studies of the t-J model reported the existence of long-lived two-hole resonances with distinct dispersion relations associated with different pairing symmetries [37]. The observed spectral features in that study can be explained by models of tightly bound holes connected with a string of displaced spins [36, 307] (light bi-polarons).

9.2   Feshbach hypothesis

To formulate our idea of Feshbach resonances, we need to describe in a common theoretical framework the individual fermionic charge carriers, which we model as magnetic polarons, and the tightly bound bosonic pairs. To this end, the parton picture provides a powerful construction, in which the fundamental constituents are decomposed into spinons (s) and chargons (c) [137, 354–356], see Figure 9.1a. Within this picture, magnetic polarons constitute a mesonic spinon-chargon bound state (sc) [32, 316] with a rich set of internal rovibrational excitations. Similarly, the tightly-bound two-hole states are viewed as mesonic chargon-chargon bound states (cc). Their internal rotational quantum numbers correspond to different pairing symmetries [36, 37, 307]. Among the evidence for the parton picture are numerical studies at low doping which have confirmed the predicted internal excitations [35, 279, 316, 320, 333] and effective masses of the mesons [32, 37].

Next, we discuss how the (sc) pairs (magnetic polarons) constituting the normal state in our model interact upon including a coupling to (cc) states. To this end, we consider an individual scattering event between two (sc) mesons with opposite spin. When they start
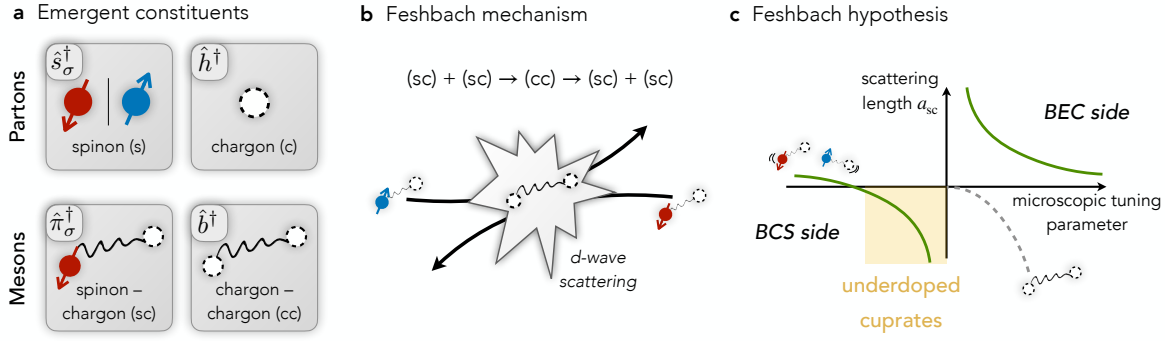
Figure 9.1: **Emergent Feshbach resonance. a** In the presence of strong AFM correlations, the emergent charge carriers can be described by partons, the spinon (s) and chargon (c), which form the meson bound states: fermionic (sc)'s and bosonic (cc)'s. If low-energy excitations in the ground state retain their fermionic character – as observed experimentally [247–249, 353] – the bosonic two-hole pairs must correspond to meta-stable excited states. This situation is familiar from the case of Feshbach resonances and in the context of two particles: on the BCS side, the tightly bound bosonic state is replaced by a low energy two-particle resonance. **b** In the low-energy scattering process between two (sc)'s with opposite spin, the mesons virtually recombine into an excited, light and tightly-bound (cc) bound state. Due to the mesons' internal structure, this process is dominated by $d_{x^2-y^2}$-wave scattering. **c** If the formation of a (cc) state is a resonant process, the scattering length diverges and yields strong effective interactions between the underlying (sc) mesons. In the Feshbach hypothesis we conjecture that the normal state of underdoped cuprates is constituted by fermionic (sc)'s, located on the BCS side and in the vicinity of the scattering resonance.

to overlap spatially, they can recombine into a virtual (cc) state, realizing the sequence

$$(\text{sc})_\uparrow + (\text{sc})_\downarrow \rightarrow (\text{cc}) \rightarrow (\text{sc})_\uparrow + (\text{sc})_\downarrow. \tag{9.1}$$

This naturally leads us to a two-channel description of the emergent (mesonic) Feshbach resonance, with $(\text{sc})^2$ defining the open- and (cc) defining the closed channel, respectively, see Figure 9.1b. As we will argue below, the scattering process is dominated by a resonant d-wave (cc) state in the doped Hubbard model.

This leads us to formulate the following hypothesis:

(i) Cuprates, as well as commonly used models of the latter, i.e., Fermi-Hubbard or t-J models at strong coupling, have a low-doping ground state close to a d-wave $(\text{sc})^2$-(cc) scattering resonance.

(ii) More specifically, underdoped cuprates are on the BCS side of the conjectured d-wave resonance, but sufficiently close for the induced attraction to overcome the intrinsic repulsion of two charge carriers in the (sc) channel.

This situation is illustrated in Figure 9.1c, where we took the liberty to include an effective microscopic parameter tuning the relative energy of (sc) and (cc) channels independently. In reality, changing microscopic model parameters always affects the structure of both (sc) and (cc) mesons. On the level of theoretical models, a nearest-neighbor (NN) Hubbard interaction V is a promising candidate to tune across the resonance [P10, 357–362].

Such tuning of the interactions may find a realization in solids when the screening of Coulomb interactions becomes increasingly poor in the low-doping regime [363]: Hence, at extremely low dopings, strong Coulomb repulsion is expected to lead to highly excited (cc) states and a normal state well in the BCS regime. Here, the attraction induced by couplings to (cc) states is expected to be unable to overcome the intrinsic repulsion between the individual dopants, caused e.g. by kinetic (Pauli repulsion) or Coulomb effects. As the Coulomb repulsion becomes screened, the emergent Feshbach resonance is approached. Once the induced attraction among (sc)'s is sufficiently large, a weak-coupling d-wave BCS state of magnetic polarons is expected to form. This is consistent with recent observations of BCS quasiparticle peaks in ARPES studies of strongly underdoped layered $Ba_2Ca_5Cu_6O_{12}(F, O)_2$ compounds [248] at 4.3 % hole doping. At higher doping, screening effects become even more effective. Here, the weak coupling BCS description can break down if near-resonant induced interactions are realized, which can lead to high critical temperatures T_c as in BCS-BEC cross-over scenarios [10, 77] and may explain the observed non-BCS nature of the superconducting transition [260].

How close a given cuprate compound, or state in a given Hubbard model, is to the conjectured resonance can depend sensitively on details. On the one hand, this may require some fine-tuning in order to reach the largest values of T_c by reaching parameters closest to resonant interactions. On the other hand, as explained below, we expect relatively strong coupling between the open and closed channels, set by the super-exchange energy J or the next-nearest neighbor (NNN) tunneling t'. This can lead to a broad Feshbach resonance, realizing strong attraction between (sc)'s even well before the resonance is reached [364]. Overall this scenario is broadly consistent with the considerable range of maximally achievable critical temperatures T_c in different compounds.

9.3   Effective string model

To support our hypothesis, we directly calculate the two-hole scattering interactions using a truncated basis approach in which we treat both the (sc) and (cc) channels on equal footing. To be concrete, we consider the t-t'-J model [112], see Chapter 8,

$$
\begin{aligned}
\hat{\mathcal{H}}_{t\text{-}t'\text{-}J} = &- t \sum_{\langle i,j \rangle} \sum_{\sigma} \hat{\mathcal{P}} \left(\hat{c}_{\mathbf{i},\sigma}^{\dagger} \hat{c}_{\mathbf{j},\sigma} + \text{h.c.} \right) \hat{\mathcal{P}} - t' \sum_{\langle\langle i,j \rangle\rangle} \sum_{\sigma} \hat{\mathcal{P}} \left(\hat{c}_{\mathbf{i},\sigma}^{\dagger} \hat{c}_{\mathbf{j},\sigma} + \text{h.c.} \right) \hat{\mathcal{P}} \\
&+ J_z \sum_{\langle i,j \rangle} \left(\hat{S}_{\mathbf{i}}^z \hat{S}_{\mathbf{j}}^z - \frac{1}{4} \hat{n}_{\mathbf{i}} \hat{n}_{\mathbf{j}} \right) + \frac{J_\perp}{2} \sum_{\langle i,j \rangle} \left(\hat{S}_{\mathbf{i}}^+ \hat{S}_{\mathbf{j}}^- + \text{h.c.} \right),
\end{aligned}
\tag{9.2}
$$

with spin-1/2 fermions $\hat{c}_{\mathbf{j},\sigma}^{\dagger}$ residing on sites $\mathbf{j}$ with spin $\sigma = \downarrow, \uparrow$, and number (spin) operator $\hat{n}_{\mathbf{j}} = \hat{n}_{\mathbf{j},\downarrow} + \hat{n}_{\mathbf{j},\uparrow}$ ($\hat{\mathbf{S}}_{\mathbf{j}}$). We denote the links between NN and NNN sites as $\langle i,j \rangle$ and $\langle\langle i,j \rangle\rangle$, respectively. The Gutzwiller projector $\hat{\mathcal{P}}$ removes energetically costly double occupancies such that $\hat{n}_{\mathbf{j}} \leq 1$ for all $\mathbf{j}$ is enforced. The ground state $|0\rangle$ at half-filling is AFM Néel ordered.

Next, we describe the (sc) and (cc) bound states, which arise in the sectors of the Hilbert space with one and two holes, respectively, upon doping the vacuum $|0\rangle$. We employ the semi-analytic geometric string theory, in which (sc) [(cc)] meson eigenstates are expanded
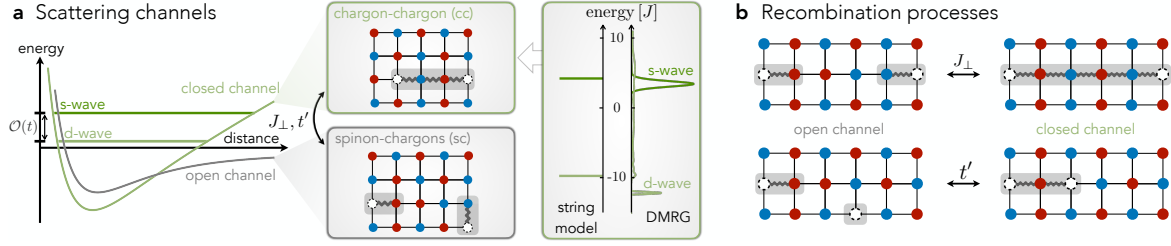
Figure 9.2: **Geometric string theory of the two-channel model. a** Magnetic polarons, i.e., (sc) mesons, are fermionic quasiparticles of single holes doped into an AFM Mott insulator. In contrast, tightly bound (cc) mesons exist as long-lived *s*- and *d*-wave resonances in the spectrum. The two types of mesons constitute open and closed scattering channels, and can be described in a truncated string basis defined in a classical Néel background (see insets); they are composed of chargons (white circles) connected to a spinon (bottom) or another chargon (top) at the opposite end of the string. We plot the (cc) excitation spectrum at $\mathbf{Q} = \mathbf{0}$ obtained from the string model [36] (left) and from DMRG studies in the *t-J* model [37] (right), which shows the large energy separation between the *s*-wave and *d*-wave (cc) resonances. **b** Two spinons, each bound to a single chargon, can recombine into a longer string connecting the two chargons. Thereby spin exchange $J_\perp$ and NNN tunneling t' processes couple the open and closed channel states and mediate an effective scattering interaction between the former.

in a truncated basis of orthonormal string states $|\mathbf{j}_\sigma, \Sigma\rangle$ [$|\mathbf{x}_c, \Sigma_{cc}\rangle$]. Here $\mathbf{j}_\sigma$ [$\mathbf{x}_c$] denotes the spinon [first chargon] position and Σ [Σ_{cc}] is a sequence of non-retracing string segments connecting to the other parton, providing a confining force. These states can be constructed explicitly for one and two holes in a classical Néel state by displacing spins along the string Σ, see Figure 9.2a and Chapter 10, and have been shown to provide an accurate, yet analytically tractable, approximation of the mesons' ground and excited states [21, 35, 36, 305–308].

The open channel (sc) states constitute the starting point of the analysis. The gap to their internal excitations is sufficiently large $\mathcal{O}(J)$ such that at low energies only s-wave (sc) mesons $\hat{\pi}_{\mathbf{k},\sigma}$ exist [320]. Therefore, in the low-doping limit, we describe the open channel by the following free-fermion Hamiltonian,

$$\hat{\mathcal{H}}_{\text{open}} = \sum_{\mathbf{k},\sigma} [\varepsilon_{\text{sc}}(\mathbf{k}) - \mu] \, \hat{\pi}^\dagger_{\mathbf{k},\sigma} \hat{\pi}_{\mathbf{k},\sigma}. \tag{9.3}$$

The dispersion relation $\varepsilon_{\text{sc}}(\mathbf{k})$ has its minimum at the nodal points $\mathbf{k} = (\pm\pi/2, \pm\pi/2)$ [313, 314], around which two Fermi pockets form upon increasing the chemical potential μ [248]. Since we assume the AFM correlation length ξ to be sufficiently larger than the size of a (sc) meson, we can analyze the case of an AFM ordered state. Thus, all excitations are defined with momenta $\mathbf{k}$ in the magnetic Brillouin zone (MBZ), which is rotated by $\pi/4$ and reduced with respect to the original crystal Brillouin zone (CBZ).

The closed channel states are constituted by (cc) mesons $\hat{b}^\dagger_{\mathbf{Q},\alpha,m_4}$, with momentum $\mathbf{Q}$ and band index α [36, 37]. As in the case of (sc) mesons we ignore vibrational excitations; it is however important to include their rotational structure described by the C_4 angular

momentum $m_4 = 0, .., 3$. The resulting free (cc) Hamiltonian is

$$\hat{\mathcal{H}}_{\text{closed}} = \sum_{\mathbf{Q}, \alpha, m_4} \varepsilon_{\text{cc}}^{m_4}(\mathbf{Q}) \hat{b}^{\dagger}_{\mathbf{Q}, \alpha, m_4} \hat{b}_{\mathbf{Q}, \alpha, m_4}, \tag{9.4}$$

with the dispersion $\varepsilon_{\text{cc}}^{m_4}(\mathbf{Q}) = -\frac{2}{3}J(\cos(Q_x) + \cos(Q_y) - 2) + \Delta E_{m_4}$ of the tightly bound pair [37]; here ΔE_{m_4} denotes the energy above the scattering threshold. In the truncated string basis, the (cc) states do not distinguish between the two magnetic sublattices and can be defined in the CBZ. In order to describe their coupling to the open channel in the next step, we fold the CBZ into the MBZ by restricting ourselves to $\mathbf{Q} \in$ MBZ and introducing the band index $\alpha = 0, 1$. Because the (cc) wavefunction of the two fermionic holes can be (anti)symmetric in the band index, any value of m_4 can be realized at the C_4-invariant momenta; in particular at $\mathbf{Q} = \mathbf{0}$ shown below to be relevant for low-energy scattering.

Now we turn to a description of the coupling between the open and closed channels. In the effective string basis, we recognize microscopic processes $\propto J_\perp, t'$ leading to recombination processes from a (sc)^2 into a (cc) configuration, see Figure 9.2b. In order to describe the corresponding low-energy two-particle scattering problem, we consider two (sc)'s in a spin-singlet state and with momenta $\pm\mathbf{k}$ from opposite sides of the Fermi surface. Note that we focus here on intra-pocket recombinations: two (sc)'s from the same hole pocket recombine into a (cc) pair with total momentum $\mathbf{Q} = \boldsymbol{\pi}$, which leads to zero-momentum Cooper pairs in the MBZ. Hence the allowed pairing symmetries are of d- or s-wave nature.

To understand into which (cc) states the (sc)^2 can recombine, we formulate the relevant selection rules associated with the translational and C_4-rotational symmetries of the system. The former ensures that total momentum is conserved, i.e., only couplings to (cc) mesons with C_4-invariant momenta $\mathbf{Q} = \mathbf{0}$ or $\boldsymbol{\pi}$ are allowed. At these momenta, the latter symmetry further ensures conservation of total C_4 angular momentum m_4. Since the individual (sc)'s have s-wave (internal) character, only the orbital angular momentum associated with their relative motion contributes to m_4, as defined by the corresponding zero-momentum Cooper pair operator,

$$\hat{\Delta}^{\dagger}_{m_4} = \frac{1}{\sqrt{2}} \sum_{\mathbf{k}} f_{m_4}(\mathbf{k}) \left(\hat{\pi}^{\dagger}_{-\mathbf{k},\uparrow} \hat{\pi}^{\dagger}_{\mathbf{k},\downarrow} - \hat{\pi}^{\dagger}_{-\mathbf{k},\downarrow} \hat{\pi}^{\dagger}_{\mathbf{k},\uparrow} \right). \tag{9.5}$$

Here, the function $f_{m_4}(\mathbf{k})$ transforms as $f_{m_4}(\mathbf{k}) \to e^{-im_4\pi/2} f_{m_4}(\mathbf{k})$ under C_4 rotations. Since only $m_4 = 0$ (s-wave) and $m_4 = 2$ (d-wave) lead to non-vanishing $\hat{\Delta}^{\dagger}_{m_4}$, we conclude from the derived selection rules that only couplings to closed channel (cc) states with d- or s-wave symmetry are allowed. In principle, our formalism allows us to include finite momentum Cooper pairs relevant for inter-pocket scattering and potentially relevant for going beyond BCS mean-field theory.

In the next step, we integrate out the closed (cc) channels, which yields mediated interactions that we can describe by the effective Hamiltonian

$$\hat{\mathcal{H}}_{\text{int}} = \sum_{\mathbf{k}, \mathbf{k}'} V_{\mathbf{k}, \mathbf{k}'} \hat{\pi}^{\dagger}_{-\mathbf{k},\uparrow} \hat{\pi}^{\dagger}_{\mathbf{k},\downarrow} \hat{\pi}_{-\mathbf{k}',\uparrow} \hat{\pi}_{\mathbf{k}',\downarrow}, \tag{9.6}$$

with scattering matrix elements $V_{\mathbf{k},\mathbf{k}'}$ of the form

$$V_{\mathbf{k},\mathbf{k}'} = \frac{1}{L^2} \sum_{m_4=0,2} \frac{1}{\Delta E_{m_4}} \mathcal{M}_{m_4}^*(\mathbf{k}) \mathcal{M}_{m_4}(\mathbf{k}'). \tag{9.7}$$

Here we sum over the two allowed closed channels, $m_4 = 0, 2$. The form factors $\mathcal{M}_{m_4}(\mathbf{k})$ will be calculated below from matrix elements coupling open and closed channels that we obtain within the effective string model. L^2 denotes the two-dimensional volume.

An emergent Feshbach resonance with divergent attractive interactions is realized when the closed channel approaches the scattering threshold from above, i.e., $\Delta E \to 0^+$. At the considered (cc) momentum $\mathbf{Q} = \mathbf{0}$, only the d-wave (cc) state has low energy ΔE_2; in contrast, the s-wave (cc) state has energy $\Delta E_0 = \mathcal{O}(t)$ owing to its strong center-of-mass dispersion. This follows from string model calculations [36, 307] and has been confirmed by large-scale exact-diagonalization [34] and DMRG studies [37] in the t-J model. We show the corresponding energy distribution curves of the pair-spectral functions at $\mathbf{Q} = \mathbf{0}$ in Figure 9.2a (right column), where the large splitting is clearly visible.

This leads to the important conclusion that low-energy scattering of magnetic polarons is dominated by couplings to the d-wave (cc) channel; namely, since $\Delta E_0 \approx t$, couplings to the s-wave channel can be safely neglected in $V_{\mathbf{k},\mathbf{k}'}$, Eq. (9.7). This justifies the simplified two-channel model underlying the Feshbach hypothesis formulated earlier in our article. Accurate numerical calculations of the (cc) gap ΔE_2 are extremely challenging: since it is defined as the distance of the bare (cc) energy from the two-particle scattering threshold, it constitutes a small difference of two much larger quantities and becomes sensitive to details. Nevertheless we note that numerous studies have concluded that tightly-bound d-wave pairs, i.e., with (cc) character, exist at low energies close to the scattering threshold, see e.g. [34, 36, 37, 308]. This justifies our conjecture that strongly interacting doped Hubbard models at low doping are close to an emergent d-wave Feshbach resonance.

9.4   Scattering interaction

Now we use the truncated string basis to calculate the form factors $\mathcal{M}_2(\mathbf{k})$ characterizing the open-closed channel coupling. From the underlying t-t'-J model we find (see Chapter 10) two contributions corresponding to the different recombination processes illustrated in Figure 9.2b,

$$\mathcal{M}_2(\mathbf{k}) = J_\perp \mathcal{M}_2^{J_\perp}(\mathbf{k}) - \mathrm{sgn}(\delta)|t'|\mathcal{M}_2^{t'}(\mathbf{k}). \tag{9.8}$$

This result assumes perturbative $|t'| \ll t$, such that the effective string model remains valid. In Chapter 10 Section 10.10, we use a more elaborate method allowing us to including non-perturbative effects of t'. Moreover we generalized our description to include hole and electron doping δ, characterized by $\mathrm{sgn}(\delta) = +1$ (holes) and $\mathrm{sgn}(\delta) = -1$ (electrons) respectively; in deriving Eq. (9.8) we further assumed $t' < 0$ in Eq. (9.2). A typical value used to model cuprates is $t'/|t| = -0.2$ [300, 301]. In the following, we extend the two-body scattering description to a many-body problem of weakly interacting magnetic polarons
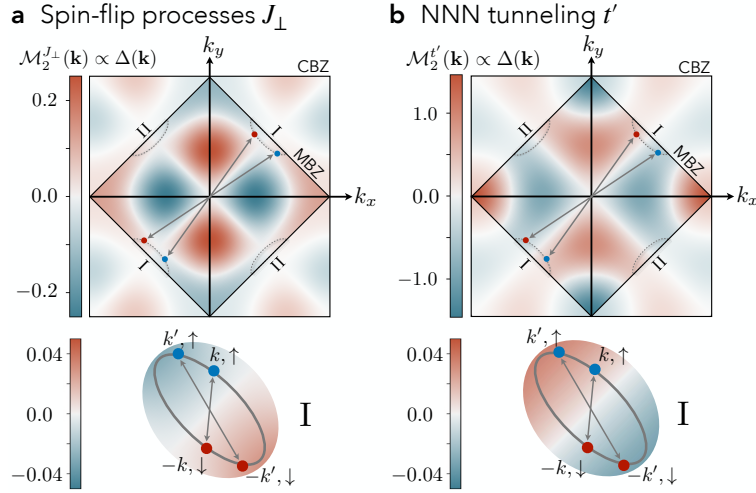
a Spin-flip processes $J_\perp$

$\mathcal{M}_2^{J_\perp}(\mathbf{k}) \propto \Delta(\mathbf{k})$

b NNN tunneling t'

$\mathcal{M}_2^{t'}(\mathbf{k}) \propto \Delta(\mathbf{k})$

Figure 9.3: **Symmetry of the pairing interaction.** We plot the dimensionless open-closed channel form factors $\mathcal{M}^{J_\perp}(\mathbf{k})$ from spin-flip processes **a**, and $\mathcal{M}^{t'}(\mathbf{k})$ from NNN tunneling processes **b**, as calculated within the two-channel model of the emergent Feshbach resonance. They directly reflect the sign structure of the resulting superconducting order parameter $\Delta(\mathbf{k})$, and show a strong momentum dependence. Outside the MBZ we used reduced opacity for clarity. Upon doping, charge carriers fill up the two hole pockets I and II, realizing scattering of total momentum $\mathbf{Q} = \mathbf{0}$ pairs on the Fermi surfaces (bottom). The mediated interactions, and hence the pairing gap, vanish along the white nodal lines, featuring a dominant $d_{x^2-y^2}$ nodal structure in the CBZ.

and discuss implications of the effective model at finite doping.

We show the two contributions to the form factor separately in Figure 9.3a and b and find a rich momentum dependence with a sign structure reflecting the underlying d-wave symmetry of (cc) mesons. Notably, within a weak coupling BCS description of the (sc) Fermi sea, the superconducting order parameter $\Delta(\mathbf{k}) \propto \mathcal{M}_2(\mathbf{k})$ follows directly from the BCS gap equation for Eq. (9.6), see Chapter 10 Section 10.2.4. Therefore, Figure 9.3 reveals the structure of the pairing gap. In particular, we find for both recombination processes that the form factor (and hence the pairing gap) is dominated by the ubiquitous $d_{x^2-y^2}$ nodal structure observed in hole doped cuprate compounds.

Beyond the $d_{x^2-y^2}$ structure dominating around the hole pockets we find additional nodal lines in the CBZ, see Figure 9.3a, originating from a superimposed extended s-wave structure of the interactions, see Chapter 10 Section 10.2.4. This rich momentum-dependence of the induced interactions reflects the extended spatial structure of the closed-channel (cc) state mediating the attractive interaction. Nevertheless, within our theory, combining $J_\perp$ and t' processes, pairing is dominated by $d_{x^2-y^2}$ structure in the entire low hole doping regime $\delta < 15\%$, with only small deviations from the ideal $\Delta_{x^2-y^2}(\mathbf{k}) \simeq |\cos(k_x) - \cos(k_y)|$ structure; therefore the additional nodal lines are outside the immediately relevant experimental regime.

The superimposed extended s-wave structure occurs from beyond point-like interactions, i.e., from the finite extend of the meson wavefunctions. In the following Chapter, we provide the function form of the extended s-wave channel in Eqs. (10.41)-(10.42) obtained
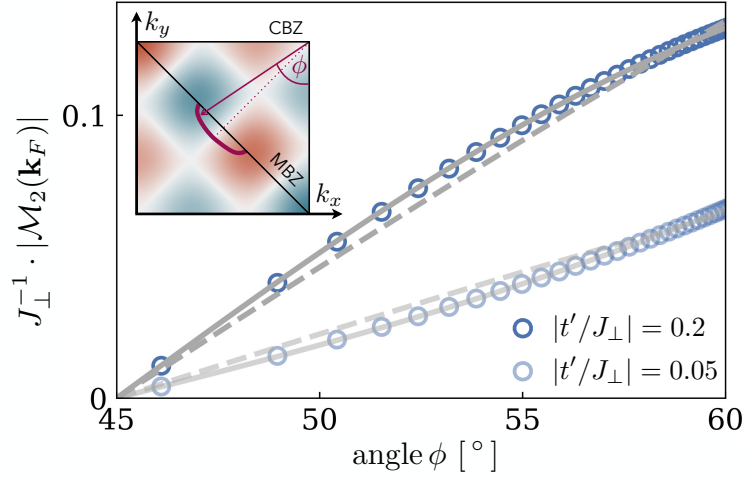
Figure 9.4: **Gap anisotropy.** The form factor $\mathcal{M}_2(\mathbf{k})$ is directly related to the pairing gap $\Delta(\mathbf{k})$. We assume an elliptical Fermi surface of magnetic polarons, i.e. hole pockets, at $\delta = 10\%$ doping. The Fermi surface is parameterized by the angle $\phi_{\mathbf{k}}$ (inset). The blue circles show the pairing gap, calculated from our two channel model, along the Fermi surface for exemplary values $|t'/J_\perp| = 0.05, 0.2$. We fit the pairing gap using a plain vanilla $d_{x^2-y^2}$ gap symmetry (dashed gray) and a refined gap function including $\cos 6\phi_{\mathbf{k}}$ terms (solid gray). The latter is an excellent fit function for an entire range of parameters $|t'/J_\perp|$.

from the phenomenological string description.

Similarly, precise measurements of the superconducting gap in underdoped Bi-2212 indicate an anisotropy in momentum space that cannot be explained by the plain vanilla $d_{x^2-y^2}$ symmetry as argued by Mesot et al [365]. Instead, it was found that the function

$$\Delta(\phi_{\mathbf{k}}) \propto B\cos(2\phi_{\mathbf{k}}) + (1 - B)\cos(6\phi_{\mathbf{k}}) \tag{9.9}$$

captures the gap structure in underdoped samples, where B is used as a fit parameter. In ARPES measurements the pairing gap is determined along the Fermi surface, conveniently parameterized by the angle $\phi_{\mathbf{k}}$, see Figure 9.4b (inset) for definition. To model the cuprates in our calculations, we assume a Fermi surface of magnetic polarons for $t' = 0$ [315] as shown in Figure 9.4 (inset). Next, we calculate the BCS pairing gap $\Delta(\mathbf{k}) \propto \mathcal{M}_2(\mathbf{k})$ for different parameters $|t'/J_\perp| = 0.05, 0.2$ and extract its features along the magnetic polaron's Fermi surface. To this end, we fit to (i) $\cos(2\phi_{\mathbf{k}})$ (i.e. $B = 1$) and (ii) to the refined gap function Eq. (9.9) with $B \in [0, 1]$. The fitted curves are shown by the dashed and solid gray lines in Figure 9.4. We find excellent agreement of our calculations to the fit for the second case (ii), consistent with ARPES measurements [365]

9.5   Experimental signatures

Now we turn to possible experimental signatures of the Feshbach hypothesis. The key ingredient of the proposed pairing mechanism is the existence of a tightly bound (cc) channel at low excitation energies above the Fermi energy. At this point it is important to con-
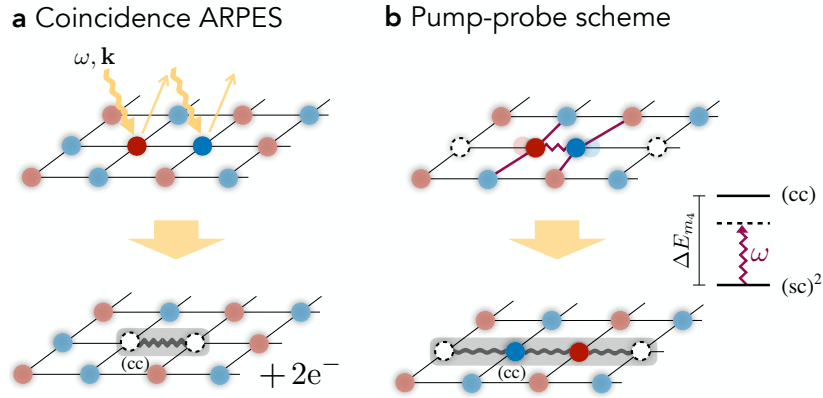
Figure 9.5: **Experimental signatures of the closed channel (cc) state. a** Two photons with energy and momentum $(\omega, \mathbf{k})$ remove two adjacent electrons from the system, which can be detected in the correlations of the photoelectrons (coincidence ARPES). This gives direct access to the dispersion relation of the (cc) meson as shown for $\mathbf{Q} = \mathbf{0}$ in Figure 9.2a (right). **b** We propose a pump-probe protocol, in which a Raman active phonon-mode is driven at frequency ω (purple). This modulates the microscopic couplings and drives a transition between the open channel $(\text{sc})^2$ and closed channel (cc) states such that the energy difference ΔE_{m_4} in the proposed Feshbach model can be overcome, potentially allowing to reach a transient state with resonant interactions.

trast the (cc) mesons to pre-formed Cooper pairs expected above the superconducting critical T_c where phase-coherence rather than pairing disappears at low doping [266, 267]. From our perspective, pre-formed Cooper pairs should be of $(\text{sc})^2$-type and exist just above T_c, whereas (cc) pairs can exist separately at higher energies and potentially well above T_c.

While the (cc) channel gives rise to a doping-dependent ARPES feature in single-particle spectroscopy, we find the signal to be very weak as discussed in Chapter 10 Section 10.11. Therefore, we turn our attention to two-hole (correlation) spectroscopy, where numerical studies [34, 37] found the pronounced (cc) peaks shown in Figure 9.2a (right column). A direct measurement of such two-hole spectra requires removal of a tightly-bound pair, with or without well-defined C_4 angular momentum, at a well-defined energy ω and momentum $\mathbf{k}$. Theoretical proposals have been made how this can be achieved in coincidence ARPES spectroscopy, in a one-photon-in-two-electron-out [366, 367] or a two-photon-in-two-electron-out [368] configuration. While the former needs high-energy photons, the latter requires low-intensity light in order to distinguish the coincidence signal from the one-particle ARPES background [369], making both challenging. In Figure 9.5a we illustrate the correlated ARPES process, which removes adjacent electrons and creates a hole pair having overlap with all angular momentum m_4 channels of the (cc) bound state if $\mathbf{k} \neq \mathbf{0}$, as we will argue using the string picture.

The two in-coming photons have momentum $\mathbf{k}_1$ and $\mathbf{k}_2$ (out-going photonelectrons have momentum $\mathbf{k}_3$ and $\mathbf{k}_4$). Here, we consider the special case with $\mathbf{k}_1 = \mathbf{k}_2 \equiv \mathbf{k}$, and $\mathbf{k}_3 = \mathbf{k} + \delta\mathbf{k}$ and $\mathbf{k}_4 = \mathbf{k} - \delta\mathbf{k}$. In this sector, there is no momentum transfer to the sample and thus we probe (cc) states with $\mathbf{Q} = \mathbf{0}, \boldsymbol{\pi}$ in the MBZ. We argue that for $\delta\mathbf{k} \neq 0$ the coupling matrix elements or spectral weight of coincidence ARPES is non-zero for any angular

momentum m_4. To show this, we consider the matrix elements $\mathcal{R}(\delta\mathbf{k})$ for removing two adjacent electrons at distance $\mathbf{r}_n$, given by four individual processes on the square lattice:

$$\mathcal{R}(\delta\mathbf{k}) \propto \sum_{n=0}^{3} e^{i\frac{\pi}{2}nm_4} e^{-i\mathbf{r}_n \cdot \delta\mathbf{k}}. \tag{9.10}$$

The matrix elements are momentum dependent ($\delta\mathbf{k}$) and admit the rotational symmetry m_4 of the (cc) channel. Since the low-energy channel has d-wave symmetry ($m_4 = 2$), the matrix elements vanish along the nodal directions, and in particular at $\delta\mathbf{k} = 0$. However, for $\delta\mathbf{k} \neq 0$ we find non-zero matrix elements to the (cc) bound state.

Thus, we predict a signal from the (cc) meson in cARPES measurement. Hereby, the energy onset of the signal relative to the Fermi energy E_F and at $\mathbf{Q} = 0$ would directly measure the detuning ΔE_{m_4} from the (cc) resonance in our proposed Feshbach scenario. More detailed analysis of the resulting two-hole spectrum for arbitrary $\delta\mathbf{k}$ may reveal characteristic, smoking gun signatures ubiquitous to the two-channel model.

Further, we suggest two potential experiments based on the coherent tunneling of pairs. First, if a sample with $T > T_c$ is brought in contact with a superconductor, the Cooper pairs from the latter can tunnel through the junction into the (cc) channel, similar to Anderson-Goldman pair tunneling [370]. Such experiments have already revealed some signatures of enhanced pairing fluctuations above T_c [371]. By adding an in-plane magnetic field and a voltage across the junction, the pair spectra could be directly probed with combined energy and momentum resolution [37, 372]. Second, scanning tunneling noise spectroscopy can directly probe local pairs by analyzing autocorrelations of the current fluctuations [373, 374]. We expect an onset of enhanced pairing fluctuations at an energy ΔE_{m_4} above E_F as a direct signature of the near-resonant (cc) state, which should be present even above $T > T_c$. This is in line with recent noise-spectroscopy experiments performed on LSCO [375] which reported an onset of enhanced pairing fluctuations around an energy scale of $10\,\text{meV}$.

Finally, we propose to verify the existence of the tightly-bound (cc) state in pump-probe experiments, in which the properties of the transient state are modified, see Figure 9.5b. By off-resonantly driving a Raman-active phonon mode, the microscopic parameters t, t' and J can be modulated in time by the pump pulse, with frequency ω. From our microscopic model we predict that this can drive the transition between the open $(\text{sc})^2$ and closed channel (cc), achieving tunable interactions in the transient state which become resonant for $\omega = \Delta E_{m_4}$. On resonance we can expect creating a large population of long lived metastable (cc) pairs. This transient state can exhibit optical properties similar to systems with strong superconducting correlations. This scenario is potentially relevant for understanding light-induced superconductivity [376].

9.6   Summary and Perspectives

To summarize, we propose a new perspective on the pairing mechanism potentially underlying high-temperature superconductivity as observed in the cuprate compounds. It is based on the idea that an emergent Feshbach resonance between magnetic polaron like con-

stituents, with spinon-chargon character, of the low-doping normal state may arise when a near-resonant tightly bound bi-polaronic state of two holes exists at low excitation energies ΔE_2. Using a truncated string basis we derive robust $d_{x^2-y^2}$ attractive interactions between the fermionic charge carriers in the open channel, inherited from the structure of the light bi-polaronic chargon-chargon state constituting the closed channel. Comparison to experiments in cuprate compounds [240, 244] as well as DMRG simulations of the t-J model [37] lead us to the Feshbach hypothesis: We conjecture that cuprates remain on the BCS side of an emergent Feshbach resonance, but realize near-resonant interactions, i.e. $\Delta E_2 \lesssim J$.

The Feshbach pairing mechanism we introduce here for cuprates, or the square lattice Hubbard model, is distinct from other proposed scenarios. In contrast to the spin-bag mechanism [325, 329], we assume a pronounced internal structure of the emergent charge carriers sustaining a long-lived chargon-chargon resonance that mediates attractive interactions. Our proposal is also different from glue-based mechanisms as in conventional phonon-based superconductors where weak retarded attraction appears, or exchange-based mechanisms where collective excitations – such as (para-) magnons – realize attractive interactions. For example, field-theoretic work [328] suggests intra-pocket d_{xy} pairing, whereas we find intra-pocket $d_{x^2-y^2}$ pairing (notably Ref. [328] found inter-pocket $d_{x^2-y^2}$ pairing, however). Nevertheless, we also conclude that magnetic interactions, in conjunction with kinetic effects, are ultimately responsible for pairing, in agreement with a large body of analytical and numerical work [245, 257, 258, 330] and experiments [259].

The Feshbach scenario [377, 378] we suggest may provide a long-sought common perspective on pairing in a whole range of strongly correlated systems, ranging from two-dimensional semiconductors [340, 379] to bilayer nickelate superconductors [P1, P10, P6, 342]. We expect that our microscopic considerations will also provide a valuable perspective on pairing in a broader class of doped antiferromagnets, such as infinite-layer nickelates or heavy fermion superconductors. A direct application of our theory is to analyze electron-doped cuprates, where the topology of the magnetic polaron Fermi surface changes [380] and the realized pairing symmetry remains subject of debate. Although in our calculations we assumed a long-range ordered AFM, our ideas directly extend to disordered normal states such as fractionalized Fermi liquids [262–264, 381, 382].

In addition to the possible experimental signature discussed above, numerical studies as well as quantum simulation experiments [P1] provide further possibilities to test our hypothesis. On one hand, advances in calculating one- and two-particle spectral functions numerically [383] will allow to search for more direct signatures of the emergent Feshbach resonance. On the other hand, ultracold atoms in optical lattices [P1] or tweezer arrays [P8] allow to study clean systems with widely tunable parameters, in and out-of equilibrium, and including higher-order correlation functions [310]. A possible application of the latter would be to look for direct signatures of the strings defining the structure of spinon-chargon and chargon-chargon pairs, in a wide range of dopings.

To reveal direct signatures of the Feshbach pairing mechanism in cuprates, we propose to use spectroscopic probes for pairs, such as coincidence ARPES. These will allow to look for spectral features ubiquitous to the chargon-chargon excitations which we argue to be

responsible for the appearance of strong attractive interactions. Additionally, we suggest pump-probe experiments, which may enable to bring the system closer to resonance, potentially resulting in higher transition temperatures.
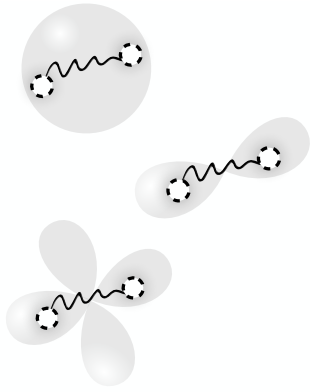
10
Multichannel perspective and Feshbach resonance

A̲N EXCEPTIONAL EFFORT has been put forward to explain the origin of the strong pairing in cuprates, starting from various proposed parent states including the magnetic polarons; hereby numerous studies have shown the importance of magnetic fluctuations for pairing [245, 252, 255–258, 325, 328–330, 384–386], see Chapter 8. However, the charge carrier's strong coupling nature, i.e., their emergence from the underlying correlated background, prohibits to develop a simple interacting theory at finite doping. In particular, developing a unifying description that includes the rich microscopic structure of the emergent charge carriers, i.e., the string and its fluctuations, has remained challenging. The goal of the Chapter formulate a low but finite doping description of these charge carriers fully including their internal structure.

Moreover, we collect further evidence for the Feshbach scattering scenario for cuprate superconductors [P11] discussed in the previous Chapter 9. In our Feshbach hypothesis, we take into account the internal structure of charge carriers in the strong-coupling low-doping regime of Fermi-Hubbard-type models [21, 33, 35, 305, 311, 366]; in particular we consider parton bound states constituted by spinons (s) and chargons (c). Based on numerical, analytical and experimental signatures [7, 21, 32–34, 36, 37, 320, 387], we recognize two distinct types of bound states, see Figure 10.1a: (i) a fermionic (sc) bound state and (ii) a bosonic resonant (cc) bipolaronic state. This picture is further corroborated by experimental facts in underdoped cuprates, where are sharp pocket-like hole Fermi surface is observed in the very low-doping regime [248]. In our hypothesis, the internal mesonic structure of the parton bound states gives rise to an emergent Feshbach resonance between open channel states constituted by (sc) mesons and closed channel states constituted by (cc) mesons.

In Chapter 9, we have developed a two-channel perspective of the Feshbach resonance. From selection rules and energetic arguments, we concluded that the d-wave symmetric (cc) meson is the dominant scattering channel. After integrating out the closed channel, the
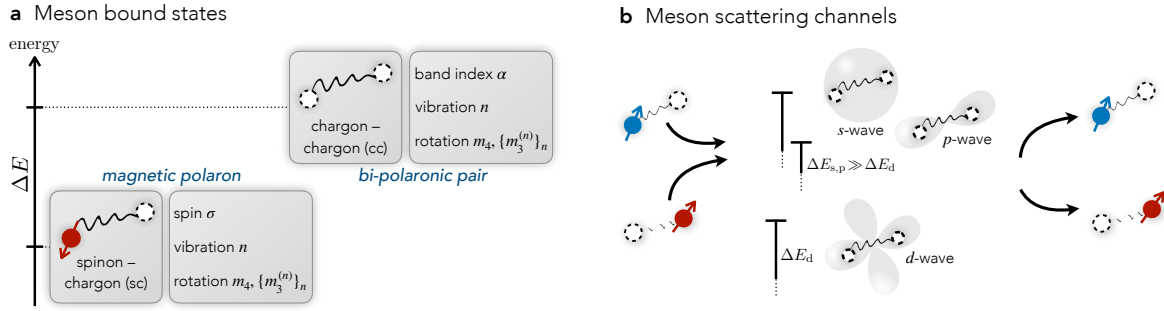
a Meson bound states

b Meson scattering channels

Figure 10.1: **Mesons in doped antiferromagnets.** Understanding the properties of charge carriers in underdoped cuprates is essential to build microscopic, strong coupling theories of the various observed phases including the d-wave superconductor. Our starting point is the very low doping regime, i.e., one or two dopants in a strongly correlated AFM Mott insulator, which feature quasiparticles with rich internal structure. **a** The confined nature of partons, i.e., the spinon (s) and chargon (c), gives rise to mesonic (sc) and (cc) bound states. The mesons carry quantum numbers associated with their internal ro-vibration structure. **b** The Feshbach scattering scenario proposed in Ref. [P11] describes two fermionic (sc) mesons, which scatter via recombination processes into the bosonic, tightly-bound (cc) state. The internal structure of the charge carriers leads to various scattering channels. If one channel approaches the scattering threshold, however, the scattering length diverges and dominates the low-energy physics. The Feshbach hypothesis of high-Tc superconductivity conjectures that cuprates remain on the BCS-side but are in close proximity to a d-wave resonant (cc) state.

Feshbach scattering induces an attractive $d_{x^2-y^2}$-wave interaction between the fermionic charge carriers. Here, we want to take into account the rich internal structure of mesons, i.e., their ro-vibrational excitation spectrum [21, 32, 34, 36, 37, 303, 320], and develop a multichannel scattering perspective, see Figure 10.1b.

To this end, we develop a truncated basis method to obtain the mesons by confining strings, and apply it to describe a multichannel model of magnetic polarons $(sc)^2$ in the open channel and tightly-bound (cc) states in the closed channel, see Section 10.1. In Section 10.2, we calculate the matrix elements of the resonant interactions by performing a controlled approximation in the length of strings and by considering open-closed channel recombination processes induced by spin-flip $J_\perp$ and weak next-nearest neighbouring (NNN) tunneling t' events. We compare our results in Section 10.3 to a more quantitative and refined truncated basis method, that cures the overcompletness of the strings states and allows us to systematically include non-perturbative effects associated with larger values of t'.

Large parts of this Chapter are based on publication [P7]. The text and figures are rearranged, adapted and supplemented.

10.1 Open and closed channel description

The starting point to describe one and two dopants (holes or electrons) in the AFM Mott insulator is a 2D square lattice t-t'-J model, introduced in Chapter 7. The Hamiltonian of
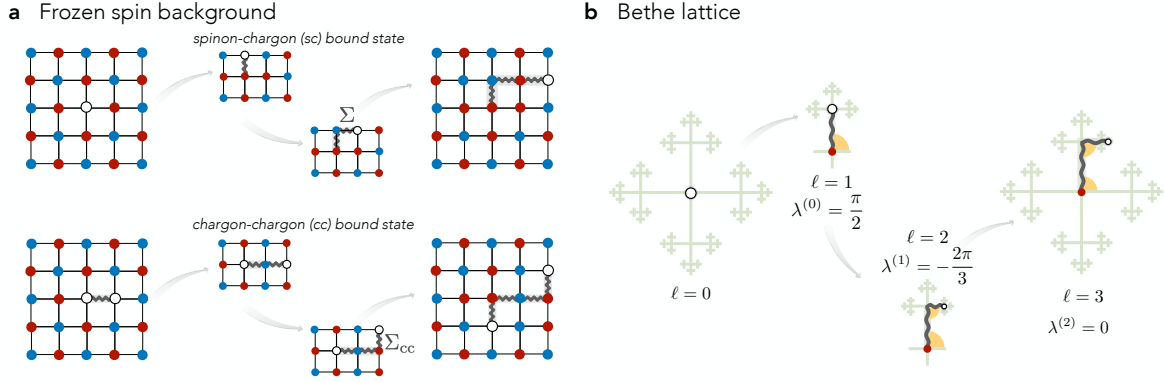
Figure 10.2: **Truncated basis of geometric strings. a** We describe the single dopant (magnetic polaron) in a parton framework giving rise to a spinon-chargon bound state (sc). For $t \gg J$, the chargon moves through a frozen spin background, i.e. the latter adapts on much slower time scales, $\tau_s \propto J_\perp^{-1}$, then the former, $\tau_c \propto t^{-1}$. The chargon's motion rearranges the spin background leaving a memory, which we encode in the geometric string Σ (gray curly line). The displacement of spins leads to parton confinement akin to a linear string tension $\propto J_z$. Analogously, the parton construction is applicable to the two dopant problem, leading to a tightly-bound, bi-polaronic chargon-chargon (cc) bound state connected by a string Σ_{cc} (bottom). **b** We map the string states on the sites of a Bethe lattice. Here, we illustrate the hopping events of the chargon as in **a** (top). The rotational symmetries of the Bethe lattice allow us to assign well-defined rotational quantum numbers to the magnetic polaron for $C4$-invariant momenta. We associate an angle $\lambda^{(N)}$ between string elements of length $\ell = N$ and $\ell = N + 1$, where ℓ is the length of the string.

the model is given by

$$
\begin{aligned}
\hat{\mathcal{H}}_{t\text{-}t'\text{-}J} = & -t \sum_{\langle i,j\rangle,\sigma} \hat{\mathcal{P}} \left(\hat{c}_{\mathbf{i},\sigma}^\dagger \hat{c}_{\mathbf{j},\sigma} + \text{h.c.} \right) \hat{\mathcal{P}} \\
& -t' \sum_{\langle\langle i,j\rangle\rangle,\sigma} \hat{\mathcal{P}} \left(\hat{c}_{\mathbf{i},\sigma}^\dagger \hat{c}_{\mathbf{j},\sigma} + \text{h.c.} \right) \hat{\mathcal{P}} \\
& + J_z \sum_{\langle i,j\rangle} \left(\hat{S}_{\mathbf{i}}^z \hat{S}_{\mathbf{j}}^z - \frac{1}{4}\hat{n}_{\mathbf{i}}\hat{n}_{\mathbf{j}} \right) \\
& + \frac{J_\perp}{2} \sum_{\langle i,j\rangle} \left(\hat{S}_{\mathbf{i}}^+ \hat{S}_{\mathbf{j}}^- + \text{h.c.} \right),
\end{aligned}
\tag{10.1}
$$

where $\hat{c}_{\mathbf{j},\sigma}$ describes the underlying electrons with spin $\sigma = \downarrow, \uparrow$ at site $\mathbf{j}$; the spin-$1/2$ operator $\hat{\mathbf{S}}_{\mathbf{j}} = \frac{1}{2}\hat{c}_{\mathbf{j},\sigma}^\dagger \hat{\boldsymbol{\tau}}_{\sigma\sigma'} \hat{c}_{\mathbf{j},\sigma'}$ is constructed from Pauli matrices $\boldsymbol{\tau}$. Furthermore, the Gutzwiller projector ensures that the particle number, $\hat{n}_{\mathbf{j}} = \hat{n}_{\mathbf{j},\downarrow} + \hat{n}_{\mathbf{j},\uparrow}$, is constrained to $\hat{n}_{\mathbf{j}} \leq 1$ for all sites $\mathbf{j}$ akin to strong Hubbard repulsion in the parent model. The first two terms in Hamiltonian (10.1) describe NN and NNN tunneling with amplitude t and t', respectively. The last two terms are the effective AFM interaction with superexchange strength $J_z = J_\perp = +4t^2/U$. In the strong-coupling limit – typically $t/J \simeq 3$ is assumed in cuprate materials – the undoped ($\hat{n}_{\mathbf{j}} = 1$ for all $\mathbf{j}$) ground state $|0\rangle$ is AFM Néel ordered.

In the following, we recap the geometric string formalism in order to describe mobile
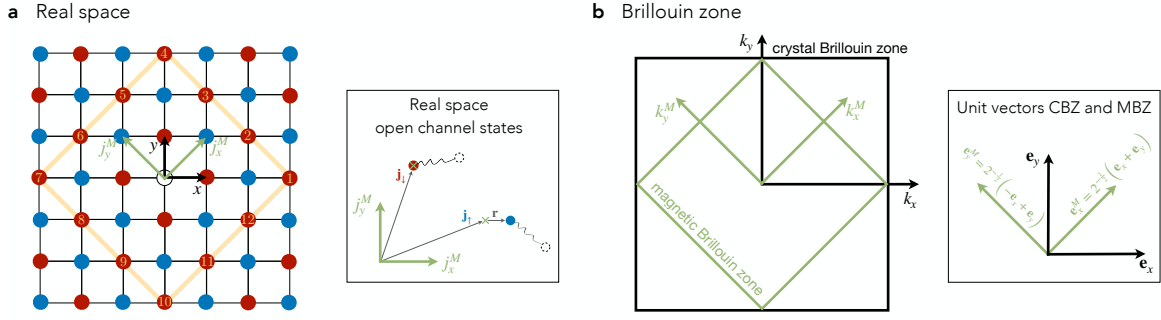
Figure 10.3: **Crystal and magnetic lattice.** **a** The long-range magnetic spin order breaks translational symmetry of the underlying crystal lattice. The magnetic lattice has a two site unit cell with basis vectors $\mathbf{j}_\downarrow = (j_x^M, j_y^M)$. **b** We illustrate the corresponding Brillouin zones of the crystal (CBZ) and magnetic (MBZ) Brillouin zone. The scattering calculations are performed in the MBZ with momenta $\mathbf{k}^M = (k_x^M, k_y^M)$.

single dopant (sc) and two dopant (cc) impurities immersed into an AFM Mott insulator $|0\rangle$; we closely follow Refs. [21, 36]. We review the basic concepts and introduce the notation required for the calculation of the Feshbach scattering length.

The geometric strings originate from the dopant's displacement of the AFM ordered spin background, see Figure 10.2, and was pointed out in early theoretical studies of the Hubbard or t-J model by Brinkman and Rice [306], Trugman [311] and Beran et al. [32], among others. The rigid string-like object naturally gives rise to a rich internal structure of the dopant's quasiparticle, explaining the long-lived vibrational excitations revealed in numerical [32, 35, 279, 320, 333] and analytical studies [21, 303, 305, 313, 317]. The string picture does not only provide a phenomenological explanation of the spectral features, but it can also be put in a stringent quantitative formalism, i.e., the geometric string theory, based on a semi-analytical truncated basis approach. In this approach, a variational wavefunction for the (sc) and (cc) bound states in the string basis is obtained. The truncated basis we introduce below is an exact description for the (sc) and (cc) bound states in the t-J_z limit ($J_\perp = t' = 0$). However, numerical simulations indicate that the qualitative features of the string description remain valid in the t-J model ($J_z = J_\perp$, $t' = 0$) [37, 303, 310, 312, 316, 317, 320, 333, 344–349], and experiments of the Fermi-Hubbard model in ultracold atoms show direct [33] and indirect [7, 8] signatures of string correlations.

10.1.1 Spinon-chargon (sc) bound state: Magnetic polarons

In the following, we consider a (classical) Néel state $|0\rangle$ with long-range AFM order and a single mobile dopant, i.e., the magnetic polaron or (sc) bound state. The perfect Néel background should be a justified approximation when the correlation length $\xi \gg a$ exceeds several lattice constants. To describe the (sc) bound state, we construct a Krylov basis by applying the hopping terms t in the Hamiltonian to the state $\hat{c}_{\mathbf{j},\bar{\sigma}}|0\rangle$ leading to string states Σ discussed below. Thus, the truncated basis for the (sc) bound state is spanned by $\{|\mathbf{j}_\sigma, \Sigma\rangle\}$ with spinon position $\mathbf{j}_\sigma$ and string Σ that connects the spinon to a spinless chargon, see Figure 10.2a.

Let us describe the physical origin of the string Σ. In the strong-coupling limit, $t \gg J$, the time scales of the dopant's motion, $\tau_c \propto t^{-1}$, and magnetic background, $\tau_s \propto J_{\perp}^{-1}$, decouple and we can treat the problem in Born-Oppenheimer approximation, i.e., we choose a product state ansatz for the (sc) bound state $|\psi_{sc}\rangle \approx |\psi_s\rangle \otimes |\psi_c\rangle$ by decomposing the wavefunction into its spinon $|\psi_s\rangle$ and chargon $|\psi_c\rangle$ contribution, see e.g. Ref. [21].

To this end, we consider a single hole $\hat{c}_{\mathbf{j},\bar{\sigma}}$ (electron $\hat{c}_{\mathbf{j},\sigma}^{\dagger}$) doped into a Néel background $|0\rangle$, creating a spinon at position $\mathbf{j}_\sigma$. The fast motion $\propto t$ of the chargon distorts the magnetic order before the magnetic background can adapt on its intrinsic time scale $\tau_s \gg \tau_c$. Thus, in the so-called frozen spin approximation, we consider the motion of the chargon through a static background of spins, where the chargon's motion rearranges the spins; this gives rise to states that we label by $|\mathbf{j}_\sigma, \Sigma\rangle$.

Formally, we define the string states as

$$|\mathbf{j}_\sigma, \Sigma = 0\rangle = \hat{c}_{\mathbf{j},\bar{\sigma}}|0\rangle = \hat{s}_{\mathbf{j},\bar{\sigma}}\hat{h}_{\mathbf{j}}^{\dagger}|0\rangle \tag{10.2a}$$

$$|\mathbf{j}_\sigma, \Sigma' = \Sigma + \mathbf{r}\rangle = (-1)^{|\Sigma'|}\sum_{\sigma}\hat{c}_{\mathbf{j}_\sigma + \Sigma', \sigma}\hat{c}_{\mathbf{j}_\sigma + \Sigma, \sigma}^{\dagger}|\mathbf{j}_\sigma, \Sigma\rangle = (-1)^{|\Sigma'|}\hat{h}_{\mathbf{j}_\sigma + \Sigma'}^{\dagger}f_{\Sigma'}(\hat{s})|0\rangle, \tag{10.2b}$$

where $|\Sigma|$ is the length of string Σ, and $\mathbf{r} = \pm\mathbf{e}_x, \pm\mathbf{e}_y$ is a unit step along the crystal lattice. In the last step, we have defined the operator $f_{\Sigma'}(\hat{s})|0\rangle$ that displaces the bosonic spinon background according to the string Σ. Now, we evaluate the hopping term $\hat{\mathcal{H}}_t$ between connected string states $|\mathbf{j}_\sigma, \Sigma_1\rangle$ and $|\mathbf{j}_\sigma, \Sigma_2\rangle$ with $|\Sigma_2| - |\Sigma_1| = 1$

$$\langle\mathbf{j}_\sigma, \Sigma_2|\hat{\mathcal{H}}_t|\mathbf{j}_\sigma, \Sigma_1\rangle = +t \cdot (-1)^{|\Sigma_1|+|\Sigma_2|}\langle 0|\hat{h}_{\mathbf{j}_\sigma + \Sigma_2}\hat{h}_{\mathbf{j}_\sigma + \Sigma_2}^{\dagger}[f_{\Sigma_2}(\hat{s})]^{\dagger}f_{\Sigma_1}(\hat{s})\hat{h}_{\mathbf{j}_\sigma + \Sigma_1}\hat{h}_{\mathbf{j}_\sigma + \Sigma_1}^{\dagger}|0\rangle = -t. \tag{10.3}$$

Therefore, the (sc) wavefunction amplitudes $\psi_{sc}(|\Sigma|)$ are positive and real for all $|\Sigma|$ in this convention. Note that we have neglected loop effects, which could lead to additional braiding of fermions.

In the string basis, the spinon and chargon position above are not sufficient to describe the state but one needs to take into account the chargon's path, i.e., the string Σ, which begins at the spinon position $\mathbf{j}_\sigma$ and ends at the chargon's position, see Figure 10.2a. Even in a perfect Néel background the string states $\{|\mathbf{j}_\sigma, \Sigma\rangle\}$ have an overcompleteness originating from so-called Trugman loops [311], where some spin configurations can be described by multiple string states. The effect of Trugman loops has been shown to be subdominant [21] to capture the chargon wavefunction $|\psi_c\rangle$ but is important to describe the fine features with precision of a fraction of J in the magnetic polaron's dispersion [319]. In Section 10.3 we will treat loop effects systematically in this model; for now we follow Ref. [21] and assume $\{|\mathbf{j}_\sigma, \Sigma\rangle\}$ to form an orthonormal basis set, for which $|\psi_c\rangle$ can be determined by solving a single-particle problem on the Bethe lattice, as we describe next.

In the orthonormal basis set, the string states can be uniquely characterized by (i) their length ℓ, which is the depth on the Bethe lattice, and (ii) the angle $\lambda^{(N)}$ between the N-th and $(N + 1)$-th string element, see Figure 10.2b. This allows us to re-label the string states

$$|\mathbf{j}_\sigma, \Sigma\rangle = |\mathbf{j}_\sigma, \ell, \lambda^{(0)}, \lambda^{(1)}, ...\rangle, \tag{10.4}$$

where $\lambda^{(0)} = 0, \pi/2, \pi, 3\pi/2$ and $\lambda^{(N)} = -2\pi/3, 0, 2\pi/3$ for $N > 0$. Note, however, that the translational invariance as well as the C4-invariance of the square lattice model can only be simultaneously exploited at C4-invariant momenta, i.e. at momenta $\mathbf{k}^M = (0,0)$ and $\mathbf{k}^M = (\pi/\sqrt{2}, \pi/\sqrt{2})$ in the magnetic Brillouin zone (MBZ).

The MBZ is defined as follows. Since the Néel AFM breaks the sublattice symmetry, the spinon position $\mathbf{j}_\sigma$ is defined in the doubled, AFM unit cell. As a consequence, momenta $\mathbf{k}^M$ are formally defined in the MBZ with band index $\sigma = \downarrow, \uparrow$, which is obtained by reducing the volume of the crystal Brillouin zone (CBZ) by $1/2$ and by rotating the CBZ by $\pi/4$, see Figure 10.3. To be precise, the unit vectors in the MBZ are given by

$$\mathbf{e}_x^M = \frac{1}{\sqrt{2}} \left(\mathbf{e}_x + \mathbf{e}_y \right) \quad \mathbf{e}_y^M = \frac{1}{\sqrt{2}} \left(-\mathbf{e}_x + \mathbf{e}_y \right) \tag{10.5}$$

such that momentum vectors in the first MBZ are given by $\mathbf{k}^M = k_x^M \mathbf{e}_x^M + k_y^M \mathbf{e}_y^M$ with $k_x^M, k_y^M \in \left[-\frac{\pi}{\sqrt{2}}, \frac{\pi}{\sqrt{2}} \right]$. The MBZ momenta $\mathbf{k}^M$ can always be obtained by folding momenta $\mathbf{k}$ from the CBZ into the MBZ; hence we only use the superscript if needed.

Next, we evaluate the t-J Hamiltonian in the string basis, where the hopping term connects different string states, the Ising term J_z corresponds to a confining potential $\propto \ell$, and the flip-flop terms $J_\perp$ give rise to spinon dispersion. At C4-invariant momenta, the total momentum $\mathbf{k}$ and rotational eigenvalues $\{m_4, m_3^{(1)}, m_3^{(2)}, ...\}$ with $m_4 = 0, ..., 3$ (s-, p-, d- and f-wave) and $m_3^{(N)} = 0, ..., 2$ form a set of quantum numbers for the magnetic polaron, see Figure 10.1, and the wavefunction of the n-th eigenstate can be written as [21]

$$|\mathbf{k}, \sigma, n, m_4, \{m_3\}\rangle = \left(\frac{L^2}{2} \right)^{-1/2} \sum_{\mathbf{j}_\sigma} e^{-i\mathbf{k}\mathbf{j}_\sigma} \sum_\ell \sum_{M=0}^{\ell-1} \sum_{\lambda^{(0)}} ... \sum_{\lambda^{(M)}} e^{-i\left[\lambda^{(0)} m_4 + \sum_{N=1}^M \lambda^{(N)} m_3^{(N)} \right]} \times$$
$$\times \frac{1}{\sqrt{4}} \left(\frac{1}{\sqrt{3}} \right)^M \psi_{\text{sc}}^{(n)}(\mathbf{k}, \ell, m_4, \{m_3^{(M)}\}) |\mathbf{j}_\sigma, \ell, \{\lambda^{(M)}\}\rangle. \tag{10.6}$$

The spinon's spin quantum number σ defines the sublattice of the magnetic polaron and L^2 is the volume of the underlying crystal lattice. Moreover, $\psi_{\text{sc}}^{(n)}(\mathbf{k}, \ell, m_4, \{m_3^{(N)}\}) \in \mathbb{R}^{\geq 0}$ are the amplitudes of the normalized wavefunction, which depend on the total momentum $\mathbf{k}$ and the internal degrees-of-freedom; note that we have made a choice of gauge for the string states $\{|\mathbf{j}_\sigma, \Sigma\rangle\}$ in order to obtain positive and real wavefunction amplitudes. Away from the C4-invariant momenta, the angular momentum is not a good quantum number anymore and the different sectors $\{m_4, m_3^{(1)}, m_3^{(2)}, ...\}$ hybridize.

This variational approach agrees with full numerical calculations [279, 316, 333], captures the scaling of the ground-state energy $\propto t^{1/3} J^{2/3}$, and explains the (gapped) excitation spectrum in terms of ro-vibrational string excitations [320, 388]. The magnetic polaron has minimal energy at the nodal points $\mathbf{k} = (\pm\pi/2, \pm\pi/2)$ (CBZ), which are not C4-invariant momenta. However, the wavefunction retains its s-wave character [319, 320]; thus to good approximation we can assume that the ground state of the magnetic polaron has no internal excitations and admits a set of ro-vibrational quantum numbers, i.e. $n = m_4 = m_3^{(N)} = 0$. Therefore we assume the low-energy physics of the doped Mott insulator to only contain magnetic polarons in their internal ground state denoted by $\hat{\pi}_{\mathbf{k},\sigma}^\dagger$; hence we only consider a

single open channel.

So far, we have solved for the chargon (string) wavefunction $|\psi_c\rangle$, which describes a light chargon bound to an infinitely heavy spinon. However, the spinon can become dispersive via (i) Trugman loops and (ii) spin flip-flop processes. Taking these processes into account, a dispersion relation $\varepsilon_{sc}(\mathbf{k})$ for the magnetic polaron can be calculated accurately. For the case of hole doping, this gives rise to the observed hole pockets centered around the nodal points $\mathbf{k} = (\pm\pi/2, \pm\pi/2)$.

This dispersion relation $\varepsilon_{sc}(\mathbf{k})$ can be obtained within our truncated basis approach by taking into account Trugman loops and spin flip-flop $J_\perp$ processes [319]. Moreover, previous studies have derived the dispersion using several methods, including $1/S$ expansion [313–315] and semi-classical theories [389], which find the following approximate expression:

$$\varepsilon_{sc}(\mathbf{k}) = A[\cos{(2k_x)} + \cos{(2k_y)}] + B[\cos{(k_x + k_y)} + \cos{(k_x - k_y)}]. \tag{10.7}$$

Here, the parameters A and B are used as fit parameters; from numerical studies of the single hole problem using a self-consistent Born approximation [315] we extract $A = 0.31$ and $B = 0.44$ for realistic cuprate material parameters, $t/J = 10/3$. This corresponds to elliptical hole pockets with mass ratio $6:1$ at low doping.

In the low-doping regime, the hole pocket-like Fermi surface [313, 314] has been observed in angle-resolved photoemission spectroscopy (ARPES) studies of hole-doped cuprate compounds [248, 335] consistent with quantum oscillation measurements [249]. As argued in Ref. [P11], we assume that at finite but low doping, magnetic polarons can be treated as free fermions forming a Fermi liquid, described by the Hamiltonian

$$\hat{\mathcal{H}}_{open} = \sum_{\mathbf{k},\sigma} [\varepsilon_{sc}(\mathbf{k}) - \mu] \, \hat{\pi}^\dagger_{\mathbf{k},\sigma} \hat{\pi}_{\mathbf{k},\sigma}. \tag{10.8}$$

Upon increasing the chemical potential μ the two hole pockets are filled up. Thus, the free fermion description of the magnetic polarons resembles the normal state of the open channel in the Feshbach hypothesis [P11].

10.1.2 Interacting magnetic polarons: Open channel

For the Feshbach scattering scenario we need to formally define the scattering channels composed of two magnetic polarons $(sc)^2$ (open channel) and the tightly-bound bosonic (cc) mesons (closed channels). The low-energy scattering in the open channel is described by two magnetic polarons $\hat{\pi}^\dagger_{\mathbf{k},\sigma}$ in their internal ground state, see Eq. (10.8). Our main goal is to calculate their scattering length, characterizing their interaction, in the vicinity of a meson Feshbach resonance [P11]. As we discuss later, we only consider low-energy, intra-pocket scattering of two fermions located on the same Fermi surface, i.e. with opposite momenta $\mathbf{k}_\uparrow = -\mathbf{k}_\downarrow$, total momentum $\mathbf{Q} = \mathbf{0}$ and well-defined $C4$-angular momentum. Nevertheless, our formalism – in principle – allows us to describe inter-pocket scattering leading to $(sc)^2$ pairs with non-zero total momentum $\mathbf{Q} \neq \mathbf{0}$.

We consider an arbitrary open-channel state with two magnetic polarons, one on each

sublattice:

$$|\mathbf{k}_\uparrow, \uparrow; \mathbf{k}_\downarrow, \downarrow\rangle = \hat{\pi}^\dagger_{\mathbf{k}_\uparrow, \uparrow} \hat{\pi}^\dagger_{\mathbf{k}_\downarrow, \downarrow}|0\rangle \in \mathscr{H}_\text{open}, \tag{10.9}$$

where $\mathscr{H}_\text{open}$ is the open channel Hilbert space. Using the expression in Eq. (10.6) and assuming no internal ro-vibrational excitations, the pair wavefunction reads

$$|\mathbf{k}_\uparrow, \uparrow; \mathbf{k}_\downarrow, \downarrow\rangle = \frac{2}{L^2} \left[\sum_{\mathbf{j}_\uparrow} e^{-i\mathbf{k}_\uparrow(\mathbf{j}_\uparrow + \mathbf{r})} \sum_{\ell_\uparrow} \sum_{M_\uparrow = 0}^{\ell_\uparrow - 1} \sum_{\lambda_\uparrow^{(0)}} \cdots \sum_{\lambda_\uparrow^{(M_\uparrow)}} \frac{1}{\sqrt{4}} \frac{1}{\sqrt{3^{M_\uparrow}}} \psi_\text{sc}(\mathbf{k}_\uparrow, \ell_\uparrow) |\mathbf{j}_\uparrow, \ell_\uparrow, \{\lambda_\uparrow^{(N)}\}\rangle \right]$$

$$\otimes \left[\sum_{\mathbf{j}_\downarrow} e^{-i\mathbf{k}_\downarrow \mathbf{j}_\downarrow} \sum_{\ell_\downarrow} \sum_{M_\downarrow = 0}^{\ell_\downarrow - 1} \sum_{\lambda_\downarrow^{(0)}} \cdots \sum_{\lambda_\downarrow^{(M_\downarrow)}} \frac{1}{\sqrt{4}} \frac{1}{\sqrt{3^{M_\downarrow}}} \psi_\text{sc}(\mathbf{k}_\downarrow, \ell_\downarrow) |\mathbf{j}_\downarrow, \ell_\downarrow, \{\lambda_\downarrow^{(N)}\}\rangle \right], \tag{10.10}$$

where we have omitted the ro-vibrational quantum numbers of the amplitudes $\psi_\text{sc}(\mathbf{k}_\sigma, \ell_\sigma) \equiv \psi_\text{sc}^{(n=0)}(\mathbf{k}_\sigma, \ell_\sigma, m_4 = 0, m_3^{(N)} = 0)$. The two spinons, $\mathbf{j}_\uparrow$ and $\mathbf{j}_\downarrow$, reside on different sublattices that are dislocated by a displacement vector $\mathbf{r} = (a, 0)$ with lattice spacing a; in the following we set $a = 1$. In our gauge choice, we assume that the $\downarrow$-spinons reside on lattice sites $\mathbf{j}$ and the $\uparrow$-spinons are displaced by $\mathbf{r}$, see Figure 10.3a (right).

Since we want to describe the low-energy properties of the charge carriers, i.e., magnetic polarons, the relevant scattering predominantly happens at the Fermi surface between a pair of (sc)'s with total (quasi)momentum $\mathbf{Q} \bmod \mathbf{G}^M = \mathbf{0}$, where the total (quasi)momentum is only defined up to reciprocal lattice vectors $\mathbf{G}^M = (\pm\pi/\sqrt{2}, \pm\pi/\sqrt{2})$ in the MBZ. We expect that the pairs of magnetic polarons we consider in the scattering problem will form Cooper pairs after integrating out the closed channel. Therefore, we restrict our following calculations to scattering, or Cooper pairs, in the spin singlet channel.

Now, we define the zero-momentum singlet pairing field operator, which we expand in angular momentum eigenfunctions

$$\hat{\Delta}^\dagger_{m_4}(\mathbf{Q} = \mathbf{0}) = \frac{1}{\sqrt{2}} \sum_{\mathbf{k}} f_{m_4}(\mathbf{k}) \left(\hat{\pi}^\dagger_{-\mathbf{k}, \uparrow} \hat{\pi}^\dagger_{\mathbf{k}, \downarrow} - \hat{\pi}^\dagger_{-\mathbf{k}, \downarrow} \hat{\pi}^\dagger_{\mathbf{k}, \uparrow} \right) \tag{10.11}$$

with the relative momentum $\mathbf{k}$, which creates two magnetic polarons in the open channel from vacuum. The function $f_{m_4}(\mathbf{k})$ is an eigenfunction of the $C4$-rotation operator, i.e. it transforms as $f_{m_4}(\mathbf{k}) \to e^{-im_4\pi/2} f_{m_4}(\mathbf{k})$ under $\pi/2$ rotations; otherwise the exact functional form of $f_{m_4}(\mathbf{k})$ is arbitrary. We note that the angular momentum m_4 refers to the *orbital* angular momentum of the pair, not to the magnetic polaron's internal degrees-of-freedom. By using the fermionic anticommutation relations of the magnetic polarons $\hat{\pi}^\dagger_{\mathbf{k}, \sigma}$, we find

$$\hat{\Delta}^\dagger_{m_4}(\mathbf{Q} = \mathbf{0}) = \frac{1}{\sqrt{2}} \sum_{\mathbf{k}} (1 + e^{-im_4\pi}) f_{m_4}(\mathbf{k}) \hat{\pi}^\dagger_{-\mathbf{k}, \uparrow} \hat{\pi}^\dagger_{\mathbf{k}, \downarrow}, \tag{10.12}$$

which is only non-zero for even parity s-wave ($m_4 = 0$) and d-wave ($m_4 = 2$) open channel states. In summary, the low-energy scattering of spin singlet and zero momentum pairs restricts the open channel states to have s-wave or d-wave spatial angular momentum.

10.1.3   Chargon-chargon (cc) bound state: Closed channel

Next, we discuss the properties, and evidence for, tightly-bound bosonic mesons formed by chargon-chargon (cc) bound states. These are the constituents of the closed channel in the Feshbach model proposed in Ref. [P11]. We closely follow the derivation in Ref. [36].

As for the (sc) bound states, the light chargons displace the frozen spin background due to their fast motion $\propto t$, see Figure 10.2a (bottom). However, one chargon can retrace the path of the other giving rise to bound states. Because the chargons are indistinguishable, spinless fermions, the particle statistics plays a crucial role. Alternatively, one may treat chargons as bosons, but in this case the fermionic statistics of the underlying spins in the Hubbard or t-J model lead to an additional statistical phase associated with the geometric string of displaced spins connecting the two chargons. This ultimately leads to an equivalent description [36]. The chargon-chargon bound state is of bosonic nature.

Again, we apply the frozen spin approximation, i.e., we consider two holes or doublons created on opposite sublattices in a Néel ordered state, and consider their correlated motion through the background. In particular, we first assume two distinguishable chargons labeled A and B, and perform an antisymmetrization procedure afterwards.

In contrast to the (sc) bound states, where the spinon was considered heavy and thus frozen, now both constituents A and B are mobile. Hence, we perform a Lee-Low-Pines transformation [390] into the co-moving frame of chargon A, which yields a model of a single chargon at one end of a string, in an effective string potential and with an effective tunneling amplitude that depends on the total momentum $\mathbf{Q}$.

Analogously to the (sc) case, we can introduce a set of orthonormal basis states $|\mathbf{x}_c, \Sigma_{cc}\rangle$ with the position $\mathbf{x}_c$ of chargon A and the string Σ_{cc} connecting the two chargons. Again, these states are defined on a Bethe lattice, see Figure 10.2b, but with chargon A in the center. Thus, we can likewise use basis states with fixed string length ℓ and angles $\{\lambda^{(N)}\}$ as above,

$$|\mathbf{x}_c, \Sigma_{cc}\rangle = |\mathbf{x}_c, \ell, \{\lambda^{(N)}\}\rangle \tag{10.13}$$

Formally, we define the (cc) basis states as

$$|\mathbf{x}_c, \Sigma = \mathbf{r}\rangle = \hat{c}_{\mathbf{x}_c,\sigma}\hat{c}_{\mathbf{x}_c+\Sigma,\bar{\sigma}}|0\rangle = \hat{s}_{\mathbf{x}_c,\sigma}\hat{s}_{\mathbf{x}_c+\Sigma,\bar{\sigma}}\hat{h}^\dagger_{\mathbf{x}_c}\hat{h}^\dagger_{\mathbf{x}_c+\Sigma}|0\rangle \tag{10.14a}$$

$$|\mathbf{x}_c, \Sigma' = \Sigma + \mathbf{r}\rangle = (-1)^{|\Sigma'|+1}\sum_\sigma \hat{c}_{\mathbf{x}_c+\Sigma',\sigma}\hat{c}^\dagger_{\mathbf{x}_c+\Sigma,\sigma}|\mathbf{x}_c, \Sigma\rangle = (-1)^{|\Sigma'|+1}\hat{h}^\dagger_{\mathbf{x}_c}\hat{h}^\dagger_{\mathbf{x}_c+\Sigma'}f_{\Sigma'}(\hat{s})|0\rangle. \tag{10.14b}$$

In a tunneling process, the string length changes by $|\Sigma_2| - |\Sigma_1| = 1$ leading to amplitudes,

$$\langle \mathbf{x}_c, \Sigma_2|\hat{\mathcal{H}}_t|\mathbf{x}_c, \Sigma_1\rangle =$$
$$= +t \cdot (-1)^{|\Sigma_1|+|\Sigma_2|+2}\langle 0|\hat{h}_{\mathbf{x}_c+\Sigma_2}\hat{h}_{\mathbf{x}_c}\hat{h}^\dagger_{\mathbf{x}_c+\Sigma_2}[f_{\Sigma_2}(\hat{s})]^\dagger f_{\Sigma_1}(\hat{s})\hat{h}_{\mathbf{x}_c+\Sigma_1}\hat{h}^\dagger_{\mathbf{x}_c}\hat{h}^\dagger_{\mathbf{x}_c,\Sigma_1}|0\rangle = -t \tag{10.15}$$

and

$$\langle \mathbf{x}_c + \mathbf{r}, \Sigma_2|\hat{\mathcal{H}}_t|\mathbf{x}_c, \Sigma_1\rangle =$$
$$= +t \cdot (-1)^{|\Sigma_1|+|\Sigma_2|+2}\langle 0|\hat{h}_{\mathbf{x}_c+\Sigma_2}\hat{h}_{\mathbf{x}_c+\mathbf{r}}\hat{h}^\dagger_{\mathbf{x}_c+\mathbf{r}}[f_{\Sigma_2}(\hat{s})]^\dagger f_{\Sigma_1}(\hat{s})\hat{h}_{\mathbf{x}_c}\hat{h}^\dagger_{\mathbf{x}_c}\hat{h}^\dagger_{\mathbf{x}_c,\Sigma_1}|0\rangle = -t \tag{10.16}$$

We perform the Fourier transformation to obtain momentum states

$$|\mathbf{Q}, \ell, \{\lambda^{(N)}\}\rangle = \frac{1}{\sqrt{L^2}} \sum_{\mathbf{x}_c} e^{-i\mathbf{Q}\mathbf{x}_c} |\mathbf{x}_c, \ell, \{\lambda^{(N)}\}\rangle. \tag{10.17}$$

Note that the momentum $\mathbf{Q}$ is now defined in the CBZ because, at the level of our approximations so far, the chargons are not restricted to a sublattice. Further, at $C4$-invariant momenta, we can define rotational eigenstates

$$|\mathbf{Q}, \ell, m_4, \{m_3^{(N)}\}\rangle = \sum_{M=0}^{\ell-1} \frac{1}{\sqrt{4}} \frac{1}{\sqrt{3^M}} e^{-i\left[\lambda^{(0)}m_4 + \sum_{N=1}^{M} \lambda^{(N)}m_3^{(N)}\right]} |\mathbf{Q}, \ell, \{\lambda^{(N)}\}\rangle. \tag{10.18}$$

To accommodate for the particle statistics, the states in Eq. (10.18) have to be (anti)symmetrized. The resulting antisymmetric states then span the closed channel Hilbert space $\mathcal{H}_{\text{closed}}$.

At the two $C4$-invariant momenta, $\mathbf{Q} = \mathbf{0}$ and $\mathbf{Q} = \boldsymbol{\pi}$, the chargon-chargon bound states have well-defined rotational quantum numbers with p- and f-wave ($\mathbf{Q} = \mathbf{0}$) as well as s- and d-wave ($\mathbf{Q} = \boldsymbol{\pi}$) symmetry in the fermionic sector.

The translational and $C4$-rotational invariance of the underlying model, Eq. (10.1), allow us to derive selection rules for the matrix elements, which couple between open and closed channel states. As discussed above, we only consider couplings to states with $\mathbf{Q} \bmod \mathbf{G}^M = \mathbf{0}$; thus the channels have well-defined angular momentum quantum numbers. Since the open channel has even parity, Eq. (10.12), we conclude that only even parity channels contribute to the scattering of magnetic polarons; hence non-zero matrix elements arise only between s-wave (d-wave) open channel and s-wave (d-wave) closed channel states at $\mathbf{Q} \bmod \mathbf{G}^M = \boldsymbol{\pi} \bmod \mathbf{G}^M = \mathbf{0}$.

A Feshbach resonance describes the scattering within an open channel in the presence of a near-resonant closed channel that can be virtually occupied. In addition to the coupling matrix elements, the bare energy difference ΔE_{m_4} between the (uncoupled) channels determines the strength $\propto 1/\Delta E_{m_4}$ of the scattering length. Here, we distinguish the two possible couplings to closed channels with s-wave ($m_4 = 0$) and d-wave ($m_4 = 2$) symmetry; hence we further reduce the multichannel description using selection rules. Numerical simulations of the t-J model [34, 37] have calculated the angular-momentum resolved two-hole spectra at $\mathbf{Q} \bmod \mathbf{G}^M = \mathbf{0}$. At the relevant momenta, they clearly indicate a large energy difference between the s-wave, $\Delta E_{m_4=0} = \mathcal{O}(t)$, and d-wave, $\Delta E_{m_4=2} = \mathcal{O}(J)$, channels; hence only the d-wave (cc) state gives rise to near-resonant scattering. Therefore, we conclude that the effective scattering length is dominated by the d-wave channel, which allows us to consider an effective two-channel model in the following [P11]. Likewise, we recognize that other scenarios are possible such as triplet pairing or inter-valley scattering, which could be described analogously within our formalism.

Now, we define the basis states $|\mathbf{Q} = \boldsymbol{\pi}, \ell, m_4 = 2\rangle$ to be the fermionic states in the relevant two-channel model. This allows us to express the closed-channel wavefunction of
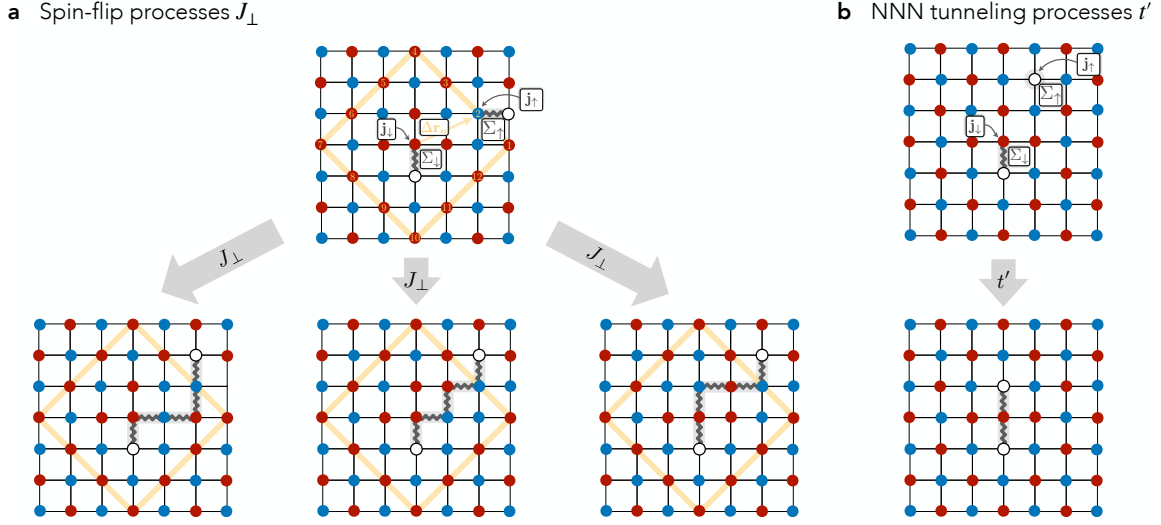
Figure 10.4: **Recombination processes: sc + sc → cc.** The open and closed channel are coupled via processes that annihilate and create pairwise spinons. **a** Spin-flip processes couple magnetic polarons at Manhattan distance $||\Delta \mathbf{r}_n||_M = ||\mathbf{j}_\uparrow - (\mathbf{j}_\downarrow + \mathbf{r})||_M = 3$. In the co-moving frame of one spinon, the other spinon has to be located on sites indicated by the yellow box. The spin flip-flop $J_\perp$ annihilates the magnetic polarons and creates a chargon-chargon pair with string length $\ell = \ell_\downarrow + \ell_\uparrow + 3$ (besides one special case with $\ell = \ell_\downarrow + \ell_\uparrow - 1$). For the shortest string length approximation (SSLA) we consider $\ell_\downarrow = \ell_\uparrow = 0$. **b** Similarly, next-nearest neighbour tunneling t' couples the open and closed channel.

the tightly-bound (cc) state without vibrational excitations,

$$
\begin{aligned}
|\mathbf{Q} = \boldsymbol{\pi}\rangle &= \hat{b}^\dagger_{m_4=2}(\mathbf{Q} = \boldsymbol{\pi})|0\rangle = \\
&= \frac{1}{\sqrt{L^2}} \sum_{\mathbf{x}_c} e^{-i\mathbf{Q}\mathbf{x}_c} \sum_\ell \phi_{cc}(\mathbf{Q} = \boldsymbol{\pi}, \ell)|\mathbf{Q} = \boldsymbol{\pi}, \ell, m_4 = 2\rangle.
\end{aligned}
\tag{10.19}
$$

Here, we have defined the bosonic creation operator for the (cc) state $\hat{b}^\dagger_{m_4=2}(\mathbf{Q})$ with angular momentum $m_4 = 2$ and total momentum $\mathbf{Q} = \boldsymbol{\pi}$. Further, we can expand the wavefunction in the angular basis of string states, Eq. (10.18),

$$
\begin{aligned}
|\mathbf{Q} = \boldsymbol{\pi}\rangle &= \\
&= \frac{1}{\sqrt{L^2}} \sum_{\mathbf{x}_c} e^{-i\mathbf{Q}\mathbf{x}_c} \sum_\ell \sum_{M=0}^{\ell-1} \sum_{\lambda^{(0)}} ... \sum_{\lambda^{(M)}} e^{-i\lambda^{(0)} m_4} \\
&\times \phi_{cc}(\mathbf{Q} = \boldsymbol{\pi}, \ell) \hat{P}_f |\mathbf{x}_c, \ell, \{\lambda^{(N)}\}\rangle,
\end{aligned}
\tag{10.20}
$$

where $\hat{P}_f$ projects onto the fermionic states.

In the next section, we will describe the coupling between the open and closed channels. To this end, we need to describe the open and closed channel on an equal footing. In the geometric string picture, the (cc) bound state does not distinguish between the sublattices and therefore, in this formulation, the momenta can be defined in the CBZ; in contrast to the magnetic polarons, which have a well-defined sublattice/spin quantum number. Therefore,

we fold the momentum from the larger CBZ into the smaller MBZ, see Figure 10.3b, by introducing a band index $\alpha = 0, 1$, such that

$$\hat{b}^\dagger_{m_4=2,\alpha}(\mathbf{Q}) = \sqrt{\frac{2}{L^2}} \sum_{\mathbf{j}_\downarrow} e^{-i(\mathbf{j}_\downarrow + \alpha \mathbf{r})\mathbf{Q}} \hat{b}^\dagger_{m_4=2,\alpha}(\mathbf{j}_\downarrow), \tag{10.21}$$

where $\mathbf{j}_\downarrow$ now labels the two site unit cells and α is a band index describing the position within the unit cell. In particular, we can consider the (cc) creation operator in the larger CBZ and relate it to the MBZ by considering

$$\hat{b}^\dagger_{m_4=2}(\mathbf{Q}) = \frac{1}{\sqrt{L^2}} \sum_{\mathbf{j}_\downarrow} e^{-i\mathbf{j}_\downarrow \mathbf{Q}} \left[\hat{b}^\dagger_{m_4=2,0}(\mathbf{j}_\downarrow) + e^{-i\mathbf{r}\mathbf{Q}} \hat{b}^\dagger_{m_4=2,1}(\mathbf{j}_\downarrow) \right] =$$

$$= \begin{cases} \frac{1}{\sqrt{2}} \left[\hat{b}^\dagger_{m_4=2,0}(\mathbf{Q}) + \hat{b}^\dagger_{m_4=2,1}(\mathbf{Q}) \right] & \text{for } \mathbf{Q} \in \text{MBZ} \\ \\ \frac{1}{\sqrt{2}} \left[\hat{b}^\dagger_{m_4=2,0}(\mathbf{Q} \bmod \mathbf{G}^\text{M}) + e^{i\mathbf{r}\mathbf{G}^\text{M}} \hat{b}^\dagger_{m_4=2,1}(\mathbf{Q} \bmod \mathbf{G}^\text{M}) \right] & \text{for } \mathbf{Q} \notin \text{MBZ} \end{cases} \tag{10.22}$$

Therefore, we find that the momentum $\mathbf{Q} = \mathbf{0}$ ($\mathbf{Q} = \pi$) corresponds to triplet (singlet) combinations in the band index sector; hence the band index equips the (cc) bound state with a pseudospin. This ultimately allows us to couple an open channel pair, see Eq. (10.12), with s- and d-wave angular momentum to a closed channel state despite their constituents being spinful (open channel) and spinless (closed channel).

Note that throughout Section 10.1, we considered a classical Néel background, i.e. $J_\perp = 0$, to derive the open and closed channel states. However the two channels still exist in the presence of spin fluctuations $J_\perp$ and only microscopic details are affected [32, 37, 303, 313]. Further, cold atom experiments in the Fermi-Hubbard model have shown signatures of strings [7, 8, 33] indicating that the geometric picture is valid beyond the t-J model and at finite temperature. While in the following we will assume a perfect product Néel state $|0\rangle$, we emphasize that strong local AFM correlations with coherence length of $\xi_\text{AFM}/a \gtrsim 10$ should lead to qualitatively similar result.

10.2   Meson scattering interaction

In the proposed Feshbach scenario [P11], it is suggested that a magnetic polaron pair $(\text{sc})^2$ and a (cc) meson can spatially overlap leading to a coupling of the two channels. Here, we explicitly calculate the coupling matrix elements (or form factors) originating from the microscopic Hamiltonian (10.1) by applying the open and closed channel string description introduced in Secs 10.1.2 and 10.1.3. The possible coupling processes between the two channels are associated with 1) spin-flip processes ($J_\perp$) and 2) NNN tunneling (t'), as illustrated

	$\ell = 0$	$\ell = 1$	$\ell = 2$	$\ell = 3$	$\ell = 4$	$\ell = 5$
$\psi_{\text{sc}}(\mathbf{k}, \ell)$	$\sqrt{0.25}$	$\sqrt{0.38/4}$	$\sqrt{0.22/(4 \cdot 3)}$	$\sqrt{0.09/(4 \cdot 3^2)}$	$\sqrt{0.05/(4 \cdot 3^3)}$	$\sqrt{0.01/(4 \cdot 3^4)}$
$p_{\mathbf{k},\text{sc}}(\ell)$	0.25	0.38	0.22	0.09	0.05	0.01
$\phi_{\text{cc}}(\mathbf{Q} = \boldsymbol{\pi}, \ell)$	–	$\sqrt{0.09/4}$	$\sqrt{0.26/8}$	$\sqrt{0.32/20}$	$\sqrt{0.22/48}$	$\sqrt{0.09/148}$
$p_{\mathbf{Q}=\pi,\text{cc}}(\ell)$	–	0.09	0.26	0.32	0.22	0.09

Table 10.1: **String length amplitudes.** The wavefunction amplitudes for the spinon-chargon ψ_{sc} are extracted from Ref. [303] for $t/J = 3$. The wavefunction amplitudes for the chargon-chargon ϕ_{cc} are extracted from Ref. [36] for $t/J = 3$. The renormalization factor for the latter includes the normalization after projection onto fermionic states at $\mathbf{Q} = \boldsymbol{\pi}$. The string length distribution can be obtained from $p_{\text{sc}}(\mathbf{k}, \ell) = \mathcal{N}_{\text{sc}}^\ell |\psi_{\text{sc}}(\mathbf{k}, \ell)|^2$, where $\mathcal{N}_{\text{sc}}^\ell$ are the number of string states of length ℓ, and further around the dispersion minimum the momentum dependency is negligible $p_{\text{sc}}(\mathbf{k}, \ell) \approx p_{\text{sc}}(\ell)$. The string length distribution for the (cc) case is obtained analogously.

in Figure 10.4 and defined by the open-closed channel coupling Hamiltonian

$$
\begin{aligned}
\hat{\mathcal{H}}_{\text{oc}} &= \hat{\mathcal{H}}_{J_\perp} + \hat{\mathcal{H}}_{t'} \\
\hat{\mathcal{H}}_{J_\perp} &= \frac{J_\perp}{2} \sum_{\langle i,j \rangle} \left(\hat{S}_i^+ \hat{S}_j^- + \text{H.c.} \right) \\
\hat{\mathcal{H}}_{t'} &= -t' \sum_{\langle\langle i,j \rangle\rangle} \sum_\sigma \left(\hat{c}_{\mathbf{i},\sigma}^\dagger \hat{c}_{\mathbf{j},\sigma} + \text{H.c.} \right),
\end{aligned}
\tag{10.23}
$$

projected to our truncated two-channel basis. The resulting scattering interaction $V_{\mathbf{k},\mathbf{k}'}$ describing the Feshbach resonance is then given by

$$
V_{\mathbf{k},\mathbf{k}'} = \frac{1}{L^2} \sum_{m_4} \frac{\mathcal{M}_{m_4}^*(\mathbf{k}') \mathcal{M}_{m_4}(\mathbf{k})}{\Delta E_{m_4}}
\tag{10.24}
$$

with the form factors/matrix elements $\mathcal{M}_{m_4}(\mathbf{k})$. In the following, we focus on the relevant d-wave scattering channel ($m_4 = 2$), i.e. we want to evaluate

$$
\mathcal{M}_2(\mathbf{k}) = J_\perp \mathcal{M}_2^{J_\perp}(\mathbf{k}) + t' \mathcal{M}_2^{t'}(\mathbf{k})
\tag{10.25a}
$$

$$
\frac{\kappa}{\sqrt{L^2}} \mathcal{M}_2^\kappa(\mathbf{k}) = \langle 0 | \hat{b}_{m_4=2}(\mathbf{Q} = \boldsymbol{\pi}) \hat{\mathcal{H}}_\kappa \hat{\pi}_{-\mathbf{k},\uparrow}^\dagger \hat{\pi}_{\mathbf{k},\downarrow}^\dagger | 0 \rangle,
\tag{10.25b}
$$

where $\kappa = J_\perp, t'$ and $\mathbf{k}'$ ($\mathbf{k}$) is the in-coming (out-going) momentum. From Eq. (10.25), we find that it is sufficient to calculate the matrix elements for spin-flip and NNN tunneling processes individually.

10.2.1 Spin-flip processes

First, we focus on the spin-flip recombination processes, i.e. we calculate the form factor $\frac{J_\perp}{\sqrt{L^2}} \mathcal{M}_2^{J_\perp}(\mathbf{k})$. To evaluate Eq. (10.25b), we expand the states in real space according to Eqs. (10.10) and (10.20). In real space, it is straightforward to determine how the spin flip-

flop interactions $J_\perp$ couple between the open and closed channel states, see Figure 10.4a. To be precise, they annihilate opposite spinons at sites $\mathbf{j}_\downarrow$ and $\mathbf{j}_\uparrow$ that are Manhattan distance $||\Delta\mathbf{r}_n||_M = ||(\mathbf{j}_\uparrow + \mathbf{r}) - \mathbf{j}_\downarrow||_M = 3$ apart. The recombination processes thus couple magnetic polarons of length $\ell_\downarrow$ and $\ell_\uparrow$ to (cc) states of length $\ell = \ell_\downarrow + \ell_\uparrow + \Delta\ell$ with $\Delta\ell = -1, 3$.

For realistic parameters $t/J \approx 2, 3$, the magnetic polaron (sc) string length is peaked around $\ell_\sigma = 0$ and the (cc) string length distribution has its maximum at $\ell = 3$, see Table 10.1. Therefore, the largest contribution to the form factors (10.25b) occurs for the peaked string lengths, which justifies a short string length approximation (SSLA). The latter includes only $\ell_\uparrow = \ell_\downarrow = 0$ and $\ell = 3$. Later, we will systematically include longer strings based on numerical calculations of the matrix elements. In SSLA the matrix elements can be written as

$$\frac{J_\perp}{\sqrt{L^2}} \mathcal{M}_2^{J_\perp}(\mathbf{k}) = \frac{2}{L^3} \sum_{\mathbf{x}_c, \mathbf{j}_\downarrow, \mathbf{j}_\uparrow} e^{i\left[\mathbf{Q}\mathbf{x}_c - \mathbf{k}(\mathbf{j}_\uparrow + \mathbf{r}) + \mathbf{k}\mathbf{j}_\downarrow\right]} \sum_{\lambda^{(0)}} \sum_{\lambda^{(1)}} \sum_{\lambda^{(2)}} e^{i\lambda^{(0)}m_4} \phi_{cc}^*(\mathbf{Q}, \ell = 3) \times$$

$$\times \psi_{sc}(\mathbf{k}, \ell_\downarrow = 0) \psi_{sc}(-\mathbf{k}, \ell_\uparrow = 0) \langle \mathbf{x}_c, \ell = 3, \{\lambda^{(N)}\} | \hat{P}_f \hat{\mathcal{H}}_{J_\perp} \left(|\mathbf{j}_\downarrow, \ell_\downarrow = 0\rangle \otimes |\mathbf{j}_\uparrow, \ell_\uparrow = 0\rangle\right).$$
$$(10.26)$$

In real space the coupling elements are given by

$$\langle \mathbf{x}_c, \ell = 3, \{\lambda^{(N)}\} | \hat{P}_f \hat{\mathcal{H}}_{J_\perp} \left(|\mathbf{j}_\downarrow, \ell_\downarrow = 0\rangle \otimes |\mathbf{j}_\uparrow, \ell_\uparrow = 0\rangle\right) = J_\perp \delta_{\mathbf{x}_c, \mathbf{j}_\downarrow} \sum_{\Delta\mathbf{r}_n} \delta_{\Delta\mathbf{r}_n, \mathbf{j}_\uparrow + \mathbf{r} - \mathbf{j}_\downarrow} \sum_{\{\lambda(N)\}} \delta_{\lambda^{(N)}, \lambda_f^{(N)}},$$
$$(10.27)$$

where the last term ensures that only fermionic string states $\lambda_f^{(N)}$ contribute and $\Delta\mathbf{r}_n$ denotes all real space configurations that can annihilate spinons, see Figure 10.4a. The non-zero matrix elements can be read off from the open and closed channel wavefunctions illustrated in Figure 10.5.

Therefore, the expression becomes

$$\frac{J_\perp}{\sqrt{L^2}} \mathcal{M}_2^{J_\perp}(\mathbf{k}) = \frac{2J_\perp}{L^3} \sum_{\mathbf{j}_\downarrow} e^{i\mathbf{j}_\downarrow \mathbf{Q}} \phi_{cc}^*(\mathbf{Q}, \ell = 3) \psi_{sc}(\mathbf{k}, \ell_\downarrow = 0) \psi_{sc}(-\mathbf{k}, \ell_\uparrow = 0) \times$$

$$\times \underbrace{\sum_{\Delta\mathbf{r}_n} e^{-i\mathbf{k}\Delta\mathbf{r}_n} \sideset{}{'}\sum_{\lambda^{(0)}} \sideset{}{'}\sum_{\lambda^{(1)}} \sideset{}{'}\sum_{\lambda^{(2)}} e^{i\lambda^{(0)}m_4}}_{\equiv \chi^{J_\perp}(\mathbf{k})}.$$
$$(10.28)$$

The restricted sum runs over the fermionic string states with strings starting at $\mathbf{j}_\downarrow$ and ending at $\mathbf{j}_\downarrow + \Delta\mathbf{r}_n$. To simplify the expression, we use the following identity

$$\sum_{\mathbf{j}_\downarrow} e^{-i\mathbf{Q}\mathbf{j}_\downarrow} = \frac{L^2}{2} \delta\left[\mathbf{Q} \bmod \mathbf{G}^M\right],$$
$$(10.29)$$

which gives the expression for the form factors.

We further define the functions

$$\Omega(\mathbf{Q}, \mathbf{k}) = \phi_{cc}^*(\mathbf{Q}, \ell = 3) \psi_{sc}(\mathbf{k}, \ell_\downarrow = 0) \psi_{sc}(-\mathbf{k}, \ell_\uparrow = 0)$$
$$(10.30)$$

a Open channel

$|-\mathbf{k}, \uparrow; \mathbf{k}, \downarrow\rangle \propto$

$\ldots + e^{\frac{i}{\sqrt{2}}\left(3k_x^M - 3k_y^M\right)}$ $+ e^{\frac{i}{\sqrt{2}}\left(3k_x^M - k_y^M\right)}$ $+ e^{\frac{i}{\sqrt{2}}\left(3k_x^M + k_y^M\right)}$

$+ e^{\frac{i}{\sqrt{2}}\left(3k_x^M + 3k_y^M\right)}$ $+ e^{\frac{i}{\sqrt{2}}\left(k_x^M + 3k_y^M\right)}$ $+ e^{\frac{i}{\sqrt{2}}\left(-k_x^M + 3k_y^M\right)}$

$+ e^{\frac{i}{\sqrt{2}}\left(-3k_x^M + 3k_y^M\right)}$ $+ e^{\frac{i}{\sqrt{2}}\left(-3k_x^M + k_y^M\right)}$ $+ e^{\frac{i}{\sqrt{2}}\left(-3k_x^M - k_y^M\right)}$

$+ e^{\frac{i}{\sqrt{2}}\left(-3k_x^M - 3k_y^M\right)}$ $+ e^{\frac{i}{\sqrt{2}}\left(-k_x^M - 3k_y^M\right)}$ $+ e^{\frac{i}{\sqrt{2}}\left(k_x^M - 3k_y^M\right)}$ $+\ldots$

b Closed channel

$|\mathbf{Q} = \boldsymbol{\pi}\rangle \propto \ldots +$ $+$ $-$

$-$ $-$ $+$

$+$ $+$ $-$

$-$ $-$ $+$ $+\ldots$

Figure 10.5: **Shortest string length approximation (SSLA) – Spin flip. a** We show the contributions to the wavefunction of the open channel, where the two chargons are Manhattan distance $||\Delta\mathbf{r}_n||_M = 3$ apart and the string length is $\ell_\uparrow = \ell_\downarrow = 0$. These states couple to the closed channel with substantial overlap to the (cc) wavefunction illustrated in **b**, where the string length is $\ell = 3$. The overlaps have to be weighted by momentum-dependent phase factors (here with momenta k_x^M, k_y^M measured in the $\pi/4$-rotated MBZ basis, see Eq. (10.5)) and symmetry properties of the d-wave closed channel have to be taken into account. The shown contributions constitute all twelve terms in the SSLA.

$$\chi^{J_\perp}(\mathbf{k}) = \sum_{\Delta\mathbf{r}_n} e^{-i\mathbf{k}\Delta\mathbf{r}_n} \sum_{\lambda^{(0)}}{}' \sum_{\lambda^{(1)}}{}' \sum_{\lambda^{(2)}}{}' e^{i2\lambda^{(0)}}, \tag{10.31}$$

where we have set $m_4 = 2$ for the d-wave channel. In the vicinity of the dispersion minimum, $\mathbf{k} = (\pm\pi/2, \pm\pi/2) + \delta\mathbf{k}$ with $|\delta\mathbf{k}| \ll \pi$, the wavefunction amplitudes are assumed to be $\mathbf{k}$-independent for s-wave magnetic polarons; in Section 10.3 we account for the full momentum dependence.

Instead, the function $\chi^{J_\perp}(\mathbf{k})$ is highly $\mathbf{k}$-dependent and determines the structure of the form factor Eq. (10.25). In particular, in SSLA we can evaluate the form factors for spin-flip
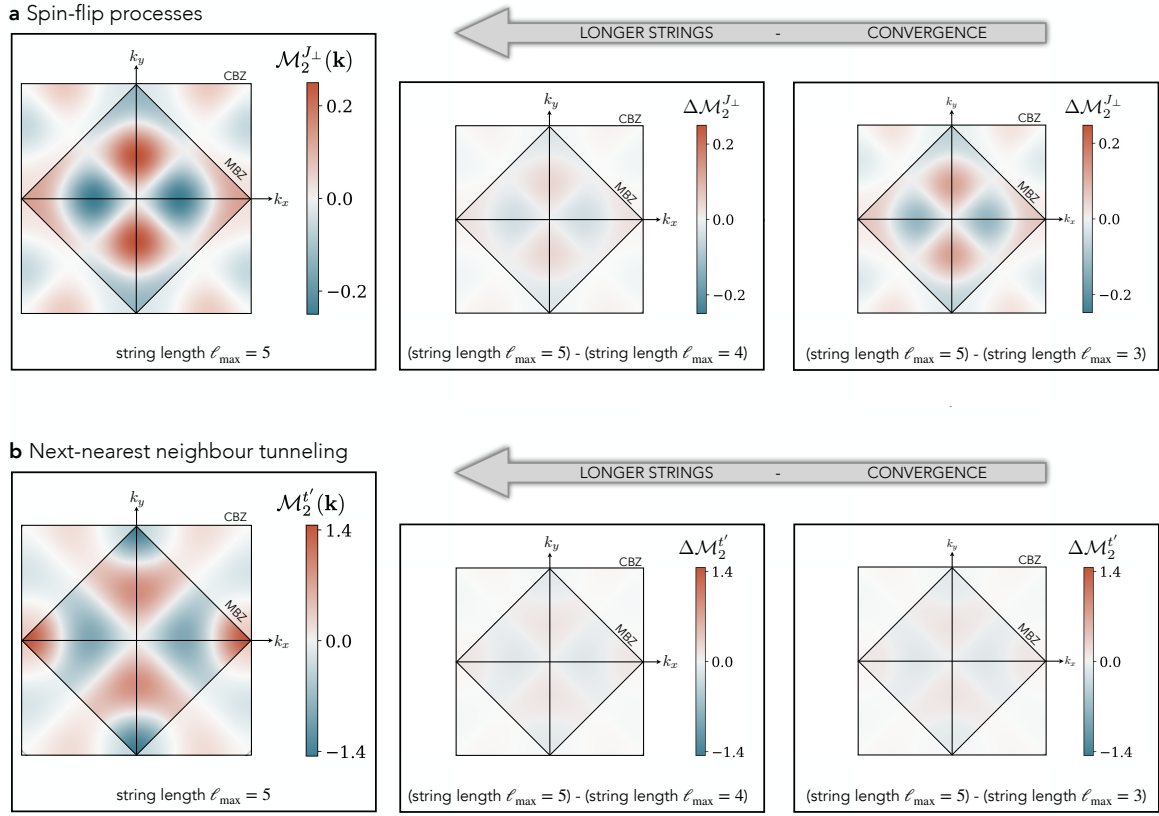
Figure 10.6: **Testing the shortest string length approximation (SSLA).** We compute the matrix element relevant for the scattering processes numerically, and cut off at different maximal string length $\ell_{\max}$ of the involved (cc) states for **a** spin-flip processes and **b** NNN tunneling. We compare the $\ell_{\max} = 5$ calculations to calculations with shorter strings. We note that the relative difference between $\ell_{\max} = 5$ and $\ell_{\max} = 3$ is relatively small, which justifies the analytically tractable SSLA approximation.

recombination processes analytically. We carefully treat the momentum $\mathbf{k}^M$ and real space vectors $\Delta \mathbf{r}_n$ in the MBZ, see Figure 10.3 and Eq. (10.5). In Figure 10.5, we show the corresponding phase factors $\chi^{J_\perp}(\mathbf{k})$ for momenta in the MBZ. We sum up the matrix element, and obtain

$$
\begin{aligned}
\chi^{J_\perp}(\mathbf{k}^M) =2\Bigg[&\cos\left(\frac{k_x^M - 3k_y^M}{\sqrt{2}}\right) + \cos\left(\frac{3k_x^M - 3k_y^M}{\sqrt{2}}\right) \\
&+ \cos\left(\frac{3k_x^M - k_y^M}{\sqrt{2}}\right) - \cos\left(\frac{3k_x^M + 3k_y^M}{\sqrt{2}}\right) \\
&- \cos\left(\frac{3k_x^M + k_y^M}{\sqrt{2}}\right) - \cos\left(\frac{k_x^M + 3k_y^M}{\sqrt{2}}\right) \Bigg],
\end{aligned}
\tag{10.32}
$$

which has $d_{x^2-y^2}$ nodal structure in the CBZ (or equivalently d_{xy} nodal structure in the $\pi/4$-rotated MBZ).

It is important to confirm the validity of the SSLA by systematically including longer

strings. We automatize the formalism described above and perform exact numerical calculations in the string picture. Each string length realization now has to be weighted by wavefunction amplitudes $\phi_{cc}(\mathbf{Q} = \boldsymbol{\pi}, \ell)$ and $\psi_{sc}(\mathbf{k}, \ell_\sigma)$, which we extract from previous studies, see Refs. [36, 303] and Table 10.1.

   We calculate the matrix element and plot $\mathcal{M}_2^{J_\perp}(\mathbf{k})$, see Eq. (10.25b), for different maximal (cc) string length cut-offs ℓ_{max} up to $\ell_{max} = 5$. Then, we compare the calculation of $\ell_{max} = 5$ with short strings as shown in Figure 10.6a. Note that for $\ell_{max} = 5$, the string lengths of the magnetic polarons are bounded to $\max(\ell_\downarrow, \ell_\uparrow) = 2$, which has the advantage that we do not have to consider Trugman loops or crossings of strings.

   We find that already the SSLA gives qualitatively the correct behaviour, while the quantitative results are only slightly renormalized by including longer string lengths. We emphasize the robustness of the proposed Feshbach mechanism [P11] with respect to the $d_{x^2-y^2}$ nodal structure, which is caused by the symmetry properties of the closed channel but not by the details of the geometric string wavefunctions.

10.2.2   Next-nearest neighbour tunnelings

Next, we perform the calculations for the NNN tunneling terms t', Eq. (10.23), which we can include perturbatively in our description. I.e., for now we do not assume that the properties of the (sc) and (cc) bound states are affected by NNN tunneling but we only include the terms in small perturbation in $|t'| < J_\perp$; in Section 10.3 we will consider the case where the open and closed channel are renormalized by t'. In cuprate materials, the NN and NNN tunneling ratio $t/t' < 0$ [391] is negative, and throughout this study we apply a gauge that fixes $t > 0$.

   In the following, we evaluate the form factor $\mathcal{M}_2^{t'}(\mathbf{k})$. To gain intuition about the processes contributing to NNN tunneling, we illustrate an example in Figure 10.4b. We find that two (sc)'s with strings of length $\ell_\downarrow = 0$ and $\ell_\uparrow$ ($\ell_\uparrow = 0$ and $\ell_\downarrow$) can combine to (cc) bound states of length $\ell = \ell_\uparrow + 1$ ($\ell = \ell_\downarrow + 1$). Again, we apply SSLA to calculate the contributions to $\mathcal{M}_2^{t'}(\mathbf{k})$ for short strings, similar to the procedure described in Section 10.2.1, and we find

$$
\chi^{t'}(\mathbf{k}^M) = 2\left[\cos\left(\frac{k_x^M - 3k_y^M}{\sqrt{2}}\right) + \cos\left(\frac{3k_x^M - k_y^M}{\sqrt{2}}\right) \right.
$$
$$
\left. - \cos\left(\frac{3k_x^M + k_y^M}{\sqrt{2}}\right) - \cos\left(\frac{k_x^M + 3k_y^M}{\sqrt{2}}\right) \right],
$$
(10.33)

where $\chi^{t'}(\mathbf{k}^M)$ takes the role of $\chi^{J_\perp}(\mathbf{k}^M)$ as in Eq. (10.28). The contributing processes are illustrated in Figure 10.7.

   To account for long strings, we numerically evaluate the dimensionless form factor $\mathcal{M}_2^{t'}(\mathbf{k})$, which we show in Figure 10.6b together with convergence plots for SSLA. From the above considerations, we conclude that a (cc) bound state with string length $\ell_{max} = 5$, can only couple to magnetic polarons with string length ($\ell_\downarrow = 0, \ell_\uparrow \leq 4$) and ($\ell_\downarrow \leq 4, \ell_\uparrow = 0$). Hence, we again do not encounter Trugman loops or crossings of magnetic polaron strings.

a Open channel

$|-\mathbf{k}, \uparrow; \mathbf{k}, \downarrow\rangle \propto$

$+e^{\frac{i}{\sqrt{2}}\left(3k_x^M - k_y^M\right)}$ $+e^{\frac{i}{\sqrt{2}}\left(3k_x^M + k_y^M\right)}$

$+e^{\frac{i}{\sqrt{2}}\left(k_x^M + 3k_y^M\right)}$ $+e^{\frac{i}{\sqrt{2}}\left(-k_x^M + 3k_y^M\right)}$

$+e^{\frac{i}{\sqrt{2}}\left(-3k_x^M + k_y^M\right)}$ $+e^{\frac{i}{\sqrt{2}}\left(-3k_x^M - k_y^M\right)}$

$+e^{\frac{i}{\sqrt{2}}\left(-k_x^M - 3k_y^M\right)}$ $+e^{\frac{i}{\sqrt{2}}\left(k_x^M - 3k_y^M\right)}$ $+...$

b Closed channel

$|\mathbf{Q} = \boldsymbol{\pi}\rangle \propto ...+$ $-$

$+$ $-$ $+...$

Figure 10.7: **Shortest string length approximation (SSLA) – NNN tunneling. a** We show the contributions to the wavefunction of the open channel relevant for NNN tunneling processes, that couple to the closed channel state with $\ell = 1$ in **b**. The overlaps have to be weighted by momentum-dependent phase factors (here with momenta k_x^M, k_y^M measured in the $\pi/4$-rotated MBZ basis, see Eq.(10.5)) and symmetry properties of the d-wave closed channel have to be taken into account. The shown contributions constitute all eight terms in the SSLA.

As for the previous case, we find robust a $d_{x^2-y^2}$ nodal structure, which is caused by the symmetry properties of the closed channel (cc) bound state. Further, we note that in our geometric string calculations, the magnitude of the NNN tunneling form factor is large compared to the coupling caused by spin-flip recombinations as can be seen from the scale in Figure 10.6. Hence, we predict notable competition between the two processes even in the perturbative regime $|t'| \ll J_\perp$, which we discuss in the following. Importantly, including both spin-flip processes as well as NNN tunneling terms in our model, allows us to analyze the trend of the scattering for doublon (i.e. electron) versus hole doping.

10.2.3   Competition between spin-flip and NNN tunneling processes

The microscopic Hamiltonian (10.1) is formulated in terms of the fermionic operators $\hat{c}^{\dagger}_{\mathbf{j},\sigma}$ describing the underlying electrons in the Fermi-Hubbard model. However, the magnetic polarons are described in a parton formulation, which requires to introduce the following chargon $\hat{h}_{\mathbf{j}}$ and spinon $\hat{s}_{\mathbf{j},\sigma}$ operators:

$$\hat{c}_{\mathbf{j},\sigma} = \begin{cases} \hat{h}^{\dagger}_{\mathbf{j}}\hat{s}^{\dagger}_{\mathbf{j},\sigma} & \text{for holes} \\[2em] \hat{h}_{\mathbf{j}}\hat{s}_{\mathbf{j},\sigma} & \text{for doublons} \end{cases} , \tag{10.34}$$

where we distinguish between hole and doublon doping. Therefore, the underlying microscopic model becomes

$$\begin{aligned} \hat{\mathcal{H}}_{t\text{-}t'\text{-}J} = &\pm t \sum_{\langle i,j \rangle} \sum_{\sigma} \hat{\mathcal{P}} \left(\hat{h}^{\dagger}_{\mathbf{i}}\hat{h}_{\mathbf{j}}\hat{s}^{\dagger}_{\mathbf{i},\sigma}\hat{s}_{\mathbf{j},\sigma} + \text{h.c.} \right) \hat{\mathcal{P}} \\ &\pm t' \sum_{\langle\langle i,j \rangle\rangle} \sum_{\sigma} \hat{\mathcal{P}} \left(\hat{h}^{\dagger}_{\mathbf{i}}\hat{h}_{\mathbf{j}}\hat{s}^{\dagger}_{\mathbf{i},\sigma}\hat{s}_{\mathbf{j},\sigma} + \text{h.c.} \right) \hat{\mathcal{P}} \\ &+ J \sum_{\langle i,j \rangle} \left(\hat{\mathbf{S}}_{\mathbf{i}} \cdot \hat{\mathbf{S}}_{\mathbf{j}} - \frac{1}{4}\hat{n}_{\mathbf{i}}\hat{n}_{\mathbf{j}} \right), \end{aligned} \tag{10.35}$$

for the hole $(+)$ and doublon $(-)$ doped case. In particular, we measure the doping δ relative to the half-filled case, $\delta = 0$, such that the sign is positive (negative) $\text{sgn}\,[\delta] = +1$ ($\text{sgn}\,[\delta] = -1$) for hole (doublon) doping. From the above Hamiltonian, the parton bound state wavefunction can be derived (for $t' = 0$), and we choose a gauge such that all wavefunction amplitudes are real and have a sign structure as follows,

$$\text{sgn}\,[\psi_{\text{sc}}(\ell)] = \text{sgn}[\phi_{\text{cc}}(\ell)] = \text{sgn}\,[\delta]^{\ell}. \tag{10.36}$$

This choice of gauge is meaningful since we have shown that the tunneling matrix elements have equal signs in the string basis, see Eqs. (10.3) and (10.15).

Next, we consider the doping dependence of the form factors, in which the wavefunction amplitudes enter as products $\psi_{\text{sc}}(\ell_{\downarrow}) \times \psi_{\text{sc}}(\ell_{\uparrow}) \times \phi^{*}_{\text{cc}}(\ell)$, see Eq. (10.30). Since $\ell = \ell_{\uparrow} + \ell_{\downarrow} + \Delta\ell$ with $\Delta\ell = -1, 3$ ($\Delta\ell = 1$) for $J_{\perp}$ (t') processes, we find

$$J_{\perp}\mathcal{M}^{J_{\perp}}(\mathbf{k}) \propto \begin{cases} J_{\perp} \cdot (+1)^{\Delta\ell} = J_{\perp} & \text{for } \delta > 0 \\[1em] J_{\perp} \cdot (-1)^{\Delta\ell} = -J_{\perp} & \text{for } \delta < 0 \end{cases} \tag{10.37a}$$

$$t'\mathcal{M}^{t'}(\mathbf{k}) \propto \begin{cases} t' \cdot (+1)^{\Delta\ell} = t' & \text{for } \delta > 0 \\[1em] -t' \cdot (-1)^{\Delta\ell} = t' & \text{for } \delta < 0 \end{cases} \tag{10.37b}$$

Therefore, we conclude that in cuprate materials with $t'/t < 0$ the individual form fac-

a Hole doping	**b** Doublon doping	**c** 1D cuts
$\mathcal{M}_2^{J_\perp}(\mathbf{k}) - \left\lvert \frac{t'}{J_\perp}\right\rvert \mathcal{M}_2^{t'}(\mathbf{k})$	$\mathcal{M}_2^{J_\perp}(\mathbf{k}) + \left\lvert \frac{t'}{J_\perp}\right\rvert \mathcal{M}_2^{t'}(\mathbf{k})$	
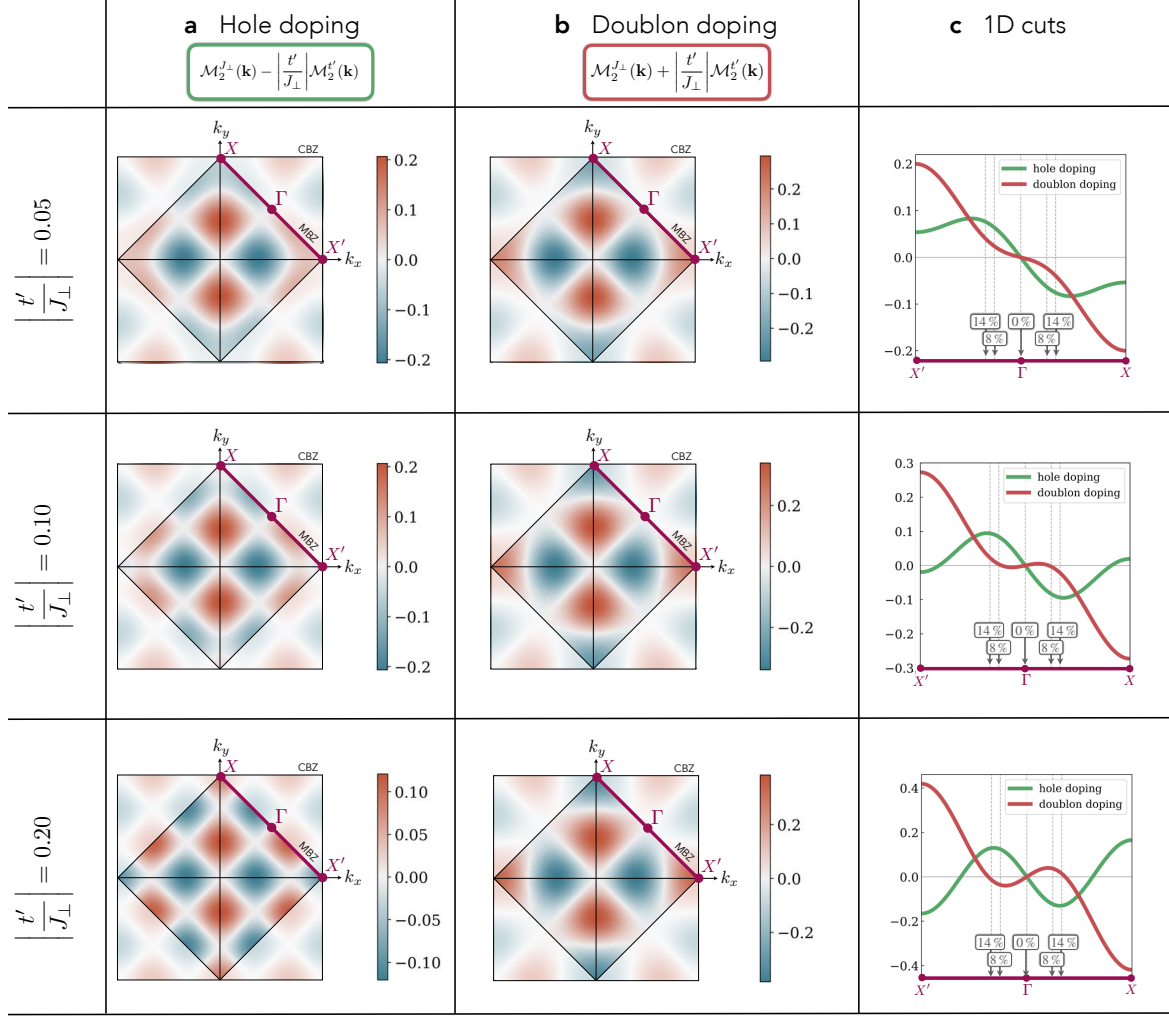
Figure 10.8: **Combined $J_\perp$ and t' scattering.** We plot the form facts, Eq. (10.25), combining spin-flip and NNN tunneling recombination processes, which enter quadratically in the scattering interaction. **a** For hole dopants in cuprate compounds, the form factors obtained for spin-flip and NNN tunneling processes are subtracted leading to a constructive interference of the matrix elements around the nodal point $\mathbf{k} = (\pm\pi/2, \pm\pi/2)$. Here we show the resulting scattering interaction for various parameters $|t'/J_\perp|$. **b** For doublon doping, the relative sign between the form factors is equal. **c** We plot 1D cuts along the edge of the Brillouin zone (purple lines in **a** and **b**). For low doping, the form factors – and hence scattering amplitude – gets enhanced (reduced) for hole (doublon) doping. Here, we assume scattering on an elliptical Fermi surface of magnetic polarons with ellipticity 5.89 [315].

tors for spin-flip and NNN tunneling recombination processes interfere with a positive (a negative) sign, i.e. the overall form factor is given by ($J_\perp, t > 0$)

$$\mathcal{M}_2^{\text{tot}}(\mathbf{k}) = \begin{cases} +J_\perp \mathcal{M}_2^{J_\perp}(\mathbf{k}) - |t'|\mathcal{M}_2^{t'}(\mathbf{k}) & \text{for } \delta > 0 \\[2ex] -J_\perp \mathcal{M}_2^{J_\perp}(\mathbf{k}) - |t'|\mathcal{M}_2^{t'}(\mathbf{k}) & \text{for } \delta < 0 \end{cases} \qquad (10.38)$$

The form factors are strongly $\mathbf{k}$-dependent and thus, to meaningful compare the interfer-

ence effects in the low-doping regime, we need to consider the form factor in the vicinity of the hole pocket's Fermi surface, where $\mathcal{M}_2^{t'}$ and $\mathcal{M}_2^{J_\perp}$ have opposite signs, see Figure 10.8. As an important result, we find that scattering is enhanced (suppressed) for small hole (doublon) doping. The form factor determines the strength of the scattering between (sc) charge carriers after integrating out the closed (cc) channel, see Eq. (10.24); hence we qualitatively predict that hole doping leads to stronger pairing interactions than doublon doping.

We use the results obtained in geometric string theory, and evaluate the form factor $\mathcal{M}_2^{\text{tot}}(\mathbf{k})$, for various $|t'/J_\perp|$ in the hole and doublon doped regime, see Figure 10.8a and b. The hole pockets are strongly elliptical and thus we expect the scattering of magnetic polarons to occur along the k_y^M axis. In Figure 10.8c, we take a 1D cut along the direction in the MBZ and we find that for small doping values, the scattering interaction is strongly enhanced (suppressed) for hole (doublon) doping. These findings have direct implications for cold atom quantum simulators that can tune NNN tunneling t' and systematically study hole and doublon doped systems [392].

10.2.4 Analytical expression of the form factors

The numerically obtained form factors $\mathcal{M}_2^{J_\perp}$ and $\mathcal{M}_2^{t'}$ give insight into the magnitude and nodal structure of the effective interactions. In the next step, we fit the form factors the analytically obtained functions from SSLA, which allows us to more carefully study the symmetry structure of the pairing interaction, and further enables future (analytical) studies of the effective model, e.g. a BCS mean-field analysis. In the following, the fitted form factors are denoted by $\tilde{\mathcal{M}}_2^{J_\perp}$ and $\tilde{\mathcal{M}}_2^{t'}$, respectively.

We use the results of the numerical calculations including (cc) states with strings up to length $\ell_{\max} = 5$ and fit with the momentum dependent functions $\Gamma_0(\mathbf{k})$ and $\Gamma_1(\mathbf{k})$ defined below in Eqs. (10.41) and (10.42). Using this parametrization, we find that the spin-flip form factor is given by

$$\tilde{\mathcal{M}}_2^{J_\perp}(\mathbf{k}) = \alpha^{J_\perp}\Gamma_0(\mathbf{k}) + \beta^{J_\perp}\Gamma_1(\mathbf{k}) \tag{10.39}$$

with $(\alpha^{J_\perp}, \beta^{J_\perp}) = (8.7 \cdot 10^{-2}, 6.0 \cdot 10^{-2})$. Analogously, the NNN tunneling form factor becomes

$$\tilde{\mathcal{M}}_2^{t'}(\mathbf{k}) = \alpha^{t'}\Gamma_0(\mathbf{k}) \tag{10.40}$$

with $\alpha^{t'} = 0.55$. We measure the validity of the fit by evaluating $\text{err}^a = ||\tilde{\mathcal{M}}^a - \mathcal{M}^a||_2/||\mathcal{M}^a||_2$ in the 2-norm. We find $\text{err}^{J_\perp} = 3.9 \cdot 10^{-3}$ and $\text{err}^{t'} = 4.7 \cdot 10^{-2}$.

Now, we consider the properties of the functions $\Gamma_0(\mathbf{k})$ and $\Gamma_1(\mathbf{k})$, which are defined as follows:

$$\Gamma_0(\mathbf{k}) = \overbrace{\sin\left(\frac{k_x^M}{\sqrt{2}}\right)\sin\left(\frac{k_y^M}{\sqrt{2}}\right)}^{d_{xy}} \cdot \underbrace{\left\{-2\sqrt{2} + 4\sqrt{2}\left[\cos^2\left(\frac{k_x^M}{\sqrt{2}}\right) + \cos^2\left(\frac{k_y^M}{\sqrt{2}}\right)\right]\right\}}_{s_0} \tag{10.41}$$

a perturbative t'

b non-perturbative t'
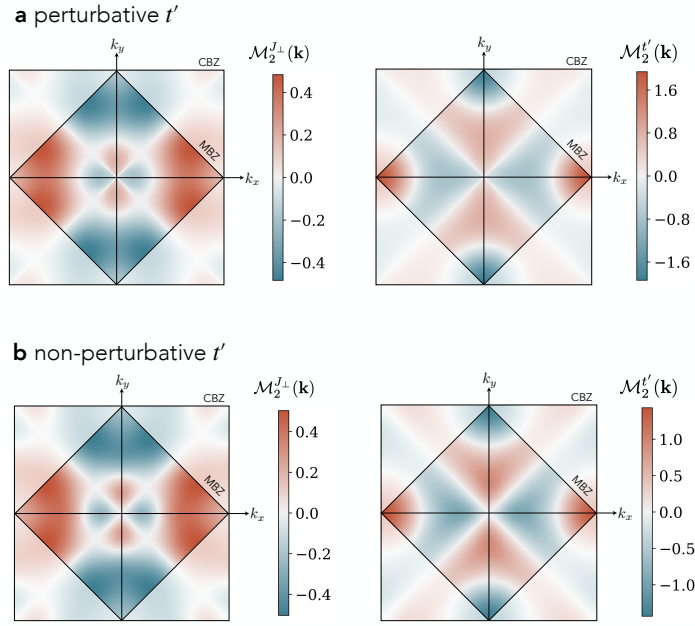
Figure 10.9: **Scattering form factors** obtained from the refined truncated basis method. The form factors, Eq. (10.25), include the full momentum dependence of the (sc) and (cc) wavefunctions. **a** We plot the form factors $\mathcal{M}_2^\kappa$ for $\kappa = J_\perp$ (left) and $\kappa = t'$ (right) without including non-perturbative t' corrections of the meson wavefunctions. **b** We include the NNN tunneling t' in the derivation of the (sc) and (cc) wavefunctions using the parameters $t/J = 3$ and $t'/t = -0.2$. The calculations for the refined truncated basis method were performed by Pit Bermes.

$$\Gamma_1(\mathbf{k}) = \overbrace{\sin\left(\frac{k_x^M}{\sqrt{2}}\right)\sin\left(\frac{k_y^M}{\sqrt{2}}\right)}^{d_{xy}} \cdot \underbrace{\left[2 + 4\cos\left(\sqrt{2}k_x^M\right)\right]\left[2 + 4\cos\left(\sqrt{2}k_y^M\right)\right]}_{s_1} \qquad (10.42)$$

The functions have d_{xy} nodal structure in the $\pi/4$-rotated MBZ basis $\mathbf{e}_\mu^M$, which translates to a $d_{x^2-y^2}$ nodal structure in the natural basis $\mathbf{e}_\mu$ of the CBZ. Additionally, we conclude that the form factors functions have dependencies on extended s-wave channels s_0 and s_1. Further the functions $\Gamma_p(\mathbf{k})$ with $p = 1, 2$ fulfill the following useful orthonormality relations:

$$1 = \frac{1}{2\pi^2}\int_{\text{MBZ}} \Gamma_p(\mathbf{k})\Gamma_p(\mathbf{k})d^2\mathbf{k}, \qquad (10.43a)$$

$$0 = \frac{1}{2\pi^2}\int_{\text{MBZ}} \Gamma_p(\mathbf{k})\Gamma_{\bar{p}}(\mathbf{k})d^2\mathbf{k}. \qquad (10.43b)$$

10.3   Refined truncated basis approach

So far, we have applied a simple Bethe lattice description of the meson bound states, see Figure 10.2, and we have neglected the momentum dependence of the wavefunction am-

plitudes. While this had the advantage to obtain analytical expressions for the form factor $\mathcal{M}_2(\mathbf{k})$, Eq. (10.28), predicting quantitative features requires more sophisticate methods. In the following, we employ a refined truncated basis method, which systematically treats the overcompleteness of the basis states and which allows us to fully take into account the momentum dependencies of the open and closed channel. We find qualitatively excellent agreement with the previous calculations. This demonstrates the robustness of the Feshbach scattering description: the scattering symmetry properties are inherited from the resonant (cc) channel which we capture correctly in the simplified model.

When using the geometric string formalism to describe magnetic polarons (sc), we have so far assumed that the string states $\{|\mathbf{j}_\sigma, \Sigma\rangle\}$ form an orthonormal basis. As mentioned in 10.1.1, this is not entirely true since every two trajectories differing by only by a Trugman loop are equivalent and give identical spin configurations (up to global translations) so that the string states form an overcomplete basis set. The same holds true for the string states of the (cc) $\{|\mathbf{x}_c, \Sigma_{cc}\rangle\}$, where similar loop effects lead to identical configurations. In addition, the definition of these strings on a Bethe lattice neglects that some trajectories lead to unphysical double occupancies of the chargons and thus overestimates the size of the Hilbert space.

In this section, we will follow [319] and use a more quantitative, refined truncated basis method avoiding the overcompleteness as well as unphysical states, and rigorously including loop effects. To describe the (sc) meson, we start again from a single hole $\hat{c}_{\mathbf{j},\bar{\sigma}}$ (or electron $\hat{c}^\dagger_{\mathbf{j},\sigma}$) doped into a perfect Néel background $|0\rangle$ and perform a Lee-Low-Pines transformation [390] into the co-moving frame of the chargon. This transformation leads to a block-diagonal form in the chargon-momentum basis so that we can compute the wavefunctions for any momentum $\mathbf{k}$ state. Similar to before, we then consider the chargon motion through a static spin background and construct a truncated basis by applying the NN hopping term $\hat{H}_t$ along sets of bonds consisting of up to ℓ_{max} segments. In contrast to the above, we now do not label the states by the string Σ but by the spin configuration and thus include every physical configuration only once. Since the Ising term J_z gives a confining potential proportional to the number of frustrated bonds, the truncated basis presents a controlled expansion of the Hilbert space relevant for low energy physics.

In order to describe the (cc) meson, we employ a similar expansion scheme but start from two holes or two doublons doped into a Néel background at neighboring sites. Here we assume the dopants to be distinguishable at first and again perform a Lee-Low-Pines transformation into the co-moving frame of the first dopant. As before, we now apply the hopping terms for either of the dopants up to ℓ_{max} and build a basis of all distinct and physical configurations. Next, we antisymmetrize the states to account for the fermionic statistics of the indistinguishable chargons.

Having constructed the truncated bases for open channel states $\mathscr{H}_{open}$ and closed channel states $\mathscr{H}_{closed}$, we can compute all the matrix elements of the Hamiltonian which do not leave the subspace spanned by the truncated bases. This includes transverse spin fluctuations $J_\perp$ and NNN hopping t' which do not break up the geometric strings. Note that we still only include a subset of all $J_\perp$ and t' processes in the system, but we include all the processes which strongly affect the (sc) and (cc) wavefunction. The truncated basis description
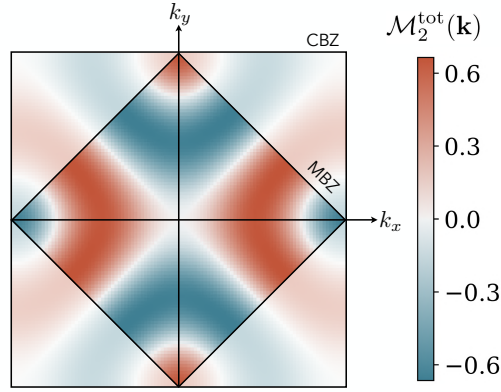
Figure 10.10: **Combined $J_\perp$ and t' scattering** obtained from the refined truncated basis method. We plot the total scattering form factor for hole dopants and realisitc parameters in cuprates, i.e. $t'/t = -0.2$ and $t/J = 3$. The calculations for the refined truncated basis method were performed by Pit Bermes.

allows us to go beyond the simple Bethe lattice description and to capture non-perturbative t' and $J_\perp$ processes; in particular we include the modifications of the open channel states in the presence of non-zero $J_\perp, t'$. This leads to a significant momentum dependence of the wavefunction and mixing of the rotational eigensectors away from the C4-invariant momenta. Nevertheless, the dominant contributions to the (sc) wavefunction near the nodal point still have s-wave symmetry and at the considered momenta $\mathbf{Q} \bmod \mathbf{G}^M = \mathbf{0}$, the (cc) ground state retains its well-defined d-wave rotational quantum number.

In order to correctly describe the open $(sc)^2$ and closed (cc) scattering channels, we have to again take care of the overcompleteness of our parton description. In fact every spin and hole (spin and doublon) configuration contributing to the (cc) bound state could be written as two individual magnetic polarons $(sc)^2$. Therefore we adapt the convention, that every spin configuration where the flipped spins form a string connecting the chargons contributes to the (cc) but not to the $(sc)^2$ state.

With this convention we obtain the scattering form factors $\mathcal{M}_2^\kappa(\mathbf{k})$ [Eq. (10.25)] shown in Figure 10.9. Here, we truncate the (sc) and (cc) Hilbert spaces at string lengths of $\ell_{max} = 8$ and $\ell_{max}^{cc} = 10$ to determine the meson wavefunctions. To compute the overlaps $\mathcal{M}_2^\kappa$, we used all (sc) states with a string length $\ell < 5$. The form factors qualitatively agree with the Bethe lattice calculations shown in Figure 10.6 but have slightly larger values. This is due to the fact, that the truncated basis method includes more possibilities for two individual polarons $(sc)^2$ to recombine into a bound (cc) pair (cc). Furthermore, in the truncated basis method we find that the nodal ring in the form factor of the spin-flip recombination processes $J_\perp$ moves away from the hole pockets and towards the center of the Brillouin zone.

We compare our calculations by (i) not including the $J_\perp$ and t' terms in the meson's wavefunctions, see Figure 10.9a, and (ii) fully including the $t/J_\perp = 3$ and $t'/t = -0.2$ dependencies of the open and closed channels, see Figure 10.9b, using typical parameters of hole doped cuprate superconductors [391]. We find that the non-perturbative correc-

tions of the meson wavefunction leads to very minor differences justifying the perturbative treatment of t'-processes. Note that including the $J_\perp$ processes is crucial to obtain the hole pockets of the magnetic polarons; a comparison between the geometric string model to numerical DMRG studies of the t-J model is discussed in Ref. [303].

In Figure 10.10, we show the combined scattering form factor $\mathcal{M}_2^{\text{tot}} = \mathcal{M}_2^{J_\perp} - |\frac{t'}{J_\perp}|\mathcal{M}_2^{t'}$ for hole dopants, see Eq. (10.38), including NNN tunneling t' non-perturbatively. In the vicinity of the hole pocket's Fermi surface, the NNN tunneling and spin-flip processes interfere constructively leading to sizable scattering form factors.

10.4 Effective Hamiltonian

So far, we have derived scattering interactions $V_{\mathbf{k},\mathbf{k}'} \propto \mathcal{M}^*(\mathbf{k})\mathcal{M}(\mathbf{k}')$ of two magnetic polarons in terms of the form factors and for zero-momentum pairs. Next, we want to take another significant step by promoting our two-body problem to a many-body theory. Our effective theory leads us to an effective model to describe d-wave superconductivity in the low-doping and strong-coupling regime arising from a Fermi sea of magnetic polarons.

The effective model derived below is valid in a regime, when (i) the antiferromagnetic background has sufficiently long-ranged correlations, $\xi_{\text{AFM}} \gg a$, and (ii) the density of magnetic polarons, i.e. charge carriers, is low, and (iii) the system can be described by low-energy scattering, i.e. at low temperatures $k_B T \ll J_\perp, t'$. The requirement (ii) ensures that the internal structure of the meson-like bound state does not have to be adjusted due to substantial overlaps of the (sc) or (cc) wavefunctions; for the former this is expected to play a role at doping $\delta \gtrsim 20\%$ [7, 309].

The coupling matrix elements (or form factors) between the open and closed channel, see Section 10.2, allow us to integrate out the closed channel and derive an effective Hamiltonian for the magnetic polarons with pairwise scattering in momentum space given by [P11]

$$\hat{\mathcal{H}}_{\text{eff}} = \hat{\mathcal{H}}_{\text{open}} + \hat{\mathcal{H}}_{\text{int}}, \tag{10.44}$$

$$\hat{\mathcal{H}}_{\text{int}} = \sum_{\mathbf{k},\mathbf{k}'} V_{\mathbf{k},\mathbf{k}'}\, \hat{\pi}^\dagger_{-\mathbf{k},\uparrow} \hat{\pi}^\dagger_{\mathbf{k},\downarrow} \hat{\pi}_{-\mathbf{k}',\uparrow} \hat{\pi}_{\mathbf{k}',\downarrow} \tag{10.45}$$

with the open channel Hamiltonian describing weakly interacting magnetic polarons, see Eq. (10.8). For low doping, the Fermi surface forms two hole pockets around the dispersion minima $\mathbf{k}_{\text{min}} = (\pm\pi/2, \pm\pi/2)$. Further, the effective interaction matrix elements $V_{\mathbf{k},\mathbf{k}'}$, Eq. (10.25), arise from the emergent d-wave Feshbach resonance between $(\text{sc})^2$ and (cc) mesons with total momentum $\mathbf{Q} = \mathbf{0}$.

The above derived analytical expressions of the form factors allow us to give a closed form of the attractive two particle scattering interaction,

$$V_{\mathbf{k},\mathbf{k}'} = \frac{1}{\mathcal{V}} \left[g_0(t')\Gamma_0(\mathbf{k}') + g_1\Gamma_1(\mathbf{k}') \right] \left[g_0(t')\Gamma_0(\mathbf{k}) + g_1\Gamma_1(\mathbf{k}) \right], \tag{10.46}$$

where $\mathcal{V} = L^2/2$ is the volume of the magnetic lattice. Further, we have defined the cou-

pling constants

$$g_0(t') := \sqrt{\frac{J_\perp^2}{2\Delta E}} \left(\alpha^{J_\perp} + \frac{t'}{J_\perp} \alpha^{t'} \right) \tag{10.47}$$

$$g_1 := \sqrt{\frac{J_\perp^2}{2\Delta E}} \beta^{J_\perp}, \tag{10.48}$$

where ΔE denotes the bare energy splitting between the open and closed channels, see Section 10.1.3. This energy splitting strongly determines the couplings strength between the two channels. While we introduce ΔE as a free tuning parameters in the meson scattering model, microscopic couplings such as extended Hubbard interactions eventually determine the proximity to the Feshbach resonance of a given model [P11, P10, P6] and may allow to tune the effective interaction strength between charge carriers in solids or cold atom experiments.

In the following, we normalize the factors of the scattering interactions,

$$\Gamma(\mathbf{k}) = \mathcal{N}^{-1/2} \left[g_0(t')\Gamma_0(\mathbf{k}') + g_1\Gamma_1(\mathbf{k}') \right] \tag{10.49}$$

such that $(2\pi^2)^{-1/2} \int_{\text{MBZ}} \Gamma^2(\mathbf{k})d^2\mathbf{k} = 1$. Using Eqs. (10.43), this gives $\mathcal{N} = g_0^2(t') + g_1^2$. This yields the final expression for the scattering interaction

$$V_{\mathbf{k},\mathbf{k}'} = \frac{g}{\mathcal{V}}\Gamma(\mathbf{k})\Gamma(\mathbf{k}'), \tag{10.50a}$$

$$g := g_0^2(t') + g_1^2, \tag{10.50b}$$

such that we arrive at a BCS Hamiltonian with highly anisotropic pairing interactions, which can lead to an instability of the Fermi surface of magnetic polarons, i.e. around the small, elliptical hole pockets at the nodal point.

10.4.1   BCS mean-field analysis

We treat the Hamiltonian (10.44) using a standard BCS mean-field ansatz in order to analyze the symmetries of the BCS pairing gap $\Delta(\mathbf{k})$. We define the d-wave BCS mean-field order parameter

$$\Delta(\mathbf{k}) = \frac{1}{\mathcal{V}}\sum_{\mathbf{k}'} \Gamma(\mathbf{k})\Gamma(\mathbf{k}')\langle \hat{\pi}_{-\mathbf{k}',\uparrow}\hat{\pi}_{\mathbf{k}',\downarrow}\rangle, \tag{10.51}$$

which is the gap equation that has to be fulfilled self-consistently in accordance with the BCS mean-field Hamiltonian,

$$\hat{\mathcal{H}}_{\text{MF}} = \sum_{\mathbf{k}} \left[\epsilon_{\text{sc}}(\mathbf{k}) - \mu \right] \hat{\pi}_{\mathbf{k},\sigma}^\dagger \hat{\pi}_{\mathbf{k},\sigma} + g\sum_{\mathbf{k}} \Delta(\mathbf{k}) \left[\hat{\pi}_{-\mathbf{k},\uparrow}^\dagger \hat{\pi}_{\mathbf{k},\downarrow}^\dagger + \text{H.c.} \right]. \tag{10.52}$$

From an ansatz for the pairing gap, $\Delta(\mathbf{k}) = \Delta\Gamma(\mathbf{k})$, it immediately follows that the pairing gap has the same symmetry and nodal structure as the form factors shown in Figure 10.8, i.e. $\Delta(\mathbf{k}) \propto \mathcal{M}_2^{\text{tot}}$.

The magnitude of the gap and hence the mean-field transition temperature has to be determined self-consistently and strongly depends on (i) the interaction strength $g \propto \Delta E_2^{-1}$ as well as (ii) the Fermi energy E_F. In particular, in the low-doping regime these two energy scales are competing, which may lead to a non-mean field character of the phase transition as the temperature is lowered going beyond the scope of this study. We conclude that in the proposed Feshbach scenario [P11] a d-wave superconductor can be established and is the leading order instability of a magnetic polaron metallic state recently observed in Ref. [248]. However, the details of the BCS state, e.g. the magnitude of the pairing gap, strongly depends on the bare energy splitting between the open channel and closed d-wave channel ΔE_2^{-1}, which requires future numerical and experimental studies, such as spectroscopy of the (cc) meson.

Before we discuss direct spectroscopic signatures of the tightly-bound (cc) state in Section 10.5, we emphasize that the Bogoliubov quasiparticle dispersion, $E(\mathbf{k}) = \sqrt{[\epsilon_{sc}(\mathbf{k}) - \mu]^2 + \Delta^2(\mathbf{k})}$, is an indirect probe of our scenario accessible in single particle spectroscopy, e.g., ARPES. The Bogoliubov dispersion is linked to the form factors derived in Section 10.2, for which we find characteristic features such as an nodal ring-like structure, see Figure 10.8. More directly, the momentum dependence of the superconducting pairing gap $\Delta(\mathbf{k}) \propto \Gamma(\mathbf{k}) \propto \mathcal{M}(\mathbf{k})$ can be analyzed as we discuss next.

10.5 ARPES signatures

An established experimental technique to probe the electronic structure of materials is ARPES [369]. The $(sc)^2$ Feshbach scattering channels described in this article rely on the existence of the tightly-bound bosonic (cc) pair [P11]. The properties of the (sc) mesons, or magnetic polaron, are directly accessible in conventional ARPES experiments, where a one-photon-in-one-electron-out process is considered. This process corresponds to the creation of a single hole excitation in the material and thus strongly couples to the individual (sc) channel.

Probing the (cc) bound state, however, is much more challenging because it involves two correlated holes. In ARPES, the (cc) bound state can be probed by (i) a process, in which an additional single hole couples to an already existing (sc) meson and forms a (cc) meson, and by (ii) correlated two-photon-in-two-electron-out processes (cARPES). In the following, we calculate the matrix elements for both processes and we find that the process described in (i) only couples very weakly to the (cc) channel.

10.5.1 Single hole ARPES

In the low but finite doping regime, we describe the fermionic charge carriers as magnetic polarons with dispersion relation $\varepsilon_{sc}(\mathbf{k})$ in a Fermi sea, see Eq. (10.7). In a photoemission process, a hole with momentum $\mathbf{k}$ and energy ω can be created. If this additional hole is in the vicinity of an already existing spinon (s) with momentum $\mathbf{p}$, which is bound to a chargon (c), they can recombine into a (cc) bound state with momentum $\mathbf{k} + \mathbf{p}$ and energy $\varepsilon_{cc}(\mathbf{k} + \mathbf{p})$ while leaving behind a hole-like $(\overline{sc})$ excitation. The (cc) dispersion for the

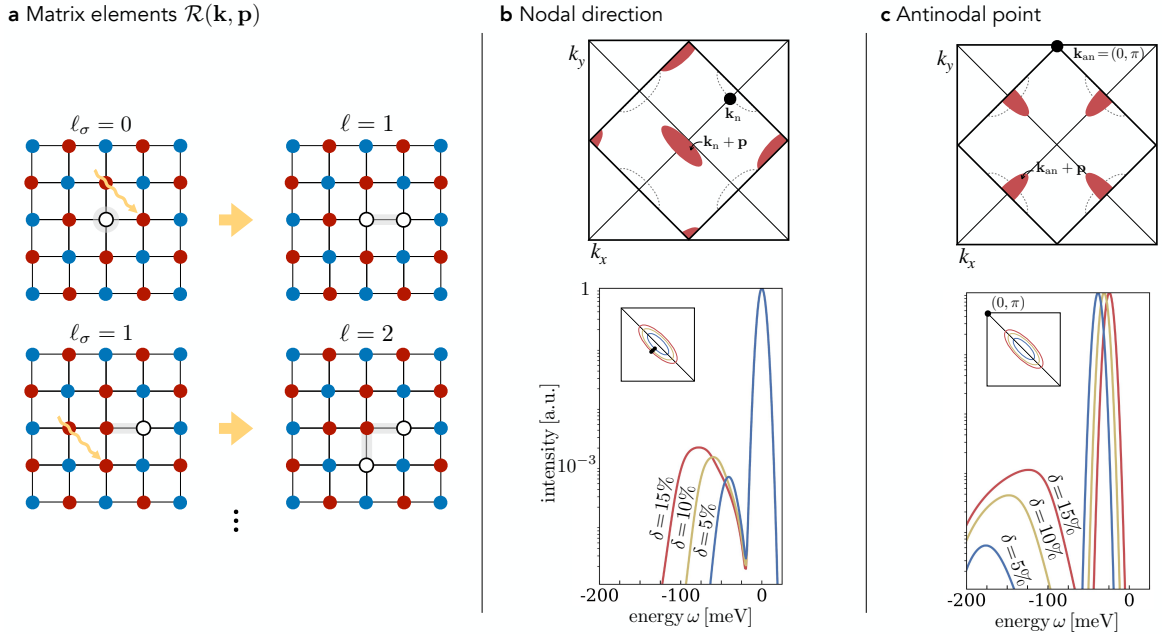**a** Matrix elements $\mathcal{R}(\mathbf{k}, \mathbf{p})$ **b** Nodal direction   **c** Antinodal point

Figure 10.11: **Single-hole ARPES. a** In single-hole ARPES, a rare but possible process describes the removal of an electron close an existing (sc) meson. The matrix elements are calculated by expanding in string length states; we include strings up to length $\ell_\sigma \leq 1$, as shown for two examples. We show the spectral signal **b** in the nodal direction, i.e. $\mathbf{k}_n$ at the Fermi surface of the hole pocket and on the diagonal of the CBZ, and **c** at the antinodal point $\mathbf{k}_{an} = (0, \pi)$. Top panels: The two-body processes, involving the removal of a (sc) and the addition of a (cc) meson, requires to convolve the (sc) dispersion ε_{sc} at the hole pocket around $\mathbf{p} = (\pm\pi/2, \pm\pi/2)$ (dotted region) with the shifted (cc) dispersion ε_{cc} at $\mathbf{k}_{(a)n} + \mathbf{p}$ (red region). The gradient of the (cc) dispersion in the red regions, together with the matrix elements $\mathcal{R}(\mathbf{k}, \mathbf{p})$ determines the width of the spectral signal. Bottom panels: We plot the spectral signal for $J = 130\,\text{meV}$, $T = 1.3\,\text{K}$, $\Delta E_2 = 20\,\text{meV}$ and various hole dopings $\delta = 5\%, 10\%, 15\%$. The large peaks corresponds to the quasiparticle peak of the (sc) mesons. We find a weak and broad feature below the Fermi surface associated with the (cc) bound state and with an energy onset at ΔE_2 (note the logarithmic scale, however).

d-wave channel in the t-J model cannot be calculated in the simple geometric string picture but has been extracted from DMRG calculations [37],

$$\varepsilon_{cc}(\mathbf{p}) = -J(\cos(p_x) + \cos(p_y) - 2] + \Delta E_2, \tag{10.53}$$

showing the relatively light mass $\propto 1/J$ of the bi-polaronic state.

The corresponding ARPES signal is determined by a convolution of the matrix elements with the Fermi sea of magnetic polarons given by

$$A_{\overline{sc}+cc}(\mathbf{k}, \omega) = \int \frac{d^2\mathbf{p}}{(2\pi)^2}\, n_T^F(\varepsilon_{sc}(\mathbf{p}) - \mu)\, \mathcal{R}(\mathbf{k}, \mathbf{p})$$
$$\times\, \delta(\omega + \varepsilon_{sc}(\mathbf{p}) - \mu - \varepsilon_{cc}(\mathbf{k} + \mathbf{p})). \tag{10.54}$$

Here, $n_T^F(\varepsilon)$ is the Fermi-Dirac distribution at temperature T and we assume sufficiently low

temperature such that the thermal occupation of the (cc) channel can be neglected; further $\mathcal{R}(\mathbf{k}, \mathbf{p})$ are coupling matrix elements, see Figure 10.11a. Note that the single-hole APRES process gives rise to a two-particle continuum and therefore a broad spectral feature.

The matrix elements $\mathcal{R}(\mathbf{k}, \mathbf{p})$ are evaluated by expanding the (cc) and (sc) wavefunctions in the string length basis analogously to the calculation of the scattering form factor in Section 10.2. Moreover, we approximate the meson wavefunction to be momentum independent and assume the ground state wavefunctions in the respective channel. Since the meson wavefunctions only extend across a few lattice sites, we only consider (sc) strings up to length $\ell_\sigma = 1$, which couple to (cc) contributions of length $\ell = 1, 2$. Using our approximation, we find

$$
\begin{aligned}
\mathcal{R}(\mathbf{k}, \mathbf{p}) = \ &\sqrt{2}\psi_{\mathrm{sc}}(\mathbf{k}, \ell_\sigma = 0)\phi_{\mathrm{cc}}(\mathbf{p}, \ell = 1)\big[\cos(k_x) - \cos(k_y) - \cos(p_x) + \cos(p_y)\big] \\
&+ \sqrt{2}\psi_{\mathrm{sc}}(\mathbf{k}, \ell_\sigma = 1)\phi_{\mathrm{cc}}(\mathbf{p}, \ell = 1)\big[\cos(k_x + p_x) - \cos(k_y + p_y)\big] \\
&+ \sqrt{2}\psi_{\mathrm{sc}}(\mathbf{k}, \ell_\sigma = 1)\phi_{\mathrm{cc}}(\mathbf{p}, \ell = 2)\big[\cos(k_x + k_y + p_x) - \cos(k_x + k_y + p_y) \\
&+ \cos(k_x - k_y + p_x) - \cos(-k_x + k_y + p_x) - 2\cos(p_x) + 2\cos(p_y)\big]
\end{aligned}
\tag{10.55}
$$

with momenta defined in the CBZ. Moreover, the matrix element (10.55) only contains contributions from s-wave (sc) states and d-wave (cc) states, despite small mixing with p-wave (sc) state at the nodal point. Nevertheless, we expect the approximation to be valid in the very low doping regime, as we confirmed using the systematic truncated basis approach from Section 10.3. For finite doping, the (sc) and (cc) wavfunctions will be adapted even further due to interactions and reduced AFM correlations; we neglect such effects to $\mathcal{R}(\mathbf{k}, \mathbf{p})$ in the following.

We use the matrix element (10.55) to calculate the spectral weight in different regions $\mathbf{k}$ of the Brillouin zone. In particular, the two-body origin of the spectral feature leads to a contribution of the (cc) state at $\mathbf{k} + \mathbf{p}$, where $\mathbf{p}$ are the occupied momenta of (sc)'s in the hole pocket, see Figure 10.11b and c (top). The confined meson bound states are assumed to exist in the low-doping regime, where sufficient AFM correlation are present. Since the density of (sc) mesons is low in this regime and the matrix elements are small, we predict only very weak spectroscopic signatures with a maximum peak height of about 10^{-3} relative to the quasiparticle peak of the (sc)'s.

In Figure 10.11b and c (bottom), we analyze the ARPES signal for typical cuprate parameters, various hole dopings δ and for two common momenta in the Brillouin zone, i.e. at the Fermi surface in the nodal direction $\mathbf{k}_{\mathrm{n}}$ and at the antinodal point $\mathbf{k}_{\mathrm{an}}$. We assume a bare open-closed channel energy difference of $\Delta E_2 = 20\,\mathrm{meV}$. Along the nodal direction, see Figure 10.11b, we find a pronounced peak with a full-width-half-max (FWHM) around $15\,\mathrm{meV}$. While the onset of the signal, at ΔE_2 below E_F, is a fit parameter the FWHM only depends on the value of J without further fit parameters. Along the antinodal direction, see Fig. 10.11c, we find a much broader hump followed by a dip between 15 to $25\,\mathrm{meV}$. The onset of this feature, defined by the dip, remains at an energy scale $\Delta E_2 \simeq 20\,\mathrm{meV}$ as observed in nodal direction.

In underdoped cuprates other, more pronounced peak-dip-hump features have previously been observed [393], dimming the prospect of detecting the weak signal we find in

Fig. 10.11.

10.5.2   Coincidence ARPES

Alternatively, it was proposed in Refs. [P11, 37] to use correlated two-hole spectroscopy, which is highly sensitive to the existence of the (cc) channel, and can be realized by cARPES [366–368, 394], see Chapter 9. We consider processes with two in-coming photons with momentum $\mathbf{K}$ and two out-going photoelectrons with momentum $\mathbf{K} \pm \mathbf{k}$, and we discuss the matrix elements $\mathcal{C}(\mathbf{k})$ for the shortest string length $\ell = 1$. For the specific momenta we consider, the process has no momentum transfer to the sample and allows us to probe the (cc) channel at $\mathbf{Q} = \mathbf{0}, \boldsymbol{\pi}$. The cARPES matrix elements for short strings is calculated to be

$$\mathcal{C}(\mathbf{k}) \propto |\psi_{\mathrm{sc}}(\mathbf{k}, \ell_\sigma = 0)|^2 \phi_{\mathrm{cc}}(\mathbf{Q}, \ell_{\mathrm{cc}} = 1) \big[\cos(k_x) \pm \cos(k_y) \big] \tag{10.56}$$

for momenta in the CBZ and the s-wave $(+)$ and d-wave $(-)$ channel. Therefore, we find a sizable lower bound for matrix elements of the (cc) channel in cARPES with distinct symmetry features such as a nodal structure of the d-wave pair inherited from its m_4 eigenvalue.
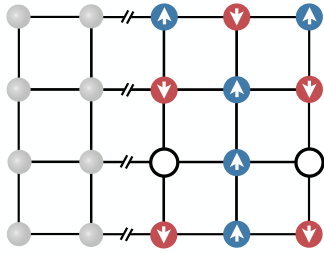
11

Bosonic, antiferromagnetic *t-J* models

O NE GOAL OF ANALOG QUANTUM SIMULATORS is to develop our understanding of the microscopic mechanisms underlying strong correlated quantum matter. Combining spin models with physical tunneling t of particles [124] yields *doped quantum magnets*, where mobile dopants frustrate magnetic order [112] and the statistics of the particles plays a crucial role, see Chapter 7. Due to its intimate connection to strongly correlated electrons, much effort has been invested in the exploration and quantum gas microscopy of the Fermi-Hubbard model [P1, 39] with on-site interaction U, using ultracold atoms in optical lattices [33, 289, 392, 395, 396]. The underlying superexchange mechanism naturally leads to AFM interactions $J = 4t^2/U$ in fermionic systems, while bosonic models have effective ferromagnetic interactions [60, 112], see Figure 11.1.

The behaviour of bosonic holes doped into an AFM background raises several interesting questions, but has so far remained elusive due to the ferromagnetic interactions in spin-1/2 Bose-Hubbard models, see Figure 11.1 For example, the microscopic mechanism of hole pairing might not be specific to the Fermi-Hubbard model but instead a universal feature of a broad class of related systems with strong spin-charge correlations.

In this Chapter, we propose an experimentally realistic scheme to realize AFM spin models with (hardcore) bosonic mobile hole dopants in tweezer arrays of cold molecules or Rydberg atoms. Using the density-matrix renormalization group technique, we study a *t-J* model with two bosonic and fermionic holes, respectively, comparing the role of statistics in a minimal instance. Lastly, we present preliminary experimental results of our proposed scheme implemented in one-dimensional Rydberg tweezer arrays.

We highlight that the exploration of doped quantum magnets with tweezer arrays offers a variety of new tuning knobs and advantages, and thus opens the door to explore previously inaccessible parameter regimes. From the technical side, Rydberg tweezer arrays operate with sub-second cycle times increasing the statistics of measurements compared to typical optical lattice experiments. Further, tweezer arrays can be rearrange into arbitrary
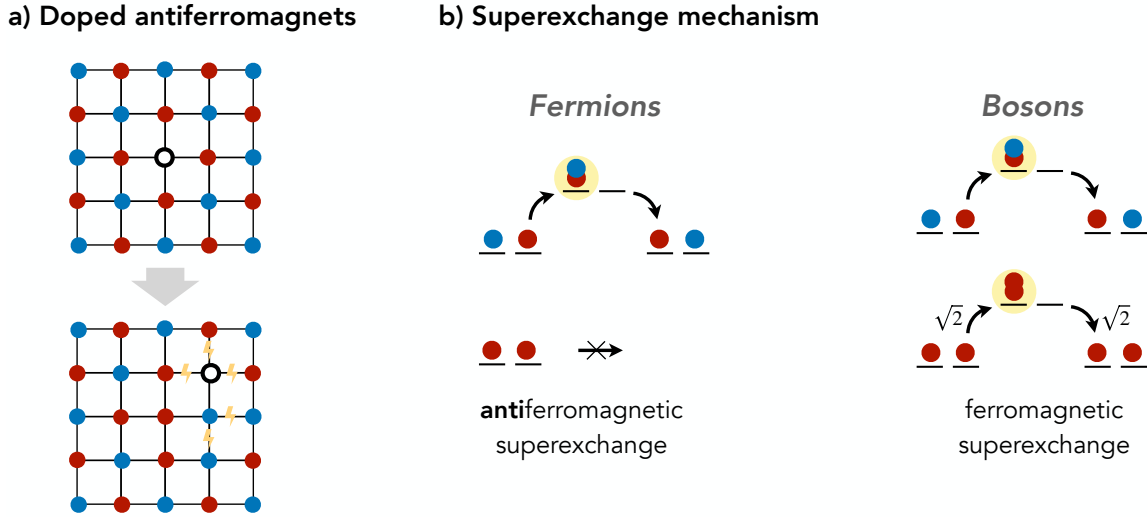
a) Doped antiferromagnets   **b) Superexchange mechanism**

Figure 11.1: **Doped quantum magnets. a)** The interplay between mobile hole dopants and antiferromagnetism leads to frustration [31]. **b)** In the strong coupling regime $U \gg t$, the superexchange mechanism in the plain-vanilla Bose- (Fermi-) Hubbard model yield effective (anti)ferromagnetic interactions. Using potential offsets or spin-dependent Feshbach resonances, antiferromagentic interactions between bosons can be engineered [397, 398] in optical lattices. In this Chapter, we propose a scheme to realize bosonic, antiferromagnetic *t-J* models in three internal states of ultracold polar molecules or Rydberg atoms.

two-dimensional lattices of up to thousands of sites [115, 116] allowing to study, e.g., transport of holes across a junction of different lattice geometries. In addition, because the magnetic interactions *J* are not generated via the superexchange mechanism [304], our proposal offers a wide tunability of the coupling t/J and gives access to regimes that are not accessible in optical lattice experiments, such as the phase separating regime at $t/J \ll 1$ [302].

The first part of the Chapter is based on publication [P8]. The text and figures are rearranged, adapted and supplemented. The scheme for Rydberg atoms, presented in the second part, was developed in collaboration with Simon Hollerith, Sebastian Geier [399] and Neng-Chun Chiu. The experiments are performed in the group of Antoine Browaeys at the Institute d'Optique in Palaiseau Cedex, France.

11.1   Bosonic *t-J* model as spin model

The main ingredient to realize doped spin models, such as the $t-J$ model shown in Figure 11.2a, is a mapping from the original model onto a new model described by Schwinger bosons. The new spin model is then suitable for implementations in established experimental platforms and the desired interactions can be engineered using the Floquet driving technique.

The $t-J$ model describes (hardcore) mobile spin-1/2 particles on a d-dimensional lattice with magnetic interactions; hence the local Hilbert space is spanned by the hole and *one* particle states $\{|h\rangle, |\downarrow\rangle, |\uparrow\rangle\}$. Here, we investigate bosonic particles $|\sigma\rangle = \hat{a}_{j,\sigma}^{\dagger}|vac\rangle$, where we express spins in the Schwinger representation $\hat{\mathbf{S}}_j = \frac{1}{2}\sum_{\sigma,\sigma'}\hat{a}_{j,\sigma}^{\dagger}\boldsymbol{\tau}_{\sigma,\sigma'}\hat{a}_{j,\sigma'}$ with Pauli
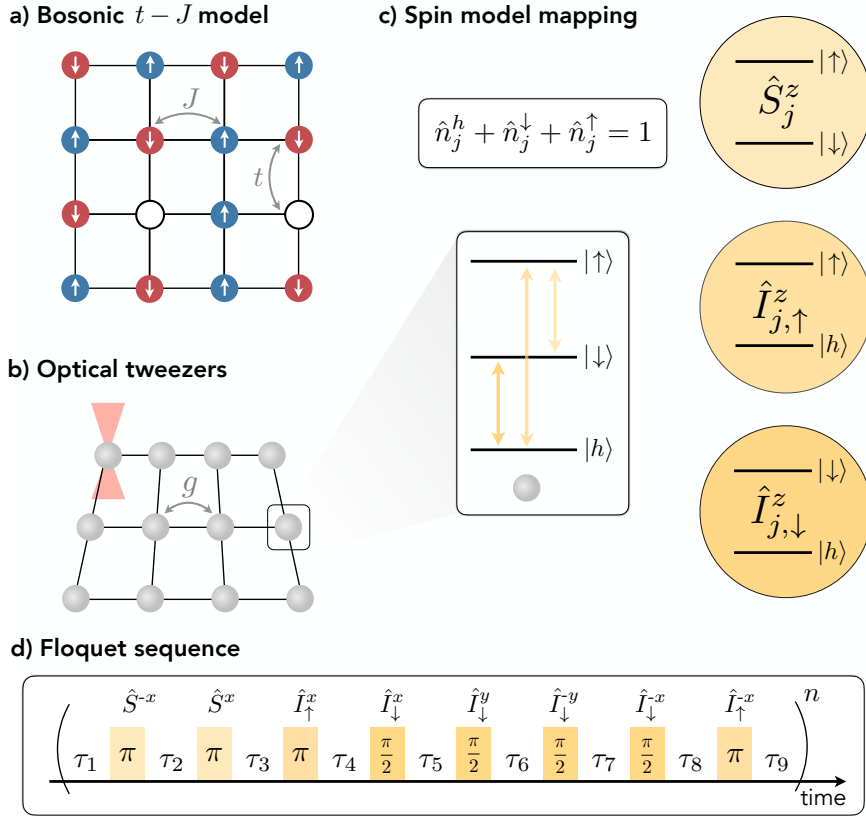
Figure 11.2: **Schwinger boson mapping. a)** The *t-J* model describes hopping of spin-1/2 particles on a lattice with tunneling amplitude *t* together with magnetic interactions *J*. For AFM interactions, the motion of holes ($|h\rangle$) or particles ($|\downarrow\rangle, |\uparrow\rangle$) frustrates the spin order yielding rich physics for both fermionic and bosonic particles. **b)** The latter can be implemented in the internal states of ultracold molecules or Rydberg atoms spatially localized in optical lattices or on an arbitrary graph of tweezer arrays. **c)** The local Hilbert space $\{|h\rangle, |\downarrow\rangle, |\uparrow\rangle\}$ can be encoded in the internal rotational states of molecules and we define the three Schwinger spins $\hat{\mathbf{S}}, \hat{\mathbf{I}}_\uparrow$ and $\hat{\mathbf{I}}_\downarrow$, which allows us to exactly represent the $t-J$ Hamiltonian as a spin model. **d)** In the isolated three level subspace of rotational states $|N\rangle$ with $N = 0, 1, 2$, the molecular Hamiltonian we consider has XY interactions between $N = 0, 1$. By performing periodic rotations on the $\hat{\mathbf{S}}$- and $\hat{\mathbf{I}}_\sigma$-Bloch spheres, the effective Floquet Hamiltonian in spin representation can be engineered. The duration τ_n of individual Floquet evolution steps determines the effective coupling strengths of the target Hamiltonian (11.4) (here with $V = 0$).

matrices $\boldsymbol{\tau} = (\tau^x, \tau^y, \tau^z)$ and $\sigma = \downarrow, \uparrow$. Further, we introduce the (hardcore) bosonic hole operator $|h\rangle = \hat{a}^\dagger_{j,h}|vac\rangle$.

To obtain the correct Hilbert space, the Schwinger bosons have to fulfill the local constraint

$$\hat{n}^h_j + \hat{n}^\downarrow_j + \hat{n}^\uparrow_j = 1, \tag{11.1}$$

where $\hat{n}^\sigma_j = \hat{a}^\dagger_{j,\sigma}\hat{a}_{j,\sigma}$ and $\hat{n}^h_j = \hat{a}^\dagger_{j,h}\hat{a}_{j,h}$ are the local spin and hole densities, respectively, see Figure 11.2c.

The bosonic t-J Hamiltonian is given by

$$\hat{\mathcal{H}}_{t-J} = -\sum_{i<j} t_{ij} \sum_{\sigma} \left(\hat{a}^{\dagger}_{i,\sigma} \hat{a}_{i,h} \hat{a}^{\dagger}_{j,h} \hat{a}_{j,\sigma} + \text{h.c.} \right) + \sum_{i<j} \sum_{\alpha} J^{\alpha}_{ij} \hat{S}^{\alpha}_i \hat{S}^{\alpha}_j + \sum_{i<j} V_{ij} \hat{n}^h_i \hat{n}^h_j, \qquad (11.2)$$

with $\alpha = x, y, z$ and the couplings can have arbitrary connectivity and range. The first term $\propto t$ describes tunneling of particles, the second term $\propto J^{\alpha}$ describes magnetic XXZ interactions with $J^x = J^y = J^{\perp}$, and the last term $\propto V$ is a hole-hole interaction.

The model (11.2) gains its importance because it captures the low-energy effective theory of the repulsive Fermi- or Bose-Hubbard models in the strong coupling regime $U \gg t$ [112]. However, the perturbative derivation exactly determines the couplings, which for nearest-neighbour (NN) hopping are given by $J^{\alpha} = \pm 4t^2/U$ and $V = -J(\pm 2 - 1)/4$ for the fermionic $(+)$ or bosonic $(-)$ models, respectively.

Our proposed scheme for realizing the model (11.2) in experiment enables broad tunability [400, 401] of the Hamiltonian parameters. In particular, the ability to tune the ratio between the hole-hole interaction V and magnetic interactions J in our model facilitates exploration of potentially interesting pairing regimes, which we study numerically in the second part of this paper.

First, we perform an exact mapping of Hamiltonian (11.2) onto a new XXZ spin model comprised of the three spin-1/2 Schwinger spins $\hat{\mathbf{S}}_j$, $\hat{\mathbf{I}}_{j,\downarrow}$ and $\hat{\mathbf{I}}_{j,\uparrow}$ with

$$\begin{aligned} \hat{S}^z_j &= \frac{1}{2} \left(\hat{n}^{\uparrow}_j - \hat{n}^{\downarrow}_j \right) & \hat{S}^+_j &= \hat{a}^{\dagger}_{j,\uparrow} \hat{a}_{j,\downarrow} \\ \hat{I}^z_{j,\sigma} &= \frac{1}{2} \left(\hat{n}^{\sigma}_j - \hat{n}^h_j \right) & \hat{I}^+_{j,\sigma} &= \hat{a}^{\dagger}_{j,\sigma} \hat{a}_{j,h}, \end{aligned} \qquad (11.3)$$

from which we obtain (up to a constant energy shift)

$$\hat{\mathcal{H}}_{t-J} = -\sum_{i<j} \sum_{\alpha,\sigma} t^{\alpha}_{ij} \hat{I}^{\alpha}_{i,\sigma} \hat{I}^{\alpha}_{j,\sigma} + \sum_{i<j} \sum_{\alpha} g^{\alpha}_{ij} \hat{S}^{\alpha}_i \hat{S}^{\alpha}_j. \qquad (11.4)$$

We neglect a chemical potential term for the holes since we assume the total number of particles is conserved. The form of Eq. (11.4) is very useful for our proposed implementation below, but we emphasize that the Schwinger spins are not mutually independent, i.e. $[\hat{S}^z_j, \hat{I}^{\pm}_{j,\sigma}] \neq 0$.

The hole-hole interaction renormalizes the XXZ models and we find the following couplings related to Eq. (11.2) and (11.4):

$$\begin{aligned} t^x_{ij} &= t^y_{ij} = \frac{1}{2} t_{ij} & t^z_{ij} &= -\frac{8}{9} V_{ij} \\ g^x_{ij} &= g^y_{ij} = J^{\perp}_{ij} & g^z_{ij} &= J^z_{ij} - \frac{4}{9} V_{ij}. \end{aligned} \qquad (11.5)$$

So far, we have performed exact transformations and re-written the t-J model in terms of Schwinger bosons. The Schwinger spins have to fulfill the the number constraint (11.1), which induces highly non-trivial spin-charge correlations and thus is beyond a simple spin-1/2 chain. Likewise, the construction can be formulated in terms of mutually hard-core
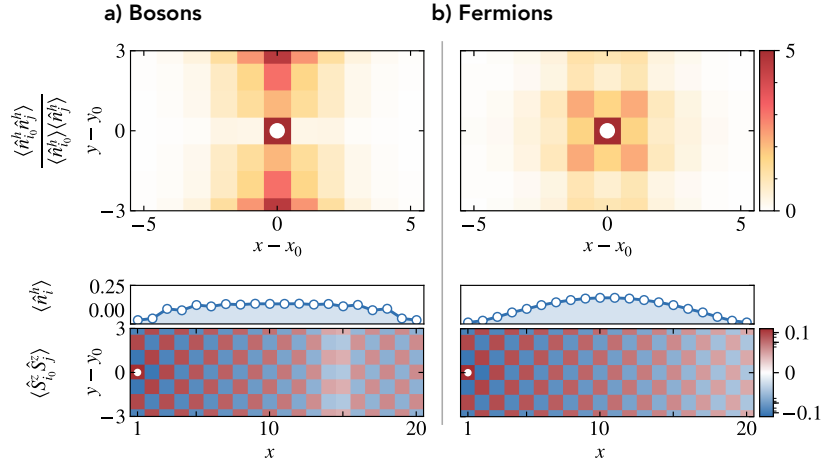
Figure 11.3: **Bosonic vs. fermionic two-hole states.** We show ground-state correlation functions for a *t-J* model with two **a)** bosonic and **b)** fermionic holes obtained from DMRG calculations on 20×6 cylinders. We find distinctly different behaviour for bosons and fermions by evaluating the hole-hole (top) and spin-spin correlation functions (bottom). **a)** The hole-hole correlator, centered around its reference site, $\mathbf{i}_0 = (x_0 = 10, y_0 = 3)$, shows a charge-density wave pattern around the short direction of the cylinder. Additionally, we find a domain wall in the spin-spin correlation function with reference site $\mathbf{i}_0 = (x_0 = 1, y_0 = 3)$, on the boundary (white dot); hence the bosons form a stripe. **b)** The fermions are tightly bound into an isotropic pair embedded in a homogeneous AFM background. For both statistics, we plot the hole density averaged around the short direction of the cylinder, which also serves as a marker for convergence of our results. The DMRG simulations were performed by Tim J. Harris and Tizian Blatz.

bosonic statistics, i.e., $\hat{a}^\dagger_{j,\Sigma} \hat{a}^\dagger_{j,\Sigma'} = 0$ for $\Sigma = \downarrow, \uparrow, h$.

The constraint can be elegantly implemented in a spin-1 manifold in, e.g., ultracold molecule or Rydberg tweezer arrays. To this end, we propose two schemes, which either utilize dipolar spin exchange interactions to engineer the desired dynamics by Floquet driving, or directly enables the realization of Hamiltonian (11.4) in three isolated Rydberg states. The former is discussed in Section 11.3, and the latter proposal is described in Section 11.6 with preliminary experimental results summarized in Section 11.7.

In the following, we elaborate on numerical density-matrix renormalization group (DMRG) studies, in which we compare the ground-state of the fermionic and bosonic *t-J* model.

11.2 Spin-charge order in the bosonic *t-J* model

Understanding the nature of mobile dopants in strongly correlated phases of matter has a long history, motivated by high-T_c superconductors and more recently by layered 2D materials [402]. The fate of the AFM Mott insulator under doping is still debated; however, experiments in cuprates have revealed that even a few percent of fermionic dopants can lead to a robust d-wave superconducting ground state [39, 284]. Hence, strong pairing of charge carriers – the hole dopants – mediated by magnetic interactions [259] likely plays a

key role.

Here, we perform a first numerical study of hole dopants in the ground state of the 2D bosonic AFM *t-J* model, comparing our results to an equivalent calculation using the standard fermionic *t-J* model. Let us emphasize that previous studies of the bosonic *t-J* model have considered either lower dimensions, high temperature expansions or *partial* AFM couplings ($J^z > 0, J^\perp \leq 0$) [397, 398, 403–407]. In contrast, our model takes a further step towards strongly correlated materials by studying fully antiferromagnetic interactions in the spin sector ($J^z, J^\perp > 0$) with the cost of introducing a sign problem at low temperatures; there our model is intractable for large-scale quantum Monte Carlo simulations.

To this end, the ground state with two holes in the zero-magnetization sector, $\hat{S}_z = 0$, of the SU(2)-invariant version of Eq. (11.2), $J^\alpha \equiv J$, was obtained from DMRG calculations on a long cylinder [54, 408–410]; the interactions are restricted to NN and have strength $t/J = 2$ and $V/J = -1/4$. We refer to the Supplementary Material of Ref. [P8] for more details. To analyze the structure of the obtained pair wavefunctions, we extract (i) the reduced hole-hole correlation $\langle \hat{n}_i^h \hat{n}_j^h \rangle / \langle \hat{n}_i^h \rangle \langle \hat{n}_j^h \rangle$ and (ii) the spin-spin correlation $\langle \hat{S}_i^z \hat{S}_j^z \rangle$ functions shown in Figure 11.3.

The well-known case of fermionic holes [283, 284, 411] indicates the formation of a tightly bound pair state, which can be seen from the C4-symmetric hole-hole correlations (Figure 11.3b, top) and the absence of a spin domain wall across the hole-rich region (Figure 11.3b, bottom). While the intuitive picture for bosons suggests the holes to condense and similarly bunch together, we find a surprising situation: the bosons have a tendency towards stripe formation. At finite density of holes, such stripes form in e.g. cuprate materials, describing periodic charge modulations bound to π-phase shifts of the spin-spin correlations (domain walls) across the hole-rich regions.

In our small system simulation, the two bosonic holes show strong tendency to pair along the short, periodic direction of the cylinder, as evident from the hole-hole correlations (Figure 11.3a, top). In contrast to the fermionic case, we observe a spin domain wall across the hole-rich region (Figure 11.3a, bottom), a hallmark of stripe formation. Additionally, the charge correlations show short-range repulsion along the short direction, distinctly different from the structure of the C4-invariant pair of the fermionic holes but resembling the situation in a stripe. Both scenarios, tightly bound pairs and stripe correlations, are marking phases observed in strongly correlated electrons [246, 284].

This minimal instance – comparing two-hole fermionic and bosonic states – already shows rich phenomenology and demonstrates an intriguing first experimental application of our proposal. Future experimental and numerical studies of the bosonic AFM *t-J* model can be expected to provide a fresh perspective from which to advance our current understanding of the physics of doped Mott insulators.

11.3   Experimental proposal: Ultracold molecules

Experimental setups with ultracold polar molecules have the capability to coherently address N-level systems [105], which interact via long-ranged flip-flop spin interactions between rotational states with $\Delta N = \pm 1$ and $\Delta m_N = 0, \pm 1$, see Section 2.1. Further, because

the dipole moment enables short Rabi pulse times between different N-levels with frequencies in the microwave regime, they are highly suitable for Floquet engineering. There, the system consecutively time evolves under the resonant dipole-dipole interactions followed by fast qubit rotations, i.e., driving microwave transitions between rotational states. Recently, the realization of an anisotropic XXZ model in a qubit subspace of rotational states [106] using Floquet engineering has been demonstrated.

Here, we extend the scheme by using three states in the rotational manifold $|N\rangle$ with $N = 0, 1, 2$ and we identify the molecular states $\{|0\rangle, |1\rangle, |2\rangle\}$ with the local Hilbert space $\{|h\rangle, |\downarrow\rangle, |\uparrow\rangle\}$ of the $t-J$ model. The molecular Hamiltonian expressed in terms of the Schwinger spins (11.3) is given by

$$\hat{\mathcal{H}}_{\mathrm{mol}} = \sum_{i<j} \chi_{ij} \left(\hat{I}^+_{i,\downarrow} \hat{I}^-_{j,\downarrow} + \mathrm{h.c.} \right), \tag{11.6}$$

with $\chi_{ij} = \chi(1 - 3\cos^2\theta_{ij})/|\mathbf{r}_{ij}|^3$. Here, $\mathbf{r}_{ij}$ is the vector connecting lattice sites i and j, and θ_{ij} is the angle between the quantization axis and $\mathbf{r}_{ij}$. In the following, we choose $\theta_{ij} = \pi/2$ and set the NN distance to $r_{ij} \equiv 1$. The XY coupling strength χ, is determined by the resonant dipole moments of the molecule [101, 109], and here we only consider interactions between $N = 0, 1$ [412], while the state $N = 2$ is non-interacting, see Figure 11.4a. This can be achieved by using the selection rules $\Delta m_N = 0, \pm 1$ of the dipole interactions, e.g. we propose to use $|N = 0, m_N = 0\rangle$, $|N = 1, m_N = 0\rangle$ and $|N = 2, m_N = -2\rangle$.

Next, we describe a scheme to realize a t-J model with tunable XXZ magnetic interactions. To this end, we consider the molecular Hamiltonian (11.6) with flip-flop interactions χ_{ij}. By comparing this model to the t-J Hamiltonian (11.4), we find that the microscopic model corresponds to a t-J model with tunneling of $|\downarrow\rangle$-particles only. Hence, we propose to perform consecutive, fast rotations between all pairs of states, i.e., on the $\hat{\mathbf{I}}_\sigma$- and $\hat{\mathbf{S}}$-Bloch spheres, to obtain a time-averaged Hamiltonian with equal strength $|\uparrow\rangle$- and $|\downarrow\rangle$-particle tunneling.

We emphasize that the long-range interactions directly transfer to the effective model and hence a t-J model with r^{-3} tails is realized in cold molecules. Enriching the Floquet protocol by spatial rearrangements [122], pure NN interactions or even models with arbitrary connectivity can be implemented in principle. Depending on the stability of DC electric fields, the fidelity of microwave transitions and coherence times across multiple rotational levels [413, 414], effective Floquet Hamiltonians [415] of differing complexity can be realized. One specific sequence of Floquet rotations is shown in Figure 11.2d: Tuning the times τ_n of Floquet steps allows for the implementation of models with tunable ratios $-t/J^z > 0$ and $J^\perp/J^z > 0$ ($J_z > 0$) and $V = 0$.

To show this, we start from the molecular Hamiltonian $\hat{\mathcal{H}}_{\mathrm{mol}}$, Eq. (11.6), and derive the effective Floquet Hamiltonian to first order, i.e., we neglect terms $\mathcal{O}(\tau^2/T_F^2)$, where τ is duration of a single step within the Floquet cycle of length T_F. We simulate the dynamics of a building block with three sites to confirm excellent agreement between the exact and the Floquet averaged dynamics.

In our molecular Hamiltonian, we assume that only two levels interact, e.g., by choosing appropriate sublevels with corresponding selection rules, see Figure 11.4. This has the ad-
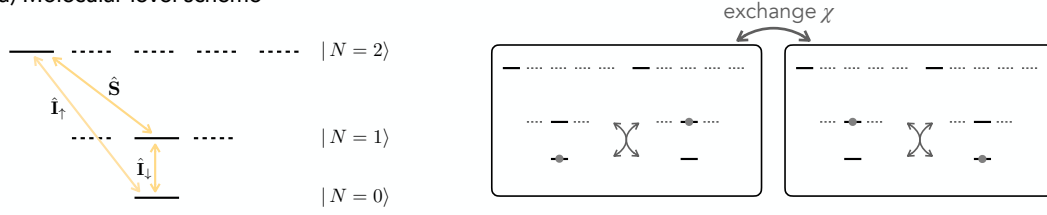
a) Molecular level scheme

b) Floquet sequence without V
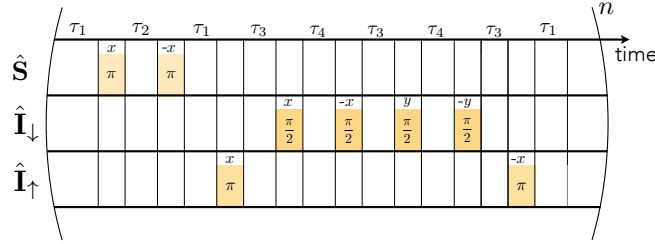
c) Floquet sequence with V
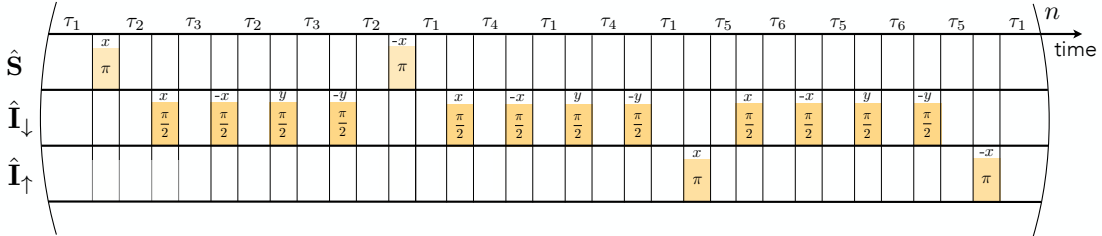
Figure 11.4: **Molecular scheme and Floquet sequence. a)** We propose to Floquet engineer a t-J-V model starting from a molecular Hamiltonian with two interacting levels (e.g. $|N = 0, m_N = 0\rangle \leftrightarrow |N = 1, m_N = 0\rangle$) and an auxiliary non-interacting level (e.g. $|N = 2, m_N = -1\rangle$)). Using one- and two-photon microwaves with Rabi frequency Ω one can rotate between all pairs of levels. To obtain a target t-J-V model, we propose to continuously time evolve the three level system under the application of periodic Rabi pulses. **b)** The sequence of microwave pulses gives rise to a t-J model ($V = 0$) with times τ_n determined by Eqs. (11.11)a-e. The time evolution under the shown sequence is demonstrated in Figure 11.5. **c)** Similarly, we propose a Floquet sequence to realize a $t-J-V$ model with times τ_n determined by Eqs. (11.13)a-f.

vantage that the Floquet sequence enables the realization of a highly tunable t-J-V model. In particular, we show how to realize target models with any

$$\epsilon^t := \frac{-t}{J^z} > 0, \tag{11.7}$$

and

$$
\begin{aligned}
&\text{(I)} \quad \epsilon^\perp := \frac{J^\perp}{J^z} > 0 \ \text{ and } \ \epsilon^V = 0 \\
&\text{(II)} \quad \epsilon^\perp := \frac{J^\perp}{J^z} > 1/2 \ \text{ and } \ 0 < \epsilon^V := \frac{V}{J^z} < \frac{9}{4}.
\end{aligned}
\tag{11.8}
$$

For the case of antiferromagentic spin interactions, we choose $J_z > 0$, which results in models with an overall positive sign for the kinetic energy term $\propto t$. Below, we propose two different Floquet sequences to realize models with $V = 0$ and $V \neq 0$, respectively. Note that more elaborate Floquet sequences, including interactions between all three levels, can be derived but lead to restricted tunability. Moreover, we can achieve parameter regimes with negative couplings by combining the Floquet scheme with spatial rearrangement and anisotropic dipolar interactions.

Our Floquet sequence requires rotations between all three Schwinger spins $\hat{\mathbf{S}}$, $\hat{\mathbf{I}}_\downarrow$ and $\hat{\mathbf{I}}_\uparrow$, see Eq. (11.3). The non-interacting levels have, by construction, a vanishing transition dipole matrix element but two-photon transitions can be efficiently implemented; therefore one and two-photon microwave transitions can fully rotate within the three level system.

To derive the Floquet sequence, we find it convenient to re-write the target *t-J-V* Hamiltonian as

$$
\begin{aligned}
\hat{\mathcal{H}}_{t-J} = \sum_{i<j} \Bigg\{ &- \sum_\sigma 2t_{ij} \left[\hat{I}^x_{i,\sigma} \hat{I}^x_{j,\sigma} + \hat{I}^y_{i,\sigma} \hat{I}^y_{j,\sigma} \right] + J^\perp_{ij} \left[\hat{S}^x_i \hat{S}^x_j + \hat{S}^y_i \hat{S}^y_j \right] \\
&+ \sum_\sigma \frac{4}{9} V_{ij} \left[(2-\xi) \hat{I}^z_{i,\sigma} \hat{I}^z_{j,\sigma} + \xi \hat{I}^z_{i,\sigma} \hat{I}^z_{j,\bar\sigma} \right] + \left[J^z_{ij} - \frac{4}{9} V_{ij}(1-\xi) \right] \hat{S}^z_i \hat{S}^z_j \Bigg\},
\end{aligned}
\tag{11.9}
$$

where we have introduced the parameter $\xi \in \mathbb{R}$ and for $\xi = 0$ we retrieve Eq. (11.4). Here, we neglect the chemical potential terms; hence we assume that the driving frequency is low compared to the internal molecular energy scales ω to suppress driving induced excitations, i.e. $1/T_F \ll \omega$. On the other hand, we require the driving frequency to be much faster than flip-flop interactions, $1/T_F \gg \chi$. Since, $\omega \sim 1$ GHz and $\chi \sim 1$ kHz the limits can be achieved without concern of heating at this stage, or higher-order processes.

The above Hamiltonian can be derived as the effective Floquet model engineered from the underlying molecular Hamiltonian, see Eq. (11.6), as we now demonstrate. To obtain the effective Hamiltonian, we define global rotations on the $\hat{\mathbf{S}}$-Bloch sphere by unitary operators $\hat{U}^\alpha(\varphi)$, where $\alpha = x, y, z$ is the rotation axis and φ the angle of rotation. To first order in τ/T_F and assuming instantaneous rotations, the effective Hamiltonian is given by

$$
\hat{\mathcal{H}}_{\text{eff}} = \sum_n \frac{\tau_n}{T_F} \hat{\mathcal{H}}_n
\tag{11.10a}
$$

$$
\hat{\mathcal{H}}_n = \hat{U}^\dagger_n \hat{\mathcal{H}}_{\text{mol}} \hat{U}_n,
\tag{11.10b}
$$

where τ_n is the evolution time of the n-th Floquet step, see Figure 11.2d, and $T_F = \sum_n \tau_n$ is the total time of one Floquet cycle. Moreover, we have defined $\hat{U}_n$ to be the product of all rotations preceding the n-th Floquet step.

11.4 Floquet sequence for *t-J* model

We propose a sequence of microwave rotations that average to an effective Floquet time evolution under a *t-J* model without hole-hole interaction $V = 0$, see Figure 11.4b. The form and coupling strengths of Hamiltonian (11.10a) are summarized in Table 11.1. Enforcing
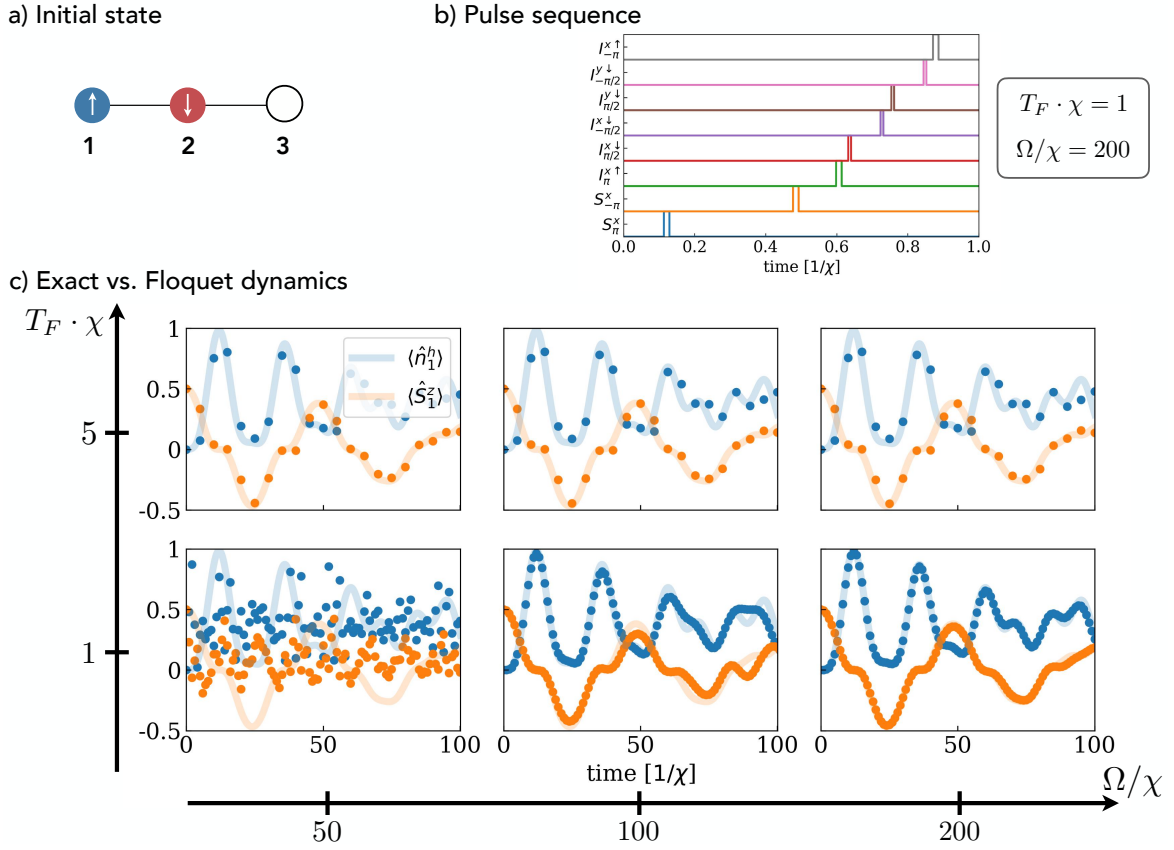
Figure 11.5: **Floquet time evolution. a)** We perform exact time evolution of a system of three molecules by quenching the initial state. **b)** The system evolves under the molecular Hamiltonian and under a sequence of finite width Rabi pulses. The sequence gives rise to a t-J model with $t/J = 1$ ($t = 2/11\chi$) in first-order Floquet theory. **c)** We compare the stroboscopic (dots) to exact target t-J (solid) time evolution the hole occupation (blue) and magnetization (orange) on site 1. We vary the Floquet cycle time T_F as well as the Rabi frequency Ω. For $\Omega/\chi = 50$ and $T_F\chi = 1$, the Rabi pulses overlap such that the Floquet prediction is invalid. For all other parameter regimes, we find very robust prediction of the dynamics.

the constraints that hopping of $\downarrow$- and $\uparrow$-particles should have equal amplitudes as well as equal magnetic XX and YY interactions constrains the time steps in the Floquet evolution. Therefore, we obtain the following set of equations:

$$\frac{\tau}{T} = \left(6\epsilon^{\perp} + 24\epsilon^{t} + 3\right)^{-1} \tag{11.11a}$$

$$\tau_1 = 4\epsilon^{t} \cdot \tau \tag{11.11b}$$

$$\tau_2 = 12\epsilon^{t} \cdot \tau \tag{11.11c}$$

$$\tau_3 = \tau \tag{11.11d}$$

$$\tau_4 = 3\tau \tag{11.11e}$$

time $\cdot T$	τ_1	τ_2	τ_1	τ_3	τ_4	τ_3	τ_4	τ_3	τ_1
$\hat{S}_i^x \hat{S}_j^x$	0	0	0	χ	0	χ	χ	χ	0
$\hat{S}_i^y \hat{S}_j^y$	0	0	0	χ	χ	χ	0	χ	0
$\hat{S}_i^z \hat{S}_j^z$	0	0	0	0	χ	0	χ	0	0
$\hat{I}_{\downarrow,i}^x \hat{I}_{\downarrow,j}^x$	χ	0	χ	0	0	0	0	0	χ
$\hat{I}_{\downarrow,i}^y \hat{I}_{\downarrow,j}^y$	χ	0	χ	0	0	0	0	0	χ
$\hat{I}_{\downarrow,i}^z \hat{I}_{\downarrow,j}^z$	0	0	0	0	0	0	0	0	0
$\hat{I}_{\uparrow,i}^x \hat{I}_{\uparrow,j}^x$	0	χ	0	0	0	0	0	0	0
$\hat{I}_{\uparrow,i}^y \hat{I}_{\uparrow,j}^y$	0	χ	0	0	0	0	0	0	0
$\hat{I}_{\uparrow,i}^z \hat{I}_{\uparrow,j}^z$	0	0	0	0	0	0	0	0	0

Table 11.1: Effective Floquet couplings with $V = 0$. Global rotations of the molecular Hamiltonian (11.6) generate the terms listed in the first column. The rotations and evolution steps τ_n correspond to the sequence shown in Figure 11.2d and Figure 11.4c. The coupling strength arise in the summands of Eq. (11.10a) and have to be multiplied by τ_n/T. Here we have suppressed site indices.

with the effective coupling strength

$$\frac{J^z}{\chi} = \left(\epsilon^\perp + 4\epsilon^t + \frac{1}{2} \right)^{-1} . \tag{11.12}$$

To justify the first-order Floquet expansion, we perform exact diagonalization studies including long-ranged dipolar interactions and finite pulse width, i.e. finite Rabi frequency Ω; for simplicity we assume the same Rabi frequency for all three transitions shown in Figure 11.4a. We compare the time evolution under the Floquet time evolution with the theoretically predicted target model for $t = J^\perp = J^z = 1$ and $V = 0$.

In our numerical calculations, we initialize a system of three molecules in a product state $|\psi(t = 0)\rangle = |\uparrow\rangle_1 \otimes |\downarrow\rangle_2 \otimes |h\rangle_3$, see Figure 11.5a. We continuously time evolve the system under Hamiltonian (11.6) (nearest-neighbour interaction strength χ) and apply periodic rotations between the three levels according to the sequence shown in Figure 11.5b with various realistic Rabi frequencies $\Omega/\chi = 50, 100, 200$. Moreover, we vary the time T_F of a single Floquet cycle. Finally, we stroboscopically measure at times $t_M = MT_F$ with $M \in \mathbb{N}$ and compare observables to the time evolution of an exact *t-J* model shown in Figure 11.5c. We find excellent agreement over the entire range of parameters demonstrating the robustness of the Floquet scheme. Note that for very short times T_F and slow Rabi frequencies Ω, the Floquet prediction breaks down due to overlapping microwave pulses. As soon as the individual pulses are separated, the time evolution is well described by the first-order Floquet Hamiltonian with increasing fidelity for shorter T_F and faster Ω.
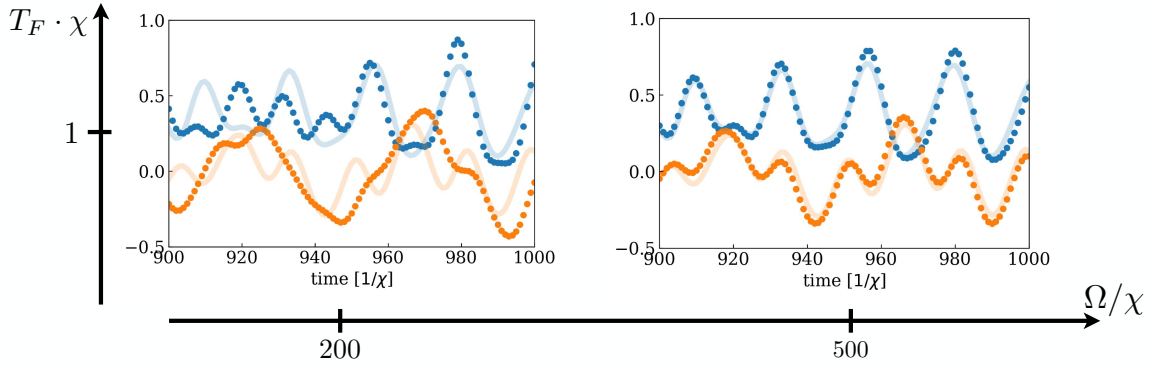
Figure 11.6: **Long time evolution.** As a consistency check, we perform the same calculation as in Figure 11.5 and show the long time behaviour. For faster Rabi frequencies the fidelity of the Floquet approximation increases demonstrating the robustness of our scheme at times exceeding current experimental capabilities.

To analyze the long time behavior of the Floquet sequence, i.e., going way beyond experimentally realistic time scales, we provide additional numerical simulations in Figure 11.6. As expected, we find that short Floquet cycle times T_F and a fast Rabi frequency Ω lead to more robust Floquet dynamics. This demonstrates that - in principle - our scheme enables to accurately explore *t*-*J* models for up to times $T \gg |t|^{-1}, |J|^{-1}$.

11.5   Floquet sequence for *t*-*J*-*V* model

The nearest-neighbour hole-hole repulsion V can tune properties of tightly-bound hole-hole states and drive a crossover from a BEC- to BCS-scenrio in mixed-dimensional *t*-*J* ladders [P10, P6]. Moreover, as we argue in Chapter 9, the hole-hole repulsion V can model the inefficient screening deep in the insulating phase of cuprate superconductors [P11]. Here, we derive a Floquet sequence, which includes a hole-hole repulsion V terms in our proposed scheme for polar molecules. The Floquet sequence is shown in Figure 11.4c. We target a *t*-*J*-*V* model as written in Eq. (11.9) with $\xi = 0$. From Table 11.2, we can read-off the required Floquet times for models with $0 < \epsilon^V < 9/4$ and $\epsilon^\perp > 1/2$:

$$\frac{\tau}{T} = \left[\left(\epsilon^\perp + 2\epsilon^t + 2 \right) \frac{\tau_3}{\tau} + 2(2\epsilon^t + \epsilon^\perp) - 1 \right]^{-1} \tag{11.13a}$$

$$\tau_1 = \left[\frac{\tau_3}{5\tau}(\epsilon^t + 1) + \frac{2}{5}\epsilon^t \right] \cdot \tau \tag{11.13b}$$

$$\tau_2 = \frac{5}{3} \cdot \tau_1 \tag{11.13c}$$

$$\tau_3 = \frac{8}{9/\epsilon^V - 4} \cdot \tau \tag{11.13d}$$

$$\tau_4 = \frac{1}{3} \left[\epsilon^\perp \left(2 + \frac{\tau_3}{\tau} \right) - 1 \right] \cdot \tau \tag{11.13e}$$

$$\tau_5 = \tau \tag{11.13f}$$

time $\cdot T$	τ_1	τ_2	τ_3	τ_2	τ_3	τ_2	τ_1	τ_3	τ_1	τ_3	τ_1	τ_4	τ_5	τ_4	τ_5	τ_4	τ_1
$\hat{S}^x_i \hat{S}^x_j$	0	0	0	0	0	0	0	0	0	0	0	χ	0	χ	χ	χ	0
$\hat{S}^y_i \hat{S}^y_j$	0	0	0	0	0	0	0	0	0	0	0	χ	χ	χ	0	χ	0
$\hat{S}^z_i \hat{S}^z_j$	0	0	0	0	0	0	0	0	0	0	0	0	χ	0	χ	0	0
$\hat{I}^x_{\downarrow,i} \hat{I}^x_{\downarrow,j}$	χ	0	0	0	0	0	χ	χ	χ	0	χ	0	0	0	0	0	χ
$\hat{I}^y_{\downarrow,i} \hat{I}^y_{\downarrow,j}$	χ	0	0	0	0	0	χ	0	χ	χ	χ	0	0	0	0	0	χ
$\hat{I}^z_{\downarrow,i} \hat{I}^z_{\downarrow,j}$	0	0	0	0	0	0	0	χ	0	χ	0	0	0	0	0	0	0
$\hat{I}^x_{\uparrow,i} \hat{I}^x_{\uparrow,j}$	0	χ	0	χ	χ	χ	0	0	0	0	0	0	0	0	0	0	0
$\hat{I}^y_{\uparrow,i} \hat{I}^y_{\uparrow,j}$	0	χ	χ	χ	0	χ	0	0	0	0	0	0	0	0	0	0	0
$\hat{I}^z_{\uparrow,i} \hat{I}^z_{\uparrow,j}$	0	0	χ	0	χ	0	0	0	0	0	0	0	0	0	0	0	0

Table 11.2: **Effective Floquet couplings with V.** Global rotations of the molecular Hamiltonian (11.6) generate the terms listed in the first column. The rotations and evolution steps τ_n correspond to the sequence shown in Figure 11.4c. The coupling strength arise in the summands of Eq. (11.10a) and have to be multiplied by τ_n/T. Here we have suppressed site indices.

with the effective coupling strength

$$\frac{J^z}{\chi} = \frac{2\tau + \tau_3}{T}. \tag{11.14}$$

11.6   Experimental proposal: Rydberg atoms

Rydberg atoms in optical lattices [416] and tweezer arrays have become an established platform in the quantum simulation of magnetism [51, 85, 89, 91, 92, 96]. In particular, tunable spin-1/2 XXZ models have previously been realized via Rydberg dressing [95], Floquet engineering [86, 87] and precise selection of Rydberg states [88].

The model (11.4) we suggest to study requires control over interactions within a three-level system. Here, we propose a direct implementation within highly excited $|nS\rangle$, $|n'P\rangle$ and $|n''S\rangle$ states [88]. As we will calculate explicitly in Section 11.7, this is natural within existing setups and constitutes a promising route because the strong resonant dipole interactions combined with van-der-Waals Ising interactions yield experimentally appealing timescales.

In our Rydberg mapping, we identify the states as follows, see Figure 11.7,

$$|nS\rangle = |\downarrow\rangle \qquad |n'P\rangle = |h\rangle \qquad |n''S\rangle = |\uparrow\rangle. \tag{11.15}$$

The dipole-dipole interaction between states of different parity, see Chapter 2.1, leads to an exchange of excitations between the pair states

$$\langle n'P, nS | \hat{\mathcal{H}}_{\mathrm{Ryd}} | nS, n'P \rangle = (1 - 3\cos^2 \theta_{ij}) \frac{C_3^{SP}}{r_{ij}^3} \tag{11.16a}$$

$$\langle n''S, n'P | \hat{\mathcal{H}}_{\mathrm{Ryd}} | n'P, n''S \rangle = (1 - 3\cos^2 \theta_{ij}) \frac{C_3^{S'P}}{r_{ij}^3} \tag{11.16b}$$

corresponding to tunneling of $\downarrow$-particles and $\uparrow$-particles, respectively. The interaction strength depends on the distance $r_{ij} = |\mathbf{r}_{ij}|$ between two sites i and j and the angle θ_{ij} between $\mathbf{r}_{ij}$ and quantization axis **B**.

Next, we consider the exchange interaction between pairs of spins, i.e., between two atoms in $|nS, n''S\rangle = |\downarrow, \uparrow\rangle$. This state is not directly dipole coupled to the state with exchanged spins $|n''S, nS\rangle = |\uparrow, \downarrow\rangle$. As proposed by Whitlock et al. [417] and as experimentally demonstrated by Franz and Geier et al. [88], van-der-Waals *exchange* interactions between a pair of S states can be implemented. Importantly, the interaction strengths of the van-der-Waals interactions and direct exchange (tunneling t) become comparable by choosing a suitable pair of states close to a Förster resonance, see Chapter 2.1. The induced exchange corresponds to spin flip-flop ($J_\perp$) interaction and the Förster resonance can be tuned by the magnitude and angle of the magnetic field, since the energy differences to virtual pair states experience Zeeman shifts[1]. A detailed derivation can be found in the PhD thesis by Sebastian Geier [399] demonstrating that non-zero coupling matrix elements

$$\langle n''S, nS | \hat{\mathcal{H}}_{\mathrm{Ryd}} | nS, n''S \rangle = \frac{C_{6,\perp}^{SS'}(\theta_{ij})}{r_{ij}^6} \tag{11.17}$$

can be found in ^{87}Rb. The van-der-Waals coefficient $C_{6,\perp}^{SS'}(\theta_{ij})$ has a non-trivial angular dependence, which for the case discussed below can be approximated by the fit function $C_{6,\perp}^{SS'}(\theta_{ij}) = a + b\cos^2 \theta_{ij} + c\cos^4 \theta_{ij}$ with fit parameters a, b and c.

Last, we consider the van-der-Waals-type diagonal interactions between pair states of strength $\propto r_{ij}^{-6}$. Those interactions give rise to spin-spin (J_z), hole-hole (V) and hole-spin (W) interactions as we derive below. Likewise, the pair interactions have a non-trivial and strong angular dependence that is well described by the fit function $C_{6,\parallel}^{SS'}(\theta_{ij}) = a + b\cos^2 \theta_{ij} + c\cos^4 \theta_{ij}$ as above.

Exact mapping of the Rydberg model to a *t-J-V-W* model. We show that the above interaction between three Rydberg states $\{|nS\rangle, |n'P\rangle, |n''S\rangle\}$ give rise to the *t-J-V-W* model with Hamiltonian

$$\hat{\mathcal{H}}_{t-J-V-W} = \hat{\mathcal{H}}_t + \hat{\mathcal{H}}_J + \hat{\mathcal{H}}_V + \hat{\mathcal{H}}_W + \hat{\mathcal{H}}_h + \hat{\mathcal{H}}_\mu, \tag{11.18}$$

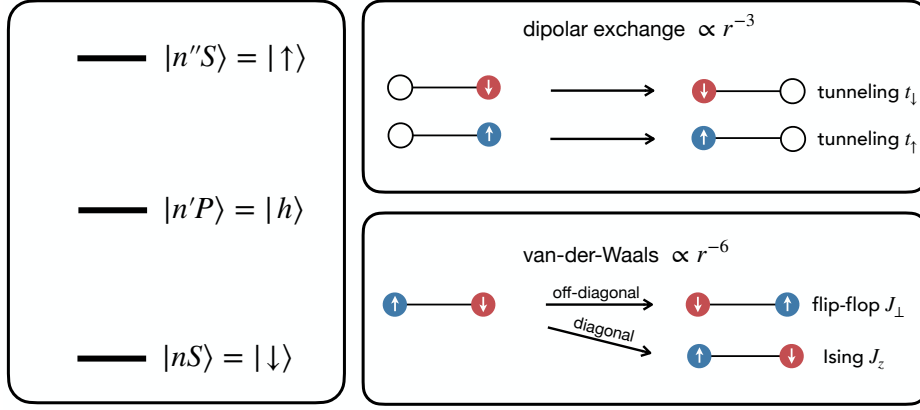[1]Note that we still assume a perturbative, van-der-Waals regime.

Figure 11.7: **Implementation of t-J model in three Rydberg state.** We map three internal Rydberg states of an atom to the local Hilbert space spanned by $\{|h\rangle, |\downarrow\rangle, |\uparrow\rangle\}$. By choosing a specific set of states, see Section 11.7, pair interaction corresponding to tunneling t_σ and spin interactions J_z, $J_\perp$ can be induced. Additional hole-hole (spin-hole) interactions V (W) appear in the exact mapping from the Rydberg Hamiltonian to a t-J-V-W model.

where the interaction terms are given by

$$\hat{\mathcal{H}}_t = -\sum_{i<j}\sum_\sigma t_\sigma(r_{ij}) \left(\hat{a}^\dagger_{i,\sigma}\hat{a}^\dagger_{j,h}\hat{a}_{i,h}\hat{a}_{j,\sigma} + \text{h.c.} \right) \tag{11.19a}$$

$$\hat{\mathcal{H}}_J = \sum_{i<j} \left[J^z(r_{ij})\hat{S}^z_i\hat{S}^z_j + \frac{J_\perp(r_{ij})}{2} \left(\hat{S}^+_i\hat{S}^-_j + \text{h.c.} \right) \right] \tag{11.19b}$$

$$\hat{\mathcal{H}}_V = \sum_{i<j} V(r_{ij})\hat{n}^h_i\hat{n}^h_j \tag{11.19c}$$

$$\hat{\mathcal{H}}_W = \sum_{i<j} W(r_{ij}) \left(\hat{S}^z_i\hat{n}^h_j + \hat{n}^h_i\hat{S}^z_j \right) \tag{11.19d}$$

and the local fields are defined as

$$\hat{\mathcal{H}}_h = \sum_j h^z_j(r_{ij})\hat{S}^z_j \tag{11.20a}$$

$$\hat{\mathcal{H}}_\mu = -\sum_j \mu_j(r_{ij})\hat{n}^h_j. \tag{11.20b}$$

The operators are defined in Section 11.1, i.e., the hardcore bosonic operators $\hat{a}_{j,\alpha}$ are associated with Schwinger spins.

Let us derive the t-J-V-W model step-by-step. First, we consider the off-diagonal terms $\propto t_\sigma, J_\perp$. From Eqs. (11.16) and (11.17), we can directly read-off the exchange processes of the tunneling Hamiltonian $\propto t_\sigma$ and the in-plane spin XY interaction $\propto J_\perp$. The coupling strength expressed in terms of the Rydberg pair exchange interactions $\propto C_3^{SP}, C_3^{S'P}$ and $C_{6,\perp}^{SS'}$ are summarized in Table 11.6.

Next, we want to obtain the diagonal part of Hamiltonian (11.18). To this end, we con-

$t\text{-}J\text{-}V\text{-}W$	Rydberg
$t_\downarrow(r_{ij}) \cdot r_{ij}^3$	$-C_3^{SP}(1 - 3\cos^2\theta_{ij})$
$t_\uparrow(r_{ij}) \cdot r_{ij}^3$	$-C_3^{S'P}(1 - 3\cos^2\theta_{ij})$
$J_z(r_{ij}) \cdot r_{ij}^6$	$C_6^{SS}(\theta_{ij}) + C_6^{S'S'}(\theta_{ij}) - 2C_6^{SS'}(\theta_{ij})$
$J_\perp(r_{ij}) \cdot r_{ij}^6$	$2 \cdot C_{6,\perp}^{SS'}(\theta_{ij})$
$V(r_{ij}) \cdot r_{ij}^6$	$\frac{1}{4}\left[C_6^{SS}(\theta_{ij}) + C_6^{S'S'}(\theta_{ij}) + 2C_6^{SS'}(\theta_{ij})\right] - C_6^{SP}(\theta_{ij}) - C_6^{S'P}(\theta_{ij}) + C_6^{PP}(\theta_{ij})$
$W(r_{ij}) \cdot r_{ij}^6$	$\frac{1}{2}\left[C_6^{SS}(\theta_{ij}) - C_6^{S'S'}(\theta_{ij})\right]$
$h_j^z(r_{ij})$	$\frac{1}{2}\sum_i \frac{1}{r_{ij}^6}\left[C_6^{S'S'}(\theta_{ij}) - C_6^{SS}(\theta_{ij})\right]$
$\mu_j(r_{ij})$	$\frac{1}{4}\sum_i \frac{1}{r_{ij}^6}\left[C_6^{SS}(\theta_{ij}) + C_6^{S'S'}(\theta_{ij}) + 2C_6^{SS'}(\theta_{ij}) - 2C_6^{SP}(\theta_{ij}) - 2C_6^{S'P}(\theta_{ij})\right]$

Table 11.3: **Mapping of interaction strengths.** We show the interaction coefficients of the *t-J-V-W* model, Eq. (11.18), expressed in terms of the C_3 and C_6 coefficients of the Rydberg pair interactions.

sider the Rydberg density-density interactions given by

$$\hat{\mathcal{H}}_{\text{Ryd}}^{\text{diag}} = \sum_{(A,B)\in\mathcal{I}} \sum_{i<j} \frac{C_6^{AB}(\theta_{ij})}{r_{ij}^6} \hat{n}_i^A \hat{n}_j^B, \qquad (11.21)$$

where the coefficients $C_6^{AB}(\theta_{ij})$ describe the diagonal van-der-Waals pair interaction between Rydberg states A and B with the angle θ_{ij} as defined above, and $\mathcal{I} = \{S, S', P\} \times \{S, S', P\}$. We use the hardcore constraint of the occupation number operators,

$$\hat{n}_j^S + \hat{n}_j^{S'} + \hat{n}_j^P = 1 \quad \forall j, \qquad (11.22)$$

to express the number operators by the spin-1/2 operator $\hat{S}_j^z$ and hole occupation $\hat{n}_j^h$ as

$$
\begin{aligned}
\hat{n}_j^S &= -\hat{S}_j^z + \frac{1}{2} - \frac{1}{2}\hat{n}_j^P \\
\hat{n}_j^{S'} &= +\hat{S}_j^z + \frac{1}{2} - \frac{1}{2}\hat{n}_j^P.
\end{aligned}
\qquad (11.23)
$$

Inserting Eqs. (11.23) into the diagonal Hamiltonian Eq. (11.21) yields

$$\hat{\mathcal{H}}_{\text{Ryd}}^{\text{diag}} = \sum_{i<j}\left[J_z(r_{ij})\hat{S}_i^z\hat{S}_j^z + V(r_{ij})\hat{n}_i^P\hat{n}_j^P + W(r_{ij})\left(\hat{S}_i^z\hat{n}_j^P + \hat{n}_i^P\hat{S}_j^z\right) + h^z(r_{ij})\hat{S}_i^z - \mu(r_{ij})\hat{n}_i^P + \text{const.}\right].$$

$$(11.24)$$

This exact mapping allows us to identify the coupling strengths of the diagonal terms in

the *t-J-V-W* model [Eq. (11.18)] with the C_6 van-der-Waals pair interactions. The coupling strength are summarized in Table 11.6. Importantly, we highlight that the dipolar $\propto r^{-3}$ scaling for tunneling and van-der-Waals $\propto r^{-6}$ scaling for the remaining interactions offers an additional tuning knob, particularly useful for application in 2D arrays, see Section 11.7.4.

We note that the re-writing from the occupation number basis in terms of spin operators, i.e., $S_j^z = \frac{1}{2}\hat{n}_j^\uparrow - \frac{1}{2}\hat{n}_j^\downarrow$, introduces linear shift corresponding to a local longitudinal field $\propto h_j^z$ and chemical potential $\propto \mu_j$. The strength of the field is obtained by summing over neighbouring atoms, see Table 11.6, weighted by their distance with r_{ij}^{-6} originating from the van-der-Waals interactions. Since the weights fall off very quickly, we can assume the local fields to be constant within the bulk. However, the boundary atoms experience smaller fields. For example, if we assume that the field in the bulk is constant and of strength $h^z = \zeta \cdot h$, where ζ is the coordination number, then the field at the boundary is to a good approximation of strength $h^z = (\zeta - 1) \cdot h$.

11.7 Experimental realization in ^{87}Rb

In the following, we consider an explicit implementation of our proposed scheme in three Rydberg states of ^{87}Rb, and discuss preliminary experimental results obtained by the group of Antoine Browaeys. The presented pair interaction strengths were calculated by the experimental collaborators using the package from Ref. [84].
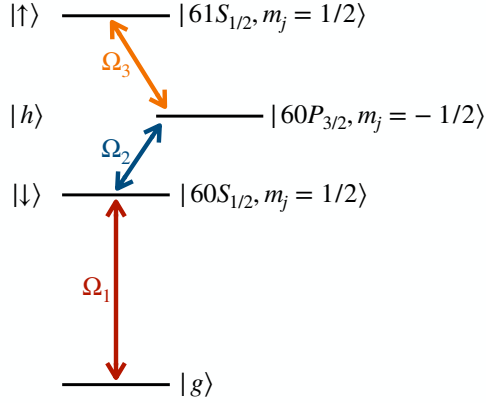
11.7.1 Pair interactions

For the commonly used atomic species ^{87}Rb, we find an experimentally feasible set of Rydberg states, see Figure 11.8a, to be given by

$$|60S_{1/2}, m_j = 1/2\rangle = |\downarrow\rangle \qquad |60P_{3/2}, m_j = -1/2\rangle = |h\rangle \qquad |61S_{1/2}, m_j = 1/2\rangle = |\uparrow\rangle.$$
$$(11.25)$$

The choice of the m_j sublevels allows to change the sign of the tunnelings t_σ; for the above choice we obtain $t_\sigma > 0$ ($t_\sigma < 0$) at $\theta > 54.7°$ ($\theta < 54.7°$). An additional tuning knob, especially for interactions between the 60S and 61S state, is the magnitude $|\mathbf{B}|$ of the magnetic field, which we set to $|\mathbf{B}| = 45\,\text{G}$. To exploit the angular tunability, we consider a 1D chain of $L = 12$ atoms, see Figure 11.8b, and the magnetic field shall be pointing in the plane of atoms. Thus, the angle θ can be tuned by rearranging the location of tweezers in the plane.

In Figure 11.8c, we show the angular dependence of the coupling in the *t-J-V-W* model using the mapping summarized in Table 11.6. For the spin-spin interaction, we find a weak angular dependence and we note that (i) $J_\perp > 0$ is antiferromagnetic, (ii) $J_z < 0$ is ferromagnetic and (iii) we have $|J_\perp| > |J_z|$ for all angles θ. Therefore, for sizable t/J the ground state of the model features AFM in-plane spin-spin correlations allowing us to explore the interplay between mobile hole dopants in an AFM spin background, see Figure 11.1a.
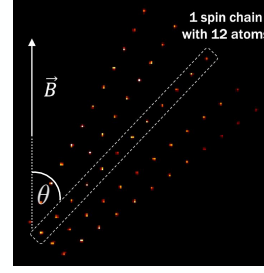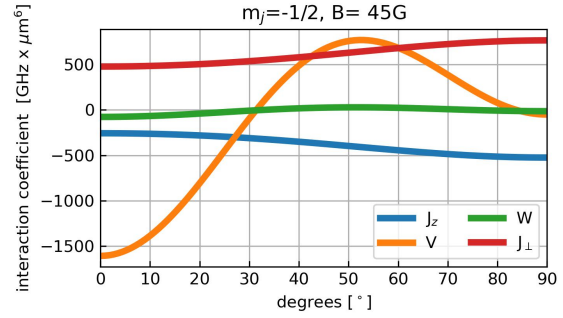
a) Implementation in ^{87}Rb

$|{\uparrow}\rangle$ ——————— $|61S_{1/2}, m_j = 1/2\rangle$

Ω_3

$|h\rangle$ ————— $|60P_{3/2}, m_j = -1/2\rangle$

Ω_2

$|{\downarrow}\rangle$ ——————— $|60S_{1/2}, m_j = 1/2\rangle$

Ω_1

——————— $|g\rangle$

b) 1D chain

c) *t-J-V-W* model

Figure 11.8: **Implementation in ^{87}Rb. a)** As proposed in Section 11.6, we identify three atomic Rydberg states in ^{87}Rb with the hole and spin states at a site. **b)** The image shows averaged fluorescence images of atoms in a tweezer array obtained by the experimental team in the Browaeys group. The magnetic field **B** points in the *x-y* plane of atoms and determines the quantization axis. The picture shows 1D chains of length $L = 12$ with different angle θ between the direction of the chain and the quantization axis. Within a single experiment, only one chain with angle θ is chosen. **c)** The pair interactions between Rydberg atom exactly map onto a *t-J-V-W* model, Eq. (11.18). We show the corresponding interaction strengths for the set of states in **a)** at $|\mathbf{B}| = 45\,\mathrm{G}$; here the hole tunneling has amplitude $t_{\downarrow}(\theta) = 1.06 \cdot t_{\uparrow}(\theta) = (1 - 3\cos^2\theta) \cdot 0.88\,\mathrm{GHz} \times \mu\mathrm{m}^3$. The calculations of the C_3 and C_6 coefficients were performed by Sebastian Geier and the Browaeys lab.

11.7.2 Experimental sequence and benchmarks

The experimental sequence developed by the Browaeys group [89, 90] allows them to prepare initial products states $|\psi(t = 0)\rangle = \otimes_{j=1}^{L}|\alpha\rangle_j$ at time $t = 0$ with $\alpha = h, \downarrow, \uparrow$. Subsequently, the system is time evolved under the Rydberg Hamiltonian, which is equivalent to the *t-J-V-W* model in Eq. (11.18), for a time $t > 0$. At the end of the protocol, one of the Rydberg states is globally transferred to the non-interacting atomic ground state and followed by imaging. Repeatedly executing the sequence collects snapshots of the many-body state $|\psi(t)\rangle$ in one specific Fock basis at discreet times t.

Let us consider absolute numbers in order to estimate available energy scales and experimental regimes. In the following, the distance between neighbouring atoms is set to $d = 9.9\,\mu\mathrm{m}$. This distance provides a trade-off between sufficiently strong interaction, while initial state preparation is still possible with the available Rabi frequencies.

In Table 11.4, we show the coupling amplitudes for a variety of different angles θ, and we find the overall energy scale sizable to observe a few tunnelings and flip-flop events

angle \ couplings	$\theta = 45°$	$\theta = 49.7°$	$\theta = 54.7°$	$\theta = 59.7°$	$\theta = 90°$
$J_\perp / 2\pi$	0.64 MHz	0.67 MHz	0.69 MHz	0.72 MHz	0.81 MHz
$J_z / J_\perp$	-0.62	-0.63	-0.64	-0.65	-0.68
$t_\downarrow / J_\perp$	-0.69	-0.33	0	0.31	1.11
$t_\uparrow / J_\perp$	-0.65	-0.31	0	0.29	1.05
$V / J_\perp$	1.11	1.20	1.17	1.02	-0.07
$W / J_\perp$	0.04	0.05	0.04	0.03	-0.02

Table 11.4: **Coupling strength in 1D chain.** We calculate the coupling strength for the Rydberg states as in Figure 11.8a-c and for different angles θ at $d = 9.9 \, \mu$m.

within experimentally realistic times of up to $t_{\max} \approx 5 \, \mu$s [89]. In the 1D chain, the angle θ can be picked closed to the magic angle $\theta_{\text{magic}} = 54.7°$ [85] to realize a parameter regime with $t/J \ll 1$. In contrast to optical lattice experiments, where the spin interaction is induced by the superexchange mechanism with $J = 4t^2/U$, the Rydberg implementation is not restricted to $t \gg J$. While Hubbard-type models are in the strong coupling regime, $t \gg J$, there are numerous theoretical prediction for $t/J < 1$. These predictions include the dynamics of single holes[2] at weak coupling [418] or phase separation [302], which remain to be confirmed experimentally.

To numerically benchmark the above described experimental protocol, we focus on the set of parameters obtained for $\theta = 45°$. In the experiment, an initial state Néel state with a hole domain wall in the middle, given by

$$|\psi(t = 0)\rangle = | \downarrow\uparrow\downarrow\uparrow \, h \, h \, h h \, \downarrow\uparrow\downarrow\uparrow\rangle, \tag{11.26}$$

is prepared and time evolved. After time t, the local occupation in the hole- and $\downarrow$-basis is measured and plotted in Figure 11.9 (top). Here, the maximal experimental time is $t_{\max} = 2.1 \, \mu$s or $t_{\max} \approx 5/t_\downarrow$. In Figure 11.9, we compare the experimental data to exact numerical simulations using the parameters from Table 11.4 without any fit parameter. We remark that we simulate the Rydberg Hamiltonian, however the Rydberg model and t-J-V-W model are equivalent as shown above[3].

Notably, we find coherence times up to all experimentally measured times, see Figure 11.9 (top right), which can be seen from the flip-flop oscillations of the Néel background. We highlight the excellent agreement to the numerical simulations obtained from ab initio calculations. In the charge sector, we see an interplay between hole motion and the strong hole-hole interactions V. Instead of ballistic spreading of the holes with tunneling t, we observe a reduced hole mobility and a bunching of holes at the center. In the numerical simulations, see Figure 11.9 (bottom left), the holes eventually reach the boundary followed by a reflection of the wavefront. In the experimental data, see Figure 11.9 (top left), we rec-

---

[2]We note that the single-hole problem is independent of the particle statistics.
[3]As a consistency check, we have compared the full spectrum of the two models in a small system.
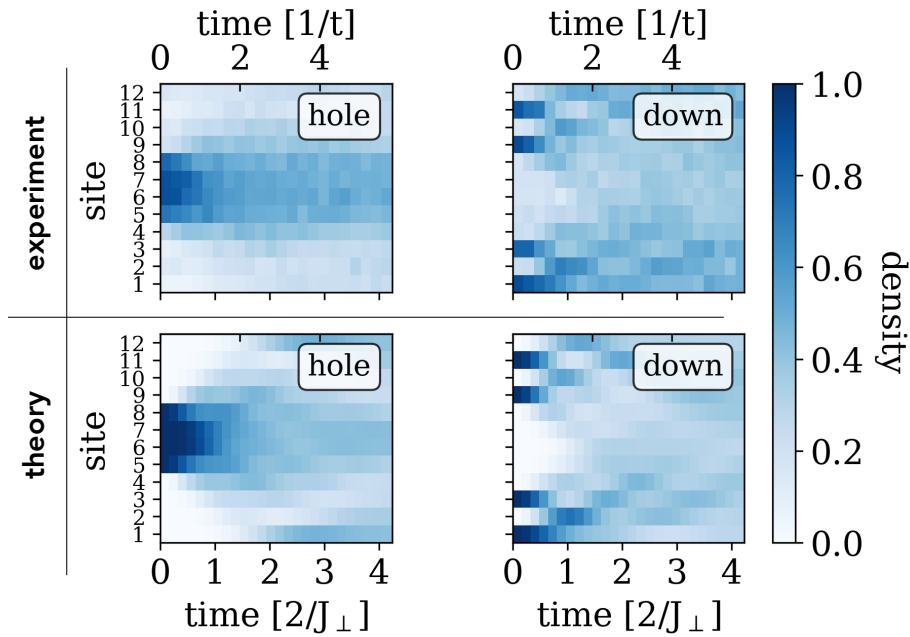
Figure 11.9: **Comparison of experimental data and numerical simulation.** We plot the local occupation of atoms in hole (down) in the left (right) column after time evolving the initial product state state $|\downarrow\uparrow\downarrow\uparrow\ h\ h\ h h\ \downarrow\uparrow\downarrow\uparrow\rangle$. Top: We show preliminary experimental data of a chain of length $L = 12$ and at angle $\theta = 45°$ obtained in the ^{87}Rb Rydberg tweezer experiment in the Browaey's group. The Rydberg state and parameters are chosen as in Figure 11.8 yielding $t_{\downarrow}/J_{\perp} = -0.69$. Bottom: We use the theoretically predicted pair interaction strength and numerically simulate the experiment without any fit parameter.

ognize a faint signal of holes at the boundary and a revival of hole probability in the center at late times.

Experimental errors. The main sources of experimental imperfections are threefold. (1) The largest error source is attributed to imperfect initial state preparation. Hereby, the strong pair interactions between Rydberg states shift the single-particle resonances making it challenging to experimentally prepare high-fidelity initial states. (2) Much smaller errors arise from the spatial fluctuations of the atoms. While the atoms are almost cooled to the ground state of the tweezer trap, the finite trap frequency leads to a spatial extend of the atomic wavefunction in the sub-micrometer range with relative positional errors of around 1%. (3) The decay of Rydberg atoms can be neglected on the time scale of the experiment. The single particle decay rate is around 1% per atom and μs.

We have benchmarked all three error sources using the numerical quantum trajectory method [419] and we compared various observables. By including the experimental errors into our numerical simulations, the experimental data can be reproduced well. As expected, the errors play a more important role in the evaluation of correlation functions. Thus far, the main source of error is purely a technical limitation and can – in principle – be overcome with either larger Rabi frequency or by working at larger distances. However, the latter will require to access longer experimental times, for which Rydberg decay may start to become
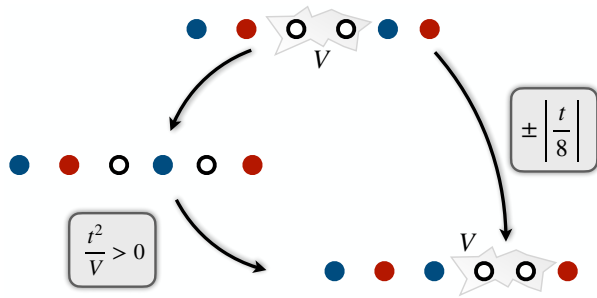
Figure 11.10: **Effective pair mass.** The leading order contributions in the motion of the pair is determined by a second-order tunneling process that interferes either constructively or destructively with NNN tunneling depending on the sign of t.

the main limitation.

11.7.3 Experimental probes for the 1D t-J-V-W model

Next, we discuss probes for the 1D t-J-V-W model that are accessible with the newly established tweezer platform and go beyond experiments in optical lattices. Particularly, we focus on the regime $|t| \ll |J_\perp|, |J_z|$, which is realized for angles $\theta = \theta_{\text{magic}} \pm 5°$ and where hole-hole repulsion V is the dominant energy scale, see Table 11.6; we set $W \equiv 0$ in the following.

Strong repulsive interactions can lead to the formation of a bound state [420]. In the Bose-Hubbard model with two particles this can be understood by a bound state that separates from the scattering continuum from above and thus remains stable. Intuitively, an isolated quantum system cannot dissipate energy and thus by initializing a high-energy state with energy $V \gg t$, it must remain stable because there are no degrees-of-freedom to decay into. Similarly, we propose to prepare an initial product state with

$$|\psi(t=0)\rangle = \left(\sum_\sigma \hat{a}^\dagger_{i_1,h} \hat{a}^\dagger_{i_2,h} \hat{a}_{i_1,\sigma} \hat{a}_{i_2,\sigma} \right) \otimes^L_{j=1} |\sigma_j\rangle \tag{11.27}$$

where $\sigma_j = \downarrow, \uparrow$ is some spin configuration with a total magnetization of $S^z_{\text{tot}} = \langle \sum_j \hat{S}^z_j \rangle$, and we have replaced the spins at sites i_1 and i_2 with holes. The energy of the initial state is determined by the repulsive V and the spin interactions scaling extensively with system size.

Let us first consider the special case where the spins $\{\sigma_j\}_j$ form a ferromagnetic background, i.e., we set the total magnetization to $S^z_{\text{tot}} = 0.5(L-2)$. In this limit, the model t-J-V-W model reduces to hard-core bosons with strong repulsive V and long-range tunnelings t. For sufficiently large V/t and in the limit of NN tunnelings, the repulsive bound state lies well-above the scattering continuum [420] and thus we find a heavy pair of mass $(2t_{\text{eff}})^{-1} = 2V/t^2$. Interestingly, the perturbative tunneling process of the pair can constructive (destructive) interfere with the NNN tunneling processes $t' = t/8$ below (above) the magic angle, see Figure 11.10. Therefore, in the perturbative regime we predict an effective tunneling of the pair given by

$$t_{\text{eff}} = \frac{t^2}{V} \pm \left| \frac{t}{8} \right| \tag{11.28}$$

Constructive interference

$\theta = 49.7°$, r = 9.90 μm, J$_\perp$ = 2$\pi \cdot$ 667kHz,
J$_z$ = -0.63, t = -0.33, W = 0.05, V = 1.20 [J$_\perp$]

Destructive interference

$\theta = 59.7°$, r = 9.90 μm, J$_\perp$ = 2$\pi \cdot$ 721kHz,
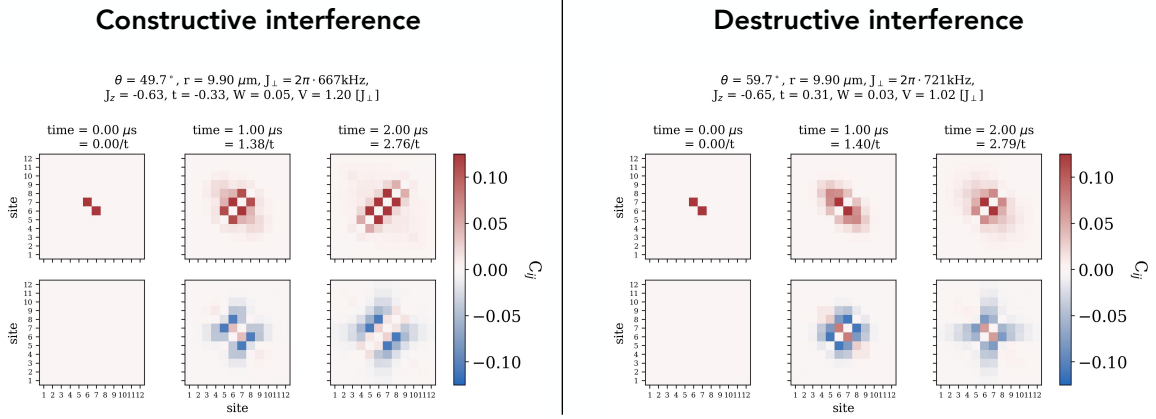J$_z$ = -0.65, t = 0.31, W = 0.03, V = 1.02 [J$_\perp$]

Figure 11.11: **Repulsively bound state in AFM background.** We initialize a Néel state with two holes in the center of a chain of length $L = 12$, and time evolve numerically under Hamiltonian (11.18). We plot the unconnected (connected) hole-hole correlation map on the top (bottom) for different times. The spreading of correlations along the diagonal is a signature of the repulsively bound hole pair. Left: Below the magic angle, $t/V = 0.30$, we find fast spreading of the hole pair. Right: Above the magic angle, $t/V = -0.28$, the NNN tunneling destructively interferes with the perturbative pair tunneling and thus the pair's effective mass is enhanced.

below (+) and above (-) the magic angle.

The situation becomes more subtle once we start to decrease the total magnetization to zero. Then, the problem cannot be reduced to a two-particle problem but instead a much larger Hilbert space is introduced by the spin background. In this scenario, it is not obvious that a repulsively bound state can exists unless the repulsive energy exceeds the extensive energy of the spin background. Experimentally, we can probe the stability of a repulsive pair by initializing the product state $| \downarrow\uparrow\downarrow\uparrow\downarrow \, h\, h \, \uparrow\downarrow\uparrow\downarrow\uparrow \rangle$ followed by time evolution.

To analyze the dynamics of holes and their bound state, we measure the hole-hole correlations

$$C_{ij}(t) = \langle \psi(t)|\hat{n}_i \hat{n}_j|\psi(t)\rangle \tag{11.29}$$

and its connected part

$$C_{ij}^c(t) = \langle \psi(t)| \left[\hat{n}_i - \bar{n}_i\right] \left[\hat{n}_j - \bar{n}_j\right] |\psi(t)\rangle, \tag{11.30}$$

with $\bar{n}_i = \langle \psi(t)|\hat{n}_i|\psi(t)\rangle$. In the presence of a bound state, i.e., correlated pair motion, we expect to observe a spreading of correlations along the diagonal of the correlation map. In Figure 11.11, we plot the correlation map obtained from numerical simulations for angles above ($t/V = 0.30$) and below ($t/V = -0.28$) the magic angle. As predicted from Eq. (11.28), we find a heavy and light pair for the two different cases, which we attribute to interference effects with long-range dipolar tunneling.

In Figure 11.12, we show preliminary experimental data of the spreading of holes at times $t = 2.76/t_\downarrow$ (left) and $t = 2.79/t_\downarrow$ (right). We find a difference in the hole spreading as predicted from the constructive and destructive interference. To understand the difference
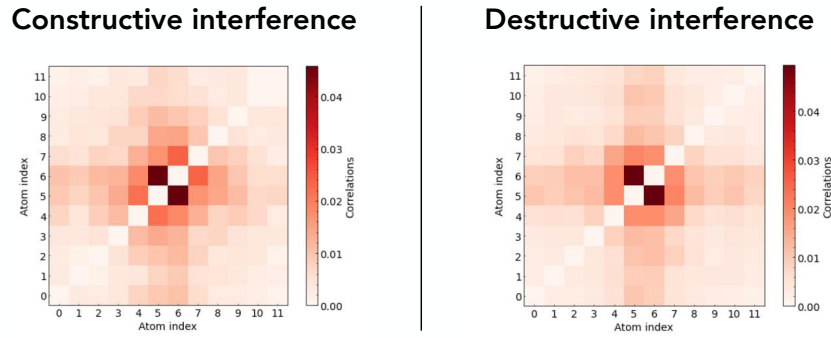
Figure 11.12: **Preliminary experimental observation of bound state.** We show preliminary experimental results obtained by the Browaeys lab. Similarly to Figure 11.11, we plot the unconnected hole-hole correlations at time $t = 2.76/t_\downarrow$ (left) and $t = 2.79/t_\downarrow$ (right). We recognize a visible difference between the constructive and destructive pair tunneling.

between the numerical prediction and the experimental data, we have simulated various sources of errors, see Section 11.7.2. Currently, the signal is mostly limited by infidelities in the state preparation, which becomes particularly challenging for the AFM background.

In conclusion, we find numerical evidence and experimental signatures for the existence of a (metastable) repulsively bound state by quenching a hole pair in the AFM spin background. The magnetic degrees-of-freedom are in principle able to absorb the large repulsive energy between the two holes. Thus, we expect that the bound state eventually decays in the limit of long times and large systems.

11.7.4 Extension to 2D tweezer arrays

The experimental implementation of t-J models in tweezer arrays opens up a promising new route to explore strongly-correlated quantum matter. Especially, the access to arbitrary two dimensional geometries, the tunability of parameters and the long-range tunnelings are new features in the toolbox for quantum simulation of doped magnets.

In this Section, we want to elaborate on experimentally relevant details for the realization of the t-J-V-W model in the Rubidium setup discussed above. We focus an spatial isotropic interaction, i.e., we set the angle $\theta = 90°$. Nevertheless, the different algebraic decay coefficients allows us to tune the ratio of tunneling couplings t to all other interactions. In Figure 11.13, we plot the interaction strength as the distance between neighbouring atoms is changed. Notably, the ratio of $t/J_\perp$ can be tuned from $t/J_\perp < 1$ to the regime relevant for cuprates, where $t/J_\perp \approx 3$. For the given magnetic field strength of $B = 45\,\text{G}$, the Ising interaction J_z is ferromagnetic and the in-plane $J_\perp$ is antiferromagnetic. Since the in-plane magnetism dominates $J_z/J_\perp = -0.68$, the spin background is in the easy-plane regime. In Appendix A, we summarize the interaction strength in the t-J-V-W model for different P-states in the $|60P_J, m_j\rangle$ manifold.

The 2D implementation enables us to experimentally explore a variety of interesting regimes, such as ground states of the bosonic t-J-V-W model or thermalization dynamics. Here, we want to focus on the role of long-range tunnelings. On the square lattice, the dipolar interactions give rise to NNN tunnelings of strength $t' \approx 0.35t$, where t is the NN
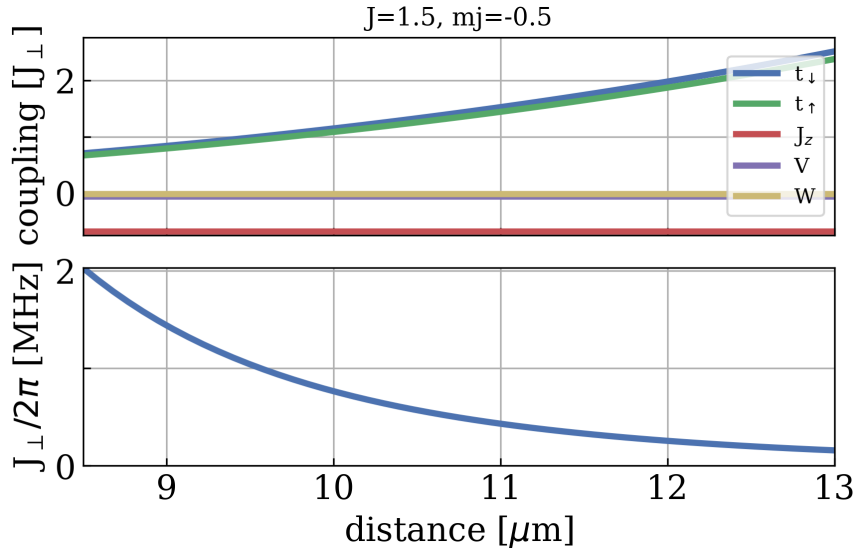
Figure 11.13: **Tunability of interaction in 2D.** We plot the interaction strength for the same Rydberg states as in Figure 11.8 for the angle $\theta = 90°$. Bottom: By increasing the distance between NN atoms, the overall energy scale $J_\perp$ drops as r^{-6}. Top: Since the tunneling arises from dipolar interactions, the ratio between $t/J_\perp$ can be tuned via the distance. For the given set of states and parameters, we find an easy-plane AFM with $J_z/J_\perp = -0.68$. The calculations of the C_3 and C_6 coefficients were performed by Sebastian Geier and the Browaeys lab.

tunneling amplitude. Hence, it introduces sizable NNN tunneling terms, which recently have raised much attention because they are believed to be relevant for the understanding of superconductivity in Fermi-Hubbard models [283, 284], see also Chapters 9 and 10. Moreover, the implementation of t' terms with $|t'| < |t|$ in optical lattice experiments have so far remained elusive.

As an interesting first experimental test in 2D, we propose to study the single-hole dynamics in the presence of NNN tunnelings t' [7]. We emphasize that for single holes, the quantum statistics of the hole does not play a role and thus it directly allows us to study the single-hole problem, see Chapter 8, which has been studied extensively since the discovery of high-Tc in cuprates [21, 32, 35, 305, 311, 313, 314, 320, 333, 349]. In the experimental protocol, we suggest to prepare an initial Néel state with a hole in the center. In the subsequent evolution, we expect a rich dynamics: (i) The spin background will thermalize to a finite temperature state, which we believe to be in the range of current optical lattice experiments [P1]. (ii) The hole's motion disturbs the spin background while associated string tension dynamically changes as the background thermalizes. (iii) At long times, we expect the hole to spread with a velocity $\propto J_\perp$.

11.8 Further experimental probes and perspectives

To summarize, we have introduced novel schemes to quantum simulate doped antiferromagnets in three-internal states of cold molecules or Rydberg tweezers. First experimen-

tal results show excellent agreement with numerical simulations in 1D with promising prospects for future experiments in 2D. The implementation in tweezer arrays allows to realize new types of experimental protocols: For example, one can prepare a superposition between different particle numbers sector, such that the many-body Green's function in the charge sector can be measured in real time and real space, see. Ref. [421]. Further, the access to non-trivial geometries is a novel tuning knob to effectively engineer new classes of strongly correlated Hamiltonians, such as non-Abelian lattice gauge theories [P9], see Chapter 5.

Notably, our scheme for cold molecules is based on Floquet engineering of dipolar interacting three-level systems, which can be found in abundance in the context of quantum simulation. Thus, other platforms such as trapped ions [13] or nitrogen vacancy centers [422] can be used to implement our scheme. In combination with previously established protocols, e.g., variational quantum eigensolvers [423], our scheme provides a powerful tool in the study of doped antiferromagnets.
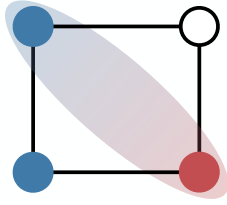
12

Mixed-dimensional *t-J* models and nickelate superconductors

THE EMULATION of an actual strongly correlated electron system in a quantum simulator would be a striking validation of its applicability beyond foundational science and for models that resist numerical simulation. For example, the simulation of the Fermi-Hubbard model at temperatures $k_B T \ll J$ could provide valuable insight or bring us one step closer to the solution of the pairing problem in cuprates, see Chapter 8. Alternatively, the search for artificially engineered and readily implementable Hamiltonians, in which the energy scales for ubiquitous phenomena such as pairing is enhanced, is another useful path. Particularly, it necessitates to develop new probes and data evaluation tools [7, 8] to analyze those phenomena, hence pushing the theoretical frontier of exploring strongly correlated systems with quantum simulators.

Here, we report on recent developments in a class of mixed-dimensional bilayer Hubbard models. In these models, the tunneling of charges is restricted to within the planes while the spin interactions are both intra-layer and inter-layer, see Figure 12.1. Intuitively, this allows two holes to occupy the same rung of the bilayer model overcoming both the strong repulsion and Pauli pressure in the 2D single-layer Hubbard model. In Ref. [P2], we show that the associated binding energy of two holes is remarkably large and within reach for ultracold atoms experiments [424]. Further, we develop a phenomenological parton model for the magnetic binding mechanism between holes based on confining strings, see Chapter 9. In addition, we performed a BCS mean-field analysis of the model indicating both *s*- and *d*-wave superconductivity with inter-layer Cooper pairing in the finite doping regime [P1].

The most relevant application of our mixed-dimensional scheme, however, became apparent with the recent discovery of high-Tc superconductivity in the pressurized nickelate compound $La_3Ni_2O_7$ (LNO) [425]. Because of its similarity in orbital structure to cuprates, the nickelate compounds have been a hot candidate in the search for superconductors
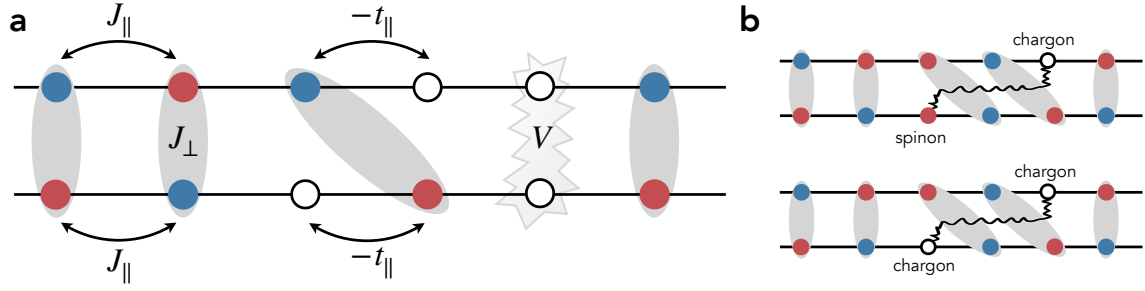
Figure 12.1: **Mixed-dimensional *t*-*J*-*V* model. a** We study a model, where charge motion is restricted to intra-layer tunneling $t_\parallel$, whereas AFM exchange interactions are allowed both in the plane $J_\parallel$ and on the rungs $J_\perp$. For strong inter-layer coupling $J_\perp \gg J_\parallel$ the undoped ground-state is determined by a valence bond solid of rung singlets [P1, P2]. In this Chapter, we examine the effect of doping the mixed-dimensional system, and find strong evidence for parton bound states with spinon-chargon and chargon-chargon character [P2] shown in panel **b**. In addition, the repulsive interaction V allows to tune an emergent Feshbach resonance mediating strong attractive interactions [P11, P7, P10, P6, 342]. Here, we illustrate the 1D mixed-dimensional ladder, but the generalization to 2D models is straight forward.

with high critical temperatures, but the critical Tc's in previous studies have not exceeded 31K [426]. The LNO compound have a bilayered structure and change their crystal structure under the application of high pressure on the order of tens of GPa [425]. The theoretical modelling of the pressurized LNO compounds suggests that the materials may be described by a mixed-dimensional bilayer Hubbard model [411, 427–429], which for strong coupling $U \gg t$ can be described by a mixed-dimensional *t*-*J* model of the form

$$
\begin{aligned}
\hat{\mathcal{H}} = & -t_\parallel \sum_{\substack{\langle i,j \rangle, \\ \sigma, \mu}} \hat{P} \left(\hat{c}^\dagger_{i,\sigma,\mu} \hat{c}_{j,\sigma,\mu} + \text{H.c.} \right) \hat{P} + J_\parallel \sum_{\langle i,j \rangle, \mu} \left(\hat{\vec{S}}_{i,\mu} \cdot \hat{\vec{S}}_{j,\mu} - \frac{1}{4} \sum_{\alpha,\beta} \hat{n}_{i,\alpha,\mu} \hat{n}_{j,\beta,\mu} \right) \\
& + J_\perp \sum_j \left(\hat{\vec{S}}_{j,1} \cdot \hat{\vec{S}}_{j,2} - \frac{1}{4} \hat{n}_{j,1} \hat{n}_{j,2} \right) + V \sum_j \hat{n}_{j,1} \hat{n}_{j,2},
\end{aligned}
\tag{12.1}
$$

where $\hat{c}^\dagger_{j,\sigma,\mu}$ creates a fermion with spin $\sigma = \downarrow, \uparrow$ on site j and in layer $\mu = 0, 1$. The number operator is given by $\hat{n}_{j,\mu} = \sum_\sigma \hat{n}_{j,\sigma,\mu}$ Here, we have included extended Hubbard interactions V on the rungs. As illustrated in Figure 12.1a, the tunneling $t_\parallel$ of particles is one dimensional, whereas the AFM spin exchange interaction can be within ($J_\parallel > 0$) and between layers ($J_\perp > 0$).

Therefore, our previous studies [P1, P2] find direct application in the pressurized nickelates and allow us to propose a magnetically induced, microscopic pairing mechanism for this material. In collaboration with Hannah Lange, we extensively studied the 1D ladder showing a pairing dome as the system is doped away from the VBS. Remarkably, the pairing dome remains present even for strong repulsion V [P10, P6]. We explain the doping induced pairing by an emergent Feshbach resonance of the parton bound states [P10, 342], see Figure 12.1b. In addition, we provide an extension of the experimental scheme for ultracold atoms in Ref. [P2] and propose to dope the bottom and top layer with holes and doublons, respectively. This allows to both realize the extended Hubbard interaction V via

a superexchange mechanism, and to probe the finite doping without actually changing the number of particles in the system [P6].

In the following, we start with a discussion of the effective spinon-chargon and chargon-chargon parton models in Section 12.1, and their experimental relevance for ultracold atoms in Section 12.2. We present results of a BCS mean-field analysis of the 2D mixed-dimensional model at finite doping in Section 12.3. Lastly, we discuss the numerical signatures for Feshbach mediated pairing in Section 12.4. This Chapter is based on publications [P1, P2, P10, P6], and has textual overlap with Refs. [P1, P2]. The text and figures are rearranged, adapted and supplemented.

12.1   Effective parton models: (sc) and (cc) bound states

Let us consider the limiting cases of the Hamiltonian (12.1) for $V = J_\parallel = 0$ and $J_\perp > 0$. The undoped ground state is given by a product state of rung singlets

$$|0\rangle = 2^{-L^d/2} \prod_j (|\uparrow\downarrow\rangle_j - |\downarrow\uparrow\rangle_j), \tag{12.2}$$

where L^d is the volume of the d-dimensional system. Upon doping the ground state with one or two holes (or doublons), the hopping of the hole tilts the singlets on the rungs, see Figure 12.1b. This results in an energy cost $E_\ell \propto J_\perp \cdot \ell$, where ℓ are the number of tilted singlets. This picture shares great similarities to the string picture used in Chapter 9. There we found that spinons and chargons can form parton bound states in the presence of an attractive string tension E_ℓ. In the following, we will construct a string model for spinon-chargon (sc) and chargon-chargon (cc) mesonic bound states, and compare it to numerical DMRG simulations.

The starting point is the parton description of the t-J model. To this end, we express the underlying electrons as slave fermions, by writing

$$\hat{c}_{j,\mu,\sigma} = \hat{h}_{j,\mu}^\dagger \hat{a}_{j,\mu,\sigma} \tag{12.3}$$

and imposing the constraint

$$\sum_\sigma \hat{a}_{j,\mu,\sigma}^\dagger \hat{a}_{j,\mu,\sigma} + \hat{h}_{j,\mu}^\dagger \hat{h}_{j,\mu} = 1 \tag{12.4}$$

with fermionic chargons $\hat{h}_{j,\mu}$ and with Schwinger bosons $\hat{a}_{j,\mu,\sigma}$. By expressing the tunneling part of Hamiltonian (12.1) with slave fermions yields

$$\hat{\mathcal{H}}_t = t_\parallel \sum_{\langle i,j \rangle} \sum_{\mu,\sigma} \left(\hat{a}_{i,\mu,\sigma}^\dagger \hat{a}_{j,\mu,\sigma} \hat{h}_{j,\mu}^\dagger \hat{h}_{i,\mu} + \text{h.c.} \right) \tag{12.5}$$

with an overall amplitude $+t_\parallel$. The spin-exchange terms $J_\perp$ and $J_\parallel$ have the usual Schwinger boson representations [112], see Chapter 11.

We use the following construction to obtain a set of string basis states. First, we remove one or two holes, respectively, from the VBS ground state (12.2) and define the length $\Sigma = 0$

string states

$$|j, \mu, \sigma, \Sigma = 0\rangle_{\text{sc}} = \hat{h}^{\dagger}_{j,\overline{\mu}} \sqrt{2} \hat{a}_{j,\overline{\mu},\overline{\sigma}} |0\rangle, \tag{12.6}$$

$$|j, \Sigma = 0\rangle_{\text{cc}} = \hat{h}^{\dagger}_{j,1} \hat{h}^{\dagger}_{j,0} \sum_{\sigma} \frac{(-1)^{\sigma}}{\sqrt{2}} \hat{a}_{j,1,\sigma} \hat{a}_{j,0,\overline{\sigma}} |0\rangle. \tag{12.7}$$

Note that the spinon-chargon (sc) state carries the quantum numbers of the spinon σ, the layer μ and charge, whereas the chargon-chargon (cc) object is a spin singlet of charge 2e.

The geometric strings are obtained by applying the tunneling operator to the initial states in Eq. (12.6). We label the states by the chargon's path $\mathcal{L}_{\Sigma}$, consisting of a series of links $\langle i, j \rangle$ defining the string, and displacing spins along the path. The string operator is

$$\hat{G}_{\Sigma,\mu} = \prod_{\langle i,j \rangle \in \mathcal{L}_{\Sigma}} \left(\hat{h}^{\dagger}_{j,\mu} \hat{h}_{i,\mu} \sum_{\sigma} \hat{a}^{\dagger}_{i,\mu,\sigma} \hat{a}_{j,\mu,\sigma} \right), \tag{12.8}$$

where the order of the product is important. The corresponding states are

$$|j, \mu, \sigma, \Sigma\rangle_{\text{sc}} = \hat{G}_{\Sigma,\overline{\mu}} |j, \mu, \sigma, \Sigma = 0\rangle_{\text{sc}}, \tag{12.9}$$

$$|j_{\mu}, \Sigma\rangle_{\text{cc}} = \hat{G}_{\Sigma,\overline{\mu}} |j, \Sigma = 0\rangle_{\text{cc}}. \tag{12.10}$$

The geometric strings, obtained by displacing spins, correspond to tilted singlets between the two layers $\mu = 0, 1$, as depicted in Figure 12.1b.

In $d = 1$, the (cc) string states form an orthonormal basis (ONB) with

$$_{\text{cc}}\langle j'_{\mu}, \Sigma' | j_{\mu}, \Sigma\rangle_{\text{cc}} = \delta_{\Sigma',\Sigma} \delta_{j_{\mu}, j'_{\mu}} \tag{12.11}$$

because states with different chargon positions have a vanishing overlap, and the string state is uniquely defined by the chargons. In $d = 2$, different paths Σ, Σ' can lead to states with the same chargon position but non-zero overlap due to the overlaps of the underlying singlets. Nevertheless, we approximate the (cc) string state as an overcomplete ONB with $_{\text{cc}}\langle j'_{\mu}, \Sigma' | j_{\mu}, \Sigma\rangle_{\text{cc}} \approx \delta_{\Sigma',\Sigma} \delta_{j_{\mu}, j'_{\mu}}$; for example, two strings Σ, Σ' whose difference defines a loop around a single plaquette in a square lattice lead to an overlap squared $|\langle \Sigma | \Sigma' \rangle|^2 = 1/16$. If the difference of the two strings defines larger loops, the overlap decays exponentially with the loop size [112].

The (sc) string states, however, do not form an orthonormal basis set. While the states are orthonormal with respect to the chargon position, the (tilted) rung singlets have non-zero overlap in both $d = 1$ and $d = 2$ and appear for any string length. In general, the overlaps of these (sc) states are

$$_{\text{sc}}\langle j'_{\text{c}}, \mu', \sigma', \Sigma' | j_{\text{c}}, \mu, \sigma, \Sigma\rangle_{\text{sc}} = \delta_{j_{\text{c}}, j'_{\text{c}}} \delta_{\mu,\mu'} \delta_{\sigma,\sigma'} g_{\Sigma,\Sigma'} \tag{12.12}$$

where we defined a metric tensor g with matrix elements

$$g_{\Sigma,\Sigma'} = 2^{-|\Sigma - \Sigma'|}. \tag{12.13}$$

This necessitates to perform a Gram-Schmidt orthonormalization procedure to construct the (sc) bound states.

In the following, we first apply a simple linear string theory to a model with an ONB for both (sc) and (cc) string states. We use the model to obtain the ground-state energy of two bound holes E_{cc}, which we compare to the ground-state energy of two single holes $2E_{sc}$. This will allow us to extract the binding energy $E_B = 2E_{sc} - E_{cc}$.

In a second step, we apply a Gram-Schmidt method to the (sc) string Hilbert space in order to derive a more accurate model of the (sc) parton bound state, which we will call Gram-Schmidt parton model (GSP model). We compare the model to energies obtained from DMRG simulations and find excellent agreement between the numerical simulations and the binding energies calculated in the GSP model.

12.1.1   Orthonormal basis: Estimating the binding energy

In the effective parton basis, the underlying t-J Hamiltonian for two distinguishable partons connected by a string Σ becomes

$$\hat{\mathcal{H}}_{2p} = +\kappa \sum_{\delta_\kappa} \sum_{\Sigma} \Big(|x_1 + \delta_\kappa, \Sigma - \delta_\kappa\rangle \langle x_1, \Sigma| + \text{H.c.} \Big) + t_\| \sum_{\langle \Sigma', \Sigma \rangle} \sum_{x_1} \Big(|x_1, \Sigma'\rangle \langle x_1, \Sigma| + \text{H.c.} \Big)$$
$$+ \sum_{x_1} \sum_{\Sigma} V(\Sigma) |x_1, \Sigma\rangle \langle x_1, \Sigma|.$$

$$(12.14)$$

Note that the string connects two partons at site x_1 and $x_2 = x_1 + \Sigma$. Thus, the first (second) term describes tunneling of the first (second) parton. If the parton is a chargon, its (fast) motion arises from tunneling $\kappa = t_\|$ and the position is shifted to a nearest-neighbor site $\delta_\kappa = \pm 1$. If the parton is a spinon, its (slow) motion arises from a spin exchange $\kappa = J_\|$ and the position is shifted to a next-nearest-neighbor site $\delta_\kappa = \pm 2$. In the following, we assume $t_\| \gg J_\|$ and therefore we neglect the spinon motion, whereas the chargon motion is of significant importance. Moreover, the last term gives rise to a linear string potential, which we will approximate in the following by a linear potential $V(\Sigma) \approx V(\ell_\Sigma)$, where ℓ_Σ is the length of a string Σ [21].

To solve Eq. (12.14), we apply a Lee-Low-Pines (LLP) transformation [390] into the co-moving frame of the parton at site x_1, using

$$\hat{U}_{\text{LLP}} = \exp[-i\hat{x}_1 \hat{p}_2], \qquad (12.15)$$

where $\hat{p}_2$ is the momentum of the second chargon. The resulting Hamiltonian

$$\hat{U}_{\text{LLP}}^\dagger \hat{\mathcal{H}}_{2p} \hat{U}_{\text{LLP}} = \sum_k |k\rangle_1 \langle k| \otimes \tilde{\mathcal{H}}_{2p}(k) \qquad (12.16)$$

is block-diagonal in the eigenbasis of $\hat{p}_1$, where each block can be labeled by the total conserved system momentum $k \in [-\pi, \pi)$ in the original basis. The individual blocks take the

form

$$\tilde{\mathcal{H}}_{2\text{p}}(k) = t_\parallel \sum_\Sigma \left[|\Sigma + 1\rangle\langle\Sigma| \, \left(1 + \kappa e^{i\delta_\kappa k}\right) + \text{h.c.} \right] + \sum_\Sigma V(\ell_\Sigma)|\Sigma\rangle\langle\Sigma|. \tag{12.17}$$

I.e. in the co-moving frame the effective chargon tunneling is given by

$$\tilde{t}(k) = t_\parallel \left(1 + \kappa e^{i\delta_\kappa k}\right) \tag{12.18}$$

and depends strongly on k.

Next, we consider the lowest-energy eigenstate with momentum $k = 0$ [P2]. For the spinon-chargon bound state, the kinetic energy is determined by the original chargon tunneling $\tilde{t} = t_\parallel$, where we have used $t_\parallel \gg J_\perp$. For the chargon-chargon bound state, the kinetic energy is enhanced and given by $\tilde{t} = 2t_\parallel$. The ground-state energy of Hamiltonian (12.17) in a linear confining string potential $V(\ell) = \sigma_0 \ell$ with string tension σ_0 is known to have the universal scaling form [21, 317]

$$E_{2\text{p}} = -2\tilde{t}\sqrt{z-1} + \alpha \, \tilde{t}^{1/3} \, \sigma_0^{2/3}. \tag{12.19}$$

The constant $\alpha > 0$ is a non-universal, geometry dependent constant and z is the coordination number.

Therefore, we can estimate the binding energy $E_B = 2E_{sc} - E_{cc}$ as

$$E_B = 2\left[-2t_\parallel\sqrt{z-1} + \alpha \, t_\parallel^{1/3}\right] - \left[-4t_\parallel\sqrt{z-1} + \alpha \, (2t_\parallel)^{1/3}\right] \tag{12.20}$$

$$= -\alpha \underbrace{\left(2 - 2^{1/3}\right)}_{=0.740\ldots} t_\parallel^{1/3}\sigma_0^{2/3}. \tag{12.21}$$

This leads to our main result: our effective parton model predicts a remarkably large binding energy depending on the sting tension $\sigma_0 \propto J_\perp$ and the tunneling $t_\parallel$. Let us try to develop an intuitive understanding of the large binding energies compared to the 2D Hubbard model. The mixed-dimensionality circumvents the Pauli exclusion of fermionic holes on same site because they are distinguishable particles with layer index $\mu = 0, 1$. This reduces the Pauli pressure present in the chargon-chargon bound states of the 2D t-J model [35, 36], see Chapter 10.1.3, and therefore the kinetic energy can be fully exploited resulting in a light chargon-chargon pair of mass $m_{\text{cc}}^{-1} \propto 2t_\parallel$.

As discussed above, the string states do not form an ONB in the spinon-chargon case and hence the above calculation is only approximate. The finite overlap of string states will effectively reduces the string tension and induces spinon motion. In the next section, we apply a Gram-Schmidt orthogonalization procedure to derive a more accurate effective parton model.

12.1.2 Gram-Schmidt parton model

Now we go beyond the dimer parton model and describe the effects of non-orthogonal string states in the mixed-dimensional bilayer $t - J$ model, Eq. (12.1), using the Gram-Schmidt method. This leads us to a microscopic description of spinon-chargon bound states
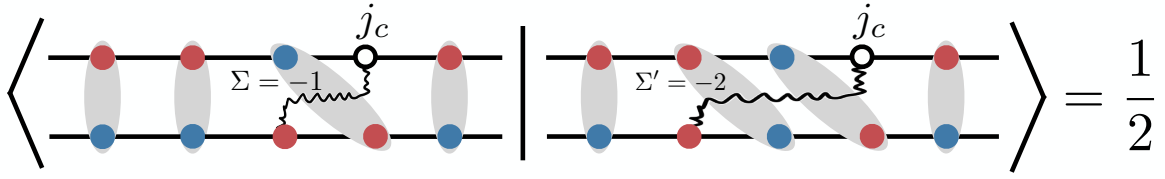
Figure 12.2: **Non-orthogonal string states.** The two parton string states with the common chargon position j_c have non-zero overlap due to the non-zero overlap of singlets. In the above example, the overlap is given by the difference in the string length $2^{-|\Sigma - \Sigma'|}$

in the system. We show that taking into account the following two corrections to the ONB parton model gives a significant quantitative improvement and leads to excellent agreement with numerical DMRG calculations in $d = 1$:

(1) non-orthogonality between different parton and string states (not relevant for the chargon-chargon bound state in the ladder), and

(2) fluctuations of the string due to magnetic interactions $J_\perp$ between the layers and $J_\parallel$ within one layer.

Moreover, we will work in the co-moving frame of the chargon to describe the parton dynamics of the spinon-chargon (chargon-chargon) pairs, see LLP transformation in Eq. (12.17).

Spinon-chargon bound state in 1D

First, we note that chargon-chargon string states $|j_\mu, \Sigma\rangle_{cc}$ in a ladder fulfill the orthogonality condition $_{cc}\langle j'_\mu, \Sigma'|j_\mu, \Sigma\rangle_{cc} = \delta_{j,j'}\delta_{\Sigma,\Sigma'}$ and thus Hamiltonian Eq. (12.14) in the co-moving frame does not need to be modified due to non-ONB effects. Further, magnetic interactions $J_\parallel$ within the layer only yield a constant energy shift but do not add additional dispersion to neither the chargon motion nor parton dispersion in the approximate string basis.

Next, we consider the spinon-chargon (sc) string states $|j_c, \mu, \sigma, \Sigma\rangle_{sc}$; here j_c denotes the location of the chargon, and the string $\Sigma \in \mathbb{Z}$ points from the chargon to the spinon. This convention is different from the notation in Eq. (12.9), but it is advantageous since two states with chargons at different positions $j'_c \neq j_c$ are orthogonal. In general, the overlaps of these sc states are

$$_{sc}\langle j'_c, \mu', \sigma', \Sigma'|j_c, \mu, \sigma, \Sigma\rangle_{sc} = \delta_{j_c, j'_c}\delta_{\mu,\mu'}\delta_{\sigma,\sigma'}g_{\Sigma,\Sigma'} \tag{12.22}$$

where we defined a metric tensor $g = g_{\Sigma,\Sigma'} = 2^{-|\Sigma-\Sigma'|}$ as in Eq. (12.13). To deal with the non-orthonormality, we first project the Hamiltonian onto a subspace of the full Hilbertspace spanned by the string states $|j_c, \Sigma\rangle$. In particular, we derive the matrix elements of the projected Hamiltonian through a variational ansatz $|\Psi^{(n)}(k)\rangle$ defined below. We then perform a basis transformation to an ONB by means of a Gram-Schmidt procedure. We thus obtain an ONB Hamiltonian that can be treated by exact diagonalization methods.

We start with a translationally-invariant variational ansatz of strings fluctuating around the chargon,

$$|\Psi^{(n)}\rangle = L^{-1/2} \sum_{j_c} e^{ikj_c} \sum_{\Sigma} \psi_\Sigma^{(n)} |j_c, \Sigma\rangle, \tag{12.23}$$

which is the most general ansatz respecting the total momentum conservation. Furthermore, without loss of generality, we have chosen to work in the sector $|j_c, \Sigma\rangle \equiv |j_c, \mu, \sigma, \Sigma\rangle_{sc} = |j_c, \mu = +1, \sigma = \uparrow, \Sigma\rangle$. This is justified because we consider no tunneling between the layers, $t_\perp = 0$, and the Hamiltonian conserves total $\hat{S}^z = \sum_{j,\mu} \hat{S}_{j,\mu}^z$. The variational kinetic energy, derived from the underlying *t-J* model, yields

$$\langle \hat{\mathcal{H}}_t(k)\rangle = \frac{t_\|}{L} \sum_{j_c, j_c'} e^{ik(j_c - j_c')} \sum_{\Sigma, \Sigma'} \bar{\psi}_{\Sigma'}^{(n)} \psi_\Sigma^{(n)} \langle j_c', \Sigma'| \left(|j_c + 1, \Sigma - 1\rangle + |j_c - 1, \Sigma + 1\rangle \right). \tag{12.24}$$

By shifting the summation indices j_c and j_c' and using Eqs. (12.22), (12.13) we find

$$\langle \hat{\mathcal{H}}_t(k)\rangle = t_\| \sum_{\Sigma, \Sigma'} \bar{\psi}_{\Sigma'}^{(n)} \psi_\Sigma^{(n)} (g_{\Sigma', \Sigma-1} e^{-ik} + g_{\Sigma', \Sigma+1} e^{ik}) \tag{12.25}$$

and define matrix elements $h_{\Sigma'', \Sigma}^t(k)$ in the non-ONB basis as

$$\sum_{\Sigma''} g_{\Sigma', \Sigma''} h_{\Sigma'', \Sigma}^t(k) = t_\| (g_{\Sigma', \Sigma-1} e^{-ik} + g_{\Sigma', \Sigma+1} e^{ik}). \tag{12.26}$$

The metric tensor $\hat{g}$ is involved when evaluating the scalar product $\langle \Psi^{(n)} | \hat{\mathcal{H}}_t | \Psi^{(n)}\rangle$ and thus appears in the expression for the variational energy. Later, we want to extract the matrix $h_{\Sigma', \Sigma}^t$ in order to derive an effective Hamiltonian. In particular, the kinetic part of the Hamiltonian yields all-to-all interactions in the non-ONB with exponentially decaying, complex hopping amplitudes, see Eq. (12.22).

Now, we introduce the basis transformation $\hat{\mathcal{G}}$ that maps from the non-ONB into a Gram-Schmidt orthonormalized basis $|j_c, \tilde{\Sigma}\rangle$ with

$$|j_c, \Sigma\rangle = \sum_{\tilde{\Sigma}} \mathcal{G}_{\tilde{\Sigma}, \Sigma} |j_c, \tilde{\Sigma}\rangle \tag{12.27}$$

$$|j_c, \Sigma = 0\rangle = |j_c, \tilde{\Sigma} = 0\rangle. \tag{12.28}$$

Since the variational kinetic energy $\langle \hat{\mathcal{H}}_t(k)\rangle$ must be invariant under basis transformations, we can deduce an effective hopping Hamiltonian $\hat{\mathcal{H}}_t^{GSP} = \hat{\mathcal{G}} \hat{h}^t \hat{\mathcal{G}}^{-1}$ in the Gram-Schmidt ONB which takes the particular form

$$(\hat{\mathcal{H}}_t^{GSP})_{\tilde{\Sigma}', \tilde{\Sigma}} = t_\| \sum_{\Sigma, \Sigma', \Sigma''} \mathcal{G}_{\tilde{\Sigma}', \Sigma''} (g^{-1})_{\Sigma'', \Sigma'} (g_{\Sigma', \Sigma-1} e^{-ik} + g_{\Sigma', \Sigma+1} e^{ik}) (\mathcal{G}^{-1})_{\Sigma, \tilde{\Sigma}} \tag{12.29}$$

The advantage of having expressions for the matrix elements in an ONB is that standard exact diagonalization techniques and algorithms can be applied; the resulting spectrum can be directly compared to the DMRG calculations shown below.

Similar as for the kinetic term, we can derive the magnetic interactions of the Gram-
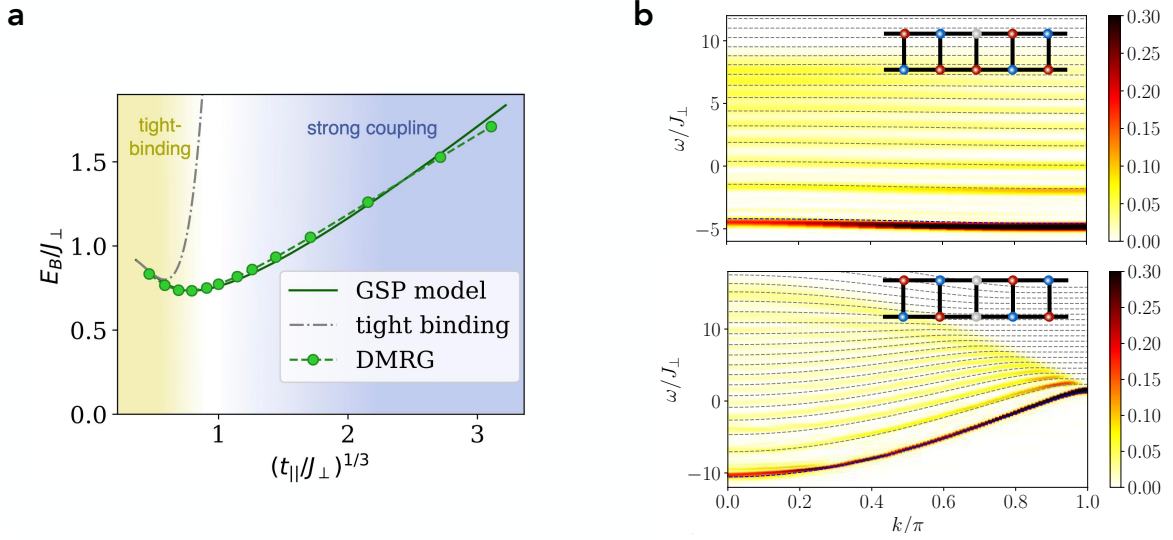
a

b

Figure 12.3: **String-based pairing in 1D mixed-D bilayer model. a** We compare the binding energy E_B obtained from DMRG simulations and the effective parton GSP model. We find excellent agreement throughout the entire parameter regime. The scaling behavior $\propto (t_\parallel / J_\perp)^{1/3}$ is characteristic of the string-based pairing mechanism [317]. In the limit $t_\parallel \ll J_\perp$ a simple tight-binding description is in agreement with our model. We highlight the remarkably large binding energy increasing with $t_\parallel / J_\perp$. **b** To furher corroborate the string picture, we calculate one- and two-hole spectral functions in time-dependent DMRG simulations and compare it to the eigenenergies from the GSP model. The discreet excitation spectrum is typical for meson-like parton bound states [21, 32, 320]. The DMRG simulations were performed by Annabelle Bohrdt.

Schmidt parton model, i.e. $\hat{\mathcal{H}}_{J_\perp}^{\mathrm{GSP}}$ and $\hat{\mathcal{H}}_{J_\parallel}^{\mathrm{GSP}}$. Here, it is convenient to re-write the nearest neighbour spin-spin interaction by $\hat{\vec{S}}_{i,\mu} \cdot \hat{\vec{S}}_{j,\mu'} = 1/2 \hat{P}_{(i,\mu),(j,\mu')} - 1/4$, where $\hat{P}_{(i,\mu),(j,\mu')}$ permutes the spins on sites (i,μ) and (j,μ'). Applying the spin-spin interaction on the variational wavefunction Eq. (12.23), i.e., $|\varphi^{(n)}\rangle = \hat{\mathcal{H}}_J |\Psi^{(n)}\rangle$, maps onto states that are not included in the subspace spanned by $\{|j_{\mathrm{c}}, \Sigma\rangle\}_{j_{\mathrm{j}} \in \mathbb{Z}, \Sigma \in \mathbb{Z}}$. Hence, the evaluation of the variational energy requires to calculate overlaps that arise from the projection $\langle \Psi^{(n)} | \varphi^{(n)} \rangle$ back onto the subspace of interest.

Carefully calculating the variational energies by taking the appropriate overlaps into account yields the following matrix elements in the non-ONB basis:

$$h_{\Sigma',\Sigma}^{J_\perp} = -J_\perp \left(L - 1 - \frac{|\Sigma|}{2} \right) + \frac{J_\perp}{2} \sum_{0 < \zeta \leq |\Sigma|} f_{\Sigma',\Sigma}^{\zeta}$$

$$f_{\Sigma',\Sigma}^{\zeta} = \begin{cases} \frac{1}{2}, & \text{for } (|\Sigma'| \geq \zeta) \wedge (\mathrm{sgn}[\Sigma'] = \mathrm{sgn}[\Sigma]) \\ -1, & \text{else} \end{cases}$$

(12.30)

and

$$
\begin{aligned}
h^{J_\parallel}_{\Sigma',\Sigma} = {} & \frac{J_\parallel}{2t_\parallel} h^t_{\Sigma',\Sigma}(k=0) - J_\parallel(L-3+\delta_{\Sigma,0}) \\
& + J_\parallel \sum_{0<\zeta<\ell_\Sigma-1} F^\zeta_{\Sigma',\Sigma} \\
& + J_\parallel \sum_{\substack{\chi\notin\{0,..,\Sigma+1\}\\ \text{if }\Sigma>0}} F^\chi_{\Sigma',\Sigma} + J_\parallel \sum_{\substack{\chi\notin\{0,..,\Sigma-1\}\\ \text{if }\Sigma<0}} F^\chi_{\Sigma',\Sigma}
\end{aligned}
\tag{12.31}
$$

$$
F^\zeta_{\Sigma',\Sigma} = \begin{cases} \frac{1}{2}, & \text{for } (|\Sigma'|\geq\zeta)\wedge(\mathrm{sgn}[\Sigma']=\mathrm{sgn}[\Sigma]) \\ 2, & \text{else.} \end{cases}
$$

$$
F^\chi_{\Sigma',\Sigma} = \begin{cases} 2, & \text{for } (|\Sigma'|>\zeta)\wedge(\mathrm{sgn}[\Sigma']=\mathrm{sgn}[\Sigma]) \\ \frac{1}{2}, & \text{else.} \end{cases}
$$

Note that after transforming into the ONB basis, the operators acquire a hermitian form. Moreover, the complete effective ONB Hamiltonian

$$
\hat{\mathcal{H}}^{\mathrm{GSP}} = \hat{\mathcal{G}}(h^t + h^{J_\perp} + h^{J_\parallel})\hat{\mathcal{G}}^{-1}
\tag{12.32}
$$

can be exactly diagonalized, where the string basis Hilbertspace is truncated at some maximum string length $\ell_\Sigma^{\mathrm{max}}$. Since in the $d=1$ ladder the Hilbertspace dimension only grows linearly with system size, we can essentially fully exactly solve the GSP model.

Next, we compare the exact diagonalization results of the GSP model to numerical DMRG calculations [P2]. In Ref. [P2], we performed DMRG calculations of the mixed-dimensional t-J model with weak $J_\parallel/J_\perp = 0.01$ on a 40×2 ladder. Particularly, (i) the ground-state energy of the one- and two-hole states were calculated as well as (ii) the one- and two-hole spectral functions are extracted from time-dependent DMRG and give access to momentum resolved spectra, see Ref. [P2] for more details on the numerical simulations. To meaningfully compare the ED results with the spectral function obtained by DMRG calculations, we need to subtract the zero-hole energy E_{0h} given by

$$
E_{0h} = -J_\perp L - \frac{J_\parallel}{2}(L-1).
\tag{12.33}
$$

In Figure 12.3a, we plot the binding energy of the 1D mixed-dimensional t-J model showing the remarkably large binding energies on the scale of the magnetic exchange $J_\perp$. Characteristic for string-based parton bound states is the universal scaling relation of the bound state energies $E\propto(t_\parallel/J_\perp)^{1/3}$ [21, 317] leading to an increasing binding energy in the strong-coupling limit. The GSP model gives is in excellent agreement with the DMRG simulations across the entire parameter regime. At weak-coupling, $t_\parallel/J_\perp\ll1$, we can further derive a simple tight-binding description of the parton bound states.

Another confirmation of the string-based pairing mechanism are the discreet excitation peaks, interpreted as ro-vibrational string excitations, see Chapter 8.3. In Figure 12.3b, we consider the momentum-resolved spectral function. The DMRG calculations indeed reveal

an excitation spectrum familiar from string-based parton bound states. The comparison to the GSP model, which is a manifestly string-based effective description, shows remarkable agreement for all momenta and energies. Note that in Figure 12.3b, we have plotted every second energy eigenstate of Hamiltonian $\hat{\mathcal{H}}^{\text{GSP}}(k)$, see Eq. (12.32), because the ARPES spectrum calculated in DMRG only couples to the even parity string states.

The momentum-resolved spectrum allows us to extract the dispersion relation of the spinon-chargon (top) and chargon-chargon (bottom) bound state in Figure 12.3b. As derived from the ONB parton model, the effective tunneling of the parton bound state is enhanced for the chargon-chargon case, see Eq. (12.18). This manifests in a light chargon-chargon pair and a heavy spinon-chargon pair responsible for the strong binding energy of two chargons.

Spinon-chargon bound state in 2D

In $d = 2$ the number of string basis states $|j_{\text{c}}, \mu, \sigma, \Sigma\rangle_{\text{sc}}$ and $|j_\mu, \Sigma\rangle_{\text{cc}}$, respectively, grows exponentially with the length of the string ℓ_Σ and thus becomes intractable to be solved using exact diagonalization. In the scope of this paper, we are only interested in the binding energy and hence in the ground-state energy of the spinon-chargon and chargon-chargon case, which are at the rotationally-invariant momenta $k = (0,0), (\pi, \pi)$. Hence, working in the co-moving frame of the chargon, we can make an ansatz in the string length basis $|\ell\rangle$ of the form

$$|\ell\rangle = \mathcal{N}_\ell^{-1/2} \sum_{\Sigma : \ell_\Sigma = \ell} |\Sigma\rangle, \tag{12.34}$$

which assumes a symmetric superposition of all strings with equal given length ℓ. The ansatz cannot capture any rotational excitation but assumes a state with no angular momentum, i.e. s-wave. Here, $\mathcal{N}$ is a normalization factor and counts the number of string state per given length ℓ.

Ignoring loop effect, the chargon-chargon string basis form an ONB. Hence, we only need consider non-linear string effects in the following, but otherwise the chargon-chargon energy is straight forward to evaluate in the ONB string basis.

The more involved problem is the spinon-chargon case, for which we want to find the ground-state energy for $|t_\parallel|, |J_\perp| > 0$ and $J_\parallel = 0$. We want to work in the string length basis $|\ell\rangle_{\text{sc}}$, see Eq. (12.34), however different string states are now not mutually orthogonal but

$$_{\text{sc}}\langle \ell' | \ell \rangle_{\text{sc}} = \mathcal{N}_{\ell'}^{-1/2} \mathcal{N}_\ell^{-1/2} \sum_{\Sigma' : \ell_{\Sigma'} = \ell'} \sum_{\Sigma : \ell_\Sigma = \ell} {}_{\text{sc}}\langle j_{\text{c}}, \Sigma' | j_{\text{c}}, \Sigma \rangle_{\text{sc}} = g_{\ell', \ell}^{d=2}. \tag{12.35}$$

Here, we have chosen to work in the sector $|j_{\text{c}}, \Sigma\rangle_{\text{sc}} = |j_{\text{c}}, \mu = +1, \sigma = \uparrow, \Sigma\rangle_{\text{sc}}$. Further we have calculated the metric tensor, for which we find rather hideous matrix elements that can be found in the Supplementary Information of Ref. [P2].

Note that the states $|\ell\rangle_{\text{sc}}$ are not normalized. The variational ansatz for the spinon-

chargon wavefunction has the form,

$$|\Psi_{\text{sc}}(k)\rangle = L^{-1} \sum_{j_c} e^{ik\cdot j_c} \sum_{\ell=0}^{\infty} \psi_\ell \sum_{\Sigma:\ell_\Sigma=\ell} |j_c, \Sigma\rangle_{\text{sc}}, \tag{12.36}$$

where we sum over the position of the chargon j_c. Again, we define $\phi_\ell = \mathcal{N}_\ell^{1/2}\psi_\ell$ and write the wavefunction in the string length basis:

$$|\Psi_{\text{sc}}(k)\rangle = L^{-1} \sum_{j_c} e^{ik\cdot j_c} \sum_{\ell=0}^{\infty} \phi_\ell |\ell\rangle_{\text{sc}}. \tag{12.37}$$

Since we are working in a non-ONB, the normalization condition requires $\sum_{\ell,\ell'} \phi_{\ell'}^* g_{\ell',\ell}^{d=2} \phi_\ell = 1$.

To derive the Gram-Schmidt parton model in $d=2$, we define a new set of orthonormal basis states $|\tilde{\ell}\rangle_{\text{sc}}$ with ${}_{\text{sc}}\langle\tilde{\ell}'|\tilde{\ell}\rangle_{\text{sc}} = \delta_{\tilde{\ell}',\tilde{\ell}}$ by

$$|\ell\rangle_{\text{sc}} = \sum_{\tilde{\ell}} \mathcal{G}_{\tilde{\ell},\ell}^{d=2} |\tilde{\ell}\rangle_{\text{sc}} \tag{12.38}$$

$$|\ell=0\rangle_{\text{sc}} = |\tilde{\ell}=0\rangle_{\text{sc}}, \tag{12.39}$$

see also Eq. (12.28) for $d=1$.

The expression for the variational energy of the hopping Hamiltonian $\langle\Psi_{\text{sc}}(k)|\hat{\mathcal{H}}_t|\Psi_{\text{sc}}(k)\rangle$ implicitly gives us the operator in matrix form $h_{\ell',\ell}^t$ in the string length basis $|\ell\rangle_{\text{sc}}$. The GSP hopping Hamiltonian $\hat{\mathcal{H}}_t^{\text{GSP}}$ for $d=2$ can then be derived by a basis transformation $\hat{\mathcal{H}}_t^{\text{GSP}} = \hat{\mathcal{G}}^{d=2}\hat{h}^t(\hat{\mathcal{G}}^{d=2})^{-1}$ analogously to $d=1$.

For the hopping Hamiltonian at $k=(0,0),(\pi,\pi)$, we find

$$\sum_{\ell''} g_{\ell',\ell''} h_{\ell'',\ell}^t(k) = t_\parallel e^{ik} \left(\tau_{\ell-1} g_{\ell',\ell-1} + \tau_\ell g_{\ell',\ell+1}\right) \tag{12.40}$$

with

$$\tau_\ell = \begin{cases} \sqrt{z}, & \text{for } \ell=0 \\ \sqrt{z-1}, & \text{for } \ell \geq 1 \end{cases} \tag{12.41}$$

The enhancement in the factor τ_0 arises from retracing $|\Sigma\rangle_{\text{sc}}$ on the Bethe lattice, where the origin, $|\Sigma=0\rangle_{\text{sc}}$, connects to z longer string states instead of $z-1$ for all other states. In order to exactly diagonalize the GSP Hamiltonian, we need to introduce a cut-off in the string length basis at ℓ_{max}. The cut-off in the non-ONB yields non-hermitian contributions for the boundary states after Gram-Schmidt orthogonalization, i.e. $(\hat{\mathcal{H}}_t^{\text{GSP}})_{\ell,\ell_{\text{max}}} \neq (\hat{\mathcal{H}}_t^{\text{GSP}})_{\ell_{\text{max}},\ell}$. Therefore, we project the GSP model onto the subspace with $\{|\tilde{\ell}\rangle_{\text{sc}}\}_{\tilde{\ell}=0,...,\tilde{\ell}_{\text{max}}-1}$ to receive a well-defined hermitian Hamiltonian.

The derivation of the magnetic interaction $J_\perp$ involves the evaluation of overlaps that arise when first applying $\hat{\mathcal{H}}_{J_\perp}$ on the variational wavefunction and then projecting back onto the subspace spanned by $\{|\ell\rangle_{\text{sc}}\}_{\ell\in\mathbb{N}_0}$. The matrix form in the string length basis is then given by
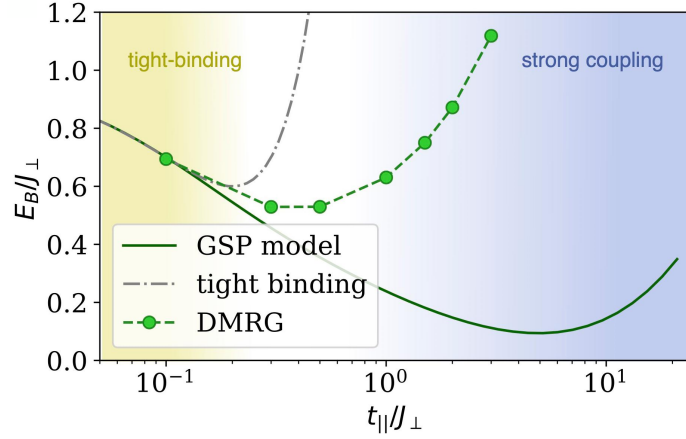
Figure 12.4: **String-based pairing in 2D mixed-D bilayer model.** We find large binding energies on the scale of the magnetic interaction $J_\perp$ for the 2D system. In the tight-binding limit, all three methods agree well. At larger $t_\parallel / J_\perp$, the GSP model deviates from the DMRG calculations, which could be explained by the neglected loop effects in the chargon-chargon parton model. The DMRG simulations were performed by Annabelle Bohrdt.

$$\sum_{\ell''} g_{\ell',\ell''} h^{J_\perp}_{\ell'',\ell} = \mathcal{N}_\ell \mathcal{N}_{\ell'}^{-1/2} \left[-\mathcal{N}_{\ell'} \ell \frac{z-1}{z} 2^{-|\ell+\ell'|} + \sum_{1 \leq \chi \leq \ell} \left(f^\chi_{\ell',\ell} + F^\chi_{\ell',\ell} \right) \right] \tag{12.42}$$

$$\text{with } f^\chi_{\ell',\ell} = \begin{cases} \left[1 - 3\Theta(\sigma - \ell')\right] 2^{-|\ell-\ell'|-1}, & \text{for } \ell \geq \ell' \\[2mm] (z-1)^{\ell'-\ell} 2^{-|\ell-\ell'|-1}, & \text{else} \end{cases} \tag{12.43}$$

$$F^\chi_{\ell',\ell} = \begin{cases} \sum_{\lambda \geq 1}^{\ell'-1} (z-2)(z-1)^{\lambda-1} \left[1 - 3\Theta(\sigma + \lambda - \ell')\right] 2^{-|\ell-\ell'|+2\lambda-1}, & \text{for } \ell \geq \ell' \\[4mm] \sum_{\lambda \geq 1}^{\ell-1} (z-2)(z-1)^{\lambda-1+\ell'-\ell} \left[1 - 3\Theta(\sigma + \lambda - \ell)\right] 2^{-|\ell-\ell'|-2\lambda-1}, & \text{else.} \end{cases}$$
$$\tag{12.44}$$

Here, $\Theta(x)$ is the Heaviside step function and we define $\Theta(0) = 0$.

The full GSP model in $d = 2$ and for $k = (0,0), (\pi, \pi)$ can be calculated by transforming into the Gram-Schmidt basis

$$\hat{\mathcal{H}}^{\text{GSP}}(k) = \hat{\mathcal{G}}^{d=2}[h^t(k) + h^{J_\perp}](\hat{\mathcal{G}}^{d=2})^{-1} \tag{12.45}$$

and for which we can calculate the ground-state energy by ED after projecting out the boundary at $\ell_{\max}$ as discussed above. In the following, we will call $\ell_{\max}$ the maximum string length after removing the boundary state. Moreover, we subtract the zero-hole en-

ergy, which for the $d = 2$ mixed-dimensional bilayer model is given by

$$E_{0h} = -J_\perp \sum_{\ell=0}^{\ell_{max}} z(z-1)^{\ell-1}. \tag{12.46}$$

We find, as expected for the spinon-chargon case, the minimum to be at $k = (\pi, \pi)$ due to the positive sign of the hopping amplitude $+t_\parallel$.

In Figure 12.4, we compare the binding energy obtained from the GSP model and from numerical DMRG calculations. In 2D, the numerical simulations of the bilayer t-J model become increasingly challenging. Here, we present results from a $12 \times 4 \times 2$ system (length×width×layer). We find good agreement of the binding energy for small $t_\parallel/J_\perp$; however at larger $t_\parallel/J_\perp$ the DMRG simulation predicts tighter binding than the GSP model. This discrepancies could have various reasons: One the one side, we assumed the chargon-chargon string basis to be orthogonal, which is only valid when we neglect loop effect. On the other hand, the effective parton model is a full 2D description, while the DMRG simulation are obtained on 4-leg cylinders, and thus quantities such as the binding energy, where two large numbers are subtracted, may be affected by finite size effects.

12.2   Experimental realization

The large binding energies we find are encouraging for ultracold atom experiments [P1]. To realize the mixed-dimensional Hamiltonian (12.1), we propose to implement a plain-vanilla bilayer Hubbard model with tunnelings $t_\parallel, t_\perp$ in the presence of a strong chemical potential offset $\Delta \gg t_\perp$ between the two layers. This potential offset leads to a localization of the atoms within the layer on experimental timescales. Nevertheless, inter-layer superexchange mechanism is possible leading to enhanced spin-exchange interactions with amplitude

$$J_\perp = \frac{2t_\perp^2}{U + \Delta} + \frac{2t_\perp^2}{U - \Delta}, \tag{12.47}$$

where U is the on-site Hubbard interaction. In Ref. [424], our proposed model has been implemented in ultracold lithium atoms in a 1D mixed-dimensional ladder. In a ladder of size 7×2, they report the observation of hole-hole correlations indicating binding of holes at temperatures of about $k_B T = 0.77 J_\perp$.

As mentioned in the beginning of this Chapter, it has further been proposed that the recently discovered high-Tc superconductor LNO may be described by a mixed-dimensional bilayer t-J model [411, 427–429], as in Eq. (12.1). Our model, therefore, provides a microscopic magnetically mediated pairing mechanism for pressurized nickelates. In Ref. [P1], we have proposed a BEC-BCS crossover scenario for the mixed-dimensional model, driven by the weakly and tightly bound chargon-chargon pairs, which have further numerically corroborated in Ref. [P6]. Additionally, we have analyzed a mean-field phase diagram of the mixed-dimensional bilayer in 2D, which predicts inter-layer s-wave superconductivity in the parameter regime relevant for the nickelates, as discussed in the following section.
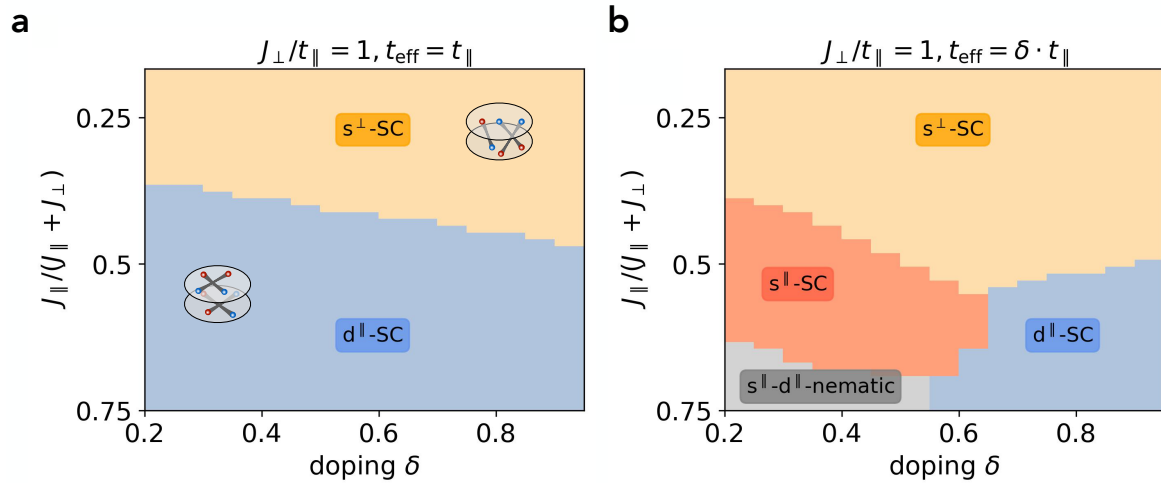
a

b

Figure 12.5: **BCS mean-field phase diagram.** We show the mean-field BCS phase diagrams of the mixed-dimensional t-J bilayer model at weak coupling, $t_\parallel \gg J_\perp, J_\parallel$ and for high dopings, with intra-layer (inter-layer) interactions $J_\parallel$ ($J_\perp$) and intra-layer (inter-layer) hoppings $t_\parallel$ ($t_\perp = 0$) at $T = 0$. In **a** we completely neglect any effect of Gutzwiller projections on the hopping term. In **b** we approximate the effect of the Gutzwiller projector by working with an effective hopping $t_\parallel^{\text{eff}} = \delta \cdot t_\parallel$.

12.3 BCS mean-field analysis

We consider the situation where $t_\parallel$ dominates, and both $J_\perp$ and $J_\parallel$ can be treated as weak perturbations in the two-dimensional mixed-dimensional bilayer. In this section we perform a BCS mean-field analysis of this situation, which, in the limit of $J_\perp \to 0$, includes the BCS analysis of the decoupled single-plane $t - J$ model where $d_{x^2-y^2}$ pairing is found [254]. Before starting, we discuss under which conditions the weak-coupling BCS ansatz is valid.

Firstly, for $t_\parallel$ to dominate we require sizable doping values $\delta > 0$, since $t_\parallel$ is suppressed when the system forms a Mott insulator around $\delta = 0$. Secondly, in two dimensions an arbitrarily weak attractive interaction leads to the formation of a two-body bound state. Since $J_\perp$ still favors the formation of inter-layer singlets, it mediates an effective attraction between fermions from the top and bottom layers. Hence, for $1 - \delta \ll 1$ the system is always in a BEC regime, namely when the typical inter-particle distance $(1 - \delta)^{-1/2}$ is larger than the extend of the two-body bound state.

The following fully self-consistent BCS mean-field analysis is thus constrained to the regime $\delta \lesssim 1$. In practise we only consider the high-doping regime beyond $\delta > 20\%$; we note that superconductivity in the LNO nickelate compounds is observed around $\delta = 50\%$ [430]. We take into account all interaction terms from Hamiltonian (12.1) and also include the 3-site term arising to lowest order in $t_\parallel^2/U \propto J_\parallel$ in the effective Hamiltonian obtained from the Hubbard model [112], see Section 8.2. The latter is shown in the middle line of Table 12.1, and is often neglected in the t-J model.

By applying an unrestricted Hartree-Fock approximation, we determine the different magnetic interaction channels with competing pairing symmetries, which are summarized in Table 12.1 (see also Appendix B). The antiferromagnetic $J_\perp$ interaction prefers singlet

$\hat{\mathcal{H}}_{\text{int}}$	pairing symmetry	spin	layer
$J_\parallel \sum\limits_{\langle i,j\rangle,\mu} \left(\hat{\vec{S}}_{\vec{i},\mu} \cdot \hat{\vec{S}}_{j,\mu} - \frac{1}{4} \sum\limits_{\alpha,\beta} \hat{n}_{\vec{i},\alpha,\mu} \hat{n}_{j,\beta,\mu} \right)$	$s^\parallel$-wave $/d^\parallel$-wave	singlet	symmetric
$-\dfrac{J_\parallel}{4} \sum\limits_{\substack{\langle i,j\rangle,\langle i,j'\rangle \\ j\neq j',\alpha,\mu}} \left(\hat{c}^\dagger_{j',\alpha,\mu} \hat{n}_{i,\bar{\alpha},\mu} \hat{c}_{j,\alpha,\mu} + \hat{c}^\dagger_{j',\alpha,\mu} \hat{c}^\dagger_{i,\bar{\alpha},\mu} \hat{c}_{i,\alpha,\mu} \hat{c}_{j,\bar{\alpha},\mu} \right)$	$p^\parallel$-wave	triplet	symmetric
$J_\perp \sum\limits_{j} \left(\hat{\vec{S}}_{j,1} \cdot \hat{\vec{S}}_{j,2} - \frac{1}{4} \sum\limits_{\alpha,\beta} \hat{n}_{j,\alpha,1} \hat{n}_{j,\beta,2} \right)$	$s^\perp$-wave	singlet	symmetric

Table 12.1: **Pairing channels in the BCS analysis.** Magnetic interactions within and between the layers have competing pairing symmetries order parameters defined in the Appendix B, which can be derived by taking all possible pairwise contractions of the fermionic operators. The combination of angular momentum, spin and layer exchange symmetry have to obey the Pauli principle, which is confirmed for all four interaction channels listed in the Table.

bonds between the layers manifested in isotropic point-like attractive interactions with $s^\perp$-wave order parameter. On the other hand, the intra-layer $J_\parallel$ interaction can lead to pairing in the anisotropic $s^\parallel_{x^2+y^2}$, $p^\parallel_{x\pm iy}$ and $d^\parallel_{x^2-y^2}$ channels. The corresponding order parameters are defined in Appendix B. By allowing the order parameters to be non-zero simultaneously, the mean-field approach can capture nematic or time-reversal symmetry broken phases within the layer, or co-existing phases between $s^\perp$ and $(s^\parallel, p^\parallel, d^\parallel)$-wave.

At low dopings, our mean-field theory formulated in terms of the bare fermions can be replaced by a slave-boson mean-field theory with bosonic chargons and fermionic spinons [31, 137]. In this case, a well-defined trial wavefunction can be obtained by applying a Gutzwiller projection to ensure that only one fermion can occupy each site. At high dopings, the Gutzwiller projection should not play a dominant role and we completely neglect it in the first version of our mean-field theory. In addition, we perform a second calculation with an effective, free fermion hopping term $t^{\text{eff}}_\parallel$ for comparison. We take into account the suppressed hopping of the fermionic spinons due to occupied sites and approximate $t^{\text{eff}}_\parallel = \delta \cdot t_\parallel$ [16], which interpolates between the exact limits for $\delta = 0$ and $\delta = 1$. The goal of this calculation is to understand on a qualitative, not a quantitative, level how the Gutzwiller projection may affect the results.

In our mean-field analysis, we consider $T = 0$ and find a phase transition from $s^\perp$ to $d^\parallel_{x^2-y^2}$ ordering for increasing interactions $J_\parallel/J_\perp$, see Figure 12.5. This reflects the different dominant magnetic ordering – into local singlets and a long-range ordered state, respectively – at half-filling. Interestingly, for the renormalized fermion hopping, $t^{\text{eff}}_\parallel = \delta \cdot t_\parallel$, the system favours $s^\parallel$-wave superconductivity in an intermediate regime at moderate dopings and comparable interactions $J_\parallel \approx J_\perp$, see Figure 12.5b. Additionally, for large enough intra-plane interactions $J_\parallel$, the systems shows nematic $(s^\parallel + d^\parallel)$-wave order for low dopings, whereas pure $d^\parallel$-wave order is obtained again for high dopings, again if the reduced hopping $t^{\text{eff}}_\parallel$ is used, see Figure 12.5b. Moreover, by solving the self-consistency equations while minimizing the ground-state energy, we find throughout that $p^\parallel$-wave order is not
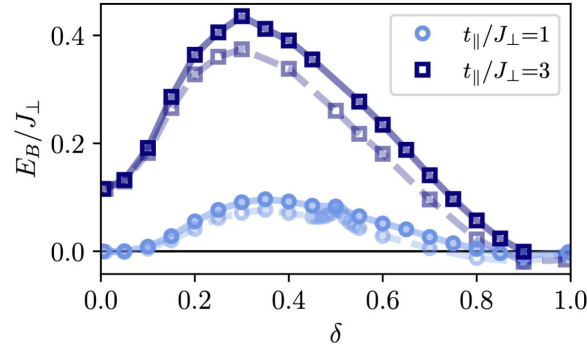
Figure 12.6: **Feshbach resonance in mixD ladder.** We show the binding energy of two holes in a mixed-dimensional ladder, see Eq. (12.1), in the presence of strong repulsion $V/J_\perp = 5$ and for finite doping of holes δ away from half filling. The results are obtained by Hannah Lange from DMRG calculations of Eq. (12.1) in ladders of length $L_x = 100$ (dashed lines) and $L_x = 200$ (solid lines), see Ref. [P10].

favored.

As in the case of half-filling, where tuning the ratio of couplings $J_\parallel/J_\perp$ can drive a phase transition, we expect interesting physics to arise in the high-doping limit. Since the system becomes $d^\parallel$-wave superconducting at values $J_\parallel/J_\perp \gtrsim 1$, the mixed-dimensional bilayer system is appealing to study cuprate physics from a new perspective and it could give insights and impulses into the pairing mechanisms of high-Tc superconductivity when approaching the superconducting dome by decreasing $J_\perp$.

12.4 Feshbach resonance in mixD ladders

The goal of this Section is to put Refs. [P10, P6] into perspective with the proposed Feshbach scenario in cuprates, see Chapter 9. There, we found that the internal structure of parton bound states gives rise to Feshbach resonance between fermionic (sc) mesons and a resonant, bi-polaronic (cc) meson in square lattice Hubbard-type models. This Section builds upon our derived string picture of (sc) and (cc) parton bound states in mixed-dimensional bilayer Hubbard models, and goes beyond by studying the finite doping regime. The presented results were predominantly obtained by Hannah Lange, including the numerical DMRG simulations.

As we have shown in Section 12.1, we can understand the origin of the spinon-chargon (sc) and chargon-chargon (cc) parton bound states by the confining strings of tilted singlets. We find large binding energies $E_B = 2E_{sc} - E_{cc} > 0$ on the order of the magnetic interaction $J_\perp$. Hence, in the limit of two holes the tightly-bound bosonic (cc) meson constitutes the ground state. This naturally brings us to the question whether we can also find pairing for the fermionic (sc) mesons.

To this end, we introduce a strong repulsive on-rung interaction V, see Figure 12.1, to energetically penalize the tightly-bound (cc) boson and restore the fermionic constituents in the ground state. Surprisingly large repulsion is needed to destroy the (cc) meson, but as expected it ceases to exist in the ground state at around $V/J_\perp \approx 3 - 5$ for typical values

of $t/J_\perp = 3$. In this case, the ground state can be described by the (sc) fermions [P10]. As we introduce more dopants into system, however, binding of two holes is restored and forms a pairing dome with remarkably high binding energies, see Figure 12.6.

We explain this recurrence of the binding energy via an emergent Feshbach resonance between two (sc)^2 fermions in the open scattering channel and (cc) bosons in the closed scattering channel [P10, 342]. Thus, the resonant (cc) state induces attractive interactions between the fermionic constituents in the ground state. Familiar from Feshbach resonances, the energy difference ΔE between the two channels controls the scattering length. In our case, we have the on-rung repulsion V as a direct tuning knob for ΔE. In addition, as the Fermi sea of (sc) mesons is filled up, they approach the resonance from below potentially explaining the dome-like feature as doping is increased.

This two-channel physics naturally leads to the scenario of a BEC-BCS crossover, that we discuss in Ref. [P6]. For strong repulsive interactions the character of the ground-state changes from extended (sc) fermions to more tightly-bound (cc) bosons as the system is doped. Therefore, our proposed mixed-dimensional bilayer model provides a platform to study ubiquitous phenomena known from strongly interacting Fermi gases in a lattice model with strong repulsive electron interactions. Notably, it has been proposed that the pressurized LNO nickelate compound [425] may be described by a mixed-dimensional bilayer model [411, 427–429]. Hence, our results find direct application in condensed matter physics and provide a magnetically mediated pairing mechanism for nickelates and cold atoms, as we lay out in Ref. [P10, P6]. Additionally, we have studied pair-pair correlations featuring quasi-long range order in the 1D ladder, consistent with the superconductivity in 2D bilayer nickelates. These results have been further corroborated in DMRG simulations of larger systems [431].

CONCLUSIONS & PERSPECTIVES

Conclusions & Perspectives

The parton picture can be a useful and natural description for phenomena in strongly correlated quantum matter, as we have argued in this thesis. This picture may become increasingly important as the focus of research shifts towards microscopic models enabled by the experimental progress in quantum simulation platforms, for which we have theoretically developed novel protocols. A central role in our description of parton phenomena is the emergent Feshbach resonance between parton bound states in high-Tc cuprate superconductors [P11, P7].

From a historical perspective, Fano-Feshbach resonances are familiar from particle and atomic physics [71, 72]. In the field of cold atom quantum simulators, Feshbach resonances have been *the* game changer because they allow us to induce strong point-like pair interactions between otherwise neutral objects. Recently, there has been a "re-discovery" of Feshbach resonances in solid state materials: (i) Experiments in transition metal dichalcogenide (TMD) report the observation of a resonance explained by the open- and closed-channel scattering between excitonic quasi particles in a semiconductor [336, 337]. This opens a path towards building solid state quantum simulators with tunable interactions [338, 432]. (ii) Feshbach resonances have been proposed to play a role for unconventional pairing in strongly correlated electron systems such as Moiré materials [338, 340, 379, 433] or bilayer nickelates [P10, P6, 342] [Chapter 12], and are considered as a way to induce topological superconductivity in semiconductors [339, 434]. Therefore, resonant interactions are gaining attention in the solid state community and are proposed as new ways to engineer quantum matter or to build effective models of strongly interacting systems.

Eventually, all these concerted efforts rely on recognizing open and closed scattering channels. Hence, they are intimately related to the task of identifying the universal constituents in strongly correlated electrons, which famously remains a controversy for the underdoped cuprates [240]. In this vein, in our Feshbach hypothesis of high-Tc in cuprates we have not "invented" Feshbach resonances, but rather we have identified potential two-channel physics in doped quantum antiferromagnets starting from a genuine microscopic strong-coupling description. From our finding a number of phenomena in cuprate superconductors are explained naturally such as the $d_{x^2-y^2}$-wave pairing symmetry or the origin of strong pairing interactions through a low-lying resonant bi-polaronic state [Chapter 9 and 10]. Our formalism provides a foundation to revisit previously suggested and debated scenarios, such as BEC-BCS crossover [269–271, 353, 364] or phase ordering of preformed pairs [267], from a microscopic perspective. The Feshbach mechanism provides a new building block for the theoretical modelling of underdoped cuprates and further extensions of our proposed pairing mechanism to more exotic normal states, such as fractionalized Fermi liquids (FL*) [262–264, 381], are possible and likely needed to construct a

theory consistent with the enigmatic Fermi arcs observed in ARPES experiments of cuprate compounds [244, 247].

The development of this new Feshbach perspective has been enabled by technological advancements: the research of strongly correlated systems experiences an increasing focus on microscopic models, driven by the experimental advances of quantum simulators and their theoretical modelling [P1]. For example, the quantum gas microscopy of doped antiferromagnetic Mott insulators has revealed signatures of the internal parton structure of charge carries at low doping [33, 387]. In the bigger picture, it was the physicist and philosopher Thomas S. Kuhn who noted in his seminal book on *The Structure of Scientific Revolutions* that *technology has often played a vital role in the emergence of new sciences* [435]. Quantum simulators certainly provide such a technological advancement for fundamental science and potentially beyond. To which extent the microscopic structure plays a role for collective phenomena yet has to be determined. Currently, we are just at the beginning of this scientific and technological revolution, which provides us with new tools to study strongly correlated quantum matter.

In this endeavor to explore microscopic correlations in systems with strong interactions, we have theoretically pushed the frontier of tweezer arrays [104]. From the experimental side, these platforms combine a toolkit of tunable geometries with dipolar interactions, generally speaking. From the theoretical side, we have used and extended this toolkit to propose protocols for the emulation of lattice gauge theories [P5, P9] [Chapter 3 and 5], and doped quantum magnets [P8] [Chapter 11], respectively.

Rydberg tweezer experiments have achieved truly remarkable advancements in the past decade. The platform kick-started in 2016 with the ability to generate deterministically filled tweezer arrays [121]. Today, experimentalists report arrays of a few thousand atoms [115, 116] and coherent control over many-body states constituted of hundreds of qubits [51, 89, 92, 94]. Most notably the platform has become a promising candidate to realize large-scale fault tolerant quantum computers [58].

As an analog quantum simulator, tweezer arrays of Rydberg atoms or cold polar molecules are ideally suited to explore the domain of two-dimensional XY or Ising quantum magnets [104]. In this thesis, we have extended this domain to *doped* quantum antiferromagnets with hard-core bosonic holes [P8]. The realization in tweezer arrays and the dipolar origin of the interactions [304] does not only allow us to study new geometries or parameter regimes beyond implementations in optical lattices [P1], but also to develop conceptually new probes, e.g., one can prepare a superposition of particle number sectors relevant to energy- and momentum-resolved spectroscopy [421]. Notably, the long-range dipolar interactions in our model enable us to realize next-nearest neighbor tunneling, which is believed to play a significant role in the understanding of high-Tc superconductivity in cuprates [284]. Hence, the proposed scheme and the presented preliminary experimental results provide a novel promising perspective to explore microscopic correlations in systems intimately related to strongly correlated electrons [Chapter 11].

Yet another route for next-generation quantum simulators is the study of lattice gauge theories, which are believed to be a genuinely useful application of quantum simulators [15, 49, 160]. Gauge theories with dynamical matter are a ubiquitous framework across various

disciplines of modern many-body physics, ranging from particle physics [40] to condensed matter physics [23] and from quantum information [29] to biophysics [45]. The parton formulation of doped quantum magnets reveals the intimate relation between lattice gauge theories and strongly correlated electrons [3]; hereby both Abelian [20] and non-Abelian [17, 18] gauge theories have been suggested to play a role for the low-energy physics of high-Tc superconductivity in cuprates. Thus, the direct implementation of lattice gauge theories in quantum simulators would enable to probe the phases of such effective theories, which remain mostly elusive in $(2+1)$D [24, 28, 44, 47].

In analogy to low-energy effective theories, we propose experimentally feasible schemes, where the gauge structure emerges from energetic constraints. Based on antiferromagnetic Ising and Heisenberg interactions in tunable geometries, we can show that Abelian $\mathbb{Z}_2$ and non-Abelian $SU(N)/U(N)$ gauge constraints can be stabilized in a quantum simulator [P4, P5, P9, P3]. The schemes are specifically tailored for Rydberg atoms or cold molecules in tweezer array, but likewise we envisage applications in $SU(N)$ Hubbard models [436] or future hybrid digital-analog experiments with fermionic tunneling gates [61, 62] [Chapter 3, 4 and 5].

In conclusion, our guiding principle of *form follows function* introduced in the beginning of this thesis, see Introduction, has led us to propose minimal schemes for the large-scale implementation of lattice gauge theories in quantum simulators. Simultaneously, the quantum simulation perspective has inspired us to revisit the form of microscopic correlations in doped quantum magnets, providing a foundation for developing effective parton models and for formulating novel pairing mechanisms for high-Tc superconductivity in nickelate and cuprate compounds.

A

Implementation of *t-J-V-W* model in 2D Rydberg tweezer arrays

In Chapter 11, Section 11.7.4 we have proposed to implement the antiferromagnetic, bosonic *t-J-V-W* model in 2D tweezer arrays of Rydberg atoms. For ^{87}Rb, the particular set of Rydberg states

$$|60S_{1/2}, m_j = 1/2\rangle = |\downarrow\rangle \qquad |60P_J, m_j\rangle = |h\rangle \qquad |61S_{1/2}, m_j = 1/2\rangle = |\uparrow\rangle. \qquad (A.1)$$

yields suitable interaction strengths and AFM in-plane magnetic interactions with $|J_\perp| > |J_z|$. Here, we discuss the dependencies of the interactions on the sublevel J, m_j of the *P*-state. In Figure 11.13, we have already presented the interaction strength for $J = 3/2, m_j = -1/2$.

For simplicity, we consider two-dimensional implementations with spatially isotropic interactions. Thus, we choose the magnetic field to point perpendicular to the plane of atoms, such that the angle $\theta = 90°$. Since the tunnelings and spin interactions scale as r^{-3} and r^{-6} with the distance between atoms, respectively, we are left with the geometry as a tuning knob for t/J. Note that there is a window of feasible distances, for which (i) the van-der-Waals interactions are not too strong such that high-fidelity state preparation is possible and (ii) not too weak for the realistic experimental coherence times of about $t = 5\,\mu$s.

From calculations of the pair interactions [84], performed by Sebastian Geier and the Browaeys lab, we find that the $J = 3/2$ manifold yields an almost perfect SU(2)-invariant model with $t_\downarrow/t_\uparrow \approx 1.06$. For the $J = 1/2$ manifold, there is a slight anisotropy with $t_\downarrow/t_\uparrow \approx 1.13$. In addition, the sign of tunneling t_α for fixed angles $\theta = 90°$ is adjustable by the relative Δm_j between the *S*- and *P*-states. For $\Delta m_j = 0$ ($\Delta m_j = \pm 1$), the sign of the dipolar interaction is positive $C_3 > 0$ (negative $C_3 < 0$) leading to negative tunnelings $t_\alpha < 0$ (positive tunnelings $t_\alpha < 0$) at $\theta = 90°$ and using our convention from the main text, see Table 11.6. We emphasize that the sign of tunnelings plays a significant role due to its long-
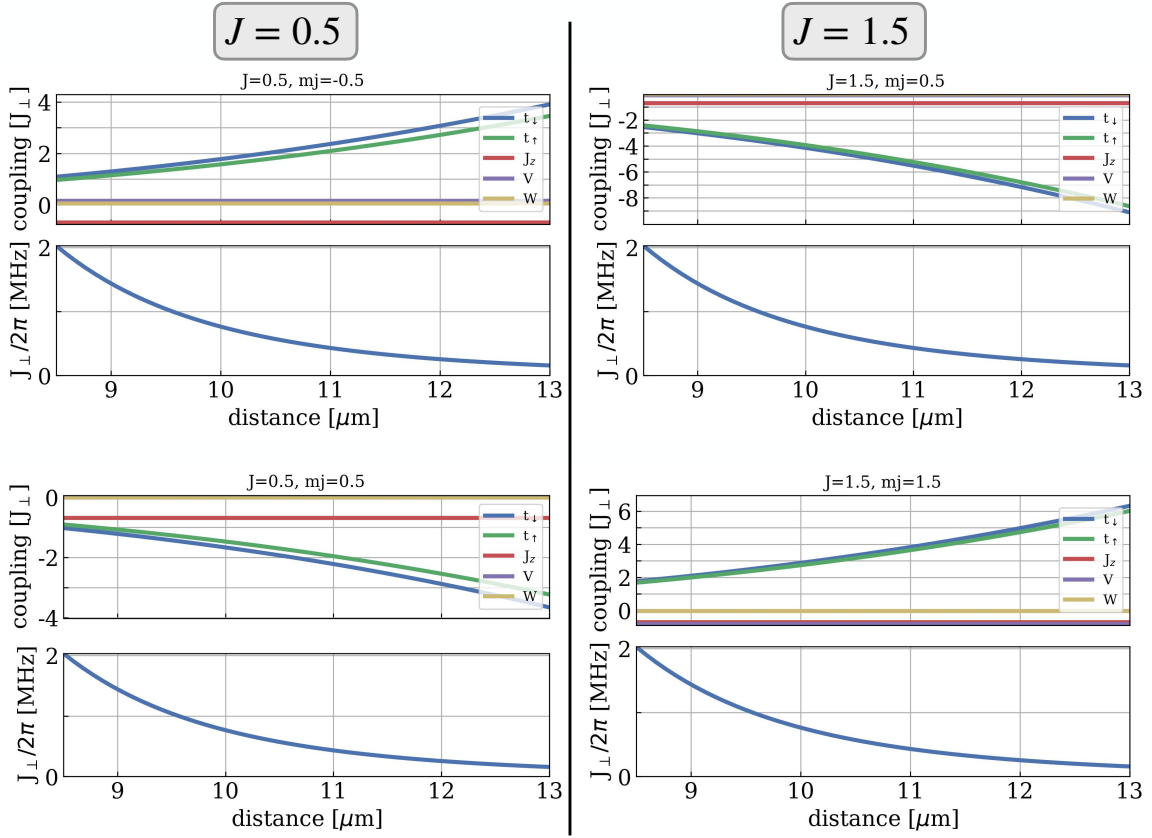
Figure A.1: **Tunability of interactions** for $|60P_{1/2}, m_j = -1/2\rangle$ (top left), $|60P_{1/2}, m_j = 1/2\rangle$ (bottom left), $|60P_{3/2}, m_j = 1/2\rangle$ (top right), and $|60P_{3/2}, m_j = 3/2\rangle$ (bottom right). The calculations of the C_3 and C_6 coefficients were performed by Sebastian Geier and the Browaeys lab.

range properties, see Section 11.7.2.

In this Appendix, we plot the couplings $J_\perp, J_z, V, W$ and tunnelings $t_\downarrow, t_\uparrow$ for the angle $\theta = 90°$ at realistic distances for tweezer arrays $r = 8.5 - 13\,\mu$m in Figure A.1. To implement a typical set of parameters for cuprates, we suggest to use the state $|60P_{3/2}, m_j = 3/2\rangle$ with

$$t = 2.9 J_\perp \tag{A.2}$$

$$J_z = -0.68 J_\perp \tag{A.3}$$

$$V = -0.8 J_\perp \tag{A.4}$$

$$W = -0.03 J_\perp \tag{A.5}$$

at distance $r = 10\,\mu$m.

B

BCS mean-field analysis of mixed-dimensional bilayer *t-J* model

Here we derive a BCS mean-field Hamiltonian from the mixed-dimensional bilayer $t - J$ model in Eq. (12.1) and solve it self-consistently by using a Bogoliubov transformation. There are three magnetic interaction terms to consider: inter-layer $J_\perp$ AFM interactions, intra-layer $J_\parallel$ AFM interactions, and the intra-layer $J_\parallel$ 3-site term, see Table 12.1. In the following, we will use a Schwinger fermion representation of the spins, $\hat{\vec{S}}_{j,\mu} = \frac{1}{2}\hat{c}^\dagger_{j,\alpha,\mu}\vec{\sigma}_{\alpha\beta}\hat{c}_{j,\beta,\mu}$, where $\vec{\sigma} = (\sigma^x, \sigma^y, \sigma^z)$ are the Pauli matrices, $\alpha, \beta = \uparrow, \downarrow$ is the spin and $\mu = 1, 2$ is the layer index.

The inter-layer coupling can be exactly written in terms of singlet pair operators on lattice site $\vec{j}$:

$$\hat{\mathcal{H}}_{J_\perp} = J_\perp \sum_{\vec{j}} \left(\hat{\vec{S}}_{\vec{j},1} \cdot \hat{\vec{S}}_{\vec{j},2} - \frac{1}{4} \sum_{\alpha,\beta} \hat{n}_{\vec{j},\alpha,1} \hat{n}_{\vec{j},\beta,2} \right) = -J_\perp \sum_{\vec{j}} \hat{s}^\dagger_{\vec{j}} \hat{s}_{\vec{j}} = -J_\perp N \sum_{\vec{k}} \hat{s}^\dagger_{\vec{k}} \hat{s}_{\vec{k}} \qquad \text{(B.1)}$$

with

$$\hat{s}^\dagger_{\vec{j}} = \frac{1}{\sqrt{2}} \left(\hat{c}^\dagger_{\vec{j},\uparrow,1} \hat{c}^\dagger_{\vec{j},\downarrow,2} - \hat{c}^\dagger_{\vec{j},\downarrow,1} \hat{c}^\dagger_{\vec{j},\uparrow,2} \right) \qquad \text{(B.2)}$$

$$\hat{s}^\dagger_{\vec{k}} = \frac{1}{N\sqrt{2}} \sum_{\vec{q}} \left(\hat{c}^\dagger_{\vec{q}+\vec{k},\uparrow,1} \hat{c}^\dagger_{-\vec{q},\downarrow,2} - \hat{c}^\dagger_{\vec{q}+\vec{k},\downarrow,1} \hat{c}^\dagger_{-\vec{q},\uparrow,2} \right), \qquad \text{(B.3)}$$

where $N = L_x \times L_y$ denotes the system size in 2D with lattice size L_x (L_y) in the x- (y-)direction, respectively. Further, the fermion creation operators written in momentum space are $\hat{c}^\dagger_{\vec{k},\alpha,\mu} = N^{-1/2} \sum_{\vec{j}} e^{-i\vec{j}\cdot\vec{k}} \hat{c}_{\vec{j},\alpha,\mu}$ with $\vec{k} = (k_x, k_y)$ and $k_j = -\pi/L_j, ..., \pi/L_j$. By defining the

$s^\perp$-wave mean-field order parameter

$$\Delta^\perp = \frac{J_\perp}{\sqrt{2}} \langle \hat{s}_{\vec{k}=\vec{0}} \rangle = \frac{J_\perp}{2N} \sum_{\vec{q}} \langle \hat{c}_{\vec{q},\downarrow,2} \hat{c}_{-\vec{q},\uparrow,1} - \hat{c}_{\vec{q},\uparrow,2} \hat{c}_{-\vec{q},\downarrow,1} \rangle, \tag{B.4}$$

we can derive the mean-field Hamiltonian

$$\hat{\mathcal{H}}_{J_\perp}^{\text{MF}} = -\sum_{\vec{k}} \left[\Delta^\perp \left(\hat{c}_{\vec{k},\uparrow,1}^\dagger \hat{c}_{-\vec{k},\downarrow,2}^\dagger - \hat{c}_{\vec{k},\downarrow,1}^\dagger \hat{c}_{-\vec{k},\uparrow,2}^\dagger \right) + \text{h.c.} \right] + \frac{2}{J_\perp} |\Delta^\perp|^2. \tag{B.5}$$

The order parameter has $s^\perp$-wave symmetry, is anti-symmetric under the exchange of spins (spin singlets) and must be – due to Pauli's principle – symmetric under layer exchange.

Next, we consider the intra-layer $J_\parallel$ AFM couplings, which can be written in momentum space as

$$\hat{\mathcal{H}}_{J_\parallel} = \frac{J_\parallel}{2} \sum_{\vec{q},\mu} V(\vec{q}) \left(\hat{\vec{S}}_{-\vec{q},\mu} \cdot \hat{\vec{S}}_{\vec{q},\mu} - \frac{1}{4} \sum_{\alpha,\beta} \hat{n}_{-\vec{q},\alpha,\mu} \hat{n}_{\vec{q},\beta,\mu} \right) \tag{B.6}$$

with $V(\vec{q}) = 2 \left[\cos(q_x) + \cos(q_y) \right]$. Normal ordering and collecting all terms, taking into account the fermionic exchange statistics, yields

$$\hat{\mathcal{H}}_{J_\parallel} = -\frac{J_\parallel}{4N} \sum_{\vec{q},\vec{k}_1,\vec{k}_2} \sum_{\alpha,\beta,\mu} V(\vec{q}) \left(\hat{c}_{\vec{k}_1+\vec{q},\alpha,\mu}^\dagger \hat{c}_{\vec{k}_2-\vec{q},\beta,\mu}^\dagger \hat{c}_{\vec{k}_1,\beta,\mu} \hat{c}_{\vec{k}_2,\alpha,\mu} + \hat{c}_{\vec{k}_1+\vec{q},\alpha,\mu}^\dagger \hat{c}_{\vec{k}_2-\vec{q},\beta,\mu}^\dagger \hat{c}_{\vec{k}_2,\beta,\mu} \hat{c}_{\vec{k}_1,\alpha,\mu} \right). \tag{B.7}$$

This exact Hamiltonian can now be used to apply mean-field theory and further we only consider Cooper pairs with net momentum zero. With these approximations, the Hamiltonian becomes

$$\begin{aligned}
\hat{\mathcal{H}}_{J_\parallel}^{\text{MF}} = -\frac{J_\parallel}{4N} \sum_{\vec{k},\vec{k}'} \sum_{\mu} \Big\{ &2 \left[V(\vec{k}'-\vec{k}) + V(\vec{k}'+\vec{k}) \right] \langle \hat{c}_{\vec{k}',\uparrow,\mu}^\dagger \hat{c}_{-\vec{k}',\downarrow,\mu}^\dagger \rangle \hat{c}_{-\vec{k},\downarrow,\mu} \hat{c}_{\vec{k},\uparrow,\mu} \\
&+ \left[V(\vec{k}'-\vec{k}) + V(\vec{k}'+\vec{k}) \right] \langle \hat{c}_{\vec{k}',\uparrow,\mu}^\dagger \hat{c}_{-\vec{k}',\uparrow,\mu}^\dagger \rangle \hat{c}_{-\vec{k},\uparrow,\mu} \hat{c}_{\vec{k},\uparrow,\mu} \\
&+ \left[V(\vec{k}'-\vec{k}) + V(\vec{k}'+\vec{k}) \right] \langle \hat{c}_{\vec{k}',\downarrow,\mu}^\dagger \hat{c}_{-\vec{k}',\downarrow,\mu}^\dagger \rangle \hat{c}_{-\vec{k},\downarrow,\mu} \hat{c}_{\vec{k},\downarrow,\mu} + \text{H.c.} \Big\} + \text{const.},
\end{aligned} \tag{B.8}$$

where the constant term will be specified later. We can see that the coupling amplitude is symmetric under $\vec{k}' \leftrightarrow -\vec{k}'$ and thus the triplet terms must vanish under summation since they have odd angular momentum. In particular, the interaction can be decomposed into an $s^\parallel$-wave and $d^\parallel$-wave contribution

$$V_{\vec{k},\vec{k}'} = V_{\vec{k},\vec{k}'}^s + V_{\vec{k},\vec{k}'}^d = V(\vec{k}'-\vec{k}) + V(\vec{k}'+\vec{k}) \tag{B.9}$$

$$V_{\vec{k},\vec{k}'}^s = 2 \left[\cos(k_x) + \cos(k_y) \right] \left[\cos(k_x') + \cos(k_y') \right] \tag{B.10}$$

$$V_{\vec{k},\vec{k}'}^d = 2 \left[\cos(k_x) - \cos(k_y) \right] \left[\cos(k_x') - \cos(k_y') \right]. \tag{B.11}$$

Taking the symmetry in Eq. (B.8) into account, the mean-field Hamiltonian can be written as

$$\hat{\mathcal{H}}_{J_\parallel}^{\mathrm{MF}} = -\sum_{\vec{k},\mu} \left[\Delta_{\vec{k},\mu}^{\parallel} \hat{c}_{\vec{k},\uparrow,\mu}^{\dagger} \hat{c}_{-\vec{k},\downarrow,\mu}^{\dagger} + \mathrm{H.c.} \right] + \frac{2}{J_\parallel} \left(|\Delta^{s,\parallel}|^2 + |\Delta^{d,\parallel}|^2 \right), \tag{B.12}$$

where we have defined the momentum dependent order parameter $\Delta_{\vec{k}}^{\parallel} = \Delta_{\vec{k}}^{s,\parallel} + e^{i\beta_d} \Delta_{\vec{k}}^{d,\parallel}$ with phase β_d as

$$\Delta_{\vec{k}}^{\parallel} = \Delta_{\vec{k},(\mu=1,2)}^{\parallel} = \frac{J_\parallel}{2N} \sum_{\vec{k}'} V_{\vec{k},\vec{k}'} \langle \hat{c}_{\vec{k}',\downarrow,\mu} \hat{c}_{-\vec{k}',\uparrow,\mu} \rangle, \tag{B.13}$$

where we drop the layer index μ because $\Delta_{\vec{k},\mu}^{\parallel}$ does not depend on μ due to the symmetry between $\mu = 1 \leftrightarrow \mu = 2$ in the system, which we will justify more rigorously below. Moreover, the order parameter written without momentum subscript $\vec{k}$ [Eq. (B.12)] describes only the amplitude, e.g. $\Delta_{\vec{k}}^{d,\parallel} = \Delta^{d,\parallel} (\cos k_x - \cos k_y)$. Note that we have introduced the superscripts, $\perp$ and $\parallel$, in the order parameters as well as in the spatial symmetry ($s^\perp$-, $s^\parallel$-, $d^\parallel$-wave) to point out whether the Cooper pair is a bound state between the layers ($\perp$) or within the layer ($\parallel$).

The last term to consider is the often neglected 3-site term, which arises in the derivation of the $t - J$ model in second-order perturbation theory from the Hubbard model. A posteriori, we find that the 3-site term indeed does not lead to $p^\parallel$-wave order in the mean-field calculation. The term is given by

$$\hat{\mathcal{H}}_{3s} = -\frac{J_\parallel}{4} \sum_{\substack{\langle i,j \rangle, \langle i,j' \rangle \\ j \neq j', \alpha}} \sum_{\mu} \left(\hat{c}_{j',\alpha,\mu}^{\dagger} \hat{n}_{i,\bar{\alpha},\mu} \hat{c}_{j,\alpha,\mu} + \hat{c}_{j',\alpha,\mu}^{\dagger} \hat{c}_{i,\bar{\alpha},\mu}^{\dagger} \hat{c}_{i,\alpha,\mu} \hat{c}_{j,\bar{\alpha},\mu} \right). \tag{B.14}$$

In momentum space, it can be written

$$\hat{\mathcal{H}}_{3s} = -\frac{J_\parallel}{4N} \sum_{\alpha,\mu} \sum_{\vec{k}_1,\vec{k}_2,\vec{k}_3} W(\vec{k}_1,\vec{k}_3) \times$$
$$\times \left[\hat{c}_{\vec{k}_1,\alpha,\mu}^{\dagger} \hat{c}_{\vec{k}_2,\bar{\alpha},\mu}^{\dagger} \hat{c}_{\vec{k}_1+\vec{k}_2-\vec{k}_3,\bar{\alpha},\mu} \hat{c}_{\vec{k}_3,\alpha,\mu} + \hat{c}_{\vec{k}_1,\alpha,\mu}^{\dagger} \hat{c}_{\vec{k}_2,\bar{\alpha},\mu}^{\dagger} \hat{c}_{\vec{k}_1+\vec{k}_2-\vec{k}_3,\alpha,\mu} \hat{c}_{\vec{k}_3,\bar{\alpha},\mu} \right]$$
$$\tag{B.15}$$

with

$$W(\vec{k}_1,\vec{k}_3) = 4 \left[\cos(k_3^x) \cos(k_1^y) + \cos(k_3^y) \cos(k_1^x) \right]$$
$$+ 2 \left[\cos(k_1^x + k_3^x) + \cos(k_1^y + k_3^y) \right]. \tag{B.16}$$

Again, when we only consider Cooper pairs with net momentum zero, we find

$$\hat{\mathcal{H}}_{3s} = -\frac{J_\parallel}{4N} \sum_{\alpha,\mu} \sum_{\vec{k},\vec{k}'} \left[W(\vec{k},\vec{k}') - W(\vec{k},-\vec{k}') \right] \langle \hat{c}_{\vec{k},\alpha,\mu}^{\dagger} \hat{c}_{-\vec{k},\bar{\alpha},\mu}^{\dagger} \rangle \hat{c}_{-\vec{k}',\bar{\alpha},\mu} \hat{c}_{\vec{k}',\alpha,\mu} + \mathrm{const.} \tag{B.17}$$

Since the interaction strength $W(\vec{k}, \vec{k}') - W(\vec{k}, -\vec{k}')$ is anti-symmetric under momentum exchange and the equation is symmetric under layer exchange, we can conclude that the order parameter describes symmetric coupling in the triplet channel to fulfill Pauli's principle. Furthermore, the interaction potential can be re-written in terms of a $p^{\parallel}$-wave interaction

$$V^p_{\vec{k},\vec{k}'} = W(\vec{k},\vec{k}') - W(\vec{k},-\vec{k}') = 2\left[\sin(k_x)\sin(k'_x) + \sin(k_y)\sin(k'_y)\right] \tag{B.18}$$

$$= 2(1-i)\left[Y^1_1(\vec{k})Y^1_1(\vec{k}') + Y^{-1}_1(\vec{k})Y^1_1(\vec{k}')\right] + 2(1+i)\left[Y^1_1(\vec{k})Y^{-1}_1(\vec{k}') + Y^{-1}_1(\vec{k})Y^{-1}_1(\vec{k}')\right] \tag{B.19}$$

with $Y^{\pm 1}_1(\vec{k}) = \frac{1}{2}\left[\sin(k_x) \pm i\sin(k_y)\right]$. The mean-field Hamiltonian then reads

$$\hat{\mathcal{H}}^{\text{MF}}_{3s} = -\sum_{\vec{k},\mu}\left[\Delta^{p,\parallel}_{\vec{k},\mu}\hat{c}^{\dagger}_{\vec{k},\uparrow,\mu}\hat{c}^{\dagger}_{-\vec{k},\downarrow,\mu} + \text{H.c.}\right] + \frac{2}{J_{\parallel}}|\Delta^{p,\parallel}|^2. \tag{B.20}$$

All together, the mean-field Hamiltonian becomes

$$\hat{\mathcal{H}}^{\text{BCS}} = \sum_{\vec{k},\alpha,\mu}\epsilon_{\vec{k}}\hat{c}^{\dagger}_{\vec{k},\alpha,\mu}\hat{c}_{\vec{k},\alpha,\mu} - \sum_{\vec{k}}\left[\Delta^{\perp}\left(\hat{c}^{\dagger}_{\vec{k},\uparrow,1}\hat{c}^{\dagger}_{-\vec{k},\downarrow,2} - \hat{c}^{\dagger}_{\vec{k},\downarrow,1}\hat{c}^{\dagger}_{-\vec{k},\uparrow,2} + \text{H.c.}\right)\right] + \frac{2}{J_{\perp}}|\Delta^{\perp}|^2$$

$$- \sum_{\vec{k},\mu}\left[\Delta^{\parallel}_{\vec{k},\mu}\hat{c}^{\dagger}_{\vec{k},\uparrow,\mu}\hat{c}^{\dagger}_{-\vec{k},\downarrow,\mu} + \text{H.c.}\right] + \frac{2}{J_{\parallel}}\sum_{\ell=s,p,d}|\Delta^{\ell,\parallel}|^2, \tag{B.21}$$

with the dispersion $\epsilon_{\vec{k}} = -2t_{\text{eff}}\left[\cos(k_x) + \cos(k_y)\right] - \mu$ including the chemical potential μ. The effective hopping $t_{\text{eff}} = t$ in the first case (see Figure 12.5a), or $t_{\text{eff}} = \delta \cdot t$ depends on the hole doping δ to approximate the effect of the Gutzwiller projectors (see Figure 12.5b). Note also that we have summarized the intra-layer couplings into a single term with $\Delta^{\parallel}_{\vec{k}} = \Delta^{s,\parallel}_{\vec{k}} + e^{i\beta_d}\Delta^{d,\parallel}_{\vec{k}} + e^{i\beta_p}\Delta^{p,\parallel}_{\vec{k}}$ with complex phases between the different angular momentum channels.

In the following, we argue that we can express any self-consistent solution of the intra-layer and inter-layer order parameters in terms of $(\Delta^{\perp}, e^{i\chi}\Delta^{\parallel}_{\vec{k}})$ with $\Delta^{\perp}, \Delta^{\parallel}_{\vec{k}} \in \mathbb{R}$. Let us consider the most general case and assume that the set of order parameters is $(e^{i\alpha_3}\Delta^{\perp}, e^{i\alpha_1}\Delta^{\parallel}_{\vec{k},1}, e^{i\alpha_2}\Delta^{\parallel}_{\vec{k},2})$, where we distinguish the order parameters $\Delta^{\parallel}_{\vec{k},\mu=1,2}$ of the two layers. Now, we want to exploit the model's symmetries and consider the transformation of Hamiltonian (B.21) under unitary transformations. The system inherits a $U(1)$ symmetry for each layer individually, which we can decompose into a global $U(1)$ and relative layer $U(1)$ symmetry.

1. Global $U(1)$ symmetry:

$$\hat{U}^{\dagger}_{\text{gl}}\hat{c}^{\dagger}_{\vec{k},\alpha,\mu}\hat{U}_{\text{gl}} = e^{i\beta_{\text{gl}}}\hat{c}^{\dagger}_{\vec{k},\alpha,\mu} \tag{B.22}$$

2. Relative $U(1)$ symmetry:

$$\hat{U}^{\dagger}_{\text{rel}}\hat{c}^{\dagger}_{\vec{k},\alpha,\mu}\hat{U}_{\text{rel}} = e^{i\beta_{\text{rel}}(-1)^{\mu}}\hat{c}^{\dagger}_{\vec{k},\alpha,\mu} \tag{B.23}$$

Applying the two unitary transformations on Hamiltonian (B.21) yields

$$\hat{U}_{\mathrm{rel}}^{\dagger}\hat{U}_{\mathrm{gl}}^{\dagger}\hat{\mathcal{H}}^{\mathrm{BCS}}\big[e^{i\alpha_3}\Delta^{\perp},e^{i\alpha_1}\Delta_{\vec{k},1}^{\parallel},e^{i\alpha_2}\Delta_{\vec{k},2}^{\parallel}\big]\hat{U}_{\mathrm{gl}}\hat{U}_{\mathrm{rel}}$$

$$=\hat{\mathcal{H}}^{\mathrm{BCS}}\big[e^{i(\alpha_3-\beta_{\mathrm{gl}})}\Delta^{\perp},e^{i(\alpha_1-\beta_{\mathrm{gl}}-\beta_{\mathrm{rel}})}\Delta_{\vec{k},1}^{\parallel},e^{i(\alpha_2-\beta_{\mathrm{gl}}+\beta_{\mathrm{rel}})}\Delta_{\vec{k},2}^{\parallel}\big] \quad (\mathrm{B.24})$$

$$=\hat{\mathcal{H}}^{\mathrm{BCS}}\big[\Delta^{\perp},e^{i\chi}\Delta_{\vec{k},1}^{\parallel},e^{i\chi}\Delta_{\vec{k},2}^{\parallel}\big],$$

where we have chosen $\beta_{\mathrm{gl}}=\alpha_3$ and $\beta_{\mathrm{rel}}=(\alpha_1-\alpha_2)/2$ in the second equality. Hence, we conclude that it is justified to take $e^{i\chi}\Delta_{\vec{k},1}^{\parallel}=e^{i\chi}\Delta_{\vec{k},2}^{\parallel}=e^{i\chi}\Delta_{\vec{k}}^{\parallel}$.

The BCS mean-field Hamiltonian (B.21), which we want to solve self-consistently, is fully quadratic and can thus be solved exactly by first performing a rotation to decouple the two layers and then applying a Bogoliubov transformation. The Hamiltonian in terms of the free fermionic Bogoliubov modes $\hat{\gamma}_{\vec{k},\alpha,\mu}$ and dispersions $E_{\vec{k}}^{\delta,\Delta}$ is given by

$$\hat{\mathcal{H}}^{\mathrm{BCS}}=\sum_{\vec{k},\alpha}\Big(E_{\vec{k}}^{\Delta}\,\gamma_{\vec{k},\alpha,1}^{\dagger}\gamma_{\vec{k},\alpha,1}+E_{\vec{k}}^{\delta}\,\gamma_{\vec{k},\alpha,2}^{\dagger}\gamma_{\vec{k},\alpha,2}\Big)+\frac{2N}{J_{\perp}}|\Delta^{\perp}|^2+\frac{2N}{J_{\parallel}}\sum_{\ell=s,p,d}|\Delta^{\ell,\parallel}|^2-\sum_{\vec{k}}\Big[E_{\vec{k}}^{\Delta}+E_{\vec{k}}^{\delta}-\epsilon(\vec{k})\Big]$$

$$(\mathrm{B.25})$$

$$E_{\vec{k}}^{\Delta}=\sqrt{\epsilon^2(\vec{k})+|\Delta_{\vec{k}}|^2} \quad (\mathrm{B.26})$$

$$E_{\vec{k}}^{\delta}=\sqrt{\epsilon^2(\vec{k})+|\delta_{\vec{k}}|^2}, \quad (\mathrm{B.27})$$

with $\Delta_{\vec{k}}=|\Delta^{\perp}+\Delta_{\vec{k}}^{\parallel}|$ and $\delta_{\vec{k}}=|\Delta^{\perp}-\Delta_{\vec{k}}^{\parallel}|$. The mean-field energy at $T=0$ in the considered parameter regime is given by

$$E^{\mathrm{BCS}}=\frac{2N}{J_{\perp}}|\Delta^{\perp}|^2+\frac{2N}{J_{\parallel}}\sum_{\ell=s,p,d}|\Delta^{\ell,\parallel}|^2$$

$$-\frac{N}{4\pi^2}\int_{\mathrm{BZ}}d^2\vec{k}\left(\sqrt{\epsilon^2(\vec{k})+|\Delta^{\perp}+\Delta_{\vec{k}}^{\parallel}|^2}+\sqrt{\epsilon^2(\vec{k})+|\Delta^{\perp}-\Delta_{\vec{k}}^{\parallel}|^2}-\epsilon(\vec{k})\right)$$

$$(\mathrm{B.28})$$

in the thermodynamic limit and integrating over the Brillouin zone (BZ).

Hamiltonian (B.25) is solved by the Fermi-Dirac distribution and for $T=0$, we can write down a set of self-consistency equations given a fixed particle number (hole density δ), which can be tuned via the chemical potential μ. W.l.o.g. we fix the gauge such that $\Delta^{\perp},\Delta_{\vec{k}}^{\parallel}\in\mathbb{R}$ with relative phase $(\Delta^{\perp},e^{i\chi}\Delta_{\vec{k}}^{\parallel})$ as discussed above:

$$\delta=\frac{1}{8\pi^2}\int_{BZ}d^2\vec{k}\left[\frac{\epsilon_{\vec{k}}}{2E_{\vec{k}}^{\delta}}+\frac{\epsilon_{\vec{k}}}{2E_{\vec{k}}^{\Delta}}\right] \quad (\mathrm{B.29})$$

$$\Delta^{\perp}=\frac{J_{\perp}}{16\pi^2}\int_{BZ}d^2\vec{k}\left[\frac{\Delta^{\perp}+\Delta_{\vec{k}}^{\parallel}}{E_{\vec{k}}^{\Delta}}+\frac{\Delta^{\perp}-\Delta_{\vec{k}}^{\parallel}}{E_{\vec{k}}^{\delta}}\right] \quad (\mathrm{B.30})$$

$$\Delta_{\vec{k}}^{\ell,\parallel}=\frac{J_{\parallel}}{32\pi^2}\int_{BZ}d^2\vec{k}'\,V_{\vec{k},\vec{k}'}^{\ell}\left[\frac{\Delta^{\perp}+\Delta_{\vec{k}'}^{\parallel}}{E_{\vec{k}'}^{\Delta}}-\frac{\Delta^{\perp}-\Delta_{\vec{k}'}^{\parallel}}{E_{\vec{k}'}^{\delta}}\right] \quad \text{with } \ell=s,p,d\,, \quad (\mathrm{B.31})$$

Let us now consider the possibility of solutions with simultaneously broken symmetries.

- $s^\perp + e^{i\chi}\ell^\parallel$ ($\ell = s, p, d$) co-existence: The l.h.s. of Eq. (B.30) is always purely real. Thus from requiring the imaginary part of the r.h.s. to vanish, it follows that $\chi = 0, \pm\pi/2, \pi$. However, we do not find evidence for a co-existing intra- and inter-layer superconducting phase in the numerical calculations.

- $\ell^\parallel \pm i\ell'^\parallel$ ($\ell, \ell' = s, p, d$) time-reversal symmetry broken phase: The symmetries in the model allow us to choose $\ell^\parallel \in \mathbb{R}$. Inserting $\ell^\parallel \pm i\ell'^\parallel$ into Eq. (B.31) gives separate equations for each coupling sector ℓ, ℓ'. However, the l.h.s. of the equation for $\Delta_{\vec{k}}^{\parallel,\ell}$ is purely real whereas the r.h.s. is complex by construction. Thus, the order parameters must be strictly zero prohibiting a time-reversal symmetry broken phase.

- $\ell^\parallel \pm \ell'^\parallel$ ($\ell, \ell' = s, p, d$) nematic phase: The self-consistency equations allow for the co-existence of two intra-plane order parameters. To have a time-reversal broken/nematic phase, we additionally require the ground states $\ell^\parallel \pm \ell'^\parallel$ to be degenerate. We can see the degeneracy from Eq. (B.28) by considering the transformation under $C4$ rotational symmetry, $E_{\vec{k}}^{\delta,\Delta}(\ell^\parallel + \ell'^\parallel) \to E_{\vec{k}}^{\delta,\Delta}(\ell^\parallel - \ell'^\parallel)$. Since the integration measure is invariant under $C4$ rotation, the two configurations $\ell^\parallel \pm \ell'^\parallel$ yield equal mean-field energies and are thus degenerate. By numerically solving the self-consistency equations, we indeed find a nematic regime in the case $t_{\text{eff}} = \delta \cdot t$ as shown in Figure 12.5b for low dopings.

The self-consistency Eqs. (B.29)-(B.31) define recursive equations, which can be solved numerically, to find the mean-field solution of the ground state. Thus, the superconducting order for a fixed set of parameters $(t, J_\parallel, J_\perp, \delta)$ can be determined. The solutions are plotted in Chapter 12, Section 12.3 in Figure 12.5.

Bibliography

[1]   L. H. Sullivan, "The tall office building artistically considered", in *Lippincott's monthly magazine*, Vol. 57 (J. B. Lippincott Co., Philadelphia, Mar. 1896), pp. 403–409.

[2]   C. Gross and W. S. Bakr, "Quantum gas microscopy for single atom and spin detection", Nature Physics **17**, 1316–1323 (2021).

[3]   X.-G. Wen, *Quantum Field Theory of Many-Body Systems* (Oxford University Press, Sept. 2007).

[4]   E. Fradkin, *Field Theories of Condensed Matter Physics* (Cambridge University Press, Feb. 2013).

[5]   E. Dagotto, "Correlated electrons in high-temperature superconductors", Reviews of Modern Physics **66**, 763–840 (1994).

[6]   T. A. Hilker, G. Salomon, F. Grusdt, A. Omran, M. Boll, E. Demler, I. Bloch, and C. Gross, "Revealing hidden antiferromagnetic correlations in doped Hubbard chains via string correlators", Science **357**, 484–487 (2017).

[7]   C. S. Chiu, G. Ji, A. Bohrdt, M. Xu, M. Knap, E. Demler, F. Grusdt, M. Greiner, and D. Greif, "String patterns in the doped Hubbard model", Science **365**, 251–256 (2019).

[8]   A. Bohrdt, C. S. Chiu, G. Ji, M. Xu, D. Greif, M. Greiner, E. Demler, F. Grusdt, and M. Knap, "Classifying snapshots of the doped Hubbard model with machine learning", Nature Physics **15**, 921–924 (2019).

[9]   S. Sachdev, *Quantum Phases of Matter* (Cambridge University Press, Mar. 2023).

[10]   G. C. Strinati, P. Pieri, G. Röpke, P. Schuck, and M. Urban, "The BCS–BEC crossover: From ultra-cold Fermi gases to nuclear systems", Physics Reports **738**, 1–76 (2018).

[11]   I. Bloch, J. Dalibard, and W. Zwerger, "Many-body physics with ultracold gases", Reviews of Modern Physics **80**, 885–964 (2008).

[12]   A. Browaeys and T. Lahaye, "Many-body physics with individually controlled Rydberg atoms", Nature Physics **16**, 132–142 (2020).

[13]   C. Monroe, W. Campbell, L.-M. Duan, Z.-X. Gong, A. Gorshkov, P. Hess, R. Islam, K. Kim, N. Linke, G. Pagano, P. Richerme, C. Senko, and N. Yao, "Programmable quantum simulations of spin systems with trapped ions", Reviews of Modern Physics **93**, 025001 (2021).

[14]   M. Kjaergaard, M. E. Schwartz, J. Braumüller, P. Krantz, J. I.-J. Wang, S. Gustavsson, and W. D. Oliver, "Superconducting Qubits: Current State of Play", Annual Review of Condensed Matter Physics **11**, 369–395 (2020).

[15]   J. C. Halimeh, M. Aidelsburger, F. Grusdt, P. Hauke, and B. Yang, "Cold-atom quantum simulators of gauge theories", arXiv **2310.12201** (2023).

[P1]   A. Bohrdt, L. Homeier, C. Reinmoser, E. Demler, and F. Grusdt, "Exploration of doped quantum magnets with ultracold atoms", Annals of Physics **435**, 168651 (2021).

[16] G. Baskaran, Z. Zou, and P. W. Anderson, "The resonating valence bond state and high-Tc superconductivity - a mean field theory", Solid State Communications **88**, 853–856 (1987).

[17] I. Affleck, Z. Zou, T. Hsu, and P. W. Anderson, "SU(2) gauge symmetry of the large-U limit of the Hubbard model", Physical Review B **38**, 745–747 (1988).

[18] E. Dagotto, E. Fradkin, and A. Moreo, "SU(2) gauge invariance and order parameters in strongly coupled electronic systems", Physical Review B **38**, 2926–2929 (1988).

[19] X.-G. Wen and P. A. Lee, "Theory of Underdoped Cuprates", Physical Review Letters **76**, 503–506 (1996).

[20] T. Senthil and M. P. A. Fisher, "Z2 gauge theory of electron fractionalization in strongly correlated systems", Physical Review B **62**, 7850–7881 (2000).

[21] F. Grusdt, M. Kánasz-Nagy, A. Bohrdt, C. S. Chiu, G. Ji, M. Greiner, D. Greif, and E. Demler, "Parton Theory of Magnetic Polarons: Mesonic Resonances and Signatures in Dynamics", Phys. Rev. X **8**, 011046 (2018).

[22] X.-G. Wen, "Colloquium : Zoo of quantum-topological phases of matter", Reviews of Modern Physics **89** (2017).

[23] S. Sachdev, "Emergent gauge fields and the high-temperature superconductors", Philosophical Transactions of the Royal Society A: Mathematical, Physical and Engineering Sciences **374**, 20150248 (2016).

[24] S. Gazit, M. Randeria, and A. Vishwanath, "Emergent Dirac fermions and broken symmetries in confined and deconfined phases of Z2 gauge theories", Nature Physics **13**, 484–490 (2017).

[25] U. Borla, R. Verresen, F. Grusdt, and S. Moroz, "Confined Phases of One-Dimensional Spinless Fermions Coupled to Z2 Gauge Theory", Physical Review Letters **124** (2020).

[26] K. G. Wilson, "Confinement of quarks", Physical Review D **10**, 2445–2459 (1974).

[27] F. J. Wegner, "Duality in Generalized Ising Models and Phase Transitions without Local Order Parameters", Journal of Mathematical Physics **12**, 2259–2272 (1971).

[28] E. Fradkin and S. H. Shenker, "Phase diagrams of lattice gauge theories with Higgs fields", Physical Review D **19**, 3682–3697 (1979).

[29] A. Y. Kitaev, "Fault-tolerant quantum computation by anyons", Ann. Phys. New York **303**, 2–30 (2003).

[P4] J. C. Halimeh, L. Homeier, C. Schweizer, M. Aidelsburger, P. Hauke, and F. Grusdt, "Stabilizing lattice gauge theories through simplified local pseudogenerators", Physical Review Research **4**, 033120 (2022).

[P5] L. Homeier, A. Bohrdt, S. Linsel, E. Demler, J. C. Halimeh, and F. Grusdt, "Realistic scheme for quantum simulation of $\mathbb{Z}_2$ lattice gauge theories with dynamical matter in $(2+1)$D", Communications Physics **6**, 127 (2023).

[P9] J. C. Halimeh∗, L. Homeier∗, A. Bohrdt, and F. Grusdt, "Spin exchange-enabled quantum simulator for large-scale non-Abelian gauge theories", arXiv **2305.06373** (2023).

[P3] J. C. Halimeh, L. Homeier, H. Zhao, A. Bohrdt, F. Grusdt, P. Hauke, and J. Knolle, "Enhancing Disorder-Free Localization through Dynamically Emergent Local Symmetries", PRX Quantum **3**, 020345 (2022).

[30] J. C. Halimeh, H. Lang, J. Mildenberger, Z. Jiang, and P. Hauke, "Gauge-Symmetry Protection Using Single-Body Terms", PRX Quantum **2** (2021).

[31] P. A. Lee, N. Nagaosa, and X.-G. Wen, "Doping a Mott insulator: physics of high-temperature superconductivity", Rev. Mod. Phys. **78**, 17–85 (2006).

[32] P. Béran, D. Poilblanc, and R. B. Laughlin, "Evidence for composite nature of quasi-particles in the 2D $t - J$ model", Nuclear Physics B **473**, 707–720 (1996).

[33] J. Koepsell, J. Vijayan, P. Sompet, F. Grusdt, T. A. Hilker, E. Demler, G. Salomon, I. Bloch, and C. Gross, "Imaging magnetic polarons in the doped Fermi–Hubbard model", Nature **572**, 358–362 (2019).

[P11] L. Homeier, H. Lange, E. Demler, A. Bohrdt, and F. Grusdt, "Feshbach hypothesis of high-Tc superconductivity in cuprates", arXiv **2312.02982** (2023).

[P7] L. Homeier, P. Bermes, and F. Grusdt, "Scattering theory of mesons in doped anti-ferromagnetic Mott insulators: Multichannel perspective and Feshbach resonance", Physical Review B **109**, 125135 (2024).

[34] D. Poilblanc, J. Riera, and E. Dagotto, "D-wave bound state of holes in an antiferromagnet", Physical Review B **49**, 12318–12321 (1994).

[35] E. Manousakis, "String excitations of a hole in a quantum antiferromagnet and photoelectron spectroscopy", Physical Review B **75**, 035106 (2007).

[36] F. Grusdt, E. Demler, and A. Bohrdt, "Pairing of holes by confining strings in antiferromagnets", SciPost Physics **14** (2023).

[37] A. Bohrdt, E. Demler, and F. Grusdt, "Dichotomy of heavy and light pairs of holes in the t-J model", Nature Communications **14** (2023).

[38] D. A. Wollman, D. J. V. Harlingen, W. C. Lee, D. M. Ginsberg, and A. J. Leggett, "Experimental determination of the superconducting pairing state in YBCO from the phase coherence of YBCO-Pb dc SQUIDs", Physical Review Letters **71**, 2134–2137 (1993).

[39] B. Keimer, S. A. Kivelson, M. R. Norman, S. Uchida, and J. Zaanen, "From quantum matter to high-temperature superconductivity in copper oxides", Nature **518**, 179–186 (2015).

[P2] A. Bohrdt, L. Homeier, I. Bloch, E. Demler, and F. Grusdt, "Strong pairing in mixed-dimensional bilayer antiferromagnetic Mott insulators", Nature Physics **18**, 651–656 (2022).

[P10] H. Lange, L. Homeier, E. Demler, U. Schollwöck, A. Bohrdt, and F. Grusdt, "Pairing dome from an emergent Feshbach resonance in a strongly repulsive bilayer model", arXiv **2309.13040** (2023).

[P6] H. Lange, L. Homeier, E. Demler, U. Schollwöck, F. Grusdt, and A. Bohrdt, "Feshbach resonance in a strongly repulsive ladder of mixed dimensionality: a possible scenario for bilayer nickelate superconductors", Physical Review B **109**, 045127 (2024).

[P12] S. M. Linsel, A. Bohrdt, L. Homeier, L. Pollet, and F. Grusdt, "Percolation as a confinement order parameter in $\mathbb{Z}_2$ lattice gauge theories", arXiv **2401.08770** (2024).

[P8] L. Homeier, T. J. Harris, T. Blatz, S. Geier, S. Hollerith, U. Schollwöck, F. Grusdt, and A. Bohrdt, "Antiferromagnetic Bosonic t–J Models and Their Quantum Simulation in Tweezer Arrays", Phys. Rev. Lett. **132**, 230401 (2024).

[40] M. D. Schwartz, *Quantum Field Theory and the Standard Model* (Cambridge University Press, 2013).

[41] D. Jaksch, C. Bruder, J. I. Cirac, C. W. Gardiner, and P. Zoller, "Cold Bosonic Atoms in Optical Lattices", Physical Review Letters **81**, 3108–3111 (1998).

[42] M. Greiner, O. Mandel, T. Esslinger, T. W. Hänsch, and I. Bloch, "Quantum phase transition from a superfluid to a Mott insulator in a gas of ultracold atoms", Nature **415**, 39–44 (2002).

[43] J. B. Kogut, "An introduction to lattice gauge theory and spin systems", Reviews of Modern Physics **51**, 659–713 (1979).

[44] S. Sachdev, "Topological order, emergent gauge fields, and Fermi surface reconstruction", Rep. Prog. Phys. **82**, 014001 (2019).

[45] P. E. Lammert, D. S. Rokhsar, and J. Toner, "Topology and nematic ordering", Physical Review Letters **70**, 1650–1653 (1993).

[46] J. C. Halimeh and P. Hauke, "Stabilizing Gauge Theories in Quantum Simulators: A Brief Review", arXiv **2204.13709v1** (2022).

[47] U. Borla, B. Jeevanesan, F. Pollmann, and S. Moroz, "Quantum phases of two-dimensional $\mathbb{Z}_2$ gauge theory coupled to single-component fermion matter", Physical Review B **105**, 075132 (2022).

[48] M. Kebrič, U. Borla, U. Schollwöck, S. Moroz, L. Barbiero, and F. Grusdt, "Confinement induced frustration in a one-dimensional Z2 lattice gauge theory", New Journal of Physics **25**, 013035 (2023).

[49] M. Aidelsburger, L. Barbiero, A. Bermudez, T. Chanda, A. Dauphin, D. González-Cuadra, P. R. Grzybowski, S. Hands, F. Jendrzejewski, J. Jünemann, G. Juzeliūnas, V. Kasper, A. Piga, S.-J. Ran, M. Rizzi, G. Sierra, L. Tagliacozzo, E. Tirrito, T. V. Zache, J. Zakrzewski, E. Zohar, and M. Lewenstein, "Cold atoms meet lattice gauge theory", Philosophical Transactions of the Royal Society A: Mathematical, Physical and Engineering Sciences **380** (2021).

[50] R. Verresen, M. D. Lukin, and A. Vishwanath, "Prediction of Toric Code Topological Order from Rydberg Blockade", Physical Review X **11**, 031005 (2021).

[51] G. Semeghini, H. Levine, A. Keesling, S. Ebadi, T. T. Wang, D. Bluvstein, R. Verresen, H. Pichler, M. Kalinowski, R. Samajdar, A. Omran, S. Sachdev, A. Vishwanath, M. Greiner, V. Vuletić, and M. D. Lukin, "Probing topological spin liquids on a programmable quantum simulator", Science **374**, 1242–1247 (2021).

[52] A. Kitaev, "Anyons in an exactly solved model and beyond", Annals of Physics **321**, 2–111 (2006).

[53] B. Yang, H. Sun, R. Ott, H.-Y. Wang, T. V. Zache, J. C. Halimeh, Z.-S. Yuan, P. Hauke, and J.-W. Pan, "Observation of gauge invariance in a 71-site Bose-Hubbard quantum simulator", Nature **587**, 392–396 (2020).

[54] U. Schollwöck, "The density-matrix renormalization group in the age of matrix product states", Annals of Physics **326**, 96–192 (2011).

[55] L. Pollet, "Recent developments in quantum Monte Carlo simulations with applications for cold gases", Reports on Progress in Physics **75**, 094501 (2012).

[56] J. Preskill, "Quantum computing 40 years later", arXiv **2106.10522** (2021).

[57]   R. P. Feynman, "Simulating physics with computers", International Journal of Theoretical Physics **21**, 467–488 (1982).

[58]   D. Bluvstein, S. J. Evered, A. A. Geim, S. H. Li, H. Zhou, T. Manovitz, S. Ebadi, M. Cain, M. Kalinowski, D. Hangleiter, J. P. Bonilla Ataides, N. Maskara, I. Cong, X. Gao, P. Sales Rodriguez, T. Karolyshyn, G. Semeghini, M. J. Gullans, M. Greiner, V. Vuletić, and M. D. Lukin, "Logical quantum processor based on reconfigurable atom arrays", Nature **626**, 58–65 (2023).

[59]   A. J. Daley, "Twenty-five years of analogue quantum simulation", Nature Reviews Physics **5**, 702–703 (2023).

[60]   L.-M. Duan, E. Demler, and M. D. Lukin, "Controlling Spin Exchange Interactions of Ultracold Atoms in Optical Lattices", Physical Review Letters **91**, 090402 (2003).

[61]   D. González-Cuadra, D. Bluvstein, M. Kalinowski, R. Kaubruegger, N. Maskara, P. Naldesi, T. V. Zache, A. M. Kaufman, M. D. Lukin, H. Pichler, B. Vermersch, J. Ye, and P. Zoller, "Fermionic quantum processing with programmable neutral atom arrays", Proceedings of the National Academy of Sciences **120** (2023).

[62]   P. Preiss, A. von Haaren, R. Groth, J. Qesja, G. Neplyakh, E. Zu, T. Hilker, and I. Bloch, "FermiQP - A Fermion Quantum Processor", APS DAMOP Meeting 2023.

[63]   L. Anderegg, L. W. Cheuk, Y. Bao, S. Burchesky, W. Ketterle, K.-K. Ni, and J. M. Doyle, "An optical tweezer array of ultracold molecules", Science **365**, 1156–1158 (2019).

[64]   R. V. Brooks, S. Spence, A. Guttridge, A. Alampounti, A. Rakonjac, L. A. McArd, J. M. Hutson, and S. L. Cornish, "Preparation of one 87Rb and one 133Cs atom in a single optical tweezer", New Journal of Physics **23**, 065002 (2021).

[65]   C. M. Holland, Y. Lu, and L. W. Cheuk, "On-demand entanglement of molecules in a reconfigurable optical tweezer array", Science **382**, 1143–1147 (2023).

[66]   A. W. Young, W. J. Eckner, N. Schine, A. M. Childs, and A. M. Kaufman, "Tweezer-programmable 2D quantum walks in a Hubbard-regime lattice", Science **377**, 885–889 (2022).

[67]   P. Solano, J. A. Grover, J. E. Hoffman, S. Ravets, F. K. Fatemi, L. A. Orozco, and S. L. Rolston, "Chapter Seven - Optical Nanofibers: A New Platform for Quantum Optics", in , Vol. 66, edited by E. Arimondo, C. C. Lin, and S. F. Yelin, Advances In Atomic, Molecular, and Optical Physics (Academic Press, 2017), pp. 439–505.

[68]   D. E. Chang, V. Vuletić, and M. D. Lukin, "Quantum nonlinear optics — photon by photon", Nature Photonics **8**, 685–694 (2014).

[69]   F. Mivehvar, F. Piazza, T. Donner, and H. Ritsch, "Cavity QED with quantum gases: new paradigms in many-body physics", Advances in Physics **70**, 1–153 (2021).

[70]   J. M. Raimond, M. Brune, and S. Haroche, "Manipulating quantum entanglement with atoms and photons in a cavity", Reviews of Modern Physics **73**, 565–582 (2001).

[71]   U. Fano, "Effects of Configuration Interaction on Intensities and Phase Shifts", Physical Review **124**, 1866–1878 (1961).

[72]   H. Feshbach, "A unified theory of nuclear reactions. II", Annals of Physics **19**, 287–313 (1962).

[73]   C. Chin, R. Grimm, P. Julienne, and E. Tiesinga, "Feshbach resonances in ultracold gases", Reviews of Modern Physics **82**, 1225–1286 (2010).

[74] J. Dalibard, "Collisional dynamics of ultra-cold atomic gases", Proceedings of the International School of Physics *Enrico Fermi* **140**, 321–349 (1999).

[75] J. R. Taylor, *Scattering Theory: The Quantum Theory of Nonrelativistic Collisions*, Dover Books on Engineering (Dover Publications, 2012).

[76] S. Inouye, M. R. Andrews, J. Stenger, H.-J. Miesner, D. M. Stamper-Kurn, and W. Ketterle, "Observation of Feshbach resonances in a Bose–Einstein condensate", Nature **392**, 151–154 (1998).

[77] Q. Chen, Z. Wang, R. Boyack, S. Yang, and K. Levin, "When superconductivity crosses over: From BCS to BEC", Reviews of Modern Physics **96**, 025002 (2024).

[78] L. Su, A. Douglas, M. Szurek, R. Groth, S. F. Ozturk, A. Krahn, A. H. Hébert, G. A. Phelps, S. Ebadi, S. Dickerson, F. Ferlaino, O. Marković, and M. Greiner, "Dipolar quantum solids emerging in a Hubbard quantum simulator", Nature **622**, 724–729 (2023).

[79] J. R. Rydberg, "XXXIV. On the structure of the line-spectra of the chemical elements", The London, Edinburgh, and Dublin Philosophical Magazine and Journal of Science **29**, 331–337 (1890).

[80] T. F. Gallagher, "Rydberg atoms", Reports on Progress in Physics **51**, 143–188 (1988).

[81] M. J. Seaton, "Quantum defect theory", Reports on Progress in Physics **46**, 167–257 (1983).

[82] S. J. Hollerith, "A microscopically and vibrationally resolved study of Rydberg macrodimers", PhD Thesis (Apr. 2022).

[83] C. J. Foot, *Atomic Physics*, en, Oxford Master Series in Physics (Oxford University Press, London, England, Nov. 2004).

[84] S. Weber, C. Tresp, H. Menke, A. Urvoy, O. Firstenberg, H. P. Büchler, and S. Hofferberth, "Calculation of Rydberg interaction potentials", Journal of Physics B: Atomic, Molecular and Optical Physics **50**, 133001 (2017).

[85] S. de Léséleuc, V. Lienhard, P. Scholl, D. Barredo, S. Weber, N. Lang, H. P. Büchler, T. Lahaye, and A. Browaeys, "Observation of a symmetry-protected topological phase of interacting bosons with Rydberg atoms", Science **365**, 775–780 (2019).

[86] S. Geier, N. Thaicharoen, C. Hainaut, T. Franz, A. Salzinger, A. Tebben, D. Grimshandl, G. Zürn, and M. Weidemüller, "Floquet Hamiltonian engineering of an isolated many-body spin system", Science **374**, 1149–1152 (2021).

[87] P. Scholl, H. J. Williams, G. Bornet, F. Wallner, D. Barredo, L. Henriet, A. Signoles, C. Hainaut, T. Franz, S. Geier, A. Tebben, A. Salzinger, G. Zürn, T. Lahaye, M. Weidemüller, and A. Browaeys, "Microwave Engineering of Programmable XXZ Hamiltonians in Arrays of Rydberg Atoms", PRX Quantum **3** (2022).

[88] T. Franz, S. Geier, C. Hainaut, N. Thaicharoen, A. Braemer, M. Gärttner, G. Zürn, and M. Weidemüller, "Observation of universal relaxation dynamics in disordered quantum spin systems", arXiv **2209.08080** (2022).

[89] C. Chen, G. Bornet, M. Bintz, G. Emperauger, L. Leclerc, V. S. Liu, P. Scholl, D. Barredo, J. Hauschild, S. Chatterjee, M. Schuler, A. M. Läuchli, M. P. Zaletel, T. Lahaye, N. Y. Yao, and A. Browaeys, "Continuous symmetry breaking in a two-dimensional Rydberg array", Nature (2023).

[90] G. Bornet, G. Emperauger, C. Chen, F. Machado, S. Chern, L. Leclerc, B. Gély, Y. T. Chew, D. Barredo, T. Lahaye, N. Y. Yao, and A. Browaeys, "Enhancing a Many-Body Dipolar Rydberg Tweezer Array with Arbitrary Local Controls", Physical Review Letters **132**, 263601 (2024).

[91] A. Keesling, A. Omran, H. Levine, H. Bernien, H. Pichler, S. Choi, R. Samajdar, S. Schwartz, P. Silvi, S. Sachdev, P. Zoller, M. Endres, M. Greiner, V. Vuletić, and M. D. Lukin, "Quantum Kibble–Zurek mechanism and critical dynamics on a programmable Rydberg simulator", Nature **568**, 207–211 (2019).

[92] S. Ebadi, T. T. Wang, H. Levine, A. Keesling, G. Semeghini, A. Omran, D. Bluvstein, R. Samajdar, H. Pichler, W. W. Ho, S. Choi, S. Sachdev, M. Greiner, V. Vuletić, and M. D. Lukin, "Quantum phases of matter on a 256-atom programmable quantum simulator", Nature **595**, 227–232 (2021).

[93] E. Urban, T. A. Johnson, T. Henage, L. Isenhower, D. D. Yavuz, T. G. Walker, and M. Saffman, "Observation of Rydberg blockade between two atoms", Nature Physics **5**, 110–114 (2009).

[94] P. Scholl, M. Schuler, H. J. Williams, A. A. Eberharter, D. Barredo, K.-N. Schymik, V. Lienhard, L.-P. Henry, T. C. Lang, T. Lahaye, A. M. Läuchli, and A. Browaeys, "Quantum simulation of 2D antiferromagnets with hundreds of Rydberg atoms", Nature **595**, 233–238 (2021).

[95] L.-M. Steinert, P. Osterholz, R. Eberhard, L. Festa, N. Lorenz, Z. Chen, A. Trautmann, and C. Gross, "Spatially Tunable Spin Interactions in Neutral Atom Arrays", Physical Review Letters **130**, 243001 (2023).

[96] H. Bernien, S. Schwartz, A. Keesling, H. Levine, A. Omran, H. Pichler, S. Choi, A. S. Zibrov, M. Endres, M. Greiner, V. Vuletić, and M. D. Lukin, "Probing many-body dynamics on a 51-atom quantum simulator", Nature **551**, 579–584 (2017).

[97] H. Levine, A. Keesling, G. Semeghini, A. Omran, T. T. Wang, S. Ebadi, H. Bernien, M. Greiner, V. Vuletić, H. Pichler, and M. D. Lukin, "Parallel Implementation of High-Fidelity Multiqubit Gates with Neutral Atoms", Physical Review Letters **123**, 170503 (2019).

[98] I. S. Madjarov, J. P. Covey, A. L. Shaw, J. Choi, A. Kale, A. Cooper, H. Pichler, V. Schkolnik, J. R. Williams, and M. Endres, "High-fidelity entanglement and detection of alkaline-earth Rydberg atoms", Nature Physics **16**, 857–861 (2020).

[99] T. M. Graham, Y. Song, J. Scott, C. Poole, L. Phuttitarn, K. Jooya, P. Eichler, X. Jiang, A. Marra, B. Grinkemeyer, M. Kwon, M. Ebert, J. Cherek, M. T. Lichtman, M. Gillette, J. Gilbert, D. Bowman, T. Ballance, C. Campbell, E. D. Dahl, O. Crawford, N. S. Blunt, B. Rogers, T. Noel, and M. Saffman, "Multi-qubit entanglement and algorithms on a neutral-atom quantum computer", Nature **604**, 457–462 (2022).

[100] S. Ma, G. Liu, P. Peng, B. Zhang, S. Jandura, J. Claes, A. P. Burgers, G. Pupillo, S. Puri, and J. D. Thompson, "High-fidelity gates and mid-circuit erasure conversion in an atomic qubit", Nature **622**, 279–284 (2023).

[101] M. L. Wall, K. R. A. Hazzard, and A. M. Rey, "Quantum Magnetism with Ultracold Molecules", in *From atomic to mesoscale* (WORLD SCIENTIFIC, June 2015), pp. 3–37.

[102] B. Gadway and B. Yan, "Strongly interacting ultracold polar molecules", Journal of Physics B: Atomic, Molecular and Optical Physics **49**, 152002 (2016).

[103] J. L. Bohn, A. M. Rey, and J. Ye, "Cold molecules: progress in quantum engineering of chemistry and quantum matter", Science **357**, 1002–1010 (2017).

[104] A. M. Kaufman and K.-K. Ni, "Quantum science with optical tweezer arrays of ultracold atoms and molecules", Nature Physics **17**, 1324–1333 (2021).

[105] J. L. Bohn, "Electric dipoles at ultralow temperature", arXiv **0901.0276** (2018).

[106] L. Christakis, J. S. Rosenberg, R. Raj, S. Chi, A. Morningstar, D. A. Huse, Z. Z. Yan, and W. S. Bakr, "Probing site-resolved correlations in a spin system of ultracold molecules", Nature **614**, 64–69 (2023).

[107] P. D. Gregory, J. A. Blackmore, S. L. Bromley, J. M. Hutson, and S. L. Cornish, "Robust storage qubits in ultracold polar molecules", Nature Physics **17**, 1149–1153 (2021).

[108] S. L. Cornish, M. R. Tarbutt, and K. R. A. Hazzard, "Quantum Computation and Quantum Simulation with Ultracold Molecules", arXiv **2401.05086** (2024).

[109] B. Sundar, B. Gadway, and K. R. A. Hazzard, "Synthetic dimensions in ultracold polar molecules", Scientific Reports **8** (2018).

[110] N. W. Ashcroft and N. D. Mermin, *Solid state physics* (Holt, Rinehart and Winston, New York, NY, 1976).

[111] M. Schreiber, S. S. Hodgman, P. Bordia, H. P. Lüschen, M. H. Fischer, R. Vosk, E. Altman, U. Schneider, and I. Bloch, "Observation of many-body localization of interacting fermions in a quasirandom optical lattice", Science **349**, 842–845 (2015).

[112] A. Auerbach, *Interacting Electrons and Quantum Magnetism* (Springer New York, 1994).

[113] A. Ashkin and J. M. Dziedzic, "Optical Trapping and Manipulation of Viruses and Bacteria", Science **235**, 1517–1520 (1987).

[114] NobelPrize.org, "Arthur Ashkin – Facts – 2018", Nobel Prize Outreach AB 2024, Wed. 10 Apr 2024.

[115] F. Gyger, M. Ammenwerth, R. Tao, H. Timme, S. Snigirev, I. Bloch, and J. Zeiher, "Continuous operation of large-scale atom arrays in optical lattices", arXiv **2402.04994** (2024).

[116] H. J. Manetsch, G. Nomura, E. Bataille, K. H. Leung, X. Lv, and M. Endres, "A tweezer array with 6100 highly coherent atomic qubits", arXiv **2403.12021** (2024).

[117] L. R. B. Picard, G. E. Patenotte, A. J. Park, S. F. Gebretsadkan, and K.-K. Ni, "Site-selective preparation and multi-state readout of molecules in optical tweezers", arXiv **2401.13659** (2024).

[118] M. F. Andersen, "Optical tweezers for a bottom-up assembly of few-atom systems", Advances in Physics: X **7** (2022).

[119] N. Schlosser, G. Reymond, I. Protsenko, and P. Grangier, "Sub-poissonian loading of single atoms in a microscopic dipole trap", Nature **411**, 1024–1027 (2001).

[120] T. Grünzweig, A. Hilliard, M. McGovern, and M. F. Andersen, "Near-deterministic preparation of a single atom in an optical microtrap", Nature Physics **6**, 951–954 (2010).

[121] M. Endres, H. Bernien, A. Keesling, H. Levine, E. R. Anschuetz, A. Krajenbrink, C. Senko, V. Vuletic, M. Greiner, and M. D. Lukin, "Atom-by-atom assembly of defect-free one-dimensional cold atom arrays", Science **354**, 1024–1027 (2016).

[122] D. Bluvstein, H. Levine, G. Semeghini, T. T. Wang, S. Ebadi, M. Kalinowski, A. Keesling, N. Maskara, H. Pichler, M. Greiner, V. Vuletić, and M. D. Lukin, "A quantum processor based on coherent transport of entangled atom arrays", Nature **604**, 451–456 (2022).

[123] D. Barredo, V. Lienhard, S. de Léséleuc, T. Lahaye, and A. Browaeys, "Synthetic three-dimensional atomic structures assembled atom by atom", Nature **561**, 79–82 (2018).

[124] A. M. Kaufman, B. J. Lester, C. M. Reynolds, M. L. Wall, M. Foss-Feig, K. R. A. Hazzard, A. M. Rey, and C. A. Regal, "Two-particle quantum interference in tunnel-coupled optical tweezers", Science **345**, 306–309 (2014).

[125] A. Guttridge, D. K. Ruttley, A. C. Baldock, R. González-Férez, H. R. Sadeghpour, C. S. Adams, and S. L. Cornish, "Observation of Rydberg Blockade Due to the Charge-Dipole Interaction between an Atom and a Polar Molecule", Physical Review Letters **131**, 013401 (2023).

[126] L. Onsager, "Crystal Statistics. I. A Two-Dimensional Model with an Order-Disorder Transition", Physical Review **65**, 117–149 (1944).

[127] H. A. Kramers and G. H. Wannier, "Statistics of the Two-Dimensional Ferromagnet. Part I", Physical Review **60**, 252–262 (1941).

[128] F. Wegner, "Fifty years of Ising lattice gauge theories", MCQST workshop on *Discrete lattice gauge theories - emergence and quantum simulations*, May 2022.

[129] L. D. Landau and E. M. Lifshitz, *Statistical physics: pt. 1*, en, 3rd ed., Course of Theoretical Physics (Butterworth-Heinemann, Oxford, England, Jan. 1980).

[130] I. S. Tupitsyn, A. Kitaev, N. V. Prokof'ev, and P. C. E. Stamp, "Topological multicritical point in the phase diagram of the toric code model and three-dimensional lattice gauge Higgs model", Physical Review B **82** (2010).

[131] K. G. Wilson, "The Origins of Lattice Gauge Theory", Nuclear Physics B - Proceedings Supplements **140**, 3–19 (2005).

[132] J. Kogut and L. Susskind, "Hamiltonian formulation of Wilson's lattice gauge theories", Physical Review D **11**, 395–408 (1975).

[133] E. Fradkin and L. Susskind, "Order and disorder in gauge systems and magnets", Physical Review D **17**, 2637–2658 (1978).

[134] D. C. Tsui, H. L. Stormer, and A. C. Gossard, "Two-Dimensional Magnetotransport in the Extreme Quantum Limit", Physical Review Letters **48**, 1559–1562 (1982).

[135] J. G. Bednorz and K. A. Müller, "Possible highTc superconductivity in the Ba-La-Cu-O system", Zeitschrift für Physik B Condensed Matter **64**, 189–193 (1986).

[136] A. A. Abrikosov, "Electron scattering on magnetic impurities in metals and anomalous resistivity effects", Physics Physique Fizika **2**, 5–20 (1965).

[137] P. Coleman, "New approach to the mixed-valence problem", Physical Review B **29**, 3035–3044 (1984).

[138] D. S. Rokhsar and S. A. Kivelson, "Superconductivity and the Quantum Hard-Core Dimer Gas", Physical Review Letters **61**, 2376–2379 (1988).

[139] L. Homeier, C. Schweizer, M. Aidelsburger, A. Fedorov, and F. Grusdt, "$\mathbb{Z}_2$ Lattice gauge theories and Kitaev's toric code: A scheme for analog quantum simulation", Physical Review B **104** (2021).

[140] Y. Chai, A. Crippa, K. Jansen, S. Kühn, V. R. Pascuzzi, F. Tacchino, and I. Tavernelli, "Fermionic wave packet scattering: a quantum computing approach", arXiv **2312.02272** (2023).

[141] R. C. Farrell, M. Illa, A. N. Ciavarella, and M. J. Savage, "Quantum simulations of hadron dynamics in the Schwinger model using 112 qubits", Physical Review D **109**, 114510 (2024).

[142] G.-X. Su, J. Osborne, and J. C. Halimeh, "A Cold-Atom Particle Collider", arXiv **2401.05489** (2024).

[143] Z. Davoudi, C.-C. Hsieh, and S. V. Kadam, "Scattering wave packets of hadrons in gauge theories: Preparation on a quantum computer", arXiv **2402.00840** (2024).

[144] E. R. Bennewitz, B. Ware, A. Schuckert, A. Lerose, F. M. Surace, R. Belyansky, W. Morong, D. Luo, A. De, K. S. Collins, O. Katz, C. Monroe, Z. Davoudi, and A. V. Gorshkov, "Simulating Meson Scattering on Spin Quantum Simulators", arXiv **2403.07061** (2024).

[145] S. Sachdev, *Quantum phase transitions*, 2nd ed. (Cambridge University Press, 2011).

[146] S. Elitzur, "Impossibility of spontaneously breaking local symmetries", Physical Review D **12**, 3978–3982 (1975).

[147] S. Chandrasekharan and U.-J. Wiese, "Quantum link models: a discrete approach to gauge theories", Nuclear Physics B **492**, 455–471 (1997).

[148] U.-J. Wiese, "Ultracold quantum gases and lattice systems: quantum simulation of lattice gauge theories", Annalen der Physik **525**, 777–796 (2013).

[149] D. Banerjee, M. Bögli, M. Dalmonte, E. Rico, P. Stebler, U.-J. Wiese, and P. Zoller, "Atomic Quantum Simulation of U(N) and SU(N) Non-Abelian Lattice Gauge Theories", Physical Review Letters **110**, 125303 (2013).

[150] A. Jaffe and E. Witten, "Quantum Yang-Mills Theory", The Millennium Prize Problems **1**, 129 (2006).

[151] D. Horn, "Finite matrix models with continuous local gauge invariance", Physics Letters B **100**, 149–151 (1981).

[152] R. Brower, S. Chandrasekharan, and U.-J. Wiese, "QCD as a quantum link model", Physical Review D **60**, 094502 (1999).

[153] D. Banerjee, F.-J. Jiang, T. Z. Olesen, P. Orland, and U.-J. Wiese, "From the SU(2) quantum link model on the honeycomb lattice to the quantum dimer model on the kagome lattice: Phase transition and fractionalized flux strings", Physical Review B **97**, 205108 (2018).

[154] C. Schweizer, F. Grusdt, M. Berngruber, L. Barbiero, E. Demler, N. Goldman, I. Bloch, and M. Aidelsburger, "Floquet approach to $\mathbb{Z}_2$ lattice gauge theories with ultracold atoms in optical lattices", Nat. Phys. (2019).

[155] E. A. Martinez, C. A. Muschik, P. Schindler, D. Nigg, A. Erhard, M. Heyl, P. Hauke, M. Dalmonte, T. Monz, P. Zoller, and R. Blatt, "Real-time dynamics of lattice gauge theories with a few-qubit quantum computer", Nature **534**, 516–519 (2016).

[156] F. M. Surace, P. P. Mazza, G. Giudici, A. Lerose, A. Gambassi, and M. Dalmonte, "Lattice Gauge Theories and String Dynamics in Rydberg Atom Quantum Simulators", Physical Review X **10**, 021041 (2020).

[157] N. H. Nguyen, M. C. Tran, Y. Zhu, A. M. Green, C. H. Alderete, Z. Davoudi, and N. M. Linke, "Digital Quantum Simulation of the Schwinger Model and Symmetry Protection with Trapped Ions", PRX Quantum **3**, 020324 (2022).

[158] M. Meth, J. F. Haase, J. Zhang, C. Edmunds, L. Postler, A. Steiner, A. J. Jena, L. Dellantonio, R. Blatt, P. Zoller, T. Monz, P. Schindler, C. Muschik, and M. Ringbauer, "Simulating 2D lattice gauge theories on a qudit quantum computer", arXiv **2310.12110** (2023).

[159] Z.-Y. Zhou, G.-X. Su, J. C. Halimeh, R. Ott, H. Sun, P. Hauke, B. Yang, Z.-S. Yuan, J. Berges, and J.-W. Pan, "Thermalization dynamics of a gauge theory on a quantum simulator", Science **377**, 311–314 (2022).

[160] Z. Davoudi, M. Hafezi, C. Monroe, G. Pagano, A. Seif, and A. Shaw, "Towards analog quantum simulations of lattice gauge theories with trapped ions", Physical Review Research **2**, 023015 (2020).

[161] D. González-Cuadra, T. V. Zache, J. Carrasco, B. Kraus, and P. Zoller, "Hardware Efficient Quantum Simulation of Non-Abelian Gauge Theories with Qudits on Rydberg Platforms", Physical Review Letters **129**, 160501 (2022).

[162] L. Barbiero, C. Schweizer, M. Aidelsburger, E. Demler, N. Goldman, and F. Grusdt, "Coupling ultracold matter to dynamical gauge fields in optical lattices: From flux attachment to $\mathbb{Z}_2$ lattice gauge theories", Science Advances **5** (2019).

[163] E. Zohar and J. I. Cirac, "Removing staggered fermionic matter in $U(N)$ and $SU(N)$ lattice gauge theories", Physical Review D **99**, 114511 (2019).

[164] J. C. Halimeh and P. Hauke, "Reliability of Lattice Gauge Theories", Physical Review Letters **125** (2020).

[165] P. Facchi and S. Pascazio, "Quantum Zeno Subspaces", Physical Review Letters **89** (2002).

[166] K. Stannigel, P. Hauke, D. Marcos, M. Hafezi, S. Diehl, M. Dalmonte, and P. Zoller, "Constrained Dynamics via the Zeno Effect in Quantum Simulation: Implementing Non-Abelian Lattice Gauge Theories with Cold Atoms", Physical Review Letters **112**, 120406 (2014).

[167] J. Carrasquilla, Z. Hao, and R. G. Melko, "A two-dimensional spin liquid in quantum kagome ice", Nature Communications **6** (2015).

[168] J. R. Schrieffer and P. A. Wolff, "Relation between the Anderson and Kondo Hamiltonians", Physical Review **149**, 491–492 (1966).

[169] J. C. Halimeh, L. Barbiero, P. Hauke, F. Grusdt, and A. Bohrdt, "Robust quantum many-body scars in lattice gauge theories", Quantum **7**, 1004 (2023).

[170] H. Labuhn, D. Barredo, S. Ravets, S. de Léséleuc, T. Macrì, T. Lahaye, and A. Browaeys, "Tunable two-dimensional arrays of single Rydberg atoms for realizing quantum Ising models", Nature **534**, 667–670 (2016).

[171] M. Hermele, M. P. A. Fisher, and L. Balents, "Pyrochlore photons: The U(1) spin liquid in a S=1/2 three-dimensional frustrated magnet", Physical Review B **69** (2004).

[172] A. W. Glaetzle, M. Dalmonte, R. Nath, I. Rousochatzakis, R. Moessner, and P. Zoller, "Quantum Spin-Ice and Dimer Models with Rydberg Atoms", Physical Review X **4** (2014).

[173] R. Samajdar, D. G. Joshi, Y. Teng, and S. Sachdev, "Emergent $\mathbb{Z}_2$ Gauge Theories and Topological Excitations in Rydberg Atom Arrays", Physical Review Letters **130**, 043601 (2023).

[174] K. Singh, S. Anand, A. Pocklington, J. T. Kemp, and H. Bernien, "Dual-Element, Two-Dimensional Atom Array with Continuous-Mode Operation", Physical Review X **12**, 011040 (2022).

[175] S. Anand, C. E. Bradley, R. White, V. Ramesh, K. Singh, and H. Bernien, "A dual-species Rydberg array", arXiv **2401.10325** (2024).

[176] P. M. Ireland, D. M. Walker, and J. D. Pritchard, "Interspecies Förster resonances for Rb-Cs Rydberg d -states for enhanced multi-qubit gate fidelities", Physical Review Research **6**, 013293 (2024).

[177] A. Chandran, F. J. Burnell, V. Khemani, and S. L. Sondhi, "Kibble–Zurek scaling and string-net coarsening in topologically ordered systems", Journal of Physics: Condensed Matter **25**, 404214 (2013).

[178] K. Bernardet, G. G. Batrouni, J.-L. Meunier, G. Schmid, M. Troyer, and A. Dorneich, "Analytical and numerical study of hardcore bosons in two dimensions", Physical Review B **65** (2002).

[179] R. G. Melko, A. W. Sandvik, and D. J. Scalapino, "Two-dimensional quantum XY model with ring exchange and external field", Physical Review B **69** (2004).

[180] R. Sedgewick, D. Scalapino, and R. Sugar, "Fractionalized phase in an XY–Z2 gauge model", Physical Review B **65** (2002).

[181] D. Podolsky and E. Demler, "Properties and detection of spin nematic order in strongly correlated electron systems", New Journal of Physics **7**, 59–59 (2005).

[182] S. Trebst, P. Werner, M. Troyer, K. Shtengel, and C. Nayak, "Breakdown of a Topological Phase: Quantum Phase Transition in a Loop Gas Model with Tension", Physical Review Letters **98** (2007).

[183] R. Moessner and K. S. Raman, "Quantum Dimer Models", in *Introduction to frustrated magnetism*, edited by C. Lacroix, P. Mendels, and F. Mila (Springer Berlin Heidelberg, Sept. 2010), pp. 437–479.

[184] R. Samajdar, W. W. Ho, H. Pichler, M. D. Lukin, and S. Sachdev, "Quantum phases of Rydberg atoms on a kagome lattice", Proceedings of the National Academy of Sciences **118**, e2015785118 (2021).

[185] G. Giudici, M. D. Lukin, and H. Pichler, "Dynamical Preparation of Quantum Spin Liquids in Rydberg Atom Arrays", Physical Review Letters **129**, 090401 (2022).

[186] R. Moessner, S. L. Sondhi, and P. Chandra, "Phase diagram of the hexagonal lattice quantum dimer model", Physical Review B **64** (2001).

[187] Z. Zeng, G. Giudici, and H. Pichler, "Quantum dimer models with Rydberg gadgets", arXiv **2402.10651** (2024).

[188] R. Tao, M. Ammenwerth, F. Gyger, I. Bloch, and J. Zeiher, "High-Fidelity Detection of Large-Scale Atom Arrays in an Optical Lattice", Physical Review Letters **133**, 013401 (2024).

[189] A. Pizzi, A. Nunnenkamp, and J. Knolle, "Classical Prethermal Phases of Matter", Physical Review Letters **127**, 140602 (2021).

[190] B. Ye, F. Machado, and N. Y. Yao, "Floquet Phases of Matter via Classical Prethermalization", Physical Review Letters **127**, 140603 (2021).

[191] M. Bukov, L. D'Alessio, and A. Polkovnikov, "Universal high-frequency behavior of periodically driven systems: from dynamical stabilization to Floquet engineering", Advances in Physics **64**, 139–226 (2015).

[192] O. Howell, P. Weinberg, D. Sels, A. Polkovnikov, and M. Bukov, "Asymptotic Prethermalization in Periodically Driven Classical Spin Chains", Physical Review Letters **122**, 010602 (2019).

[193] J. Koepsell, S. Hirthe, D. Bourgund, P. Sompet, J. Vijayan, G. Salomon, C. Gross, and I. Bloch, "Robust Bilayer Charge Pumping for Spin- and Density-Resolved Quantum Gas Microscopy", Physical Review Letters **125**, 010403 (2020).

[194] A. Impertro, S. Karch, J. F. Wienand, S. Huh, C. Schweizer, I. Bloch, and M. Aidelsburger, "Local readout and control of current and kinetic energy operators in optical lattices", arXiv **2312.13268** (2023).

[195] J. Schwinger, "On Gauge Invariance and Vacuum Polarization", Physical Review **82**, 664–679 (1951).

[196] A. L. Shaw, Z. Chen, J. Choi, D. K. Mark, P. Scholl, R. Finkelstein, A. Elben, S. Choi, and M. Endres, "Benchmarking highly entangled states on a 60-atom analogue quantum simulator", Nature **628**, 71–77 (2024).

[197] M. Kebrič, L. Barbiero, C. Reinmoser, U. Schollwöck, and F. Grusdt, "Confinement and Mott Transitions of Dynamical Charges in One-Dimensional Lattice Gauge Theories", Physical Review Letters **127** (2021).

[198] D. A. Abanin, E. Altman, I. Bloch, and M. Serbyn, "Colloquium : many-body localization, thermalization, and entanglement", Reviews of Modern Physics **91**, 021001 (2019).

[199] N. Mueller, T. V. Zache, and R. Ott, "Thermalization of Gauge Theories from their Entanglement Spectrum", Physical Review Letters **129**, 011601 (2022).

[200] A. Smith, J. Knolle, D. Kovrizhin, and R. Moessner, "Disorder-Free Localization", Physical Review Letters **118** (2017).

[201] A. Smith, J. Knolle, R. Moessner, and D. L. Kovrizhin, "Dynamical localization in $\mathbb{Z}_2$ lattice gauge theories", Phys. Rev. B **97**, 245137 (2018).

[202] P. Karpov, R. Verdel, Y.-P. Huang, M. Schmitt, and M. Heyl, "Disorder-Free Localization in an Interacting 2D Lattice Gauge Theory", Physical Review Letters **126** (2021).

[203] N. Chakraborty, M. Heyl, P. Karpov, and R. Moessner, "Disorder-free localization transition in a two-dimensional lattice gauge theory", Phys. Rev. B **106**, L060308 (2022).

[204] J. C. Halimeh, H. Zhao, P. Hauke, and J. Knolle, "Stabilizing Disorder-Free Localization", arXiv **2111.02427** (2021).

[205] K. Fredenhagen and M. Marcu, "Confinement criterion for QCD with dynamical quarks", Physical Review Letters **56**, 223–224 (1986).

[206] K. Gregor, D. A. Huse, R. Moessner, and S. L. Sondhi, "Diagnosing deconfinement and topological order", New Journal of Physics **13**, 025009 (2011).

[207] W.-T. Xu, F. Pollmann, and M. Knap, "Critical behavior of the Fredenhagen-Marcu order parameter at topological phase transitions", arXiv **2402.00127** (2024).

[208] A. M. Polyakov, "Compact gauge fields and the infrared catastrophe", Physics Letters B **59**, 82–84 (1975).

[209] M. Kebrič, J. C. Halimeh, U. Schollwöck, and F. Grusdt, "Confinement in $(1+1)$-dimensional $\mathbb{Z}_2$ lattice gauge theories at finite temperature", Physical Review B **109**, 245110 (2024).

[210] L. Hahn, A. Bohrdt, and F. Grusdt, "Dynamical signatures of thermal spin-charge deconfinement in the doped Ising model", Physical Review B **105**, l241113 (2022).

[211] C. Muschik, M. Heyl, E. Martinez, T. Monz, P. Schindler, B. Vogell, M. Dalmonte, P. Hauke, R. Blatt, and P. Zoller, "U(1) Wilson lattice gauge theories in digital quantum simulators", New Journal of Physics **19**, 103020 (2017).

[212] N. Klco, E. F. Dumitrescu, A. J. McCaskey, T. D. Morris, R. C. Pooser, M. Sanz, E. Solano, P. Lougovski, and M. J. Savage, "Quantum-classical computation of Schwinger model dynamics using quantum computers", Physical Review A **98**, 032331 (2018).

[213] C. Kokail, C. Maier, R. van Bijnen, T. Brydges, M. K. Joshi, P. Jurcevic, C. A. Muschik, P. Silvi, R. Blatt, C. F. Roos, and P. Zoller, "Self-verifying variational quantum simulation of lattice models", Nature **569**, 355–360 (2019).

[214] F. Görg, K. Sandholzer, J. Minguzzi, R. Desbuquois, M. Messer, and T. Esslinger, "Realization of density-dependent Peierls phases to engineer quantized gauge fields coupled to ultracold matter", Nature Physics **15**, 1161–1167 (2019).

[215] A. Mil, T. V. Zache, A. Hegde, A. Xia, R. P. Bhatt, M. K. Oberthaler, P. Hauke, J. Berges, and F. Jendrzejewski, "A scalable realization of local U(1) gauge invariance in cold atomic mixtures", Science **367**, 1128–1130 (2020).

[216] N. Klco, M. J. Savage, and J. R. Stryker, "SU(2) non-Abelian gauge field theory in one dimension on digital quantum computers", Physical Review D **101**, 074512 (2020).

[217] Y. Y. Atas, J. Zhang, R. Lewis, A. Jahanpour, J. F. Haase, and C. A. Muschik, "SU(2) hadrons on a quantum computer via a variational approach", Nature Communications **12** (2021).

[218] Z. Wang, Z.-Y. Ge, Z. Xiang, X. Song, R.-Z. Huang, P. Song, X.-Y. Guo, L. Su, K. Xu, D. Zheng, and H. Fan, "Observation of emergent Z2 gauge invariance in a superconducting circuit", Physical Review Research **4**, l022060 (2022).

[219] H.-Y. Wang, W.-Y. Zhang, Z. Yao, Y. Liu, Z.-H. Zhu, Y.-G. Zheng, X.-K. Wang, H. Zhai, Z.-S. Yuan, and J.-W. Pan, "Interrelated Thermalization and Quantum Criticality in a Lattice Gauge Simulator", Physical Review Letters **131**, 050401 (2023).

[220] C. Charles, E. J. Gustafson, E. Hardt, F. Herren, N. Hogan, H. Lamm, S. Starecheski, R. S. Van de Water, and M. L. Wagman, "Simulating Z2 lattice gauge theory on a quantum computer", Physical Review E **109**, 015307 (2024).

[221] G. Calajò, G. Magnifico, C. Edmunds, M. Ringbauer, S. Montangero, and P. Silvi, "Digital quantum simulation of a (1+1)D SU(2) lattice gauge theory with ion qudits", arXiv **2402.07987** (2024).

[222] J. C. Halimeh, H. Lang, and P. Hauke, "Gauge protection in non-abelian lattice gauge theories", New Journal of Physics **24**, 033015 (2022).

[223] E. Mathew and I. Raychowdhury, "Protecting local and global symmetries in simulating $(1 + 1)$D non-Abelian gauge theories", Physical Review D **106**, 054510 (2022).

[224] V. Kasper, T. V. Zache, F. Jendrzejewski, M. Lewenstein, and E. Zohar, "Non-Abelian gauge invariance from dynamical decoupling", Physical Review D **107**, 014506 (2023).

[225] L. Tagliacozzo, A. Celi, P. Orland, M. W. Mitchell, and M. Lewenstein, "Simulation of non-Abelian gauge theories with optical lattices", Nature Communications **4** (2013).

[226] E. Zohar, J. I. Cirac, and B. Reznik, "Cold-Atom Quantum Simulator for SU(2) Yang-Mills Lattice Gauge Theory", Physical Review Letters **110**, 125304 (2013).

[227] H. Haber, "Useful relations among the generators in the defining and adjoint representations of SU(N)", SciPost Physics Lecture Notes (2021).

[228] B. Yan, S. A. Moses, B. Gadway, J. P. Covey, K. R. A. Hazzard, A. M. Rey, D. S. Jin, and J. Ye, "Observation of dipolar spin-exchange interactions with lattice-confined polar molecules", Nature **501**, 521–525 (2013).

[229] D. Luo, J. Shen, M. Highman, B. K. Clark, B. DeMarco, A. X. El-Khadra, and B. Gadway, "Framework for simulating gauge theories with dipolar spin systems", Physical Review A **102**, 032617 (2020).

[230] A. Schindewolf, R. Bause, X.-Y. Chen, M. Duda, T. Karman, I. Bloch, and X.-Y. Luo, "Evaporation of microwave-shielded polar molecules to quantum degeneracy", Nature **607**, 677–681 (2022).

[231] N. Bigagli, C. Warner, W. Yuan, S. Zhang, I. Stevenson, T. Karman, and S. Will, "Collisionally stable gas of bosonic dipolar ground-state molecules", Nature Physics **19**, 1579–1584 (2023).

[232] N. Bigagli, W. Yuan, S. Zhang, B. Bulatovic, T. Karman, I. Stevenson, and S. Will, "Observation of Bose–Einstein condensation of dipolar molecules", Nature (2024).

[233] J. Osborne, I. P. McCulloch, B. Yang, P. Hauke, and J. C. Halimeh, "Large-Scale $2+1$D U(1) Gauge Theory with Dynamical Matter in a Cold-Atom Quantum Simulator", arXiv **2211.01380** (2022).

[234] F. M. Surace, P. Fromholz, N. D. Oppong, M. Dalmonte, and M. Aidelsburger, "Ab Initio Derivation of Lattice-Gauge-Theory Dynamics for Cold Gases in Optical Lattices", PRX Quantum **4**, 020330 (2023).

[235] C. Hofrichter, L. Riegger, F. Scazza, M. Höfer, D. R. Fernandes, I. Bloch, and S. Fölling, "Direct Probing of the Mott Crossover in the SU(N) Fermi-Hubbard Model", Physical Review X **6**, 021030 (2016).

[236] S. Taie, E. Ibarra-García-Padilla, N. Nishizawa, Y. Takasu, Y. Kuno, H.-T. Wei, R. T. Scalettar, K. R. A. Hazzard, and Y. Takahashi, "Observation of antiferromagnetic correlations in an ultracold SU(N) Hubbard model", Nature Physics **18**, 1356–1361 (2022).

[237] T. Hartke, B. Oreg, N. Jia, and M. Zwierlein, "Quantum register of fermion pairs", Nature **601**, 537–541 (2022).

[238] J. Nemirovsky and Y. Sagi, "Fast universal two-qubit gate for neutral fermionic atoms in optical tweezers", Physical Review Research **3**, 013113 (2021).

[239] C. Nayak, S. H. Simon, A. Stern, M. Freedman, and S. Das Sarma, "Non-Abelian anyons and topological quantum computation", Reviews of Modern Physics **80**, 1083–1159 (2008).

[240] C. Proust and L. Taillefer, "The Remarkable Underlying Ground States of Cuprate Superconductors", Annual Review of Condensed Matter Physics **10**, 409–429 (2019).

[241] S. E. Barrett, D. J. Durand, C. H. Pennington, C. P. Slichter, T. A. Friedmann, J. P. Rice, and D. M. Ginsberg, "^{63}Cu Knight shifts in the superconducting state of $YBa_2Cu_3O_{7-\delta}$ (T_c=90 K)", Physical Review B **41**, 6283–6296 (1990).

[242]   P. L. Gammel, D. J. Bishop, G. J. Dolan, J. R. Kwo, C. A. Murray, L. F. Schneemeyer, and J. V. Waszczak, "Observation of hexagonally correlated flux quanta in yba2cu3o7", Physical Review Letters **59**, 2592–2595 (1987).

[243]   J. Bardeen, L. N. Cooper, and J. R. Schrieffer, "Theory of Superconductivity", Physical Review **108**, 1175–1204 (1957).

[244]   M. Hashimoto, I. M. Vishik, R.-H. He, T. P. Devereaux, and Z.-X. Shen, "Energy gaps in high-transition-temperature cuprate superconductors", Nature Physics **10**, 483–495 (2014).

[245]   D. J. Scalapino, "The case for $d_{x^2-y^2}$ pairing in the cuprate superconductors", Physics Reports **250**, 329–365 (1995).

[246]   A. Wietek, Y.-Y. He, S. R. White, A. Georges, and E. M. Stoudenmire, "Stripes, Antiferromagnetism, and the Pseudogap in the Doped Hubbard Model at Finite Temperature", Physical Review X **11**, 031007 (2021).

[247]   K. M. Shen, F. Ronning, D. H. Lu, F. Baumberger, N. J. C. Ingle, W. S. Lee, W. Meevasana, Y. Kohsaka, M. Azuma, M. Takano, H. Takagi, and Z.-X. Shen, "Nodal Quasiparticles and Antinodal Charge Ordering in $Ca_{2-x}Na_xCuO_2Cl_2$", Science **307**, 901–904 (2005).

[248]   K. Kurokawa, S. Isono, Y. Kohama, S. Kunisada, S. Sakai, R. Sekine, M. Okubo, M. D. Watson, T. K. Kim, C. Cacho, S. Shin, T. Tohyama, K. Tokiwa, and T. Kondo, "Unveiling phase diagram of the lightly doped high-Tc cuprate superconductors with disorder removed", Nature Communications **14** (2023).

[249]   N. Doiron-Leyraud, C. Proust, D. LeBoeuf, J. Levallois, J.-B. Bonnemaison, R. Liang, D. A. Bonn, W. N. Hardy, and L. Taillefer, "Quantum oscillations and the Fermi surface in an underdoped high-Tc superconductor", Nature **447**, 565–568 (2007).

[250]   S. Badoux, W. Tabis, F. Laliberté, G. Grissonnanche, B. Vignolle, D. Vignolles, J. Béard, D. A. Bonn, W. N. Hardy, R. Liang, N. Doiron-Leyraud, L. Taillefer, and C. Proust, "Change of carrier density at the pseudogap critical point of a cuprate superconductor", Nature **531**, 210–214 (2016).

[251]   P. W. Anderson, "Is There Glue in Cuprate Superconductors?", Science **316**, 1705–1707 (2007).

[252]   D. J. Scalapino, E. Loh, and J. E. Hirsch, "d-wave pairing near a spin-density-wave instability", Physical Review B **34**, 8190–8192 (1986).

[253]   F. J. Ohkawa, "Anisotropie Cooper Pairs in High-Tc Superconductors", Japanese Journal of Applied Physics **26**, L652 (1987).

[254]   P. Coleman, *Introduction to Many-Body Physics* (Cambridge University Press, 2015).

[255]   K. Miyake, S. Schmitt-Rink, and C. M. Varma, "Spin-fluctuation-mediated even-parity pairing in heavy-fermion superconductors", Physical Review B **34**, 6554–6556 (1986).

[256]   P. Monthoux, A. V. Balatsky, and D. Pines, "Toward a theory of high-temperature superconductivity in the antiferromagnetically correlated cuprate oxides", Physical Review Letters **67**, 3448–3451 (1991).

[257]   W. Metzner, M. Salmhofer, C. Honerkamp, V. Meden, and K. Schönhammer, "Functional renormalization group approach to correlated fermion systems", Reviews of Modern Physics **84**, 299–352 (2012).

[258] C. J. Halboth and W. Metzner, "d-Wave Superconductivity and Pomeranchuk Instability in the Two-Dimensional Hubbard Model", Physical Review Letters **85**, 5162–5165 (2000).

[259] S. M. O'Mahony, W. Ren, W. Chen, Y. X. Chong, X. Liu, H. Eisaki, S. Uchida, M. H. Hamidian, and J. C. S. Davis, "On the electron pairing mechanism of copper-oxide high temperature superconductivity", Proceedings of the National Academy of Sciences **119** (2022).

[260] J. W. Loram, K. A. Mirza, J. M. Wade, J. R. Cooper, and W. Y. Liang, "The electronic specific heat of cuprate superconductors", Physica C: Superconductivity **235-240**, 134–137 (1994).

[261] S. Sachdev, "Colloquium: order and quantum phase transitions in the cuprate superconductors", Reviews of Modern Physics **75**, 913–932 (2003).

[262] T. Senthil, S. Sachdev, and M. Vojta, "Fractionalized Fermi Liquids", Physical Review Letters **90**, 216403 (2003).

[263] M. Christos, Z.-X. Luo, H. Shackleton, Y.-H. Zhang, M. S. Scheurer, and S. Sachdev, "A model of d-wave superconductivity, antiferromagnetism, and charge order on the square lattice", Proceedings of the National Academy of Sciences **120** (2023).

[264] M. Punk, A. Allais, and S. Sachdev, "Quantum dimer model for the pseudogap metal", Proceedings of the National Academy of Sciences **112**, 9552–9557 (2015).

[265] Y. Fang, G. Grissonnanche, A. Legros, S. Verret, F. Laliberté, C. Collignon, A. Ataei, M. Dion, J. Zhou, D. Graf, M. J. Lawler, P. A. Goddard, L. Taillefer, and B. J. Ramshaw, "Fermi surface transformation at the pseudogap critical point of a cuprate superconductor", Nature Physics **18**, 558–564 (2022).

[266] Y. J. Uemura, L. P. Le, G. M. Luke, B. J. Sternlieb, W. D. Wu, J. H. Brewer, T. M. Riseman, C. L. Seaman, M. B. Maple, M. Ishikawa, D. G. Hinks, J. D. Jorgensen, G. Saito, and H. Yamochi, "Basic similarities among cuprate, bismuthate, organic, Chevrel-phase, and heavy-fermion superconductors shown by penetration-depth measurements", Physical Review Letters **66**, 2665–2668 (1991).

[267] V. J. Emery and S. A. Kivelson, "Importance of phase fluctuations in superconductors with small superfluid density", Nature **374**, 434–437 (1995).

[268] P. Nozières and S. Schmitt-Rink, "Bose condensation in an attractive fermion gas: from weak to strong coupling superconductivity", Journal of Low Temperature Physics **59**, 195–211 (1985).

[269] A. J. Leggett, "Diatomic molecules and cooper pairs", in Modern trends in the theory of condensed matter, edited by A. Pękalski and J. A. Przystawa (1980), pp. 13–27.

[270] M. Randeria, J.-M. Duan, and L.-Y. Shieh, "Bound states, Cooper pairing, and Bose condensation in two dimensions", Physical Review Letters **62**, 981–984 (1989).

[271] Y. J. Uemura, "Bose-Einstein to BCS crossover picture for high-T_c cuprates", Physica C: Superconductivity **282-287**, 194–197 (1997).

[272] M. Randeria and E. Taylor, "Crossover from Bardeen-Cooper-Schrieffer to Bose-Einstein Condensation and the Unitary Fermi Gas", Annual Review of Condensed Matter Physics **5**, 209–232 (2014).

[273] P. A. Lee and N. Nagaosa, "Gauge theory of the normal state of high-Tc superconductors", Physical Review B **46**, 5621–5639 (1992).

[274] J. Hubbard, "Electron correlations in narrow energy bands", Proceedings of the Royal Society of London. Series A. Mathematical and Physical Sciences **276**, 238–257 (1963).

[275] P. W. Anderson, "The Resonating Valence Bond State in La2CuO4 and Superconductivity", Science **235**, 1196–1198 (1987).

[276] P. W. Anderson, "Resonating valence bonds: A new kind of insulator?", Materials Research Bulletin **8**, 153–160 (1973).

[277] J. M. Luttinger, "An Exactly Soluble Model of a Many-Fermion System", Journal of Mathematical Physics **4**, 1154–1162 (1963).

[278] J. Vijayan, P. Sompet, G. Salomon, J. Koepsell, S. Hirthe, A. Bohrdt, F. Grusdt, I. Bloch, and C. Gross, "Time-resolved observation of spin-charge deconfinement in fermionic Hubbard chains", Science **367**, 186–189 (2020).

[279] A. S. Mishchenko, N. V. Prokof'ev, and B. V. Svistunov, "Single-hole spectral function and spin-charge separation in the t-J model", Physical Review B **64**, 033101 (2001).

[280] G. Dopf, J. Wagner, P. Dieterich, A. Muramatsu, and W. Hanke, "Direct comparison of angle-resolved photoemission and numerical simulations for high-Tc superconductors", Physical Review Letters **68**, 2082–2085 (1992).

[281] Y. M. Vilk, L. Chen, and A.-M. S. Tremblay, "Theory of spin and charge fluctuations in the Hubbard model", Physical Review B **49**, 13267–13270 (1994).

[282] A.-M. S. Tremblay, "Two-Particle-Self-Consistent Approach for the Hubbard Model", in *Strongly correlated systems* (Springer Berlin Heidelberg, Aug. 2011), pp. 409–453.

[283] M. Qin, C.-M. Chung, H. Shi, E. Vitali, C. Hubig, U. Schollwöck, S. R. White, and S. Zhang (Simons Collaboration on the Many-Electron Problem), "Absence of Superconductivity in the Pure Two-Dimensional Hubbard Model", Physical Review X **10** (2020).

[284] H. Xu, C.-M. Chung, M. Qin, U. Schollwöck, S. R. White, and S. Zhang, "Coexistence of superconductivity with partially filled stripes in the Hubbard model", Science **384** (2024).

[285] S. White, "Do the single band Hubbard models describe superconductivity in the cuprates?", Bulletin of the American Physical Society (2024).

[286] F. C. Zhang and T. M. Rice, "Effective Hamiltonian for the superconducting Cu oxides", Physical Review B **37**, 3759–3761 (1988).

[287] S. Jiang, D. J. Scalapino, and S. R. White, "Density matrix renormalization group based downfolding of the three-band Hubbard model: Importance of density-assisted hopping", Physical Review B **108**, l161111 (2023).

[288] R. A. Hart, P. M. Duarte, T.-L. Yang, X. Liu, T. Paiva, E. Khatami, R. T. Scalettar, N. Trivedi, D. A. Huse, and R. G. Hulet, "Observation of antiferromagnetic correlations in the Hubbard model with ultracold atoms", Nature **519**, 211–214 (2015).

[289] A. Mazurenko, C. S. Chiu, G. Ji, M. F. Parsons, M. Kanász-Nagy, R. Schmidt, F. Grusdt, E. Demler, D. Greif, and M. Greiner, "A cold-atom Fermi–Hubbard antiferromagnet", Nature **545**, 462–466 (2017).

[290] W. S. Bakr, J. I. Gillen, A. Peng, S. Fölling, and M. Greiner, "A quantum gas micro-scope for detecting single atoms in a Hubbard-regime optical lattice", Nature **462**, 74–77 (2009).

[291] J. F. Sherson, C. Weitenberg, M. Endres, M. Cheneau, I. Bloch, and S. Kuhr, "Single-atom-resolved fluorescence imaging of an atomic Mott insulator", Nature **467**, 68–72 (2010).

[292] M. Qin, T. Schäfer, S. Andergassen, P. Corboz, and E. Gull, "The Hubbard Model: A Computational Perspective", Annual Review of Condensed Matter Physics **13**, 275–302 (2022).

[293] Y. Nagaoka, "Ferromagnetism in a Narrow, Almost Half-Filled s Band", Phys. Rev. **147**, 392–405 (1966).

[294] M. Lebrat, M. Xu, L. H. Kendrick, A. Kale, Y. Gang, P. Seetharaman, I. Morera, E. Khatami, E. Demler, and M. Greiner, "Observation of Nagaoka polarons in a Fermi–Hubbard quantum simulator", Nature **629**, 317–322 (2024).

[295] M. L. Prichard, B. M. Spar, I. Morera, E. Demler, Z. Z. Yan, and W. S. Bakr, "Directly imaging spin polarons in a kinetically frustrated Hubbard system", Nature **629**, 323–328 (2024).

[296] E. H. Lieb, "Two theorems on the Hubbard model", Physical Review Letters **62**, 1201–1204 (1989).

[297] P. T. Brown, D. Mitra, E. Guardado-Sanchez, R. Nourafkan, A. Reymbaut, C.-D. Hébert, S. Bergeron, A.-M. S. Tremblay, J. Kokalj, D. A. Huse, P. Schauß, and W. S. Bakr, "Bad metallic transport in a cold atom Fermi-Hubbard system", Science **363**, 379–382 (2019).

[298] B. Ammon, M. Troyer, and H. Tsunetsugu, "Effect of the three-site hopping term on the t-J model", Physical Review B **52**, 629–636 (1995).

[299] Q. P. Li, B. E. C. Koltenbah, and R. Joynt, "Mixed s-wave and d-wave superconduc-tivity in high-Tc systems", Physical Review B **48**, 437–455 (1993).

[300] O. K. Andersen, A. I. Liechtenstein, O. Jepsen, and F. Paulsen, "LDA energy bands, low-energy hamiltonians, t', t'', $t_\perp(k)$, and $J_\perp$", Journal of Physics and Chemistry of Solids **56**, 1573–1591 (1995).

[301] M. Hirayama, Y. Yamaji, T. Misawa, and M. Imada, "*Ab initio* effective hamiltonians for cuprate superconductors", Physical Review B **98**, 134501 (2018).

[302] V. J. Emery, S. A. Kivelson, and H. Q. Lin, "Phase separation in the t-J model", Phys-ical Review Letters **64**, 475–478 (1990).

[303] F. Grusdt, A. Bohrdt, and E. Demler, "Microscopic spinon-chargon theory of mag-netic polarons in the $t-J$ model", Phys. Rev. B **99**, 224422 (2019).

[304] A. N. Carroll, H. Hirzler, C. Miller, D. Wellnitz, S. R. Muleady, J. Lin, K. P. Zamarski, R. R. W. Wang, J. L. Bohn, A. M. Rey, and J. Ye, "Observation of Generalized t-J Spin Dynamics with Tunable Dipolar Interactions", arXiv **2404.18916** (2024).

[305] L. Bulaevski, É. Nagaev, and D. Khomskii, "A New Type of Auto-localized State of a Conduction Electron in an Antiferromagnetic Semiconductor", Journal of Experi-mental and Theoretical Physics - J EXP THEOR PHYS **27** (1968).

[306] W. F. Brinkman and T. M. Rice, "Single-Particle Excitations in Magnetic Insulators", Physical Review B **2**, 1324–1338 (1970).

[307]   B. I. Shraiman and E. D. Siggia, "Two-particle excitations in antiferromagnetic insulators", Physical Review Letters **60**, 740–743 (1988).

[308]   L. Vidmar and J. Bonča, "Two Holes in the t-J Model Form a Bound State for Any Nonzero J/t", Journal of Superconductivity and Novel Magnetism **26**, 2641–2645 (2013).

[309]   J. Koepsell, D. Bourgund, P. Sompet, S. Hirthe, A. Bohrdt, Y. Wang, F. Grusdt, E. Demler, G. Salomon, C. Gross, and I. Bloch, "Microscopic evolution of doped Mott insulators from polaronic metal to Fermi liquid", Science **374**, 82–86 (2021).

[310]   A. Bohrdt, Y. Wang, J. Koepsell, M. Kánasz-Nagy, E. Demler, and F. Grusdt, "Dominant Fifth-Order Correlations in Doped Quantum Antiferromagnets", Physical Review Letters **126** (2021).

[311]   S. A. Trugman, "Interaction of holes in a Hubbard antiferromagnet and high-temperature superconductivity", Phys. Rev. B **37**, 1597–1603 (1988).

[312]   S. A. Trugman, "Spectral function of a hole in a Hubbard antiferromagnet", Physical Review B **41**, 892–895 (1990).

[313]   C. L. Kane, P. A. Lee, and N. Read, "Motion of a single hole in a quantum antiferromagnet", Phys. Rev. B **39**, 6880–6897 (1989).

[314]   S. Sachdev, "Hole motion in a quantum Néel state", Physical Review B **39**, 12232–12247 (1989).

[315]   G. Martinez and P. Horsch, "Spin polarons in the t-J model", Physical Review B **44**, 317–331 (1991).

[316]   A. Bohrdt, E. Demler, F. Pollmann, M. Knap, and F. Grusdt, "Parton theory of angle-resolved photoemission spectroscopy spectra in antiferromagnetic Mott insulators", Physical Review B **102** (2020).

[317]   Z. Liu and E. Manousakis, "Spectral function of a hole in t-J model", Physical Review B **44**, 2414–2417 (1991).

[318]   Z. Liu and E. Manousakis, "Dynamical properties of a hole in a Heisenberg antiferromagnet", Physical Review B **45**, 2425–2437 (1992).

[319]   P. Bermes, A. Bohrdt, and F. Grusdt, "Magnetic polarons beyond linear spin-wave theory: mesons dressed by magnons", Physical Review B **109**, 205104 (2024).

[320]   A. Bohrdt, E. Demler, and F. Grusdt, "Rotational Resonances and Regge-like Trajectories in Lightly Doped Antiferromagnets", Physical Review Letters **127** (2021).

[321]   H. Fröhlich, "Theory of the Superconducting State. I. The Ground State at the Absolute Zero of Temperature", Physical Review **79**, 845–856 (1950).

[322]   J. Bardeen and D. Pines, "Electron-Phonon Interaction in Metals", Physical Review **99**, 1140–1150 (1955).

[323]   P. Morel and P. W. Anderson, "Calculation of the Superconducting State Parameters with Retarded Electron-Phonon Interaction", Physical Review **125**, 1263–1271 (1962).

[324]   W. Kohn and J. M. Luttinger, "New Mechanism for Superconductivity", Physical Review Letters **15**, 524–526 (1965).

[325]   J. R. Schrieffer, X.-G. Wen, and S.-C. Zhang, "Spin-bag mechanism of high-temperature superconductivity", Physical Review Letters **60**, 944–947 (1988).

[326]   A. Kampf and J. R. Schrieffer, "Pseudogaps and the spin-bag approach to high-Tcsuperconductivity", Physical Review B **41**, 6399–6408 (1990).

[327] F. Kämpfer, M. Moser, and U.-J. Wiese, "Systematic low-energy effective theory for magnons and charge carriers in an antiferromagnet", Nuclear Physics B **729**, 317–360 (2005).

[328] C. Brügger, F. Kämpfer, M. Moser, M. Pepe, and U.-J. Wiese, "Two-hole bound states from a systematic low-energy effective field theory for magnons and holes in an antiferromagnet", Physical Review B **74**, 224432 (2006).

[329] W. P. Su, "Spin polarons in the two-dimensional Hubbard model: A numerical study", Physical Review B **37**, 9904–9906 (1988).

[330] D. Vilardi, C. Taranto, and W. Metzner, "Antiferromagnetic and d-wave pairing correlations in the strongly interacting two-dimensional Hubbard model from the functional renormalization group", Physical Review B **99**, 104501 (2019).

[331] G. Deutscher, "Coherence and single-particle excitations in the high-temperature superconductors", Nature **397**, 410–412 (1999).

[332] M. L. Tacon, A. Sacuto, A. Georges, G. Kotliar, Y. Gallais, D. Colson, and A. Forget, "Two energy scales and two distinct quasiparticle dynamics in the superconducting state of underdoped cuprates", Nature Physics **2**, 537–543 (2006).

[333] M. Brunner, F. F. Assaad, and A. Muramatsu, "Single-hole dynamics in the *t-J* model on a square lattice", Physical Review B **62**, 15480–15492 (2000).

[334] B. O. Wells, Z.-X. Shen, A. Matsuura, D. M. King, M. A. Kastner, M. Greven, and R. J. Birgeneau, "*E* versus k Relations and Many Body Effects in the Model Insulating Copper Oxide $Sr_2CuO_2Cl_2$", Physical Review Letters **74**, 964–967 (1995).

[335] S. Kunisada, S. Isono, Y. Kohama, S. Sakai, C. Bareille, S. Sakuragi, R. Noguchi, K. Kurokawa, K. Kuroda, Y. Ishida, S. Adachi, R. Sekine, T. K. Kim, C. Cacho, S. Shin, T. Tohyama, K. Tokiwa, and T. Kondo, "Observation of small Fermi pockets protected by clean CuO of a high Tc superconductor", Science **369**, 833–838 (2020).

[336] M. Sidler, P. Back, O. Cotlet, A. Srivastava, T. Fink, M. Kroner, E. Demler, and A. Imamoglu, "Fermi polaron-polaritons in charge-tunable atomically thin semiconductors", Nature Physics **13**, 255–261 (2016).

[337] I. Schwartz, Y. Shimazaki, C. Kuhlenkamp, K. Watanabe, T. Taniguchi, M. Kroner, and A. Imamoglu, "Electrically tunable Feshbach resonances in twisted bilayer semiconductors", Science **374**, 336–340 (2021).

[338] M. Wagner, R. Ołdziejewski, F. Rose, V. Köder, C. Kuhlenkamp, A. Imamoglu, and R. Schmidt, "Feshbach resonances of composite charge carrier states in atomically thin semiconductor heterostructures", arXiv **2310.08729** (2023).

[339] J. von Milczewski, X. Chen, A. Imamoglu, and R. Schmidt, "Superconductivity induced by strong electron-exciton coupling in doped atomically thin semiconductor heterostructures", arXiv **2310.10726** (2023).

[340] V. Crépel and L. Fu, "New mechanism and exact theory of superconductivity from strong repulsive interaction", Science Advances **7**, eabh2233 (2021).

[341] V. Crépel and L. Fu, "Spin-triplet superconductivity from excitonic effect in doped insulators", Proceedings of the National Academy of Sciences **119** (2022).

[342] H. Yang, H. Oh, and Y.-H. Zhang, "Strong pairing from doping-induced Feshbach resonance and second Fermi liquid through doping a bilayer spin-one Mott insulator: application to $La_3Ni_2O_7$", arXiv **2309.15095** (2023).

[343] J. van den Brink and O. P. Sushkov, "Single-hole Green's functions in insulating copper oxides at nonzero temperature", Physical Review B **57**, 3518–3524 (1998).

[344] K. J. von Szczepanski, P. Horsch, W. Stephan, and M. Ziegler, "Single-particle excitations in a quantum antiferromagnet", Physical Review B **41**, 2017–2029 (1990).

[345] C.-H. Chen, H.-B. Schüttler, and A. J. Fedro, "Hole excitation spectra in cuprate superconductors: a comparative study of single- and multiple-band strong-coupling theories", Physical Review B **41**, 2581–2584 (1990).

[346] M. D. Johnson, C. Gros, and K. J. von Szczepanski, "Geometry-controlled conserving approximations for the *t-J* model", Physical Review B **43**, 11207–11239 (1991).

[347] D. Poilblanc, T. Ziman, H. J. Schulz, and E. Dagotto, "Dynamical properties of a single hole in an antiferromagnet", Physical Review B **47**, 14267–14279 (1993).

[348] D. Poilblanc, H. J. Schulz, and T. Ziman, "Single-hole spectral density in an antiferromagnetic background", Physical Review B **47**, 3268–3272 (1993).

[349] E. Dagotto, R. Joynt, A. Moreo, S. Bacci, and E. Gagliano, "Strongly correlated electronic systems with one hole: dynamical properties", Physical Review B **41**, 9049–9073 (1990).

[350] M. M. Mohan and N. Kumar, "Spin singlet d wave hole pairing in the new high-Tc superconductors", Journal of Physics C: Solid State Physics **20**, L527–L531 (1987).

[351] E. Dagotto, A. Moreo, R. L. Sugar, and D. Toussaint, "Binding of holes in the Hubbard model", Physical Review B **41**, 811–814 (1990).

[352] S. R. White and D. J. Scalapino, "Hole and pair structures in the t-J model", Physical Review B **55**, 6504–6517 (1997).

[353] J. Sous, Y. He, and S. A. Kivelson, "Absence of a BCS-BEC crossover in the cuprate superconductors", npj Quantum Materials **8** (2023).

[354] D. M. Newns and N. Read, "Mean-field theory of intermediate valence/heavy fermion systems", Advances in Physics **36**, 799–849 (1987).

[355] P. Coleman, "Mixed valence as an almost broken symmetry", Physical Review B **35**, 5072–5116 (1987).

[356] G. Kotliar and J. Liu, "Superexchange mechanism and d-wave superconductivity", Phys. Rev. B **38**, 5142–5145 (1988).

[357] L. F. Feiner, J. H. Jefferson, and R. Raimondi, "Effective single-band models for the high-Tc cuprates. I. Coulomb interactions", Physical Review B **53**, 8751–8773 (1996).

[358] Q.-H. Wang, J. H. Han, and D.-H. Lee, "Pairing near the Mott insulating limit", Physical Review B **65**, 054501 (2001).

[359] A. Greco, H. Yamase, and M. Bejas, "Plasmon excitations in layered high-T_c cuprates", Physical Review B **94**, 075139 (2016).

[360] A. Greco, H. Yamase, and M. Bejas, "Origin of high-energy charge excitations observed by resonant inelastic X-ray scattering in cuprate superconductors", Communications Physics **2** (2019).

[361] L. Zinni, M. Bejas, and A. Greco, "Superconductivity with and without glue and the role of the double-occupancy forbidding constraint in the *t-J-V* model", Physical Review B **103**, 134504 (2021).

[362] M. Hepting, T. D. Boyko, V. Zimmermann, M. Bejas, Y. E. Suyolcu, P. Puphal, R. J. Green, L. Zinni, J. Kim, D. Casa, M. H. Upton, D. Wong, C. Schulz, M. Bartkowiak, K. Habicht, E. Pomjakushina, G. Cristiani, G. Logvenov, M. Minola, H. Yamase, A. Greco, and B. Keimer, "Evolution of plasmon excitations across the phase diagram of the cuprate superconductor $La_{2-x}Sr_xCuO_4$", Physical Review B **107**, 214516 (2023).

[363] I. Battisti, V. Fedoseev, K. M. Bastiaans, A. de la Torre, R. S. Perry, F. Baumberger, and M. P. Allan, "Poor electronic screening in lightly doped Mott insulators observed with scanning tunneling microscopy", Physical Review B **95**, 235141 (2017).

[364] Q. Chen, Z. Wang, R. Boyack, and K. Levin, "Test for BCS-BEC crossover in the cuprate superconductors", npj Quantum Materials **9** (2024).

[365] J. Mesot, M. R. Norman, H. Ding, M. Randeria, J. C. Campuzano, A. Paramekanti, H. M. Fretwell, A. Kaminski, T. Takeuchi, T. Yokoya, T. Sato, T. Takahashi, T. Mochiku, and K. Kadowaki, "Superconducting Gap Anisotropy and Quasiparticle Interactions: A Doping Dependent Photoemission Study", Physical Review Letters **83**, 840–843 (1999).

[366] J. Berakdar, "Emission of correlated electron pairs following single-photon absorption by solids and surfaces", Physical Review B **58**, 9808–9816 (1998).

[367] F. Mahmood, T. Devereaux, P. Abbamonte, and D. K. Morr, "Distinguishing finite-momentum superconducting pairing states with two-electron photoemission spectroscopy", Physical Review B **105**, 064515 (2022).

[368] Y. Su and C. Zhang, "Coincidence angle-resolved photoemission spectroscopy: proposal for detection of two-particle correlations", Physical Review B **101**, 205110 (2020).

[369] J. A. Sobota, Y. He, and Z.-X. Shen, "Angle-resolved photoemission studies of quantum materials", Reviews of Modern Physics **93**, 025006 (2021).

[370] J. T. Anderson, R. V. Carlson, and A. M. Goldman, "Pair tunneling as a probe of order-parameter fluctuations in superconductors: zero magnetic field effects", Journal of Low Temperature Physics **8**, 29–46 (1972).

[371] N. Bergeal, J. Lesueur, M. Aprili, G. Faini, J. P. Contour, and B. Leridon, "Pairing fluctuations in the pseudogap state of copper-oxide superconductors probed by the Josephson effect", Nature Physics **4**, 608–611 (2008).

[372] D. J. Scalapino, "Pair Tunneling as a Probe of Fluctuations in Superconductors", Physical Review Letters **24**, 1052–1055 (1970).

[373] K. M. Bastiaans, D. Cho, T. Benschop, I. Battisti, Y. Huang, M. S. Golden, Q. Dong, Y. Jin, J. Zaanen, and M. P. Allan, "Charge trapping and super-Poissonian noise centres in a cuprate superconductor", Nature Physics **14**, 1183–1187 (2018).

[374] K. M. Bastiaans, D. Chatzopoulos, J.-F. Ge, D. Cho, W. O. Tromp, J. M. van Ruitenbeek, M. H. Fischer, P. J. de Visser, D. J. Thoen, E. F. C. Driessen, T. M. Klapwijk, and M. P. Allan, "Direct evidence for Cooper pairing without a spectral gap in a disordered superconductor above T_c", Science **374**, 608–611 (2021).

[375] P. Zhou, L. Chen, Y. Liu, I. Sochnikov, A. T. Bollinger, M.-G. Han, Y. Zhu, X. He, I. Božović, and D. Natelson, "Electron pairing in the pseudogap state revealed by shot noise in copper oxide junctions", Nature **572**, 493–496 (2019).

[376] D. Fausti, R. I. Tobey, N. Dean, S. Kaiser, A. Dienst, M. C. Hoffmann, S. Pyon, T. Takayama, H. Takagi, and A. Cavalleri, "Light-Induced Superconductivity in a Stripe-Ordered Cuprate", Science **331**, 189–191 (2011).

[377] R. Caivano, M. Fratini, N. Poccia, A. Ricci, A. Puri, Z.-A. Ren, X.-L. Dong, J. Yang, W. Lu, Z.-X. Zhao, L. Barba, and A. Bianconi, "Feshbach resonance and mesoscopic phase separation near a quantum critical point in multiband FeAs-based superconductors", Superconductor Science and Technology **22**, 014004 (2008).

[378] R. H. Squire and N. H. March, "Microscopic model of cuprate superconductivity", International Journal of Quantum Chemistry **110**, 2808–2822 (2010).

[379] V. Crépel, D. Guerci, J. Cano, J. Pixley, and A. Millis, "Topological Superconductivity in Doped Magnetic Moiré Semiconductors", Physical Review Letters **131**, 056001 (2023).

[380] N. P. Armitage, F. Ronning, D. H. Lu, C. Kim, A. Damascelli, K. M. Shen, D. L. Feng, H. Eisaki, Z.-X. Shen, P. K. Mang, N. Kaneko, M. Greven, Y. Onose, Y. Taguchi, and Y. Tokura, "Doping Dependence of an n-Type Cuprate Superconductor Investigated by Angle-Resolved Photoemission Spectroscopy", Physical Review Letters **88**, 257001 (2002).

[381] E. G. Moon and S. Sachdev, "Underdoped cuprates as fractionalized Fermi liquids: Transition to superconductivity", Physical Review B **83**, 224508 (2011).

[382] S. Chatterjee and S. Sachdev, "Fractionalized Fermi liquid with bosonic chargons as a candidate for the pseudogap metal", Physical Review B **94**, 205117 (2016).

[383] S. Paeckel, T. Köhler, A. Swoboda, S. R. Manmana, U. Schollwöck, and C. Hubig, "Time-evolution methods for matrix-product states", Annals of Physics **411**, 167998 (2019).

[384] A. J. Millis, H. Monien, and D. Pines, "Phenomenological model of nuclear relaxation in the normal state of $YBa_2Cu_3O_7$", Physical Review B **42**, 167–178 (1990).

[385] J. Schmalian, D. Pines, and B. Stojković, "Weak pseduogap behavior in the underdoped cuprate superconductors", Journal of Physics and Chemistry of Solids **59**, 1764–1768 (1998).

[386] A. Abanov, A. V. Chubukov, and J. Schmalian, "Quantum-critical theory of the spin-fermion model and its application to cuprates: normal state analysis", Advances in Physics **52**, 119–218 (2003).

[387] G. Ji, M. Xu, L. H. Kendrick, C. S. Chiu, J. C. Brüggenjürgen, D. Greif, A. Bohrdt, F. Grusdt, E. Demler, M. Lebrat, and M. Greiner, "Coupling a Mobile Hole to an Antiferromagnetic Spin Background: Transient Dynamics of a Magnetic Polaron", Physical Review X **11** (2021).

[388] B. D. Simons and J. M. F. Gunn, "Internal structure of hole quasiparticles in antiferromagnets", Physical Review B **41**, 7019–7027 (1990).

[389] B. I. Shraiman and E. D. Siggia, "Mobile Vacancies in a Quantum Heisenberg Antiferromagnet", Physical Review Letters **61**, 467–470 (1988).

[390] T. D. Lee, F. E. Low, and D. Pines, "The Motion of Slow Electrons in a Polar Crystal", Physical Review **90**, 297–302 (1953).

[391] B. Ponsioen, S. S. Chung, and P. Corboz, "Period 4 stripe in the extended two-dimensional Hubbard model", Physical Review B **100**, 195141 (2019).

[392] M. Xu, L. H. Kendrick, A. Kale, Y. Gang, G. Ji, R. T. Scalettar, M. Lebrat, and M. Greiner, "Frustration- and doping-induced magnetism in a Ferm-Hubbard simulator", Nature **620**, 971–976 (2023).

[393] X. J. Zhou, Z. Hussain, and Z.-X. Shen, "High resolution angle-resolved photoemission study of high temperature superconductors: charge-ordering, bilayer splitting and electron–phonon coupling", Journal of Electron Spectroscopy and Related Phenomena **126**, 145–162 (2002).

[394] J. Zwettler, H. Amir, F. H. Marashi, N. Bielinski, S. Patel, P. Mahaadev, Y. Huang, D. Chaudhuri, X. Guo, T. C. Chiang, D. K. Morr, P. Abbamonte, and F. Mahmood, "An extreme ultraviolet 2e-ARPES setup based on dual time-of-flight analyzers", Journal of Electron Spectroscopy and Related Phenomena **270**, 147417 (2024).

[395] L. W. Cheuk, M. A. Nichols, K. R. Lawrence, M. Okan, H. Zhang, E. Khatami, N. Trivedi, T. Paiva, M. Rigol, and M. W. Zwierlein, "Observation of spatial charge and spin correlations in the 2D Fermi-Hubbard model", Science **353**, 1260–1264 (2016).

[396] D. Mitra, P. T. Brown, E. Guardado-Sanchez, S. S. Kondov, T. Devakul, D. A. Huse, P. Schauß, and W. S. Bakr, "Quantum gas microscopy of an attractive Fermi-Hubbard system", Nature Physics **14**, 173–177 (2017).

[397] H. Sun, B. Yang, H.-Y. Wang, Z.-Y. Zhou, G.-X. Su, H.-N. Dai, Z.-S. Yuan, and J.-W. Pan, "Realization of a bosonic antiferromagnet", Nature Physics **17**, 990–994 (2021).

[398] P. N. Jepsen, W. W. Ho, J. Amato-Grill, I. Dimitrova, E. Demler, and W. Ketterle, "Transverse Spin Dynamics in the Anisotropic Heisenberg Model Realized with Ultracold Atoms", Physical Review X **11**, 041054 (2021).

[399] S. Geier, "Shaping the Hamiltonian of many-body spin systems on a Rydberg-atom quantum simulator", PhD Thesis (Dec. 2023).

[400] A. V. Gorshkov, S. R. Manmana, G. Chen, J. Ye, E. Demler, M. D. Lukin, and A. M. Rey, "Tunable Superfluidity and Quantum Magnetism with Ultracold Polar Molecules", Physical Review Letters **107**, 115301 (2011).

[401] J. R. Coulthard, S. R. Clark, S. Al-Assam, A. Cavalleri, and D. Jaksch, "Enhancement of superexchange pairing in the periodically driven Hubbard model", Physical Review B **96**, 085104 (2017).

[402] Y. Cao, V. Fatemi, S. Fang, K. Watanabe, T. Taniguchi, E. Kaxiras, and P. Jarillo-Herrero, "Unconventional superconductivity in magic-angle graphene superlattices", Nature **556**, 43–50 (2018).

[403] J. Šmakov, C. D. Batista, and G. Ortiz, "Stripes, Topological Order, and Deconfinement in a Planar t-J_z Model", Physical Review Letters **93**, 067201 (2004).

[404] M. Boninsegni and N. V. Prokof'ev, "Phase diagram of an anisotropic bosonic t-J model", Physical Review B **77**, 092502 (2008).

[405] K. Aoki, K. Sakakibara, I. Ichinose, and T. Matsui, "Magnetic order, Bose-Einstein condensation, and superfluidity in a bosonic t-J model of CP^1 spinons and doped Higgs holons", Physical Review B **80**, 144510 (2009).

[406] Y. Nakano, T. Ishima, N. Kobayashi, K. Sakakibara, I. Ichinose, and T. Matsui, "Finite-temperature phase diagram of the three-dimensional hard-core bosonic t-J model", Physical Review B **83**, 235116 (2011).

[407] Y. Nakano, T. Ishima, N. Kobayashi, T. Yamamoto, I. Ichinose, and T. Matsui, "Finite-temperature phase diagram of two-component bosons in a cubic optical lattice: Three-dimensional t-J model of hard-core bosons", Physical Review A **85**, 023617 (2012).

[408] S. R. White, "Density matrix formulation for quantum renormalization groups", Physical Review Letters **69**, 2863–2866 (1992).

[409] C. Hubig, "Symmetry-protected tensor networks", PhD thesis (Ludwig-Maximilians Universität", 2017).

[410] C. Hubig, F. Lachenmaier, N.-O. Linden, T. Reinhard, L. Stenzel, A. Swoboda, and M. Grundner, "The SYTEN Toolkit",

[411] X. Lu, F. Chen, W. Zhu, D. N. Sheng, and S.-S. Gong, "Emergent Superconductivity and Competing Charge Orders in Hole-Doped Square-Lattice *t-J* Model", Physical Review Letters **132**, 066002 (2024).

[412] A. J. Park, L. R. B. Picard, G. E. Patenotte, J. T. Zhang, T. Rosenband, and K.-K. Ni, "Extended Rotational Coherence of Polar Molecules in an Elliptically Polarized Trap", Physical Review Letters **131**, 183401 (2023).

[413] K.-K. Ni, T. Rosenband, and D. D. Grimes, "Dipolar exchange quantum logic gate with polar molecules", Chemical Science **9**, 6830–6838 (2018).

[414] T. Rosenband, D. D. Grimes, and K.-K. Ni, "Elliptical polarization for molecular Stark shift compensation in deep optical traps", Optics Express **26**, 19821 (2018).

[415] B.-Y. Sun, N. Goldman, M. Aidelsburger, and M. Bukov, "Engineering and Probing Non-Abelian Chiral Spin Liquids Using Periodically Driven Ultracold Atoms", PRX Quantum **4**, 020329 (2023).

[416] J. Zeiher, R. van Bijnen, P. Schauß, S. Hild, J.-y. Choi, T. Pohl, I. Bloch, and C. Gross, "Many-body interferometry of a Rydberg-dressed spin lattice", Nature Physics **12**, 1095–1099 (2016).

[417] S. Whitlock, A. W. Glaetzle, and P. Hannaford, "Simulating quantum spin models using Rydberg-excited atomic ensembles in magnetic microtrap arrays", Journal of Physics B: Atomic, Molecular and Optical Physics **50**, 074001 (2017).

[418] V. Elser, D. A. Huse, B. I. Shraiman, and E. D. Siggia, "Ground state of a mobile vacancy in a quantum antiferromagnet: small-cluster study", Physical Review B **41**, 6715–6723 (1990).

[419] A. J. Daley, "Quantum trajectories and open many-body quantum systems", Advances in Physics **63**, 77–149 (2014).

[420] K. Winkler, G. Thalhammer, F. Lang, R. Grimm, J. Hecker Denschlag, A. J. Daley, A. Kantian, H. P. Büchler, and P. Zoller, "Repulsively bound atom pairs in an optical lattice", Nature **441**, 853–856 (2006).

[421] M. Knap, A. Kantian, T. Giamarchi, I. Bloch, M. D. Lukin, and E. Demler, "Probing Real-Space and Time-Resolved Correlation Functions with Many-Body Ramsey Interferometry", Physical Review Letters **111**, 147205 (2013).

[422] M. W. Doherty, N. B. Manson, P. Delaney, F. Jelezko, J. Wrachtrup, and L. C. L. Hollenberg, "The nitrogen-vacancy colour centre in diamond", Physics Reports **528**, 1–45 (2013).

[423] J. Tilly, H. Chen, S. Cao, D. Picozzi, K. Setia, Y. Li, E. Grant, L. Wossnig, I. Rungger, G. H. Booth, and J. Tennyson, "The Variational Quantum Eigensolver: A review of methods and best practices", Physics Reports **986**, 1–128 (2022).

[424] S. Hirthe, T. Chalopin, D. Bourgund, P. Bojović, A. Bohrdt, E. Demler, F. Grusdt, I. Bloch, and T. A. Hilker, "Magnetically mediated hole pairing in fermionic ladders of ultracold atoms", Nature **613**, 463–467 (2023).

[425] H. Sun, M. Huo, X. Hu, J. Li, Z. Liu, Y. Han, L. Tang, Z. Mao, P. Yang, B. Wang, J. Cheng, D.-X. Yao, G.-M. Zhang, and M. Wang, "Signatures of superconductivity near 80K in a nickelate under high pressure", Nature **621**, 493–498 (2023).

[426] N. N. Wang, M. W. Yang, Z. Yang, K. Y. Chen, H. Zhang, Q. H. Zhang, Z. H. Zhu, Y. Uwatoko, L. Gu, X. L. Dong, J. P. Sun, K. J. Jin, and J.-G. Cheng, "Pressure-induced monotonic enhancement of Tc to over 30K in superconducting $Pr_{0.82}Sr_{0.18}NiO_2$ thin films", Nature Communications **13** (2022).

[427] H. Oh and Y.-H. Zhang, "Type-II $t - J$ model and shared superexchange coupling from Hund's rule in superconducting $La_3Ni_2O_7$", Physical Review B **108**, 174511 (2023).

[428] W. Wú, Z. Luo, D.-X. Yao, and M. Wang, "Superexchange and charge transfer in the nickelate superconductor La3Ni2O7 under pressure", Science China Physics, Mechanics & Astronomy **67** (2024).

[429] X.-Z. Qu, D.-W. Qu, J. Chen, C. Wu, F. Yang, W. Li, and G. Su, "Bilayer $t-J-J_{\perp}$ Model and Magnetically Mediated Pairing in the Pressurized Nickelate $La_3Ni_2O_7$", Physical Review Letters **132**, 036502 (2024).

[430] C. Lu, Z. Pan, F. Yang, and C. Wu, "Interlayer-Coupling-Driven High-Temperature Superconductivity in La3Ni2O7 under Pressure", Physical Review Letters **132**, 146002 (2024).

[431] H. Schlömer, U. Schollwöck, F. Grusdt, and A. Bohrdt, "Superconductivity in the pressurized nickelate $La_3Ni_2O_7$ in the vicinity of a BEC-BCS crossover", arXiv **2311.03349** (2023).

[432] C. Kuhlenkamp, M. Knap, M. Wagner, R. Schmidt, and A. Imamoglu, "Tunable Feshbach Resonances and Their Spectral Signatures in Bilayer Semiconductors", Physical Review Letters **129**, 037401 (2022).

[433] K. Slagle and L. Fu, "Charge transfer excitations, pair density waves, and superconductivity in moiré materials", Physical Review B **102**, 235423 (2020).

[434] C. Zerba, C. Kuhlenkamp, A. Imamoglu, and M. Knap, "Realizing Topological Superconductivity in Tunable Bose-Fermi Mixtures with Transition Metal Dichalcogenide Heterostructures", arXiv **2310.10720** (2023).

[435] T. S. Kuhn, *The Structure of Scientific Revolutions*, 3rd Edition (University of Chicago Press, 1996).

[436] A. V. Gorshkov, M. Hermele, V. Gurarie, C. Xu, P. S. Julienne, J. Ye, P. Zoller, E. Demler, M. D. Lukin, and A. M. Rey, "Two-orbital SU(N) magnetism with ultracold alkaline-earth atoms", Nature Physics **6**, 289–295 (2010).